STAB

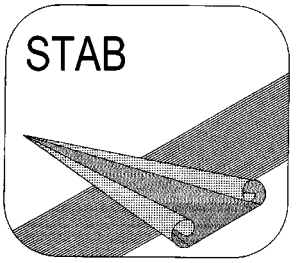

J A H R E S B E R I C H T

2025

zum

22. STAB-Workshop

10. - 12. November 2025

Göttingen

„Deutsche Strömungsmechanische Arbeitsgemeinschaft, STAB“

INHALT

Mitteilungen der Geschäftsstelle

Die STAB-Jahresberichte werden als Sammlung der Kurzfassungen der Vorträge an die Teilnehmer/innen der abwechselnd stattfindenden Symposien und Workshops verteilt. So erscheint der vorliegende STAB-Jahresbericht 2025 anlässlich des 22. STAB-Workshops, der vom 10. bis 12. November 2025 in Göttingen stattfindet. In diesem Jahr findet der Workshop an drei aufeinanderfolgenden Tagen statt, da er um eine Sonder-Session zum Thema „100 Years of Ludwig Prandtl's Mixing Length Model" erweitert wird.

Der Bericht enthält 73 „Mitteilungen" über Arbeiten aus den Fachgruppen, die beim Workshop vorgestellt werden. Den „Mitteilungen" ist ein Inhaltsverzeichnis (Seite 14 bis Seite 19) vorangestellt, das nach Fachgruppen gegliedert ist. Innerhalb der Fachgruppen sind die Beiträge alphabetisch nach Autor/in geordnet. Die Beiträge verteilen sich (bezogen auf die Erstautorin/den Erstautor) zu 5 % auf die Industrie, zu 44 % auf Hochschulen und zu 51 % auf Forschungseinrichtungen (DLR, DNW, ISL, etc.). Die Autoren und Autorinnen dieses Berichts sind auf den Seiten 166 und 167 aufgeführt.

Die Jahresberichte werden nur an den tatsächlich daran interessierten Personenkreis verteilt. Alle Teilnehmer/innen des diesjährigen STAB-Workshops erhalten ein Exemplar zur Veranstaltung.

Dieser Jahresbericht erscheint in einer Auflage von 140 Exemplaren. Erfahrungsgemäß sind einige Restexemplare bis zum Ende des jeweiligen Jahres verfügbar.

Der jeweils aktuelle Jahresbericht ist auch unter dem unten angegebenen Link als Datei zum Herunterladen verfügbar. Bei Interesse können STAB-Jahresberichte zurückliegender Jahre (ab 1988) bei der STAB-Geschäftsstelle (stab@dlr.de) angefragt werden.

Aktualisierte Informationen über STAB finden Sie auch unter:

STAB - Deutsche Strömungsmechanische Arbeitsgemeinschaft (dlr.de)

Göttingen, im Oktober 2025

Zielsetzungen, chronologische Entwicklung und Organisation

Die Arbeitsgemeinschaft „Strömungen mit Ablösung“ (STAB) wurde 1979 auf Initiative der Deutschen Gesellschaft für Luft- und Raumfahrt (DGLR) - Lilienthal-Oberth, e.V. - von Strömungsforschern, Aerodynamikern und Luftfahrtingenieuren des DLR, der Hochschulen und der Industrie gegründet.

Sie entstand aus „dem gemeinschaftlichen Bestreben, die Strömungsforschung in Deutschland generell zu fördern und durch Konzentration auf ein wirtschaftlich und forschungspolitisch zukunftsträchtiges Teilgebiet zu vertiefen“ (Auszug aus der Präambel der Verfahrensordnung der STAB).

In Zeiten knapper werdender Budgets bei gleichzeitig massiv steigendem Wettbewerbsdruck sind diese Ansätze notwendiger denn je. Aber auch die öffentlichen Geldgeber setzen diese Kooperationsbereitschaft inzwischen voraus. Da dieser Leitgedanke der STAB inzwischen auf andere Weise verfolgt wird, konzentriert sich die STAB verstärkt auf Fachveranstaltungen.

Die Arbeitsgemeinschaft STAB ist der DGLR als ‚Kompetenznetzwerk’ angegliedert.

Auf der Homepage der DGLR ist die STAB zu finden unter:
https://www.dglr.de/vernetzen/fachbereiche/kompetenznetzwerk-stab/

Die STAB vereint alle wichtigen Gebiete der Strömungsmechanik - insbesondere der Luft- und Raumfahrt - aus Grundlagenforschung, Großforschung und Industrie in Deutschland. Die Gründung basierte auf der Idee, Forschungsverbünde aus Industrie, Hochschulen und Großforschung zu einem hochaktuellen Fachthema zu organisieren, das damals als „Strömungen mit Ablösungen“ identifiziert wurde. In den Folgejahren wurden weitere strömungsmechanische Fragestellungen aufgegriffen, die STAB zu einem in der Fachwelt bekannten Namen werden ließen. So werden heute nicht nur die klassischen Themen der Strömungsmechanik behandelt, sondern auch Probleme aus dem Fahrzeugbau, der Gebäudeaerodynamik, der Verfahrenstechnik, dem Motorenbau usw. diskutiert.

Die Programmleitung hat im November 2000 beschlossen, in Zukunft auf den Zusatz „AG“ im Namen zu verzichten.

Die für die Öffentlichkeit relevanten wissenschaftlichen Aktivitäten spiegeln sich in der folgenden chronologischen Entwicklung wider:

DGLR-Symposium „Forschung und Entwicklung auf dem Gebiet der Strömungsmechanik und Aerodynamik in der Bundesrepublik Deutschland“	Bonn, 29.11.-01.12.1978
„Gespräch über Strömungsforschung in Deutschland“	Ottobrunn, 30.01.1979
„Memorandum über zukünftige nationale Zusammenarbeit in der Strömungsforschung, insbesondere der Aerodynamik auf dem Gebiet der Strömungen mit Ablösung“	Oktober 1979
Programmpräsentation anlässlich der BDLI-Jahrestagung	Bonn, 01.07.1980

Programm der Arbeitsgemeinschaft „Strömungen mit Ablösung“	September 1980
Programmpräsentation im Bundesministerium für Forschung und Technologie	Bonn, 19.03.1981
Konstituierung des Kuratoriums und Neuorganisation der Arbeitsgemeinschaft „Strömungen mit Ablösung" (AG STAB)	Köln-Porz, 23.02.1982
Konstituierung von Programmleitung/Programmausschuss	Göttingen, 24.03.1982
Erfassung STAB-relevanter Aktivitäten in der Bundesrepublik Deutschland (Stand Mitte 1981)	April 1982
Fachtagung anlässlich der ILA '82 „Strömungen mit Ablösung“	Hannover, 19.05.1982
Neue Impulse für die Strömungsforschung- und Aerodynamik; Vortrag von H.-G. Knoche, DGLR-Jahrestagung	Hamburg, 01.-03.10.1984
DGLR Workshop „2D-Messtechnik“	Markdorf, 18.-19.10.1988

Symposium

1. DGLR-Fachsymposium	München, 19. - 20.09.1979
2. DGLR- Fachsymposium	Bonn, 30.06. - 01.07.1980
3. DGLR- Fachsymposium	Stuttgart, 23. - 25.11.1981
4. DGLR- Fachsymposium	Göttingen, 10. - 12.10.1983
5. DGLR- Fachsymposium	München, 09. - 10.10.1986
6. DGLR-Fachsymposium	Braunschweig,08. - 10.11.1988
7. DGLR- Fachsymposium	Aachen, 07. - 09.11.1990
8. DGLR- Fachsymposium	Köln-Porz, 10. - 12.11.1992
9. DGLR- Fachsymposium	Erlangen, 04. - 07.10.1994
10. DGLR- Fachsymposium	Braunschweig,11. - 13.11.1996
11. DGLR- Fachsymposium	Berlin, 10. - 12.11.1998
12. DGLR- Fachsymposium	Stuttgart, 15. - 17.11.2000
13. DGLR- Fachsymposium	München, 13. - 15.11.2002
14. DGLR- Fachsymposium	Bremen, 16. - 18.11.2004

15. DGLR- Fachsymposium	Darmstadt, 29.11. - 01.12.2006
16. DGLR- Fachsymposium	Aachen, 03. - 04.11.2008
17. DGLR- Fachsymposium	Berlin, 09. - 10.11.2010
18. DGLR- Fachsymposium	Stuttgart, 06. - 07.11.2012
19. DGLR- Fachsymposium	München, 04. - 05.11.2014
20. DGLR- Fachsymposium	Braunschweig,08. - 09.11.2016
21. DGLR- Fachsymposium	Darmstadt, 06. - 07.11.2018
22. DGLR- Fachsymposium	Präsenzveranstaltung aufgrund der Corona-Pandemie abgesagt
23. DGLR-Fachsymposium	Berlin, 09. - 10.11.2022
23. DGLR-Fachsymposium	Regensburg, 13.-14.11.2024

Workshop

1. STAB-Workshop	Göttingen, 07. - 08.03.1983
2. STAB-Workshop	Köln-Porz, 18. - 20.09.1984
3. STAB-Workshop	Göttingen, 10. - 11.11.1987
4. STAB-Workshop	Göttingen, 08. - 10.11.1989
5. STAB-Workshop	Göttingen, 13. - 15.11.1991
6. STAB-Workshop	Göttingen, 10. - 12.11.1993
7. STAB-Workshop	Göttingen, 14. - 16.11.1995
8. STAB-Workshop	Göttingen, 11. - 13.11.1997
9. STAB-Workshop	Göttingen, 09. - 11.11.1999
10. STAB-Workshop	Göttingen, 14. - 16.11.2001
11. STAB-Workshop	Göttingen, 04. - 06.11.2003
12. STAB-Workshop	Göttingen, 08. - 09.11.2005
13. STAB-Workshop	Göttingen, 14. - 15.11.2007
14. STAB-Workshop	Göttingen, 11. - 12.11.2009
15. STAB-Workshop	Göttingen, 09. - 10.11.2011
16. STAB-Workshop	Göttingen, 12. - 13.11.2013
17. STAB-Workshop	Göttingen, 10. - 11.11.2015
18. STAB-Workshop	Göttingen, 07. - 08.11.2017

19. STAB-Workshop	Göttingen, 05. - 06.11.2019
20. STAB-Workshop	Göttingen, 16.- 17.11.2021
21. STAB-Workshop	Göttingen, 07. - 08.11.2023

Ein Kurs über „Application of Particle Image Velocimetry, PIV“
findet seit 1993 regelmäßig im DLR in Göttingen statt,
letztmalig am: 17.03. - 21.03.2025

Der nächste Kurs findet vom 16. bis 20. März 2026 statt : PIV-Kurs 2026

Die Symposiums-Tagungsbände durchlaufen einen Begutachtungsprozess.
Die Bände der letzten Jahre finden Sie hier aufgelistet.

- Notes on Numerical Fluid Mechanics, Vol. 60; Eds.: H. Körner, R. Hilbig; Friedr. Vieweg & Sohn Verlagsgesellschaft mbH, Braunschweig/Wiesbaden 1997
- Notes on Numerical Fluid Mechanics, Vol. 72; Eds.: W. Nitsche, H.-J. Heinemann, R. Hilbig; Springer-Verlag Berlin Heidelberg 1999
- Notes on Numerical Fluid Mechanics, Vol. 77; Eds.: S. Wagner, U. Rist, H.-J. Heinemann, R. Hilbig; Springer-Verlag Berlin Heidelberg 2002
- Notes on Numerical Fluid Mechanics and Multidisciplinary Design, Vol. 87; Eds.: Chr. Breitsamter, B. Laschka, H.-J. Heinemann, R. Hilbig; Springer-Verlag Berlin Heidelberg 2004
- Notes on Numerical Fluid Mechanics and Multidisciplinary Design, Vol. 92; Eds.: H. J. Rath, C. Holze, H.-J. Heinemann, R. Henke, H. Hönlinger; Springer-Verlag, Berlin Heidelberg 2006
- Notes on Numerical Fluid Mechanics and Multidisciplinary Design, Vol. 96; Eds.: C. Tropea, S. Jakirlic, H.-J. Heinemann, R. Henke, H. Hönlinger; Springer-Verlag Berlin Heidelberg 2008
- Notes on Numerical Fluid Mechanics and Multidisciplinary Design, Vol. 112; Eds.: A. Dillmann, G. Heller, M. Klaas, H.-P. Kreplin, W. Nitsche, W. Schröder; Springer Berlin Heidelberg 2010
- Notes on Numerical Fluid Mechanics and Multidisciplinary Design, Vol. 121; Eds.: A. Dillmann, G. Heller, H.-P. Kreplin, W. Nitsche, I. Peltzer; Springer-Verlag Berlin Heidelberg 2013
- Notes on Numerical Fluid Mechanics and Multidisciplinary Design, Vol. 124; Eds.: A. Dillmann, G. Heller, E. Krämer, H.-P. Kreplin, W. Nitsche, U. Rist; Springer International Publishing Switzerland, 2014
- Notes on Numerical Fluid Mechanics and Multidisciplinary Design, Vol. 132; Eds.: A. Dillmann, G. Heller, E. Krämer, C. Wagner, C. Breitsamter; Springer International Publishing Switzerland 2016
- Notes on Numerical Fluid Mechanics and Multidisciplinary Design, Vol. 136; Eds.: A. Dillmann, G. Heller, E. Krämer, C. Wagner, S. Bansmer, R. Radespiel, R. Semaan; Springer International Publishing AG 2018
- Notes on Numerical Fluid Mechanics and Multidisciplinary Design, Vol. 142; Eds.: A. Dillmann, G. Heller, E. Krämer, C. Wagner, C. Tropea, S. Jakirlic; Springer Nature Switzerland AG 2020
- Notes on Numerical Fluid Mechanics and Multidisciplinary Design, Vol. 151, Eds.: A. Dillmann, G. Heller, E. Krämer, C. Wagner; Springer Nature Switzerland AG 2021
- Notes on Numerical Fluid Mechanics and Multidisciplinary Design, Vol. 154 Eds.: A. Dillmann, G. Heller, E. Krämer, C. Wagner, J. Weiss; Springer Nature Switzerland AG 2024

Vorschau:

24. DGLR-Fachsymposium	26. - 28. November 2026, Aachen
Kurs „ Application of Particle Image Velocimetry, PIV”	16. - 20. März 2026, Göttingen

Programmleitung

Prof. Dr. C. Breitsamter
christian.breitsamter@tum.de
(Sprecher)
Technische Universität München
Tel.: 089 289-16137

Prof. Dr. A. Dillmann
andreas.dillmann@dlr.de
(Sprecher)
DLR, Göttingen
Tel.: 0551 709-2177

Dr. G. Heller
gerd.heller@airbus.com
(Sprecher)
Airbus, Manching
Tel.: 08459-8112582

Prof. Dr. J. Fröhlich
jochen.froehlich@tu-dresden.de
TU Dresden
Tel.: 0351 463-37607

Dr. R. Höld
roland.hoeld@mbda-systems.de
MBDA Deutschland GmbH,
Schrobenhausen
Tel.: 08252 99-8845

Prof. Dr. E. Krämer
kraemer@iag.uni-stuttgart.de
Universität Stuttgart
Tel.: 0711 685-63401

Prof. Dr. W. Schröder
office@aia.rwth-aachen.de
RWTH, Aachen
Tel.: 0241 80-95410

Prof. Dr. C. Stemmer
christian.stemmer@tum.de
Technische Universität München
Tel.: 089 289-16142

Prof. Dr. L. Tichy
lorenz.tichy@dlr.de
DLR, Göttingen
Tel.: 0551 709-2341

Prof. Dr. Kai Richter
kai.richter@dlr.de
DLR, Braunschweig
Tel.: 0531 295-2400

Fachgruppen	**Sprecher:**
Aeroelastik und Strukturdynamik*	Prof. Dr. L. Tichy (DLR, Göttingen) Tel.: 0551 709-2341 E-Mail: Lorenz.Tichy@dlr.de
Experimentelle Aerodynamik*	Prof. Dr. C. Breitsamter (Technische Universität München) Tel.: 089 289-16137 E-Mail: Christian.Breitsamter@tum.de
Hyperschallaerothermodynamik	Dr. B. Reimann (DLR, Braunschweig) Tel.: 0531 295-3319 E-Mail: Bodo.Reimann@DLR.de und Dr. M. Konopka (ArianeGroup GmbH, Bremen) Tel.: 0421 4372-4788 E-Mail: martin.konopka@ariane.group
Multidisziplinäre Optimierung	Dr. M. Hepperle (DLR, Braunschweig) Tel.: 0531 295-3337 E-Mail: Martin.Hepperle@dlr.de und Dipl.-Ing. D. Reckzeh (Airbus, Bremen) Tel.: 0421 538-2136 E-Mail: Daniel.Reckzeh@airbus.com
Numerische Aerodynamik*	Dr. C. Grabe (DLR, Göttingen) Tel.: 0551 709-2628 E-Mail: Cornelia.Grabe@dlr.de
Strömungsakustik*	Prof. Dr. J. Delfs (DLR, Braunschweig) Tel.: 0531 295-2170 E-Mail: Jan.Delfs@dlr.de
Strömungsbeeinflussung	Dr. A. Büscher (Airbus, Bremen) Tel.: 0172 8468 782 E-Mail: Alexander.Buescher@airbus.com
Turbulenz und Transition	Prof. Dr. W. Schröder (RWTH Aachen) Tel.: 0241 80-95410 E-Mail: office@aia.rwth-aachen.de und Prof. Dr. N. Adams (Technische Universität München) Tel.: 089 289-16120 E-Mail: Nikolaus.Adams@tum.de

*assoziierte DGLR-Fachkreise
grundlagenorientiert

Fachgruppen	**Sprecher:**
Allgemeine Strömungstechnik	Dr. P. Bahavar (DLR, Göttingen) Tel.: 0551 709-2306 E-Mail: Philipp.Bahavar@dlr.de
Aerodynamik bodengebundener Fahrzeuge	Dr. A. Wäschle (Mercedes-Benz AG, Sindelfingen) Tel: 0151 586-26046 E-Mail: alexander.waeschle@mercedes-benz.com
Bio- und Mikrofluidmechanik	Prof. Dr. L. Krenkel (OTH Regensburg) Tel.: 0941 943-9689 E-Mail: lars.krenkel@oth-regensburg.de
Drehflügler	Dr. A. Gardner (DLR, Göttingen) Tel.: 0551 709-2267 E-Mail: Anthony.Gardner@dlr.de
Hochagile Konfigurationen	Dr. R. Höld (MBDA Deutschland GmbH, Schrobenhausen) Tel.: 08252 99-8845 E-Mail: Roland.Hoeld@mbda-systems.de
Transportflugzeugkonfigurationen	Dr. A. Seitz (DLR, Braunschweig) Tel.: 0531 295-2888 E-Mail: Arne.Seitz@dlr.de
Versuchsanlagen	Dr. G. Dietz (European Transonic Windtunnel GmbH, Köln) Tel.: 02203 609-110 E-Mail: gd@etw.de
Windenergie	Dr. T. Lutz (Universität Stuttgart) Tel.: 0711 685-63406 E-Mail: lutz@iag.uni-stuttgart.de
Wissenschaftlicher Koordinator	Prof. Dr. C. Wagner (DLR, Göttingen) Tel.: 0551 709-2261 E-Mail: Claus.Wagner@dlr.de

anwendungsorientiert

Stand: Oktober 2025

Verfassen von „Mitteilungen“ für den nächsten Jahresbericht

Die Anmeldungen zum STAB-Symposium bzw. STAB-Workshop werden bei der jeweiligen Veranstaltung als Bericht/Proceedings an die Teilnehmer/innen verteilt.

Die Mitteilung ist eine zweiseitige Kurzfassung des Beitrags, bei der nur der unten dargestellte Kopf vorgegeben ist.

Mitteilung

Fachgruppe:

Thema/Titel des Beitrags

Autor(inn)en
Institution
Adresse
E-Mail-Adresse

Bitte halten Sie sich bei der Anmeldung zur STAB-Veranstaltung unbedingt an die vorgegebenen zwei Seiten pro „Mitteilung“. Tragen Sie bitte keine Seitenzahlen ein.

Der Druck erfolgt weiterhin ausschließlich in schwarz/weiß.

Für Rückfragen steht Ihnen die Geschäftsstelle gerne zur Verfügung:

Tel.: 0551 709 - 2464
E-Mail: stab@dlr.de

Mit freundlichen Grüßen
Ihre Fachgruppenleiter/innen und Ihre Geschäftsstelle

The **CEAS Aeronautical Journal** and the **CEAS Space Journal** have been created under the umbrella of CEAS to provide an appropriate platform for excellent scientific publications submitted by scientists and engineers. The German Aerospace Center (DLR) and the European Space Agency (ESA) support the journals.

CEAS Aeronautical Journal

An official journal of the Council of European Aerospace Societies
ISSN: 1869-5582 (Print), 1869-5590 (Online)
Springer
http://www.springer.com/13272

The journal is devoted to publishing results and findings in all areas of aeronautics-related science and technology as well as reports on new developments in the design and manufacturing of aircraft, rotorcraft, and unmanned aerial vehicles. Of interest are also (invited) in-depth reviews of the status of development in specific areas of relevance to aeronautics, and descriptions of the potential way forward. Typical disciplines of interest include flight physics and aerodynamics, aeroelasticity and structural mechanics, aeroacoustics, structures and materials, flight mechanics and flight control systems, flight guidance, air traffic management, communication, navigation and surveillance, aircraft and aircraft design, rotorcraft and propulsion.

The journal publishes peer-reviewed original articles, (invited) reviews and short communications.

CEAS Space Journal

An official journal of the Council of European Aerospace Societies
ISSN: 1868-2502 (Print), 1868-2510 (Online)
Springer
http://www.springer.com/12567

The journal is devoted to new developments and results in all areas of space-related science and technology, including important spin-off capabilities and applications as well as ground-based support systems and manufacturing advancements. Of interest are also (invited) in-depth reviews of the status of development in specific areas of relevance to space, and descriptions of the potential way forward. Typical disciplines of interest include mission design and space systems, satellite communications, aerothermodynamics (including physical fluid dynamics), environmental control and life support systems, materials, operations, space debris, optics, optoelectronics and photonics, guidance, navigation and control, mechanisms, propulsion, power, robotics, structures, testing, thermal issues, and small satellites.

The journal publishes peer-reviewed original articles, (invited) reviews and short communications.

Mitteilung

Fachgruppe: Aerodynamik bodengebundener Fahrzeuge

Investigating extreme crosswind-stability of vehicles on bridges: applying a moving-model and side wind-tunnel methodology with full-scale validation

James R. Bell[1*], Isak Tolo[2], Jonas T. Snæbjörnsson[2,3], Jasna B. Jakobsen[2],

1. Institute of Aerodynamics and Flow Technology, German Aerospace Center (DLR), Göttingen, Germany, *james.bell@dlr.de
2. Department of Mechanical and Structural Engineering and Material Science, University of Stavanger, Stavanger, Norway
3. Department of Engineering, Reykjavik University, Reykjavik, Iceland

A multi-disciplinary approach – combining wind engineering and vehicle aerodynamics – is being developed for investigations into the stability of vehicles operating in extreme cross-wind conditions. In this case, heavy vehicles travelling over a 56m high bridge across a Norwegian fjord that could encounter wind gusts of up to 40m/s. Potential changes to the climate and weather conditions could result in increased occurrence of extreme wind events, in addition to ever increasing road usage and infrastructure development. Crosswind exposure and vehicle-infrastructure interaction are inherently transient, non-statistically stationary aerodynamic events that require novel scaled experimental methodologies and full-scale measurements for realistic, representative aerodynamic investigations.

In this work, a new configuration of the moving-model facility in DLR Göttingen is presented. Originally intended for high-speed-train and tunnel interaction, the test-section has been modified to include a 1:15 scale model of the Lysefjord Bridge, and a generic truck model within the side-wind tunnel jet (Fig. 1). Previous work on passenger automotive-vehicle crosswind-stability over flat-ground in the facility [1] has identified transient characteristics (not able to be modelled in traditional, quasi-steady wind-tunnel experiments), as well as agreeable validation with full-scale measurements in BMW Aschheim side-wind facility [1]. Here, the scaled moving-model experiments are validated against novel full-scale measurements taken by the University of Stavanger on the Lysefjord bridge, where surface pressure and ultrasonic anemometers measure real-world aerodynamic characteristics [2-5]. The scaled moving-model wind-tunnel area will be tuned in an attempt to represent the oncoming and local flow (magnitude, turbulence intensity and length-scales, frequency spectra and gust profiles) experienced by the bridge (and to which the vehicle is exposed to), as well as their effects: transient surface pressure on the bridge. Additional, real-world validation is planned, with measurements on an operational truck loaded with the DLR FR8-LAB – a measurement equipped shipping container [6]. Transient pressures and inferred global forces can be compared to measurements made on-board the scaled moving-model truck in the experiments.

Figure 1: Left : Wind-tunnel setup:1 :15 model of Lysefjord bridge, towers, railing and (center) generic truck, and (right) the real Lysefjord bridge in Norway.

Surface-pressure measurements on the 1:15 scale moving-model (MM) results at 10m/s wind velocity (Reynolds number, based on bridge width, Re_W=5.5x10^5) show reasonable comparison to the full-scale (FS) bridge from a 1 hour sample with moderate winds of 10m/s (Re_W=8.2x10^6). These results are presented as vectors of normalized pressure, C_P, in Figure 2. A difference is the pressure on the lower windward surface, which is C_P~0.5 for MM and C_P~-0.4 for FS. This is proposed to be due to the minor angle of attack in the natural wind. The real bridge also exhibits wider variability due to natural wind fluctuations; to explore this, different windowed-averages and filters were applied. The fluctuating pressure and velocity characteristics: standard deviation, transient signals and spectra have also been compared.

The transient surface pressure experienced by the bridge during crosswind exposure and as the moving vehicle (20m/s, Re_W=2.3x10^5, where a full-scale truck at 50km/h ~Re_W=2.4x10^6) passes over the pressure measurement-position is presented in Figure 3. With C_P calculated using the vehicle speed, wind speed and resultant, ($C_{P,V}$, $C_{P,W}$ & $C_{P,R}$). The moving vehicle generates a clear high pressure, then low pressure and then flucutations in its wake; clearly visible with no crosswind (Fig 3a). During crosswind, the pressure at the windward (B1), leeward (B12) and upper surface (B15) exhibit different characteristics (Fig 3b). The bridge during crosswind and vehicle passing exhibit signs of both (Fig. 3c), however, not with simple superposition, indicating complex interaction. Transient pressures on the moving-truck (Fig. 4) show clear the acceleration of the model, complex, unsteady interaction with the crosswind (t=1.3-1.5s), as well as local effects of the bridges vertical towers (t=1.4s).

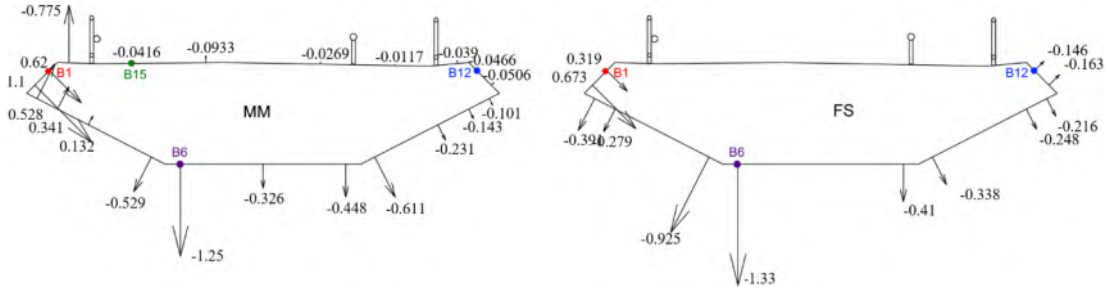

Figure 2: Average pressure (C_P) on moving-model-bridge MM, and full-scale-bridge (FS).

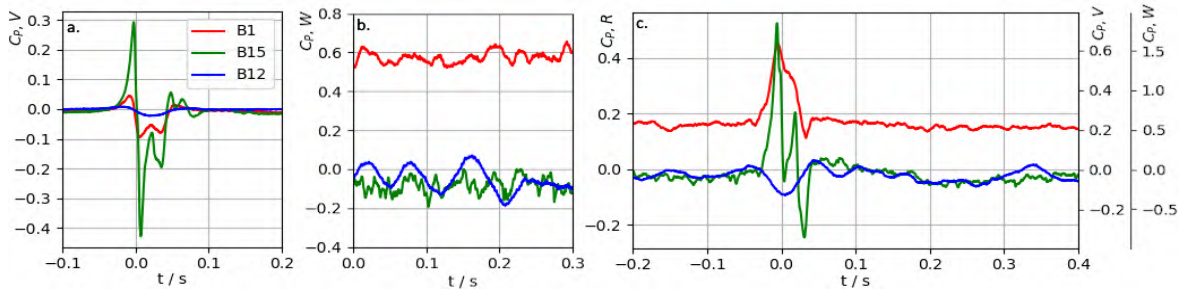

Figure 3: Transient surface-pressure from the bridge with a. a moving vehicle (20m/s, Re_W=2.3x10^5) with no crosswind, b. during crosswind (12m/s), and c. moving vehicle (20m/s) with crosswind (12m/s).

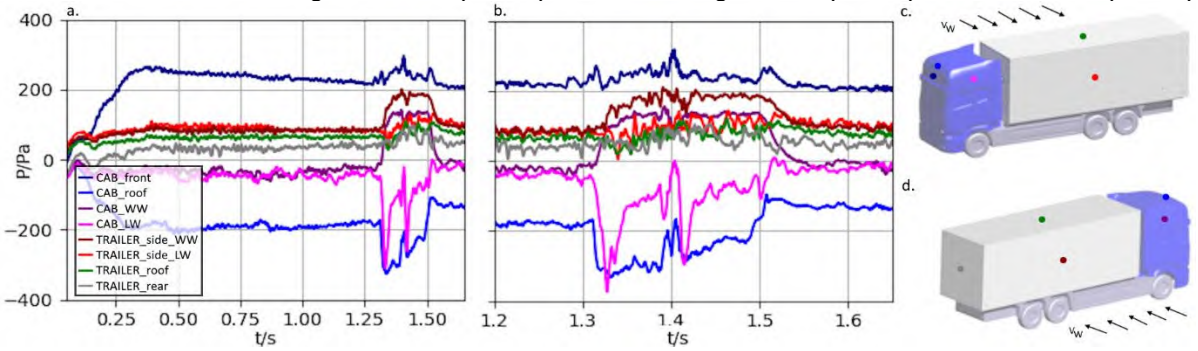

Figure 4: Transient surface-pressure on the moving truck (27m/s) during a. the entire run, b. crosswind (V_W = 10m/s) section, at c. leeward (LW) and d. windward (WW) locations.

This work demonstrates the functionality of the novel methodology with encouraging comparison to full scale results. Future work is planned for further optimisation, and additional variability (e.g. turbulence, yaw/pitch of oncoming flow) and subsequent optimization and assessment of bridge geometry and infrastructure effects such as towers, as well as engineering solutions like wind fences, and safety operational guidelines.

1. Bell, J.R., Wilhelmi, H., Heine, D., Jessing, C. et al., “Experimental Investigation of Automotive Vehicle Transient Aerodynamics with a Reduced-Scale Moving-Model Crosswind Facility,” SAE Technical Paper 2020-01-0671, 2020, DOI
2. Daniotti, N., Jakobsen, J.B., Cheynet, E., Snæbjörnsson, J.T., Surface pressure measurement system for investigating bridge aerodynamics,Measurement, 254, 2025, DOI
3. Daniotti, N., Jakobsen, J.B., Snæbjörnsson, J.T., Cheynet, E., Wind turbulence around a bridge deck in full scale, Journal of Fluids and Structures, 135, 2025, DOI
4. Tolo, I., Wind Tunnel Testing of a Bridge with a Moving Vehicle: Safety of Road Vehicles on a Bridge. Masters Thesis, University of Stavanger, 2025.
5. https://windengineeringuis.github.io/, Wind Engineering, University of Stavanger, accessed September 2025.
6. Bell, J.R., Buhr, A., Henning, A. (2024). Measuring the Oncoming Flow that Operational Freight-Trains Experience Using the DLR FR8-LAB. New Results in Numerical and Experimental Fluid Mechanics XIV. STAB/DGLR Symposium 2022. DOI

Mitteilung

Fachgruppe: Aerodynamik bodengebundener Fahrzeuge

Investigation of the Tunnel Passage of Coupled Trains

Klaus Ehrenfried and Daniela Heine

Institute of Aerodynamics and Flow Technology, DLR
Bunsenstraße 10, 37073 Göttingen
klaus.ehrenfried@dlr.de

The aerodynamic drag experienced by trains in tunnels is significantly higher than in open space. This applies in particular to new single-track, twin-tube tunnels with a relatively narrow cross-section. A special situation arises when two trains pass through a tunnel relatively close together, as is the case with virtually coupled trains. This raises the question of how the aerodynamic resistance of the two train sections compares with that of directly coupled train sections or a uniform single train of the same length.

In the first step, the aerodynamic drag caused by the coupling point between two train sections during tunnel travel will be analyzed in more detail. The tests are carried on a 1:25 scale ICE3 model in the Tunnel Simulation Facility Göttingen (TSG). In this facility, the train models are accelerated using a catapult and then travel along a rail track through a model tunnel due to inertia.

Figure 1: Left: Coupling point of the original ICE3. Right: Model of a coupled ICE3 at the entrance of the model tunnel in the TSG facility.

Figure 1 (left) shows a photograph of the ICE3 coupling point. On the right-hand side, the test model is shown at the entrance of the model tunnel. The model has a length of about 2.5 m (62.5 m in full scale). It consists of two carriages, with the ICE3 coupling point reproduced between them. The head of the model has a generic geometry. The rear complies with the shape of an ICE3 head. Converted to full scale, the model tunnel has a cross-sectional area of 44 m² and a length of 400 m. The relatively small cross-sectional area corresponds approximately to the new Koramltunnel in Austria, which is due to open in 2026.

Pressure sensors are installed at several locations in the side wall of the tunnel. In addition, there are light barriers in front of and behind the tunnel to determine the speed of the model. The

model also incorporates a data acquisition unit and various sensors. The surface pressure and the pressure drop across the coupling point are measured onboard. The position of the model is simultaneously recorded by an optical sensor.

Parallel to the measurements, the passage of the train model through the tunnel is simulated numerically using a quasi-one-dimensional model of both the flow and the pressure waves in the tunnel. This model requires empirical parameters to describe friction losses. These parameters are adjusted so that at a position of 3 m in the model tunnel (75 m in full scale) the calculated and measured variations in wall pressure match as closely as possible. The calculation model is calibrated against the wall pressure at this point.

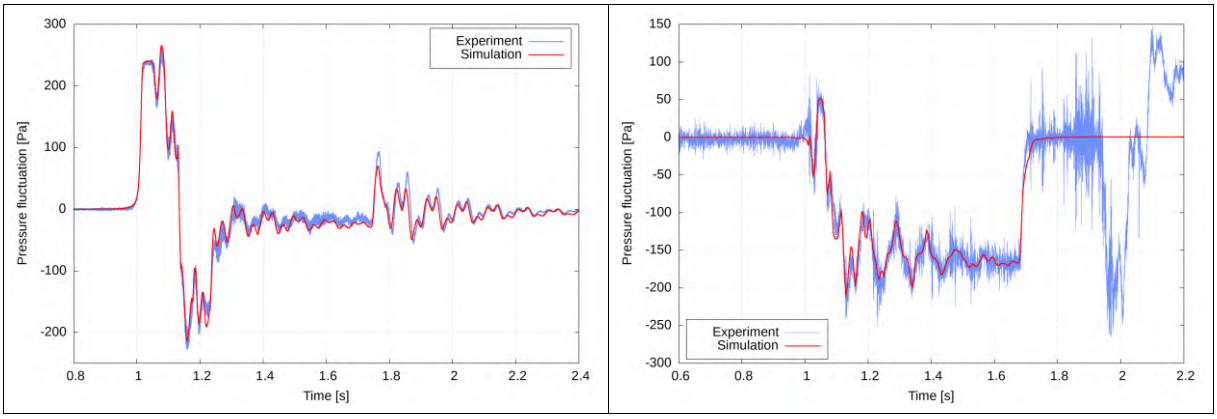

Figure 2: Left: Measured and calculated pressure at the tunnel wall, 3 m inside the model tunnel. Right: Measured and calculated pressure at the side of the first carriage of the model train (approx. 0.4 m behind the nose).

Figure 2 (left) shows a comparison of the pressure curve measured at the 3 m point (75 m full scale) with the calculated curve. The right side of Figure 2 shows the pressure at the outer wall of the first carriage. The model speed is 23 m/s. The nose enters the tunnel at about t = 1 s. The tail leaves the tunnel at t = 1.75 s. The figures show a good agreement between the calculated results and the measured data. It should be noted that the calculation was calibrated against the measured curve on the left-hand side of Figure 2 only. The good agreement between the curves on the right-hand side of Figure 2 demonstrates that the numerical method accurately captures pressure fluctuations throughout the tunnel, not just at the calibration point. Of course, quasi-one-dimensional modeling cannot describe all effects. For example, the noise in the measurement data in the curve on the right-hand side of Figure 2 is caused by the turbulent boundary layer on the outer skin of the train model. Turbulence effects are not included in the calculation model. At around t = 1.8 s, the train model smashes into a bed of polystyrene beads and decelerates. This leads to strong fluctuations in the measured surface pressure, which of course are not present in the calculations.

The calibrated calculation model can now be used to determine the additional resistance caused by the coupling point compared to a single uniform train. In terms of resistance, the directly coupled train can then also be compared with configurations in which two train sections are not directly coupled, but travel through the tunnel at a relatively close distance (virtual coupling).

Mitteilung

Fachgruppe: Aerodynamik bodengebundener Fahrzeuge

Application of Pressure-Sensitive Paint for Unsteady Rim Pressure Measurements on a Passenger Car

Jan Marcel Hübner – jan.marcel.huebner@volkswagen.de
Dr. Sven Lange – sven.lange5@volkswagen.de
Mathias Hähnel – mathias.haehnel@volkswagen.de
Volkswagen AG
Berliner Ring 2, 38440 Wolfsburg

Dr. Michael Hilfer – michael.hilfer@tu-braunschweig.de
Institut für Strömungsmechanik
Technische Universität Braunschweig
Hermann-Blenk-Straße 37, 38108 Braunschweig

In the context of growing environmental awareness, increasing demand for electric vehicles with extended range, and tightening regulatory requirements, the reduction of aerodynamic drag has become a key objective in vehicle development. Approximately 20-30 % [1] of the total aerodynamic drag of an electric vehicle originates from the airflow around the wheels and wheel housings. However, due to the complex geometries of tires and rims and their rotation, capturing the flow phenomena in these regions remains a significant experimental challenge.

To overcome these limitations, this study introduces a novel optical pressure measurement approach based on pressure-sensitive paint (PSP) and motivated by the previous application of PSP on rotating surfaces for high-frequency pressure measurements [2]. The PSP used in this study is a single-component, polymer-ceramic coating (PC-PSP) based on platinum luminophores [3, 4], optimized for high sensitivity and high temporal resolution in the pressure range relevant to automotive aerodynamics.
The measurement system is designed for use in both wind tunnel and on-road tests, allowing for comparative analysis. It consists of a streamlined support bar (Figure 1, a) and measurement pod (Figure 1, b). The latter contains a high-speed camera and 4 UV LED spotlights. CFD simulations were conducted to quantify the aerodynamic influence of the support wing and measurement pod, revealing that the pressure field around the wheels was altered by no more than $\Delta cp = \pm 0.02$, confirming the setup's suitability for high-fidelity measurements without significant impact on relevant flow structures.

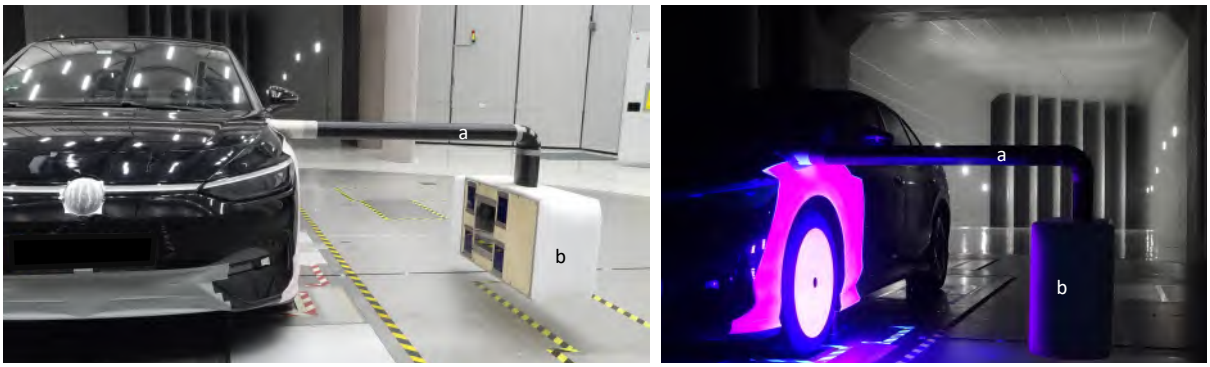

Figure 1: Left: Measurement setup for PSP measurements. Right: UV LED spotlights are switched on and PSP is emitting light with a wavelength of 650 nm.

Measurements were performed in the Aerodynamics-Acoustics Wind Tunnel (AAK) at Volkswagen AG in Wolfsburg with a Volkswagen ID.7 with stationary wheels at a freestream velocity of 140 km/h using a 12-bit high-speed camera operating at 4000 fps. The PSP

technique was applied using an intensity-based method under continuous illumination. To calibrate the relative pressure data obtained from PSP, wall pressure taps were distributed across the wheel arch and connected to a pressure measurement system. The UV LED spotlights were tested via FFT analysis to ensure minimal frequency interference with the pressure induced light intensity signal of the PSP.
For the steady-state results, normalized intensity fields were scaled using pressure tap data, yielding spatially resolved pressure distributions, as seen in Figure 2. The maximum deviation between PSP-derived pressures and tap measurements (Figure 2, black circles) was approximately 50 Pa, corresponding to Δcp = ±0.05. Additionally, the pressure distributions of both methods are in good agreement with the pressure tab data ranging from -260 Pa to -660 Pa. The pressure sensitivity of the system was determined to be approximately 0.17% / 100 Pa, enabling the detection of pressure gradients across the body and wheel rim surface.

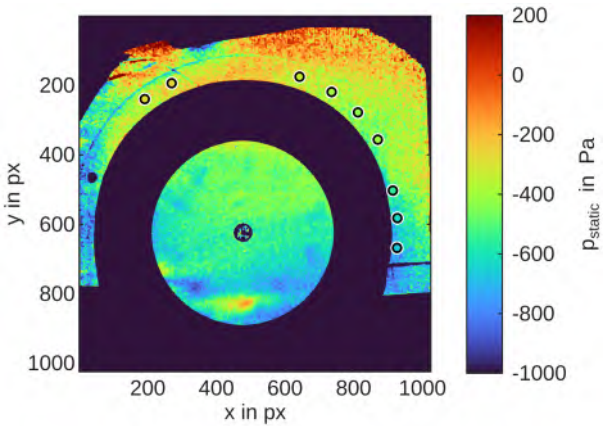

Figure 2: Time-averaged pressure field resulting from PSP measurements. Pressure tap data is shown inside the black circles.

Additionally, CFD simulations were conducted to provide a reference for validating the experimental results. Key flow structures such as separation zones and pressure gradients are comparable. However, some discrepancies in vortex positions and strengths were noted and will be subject to further investigation.
In addition, unsteady pressure fluctuations in the PSP data were analyzed using frame-wise normalization and Fast Fourier Transform (FFT), resulting in frequency maps that reveal, for example, rim vortex footprints and their associated frequencies on both the body and the disc mounted to the rim.

In conclusion, the presented measurement setup and methodology offer a powerful tool for capturing both steady and unsteady surface pressure distributions on passenger car wheels and adjacent body surfaces. Future work will focus on extending the measurements to rotating wheels and conducting comparative studies between wind tunnel and on-road conditions.

References

[1] J. Hurlbrink, „Analyse der aerodynamischen Verlustmechanismen der Radhausströmung von Pkw und Entwicklung von Maßnahmen zur Luftwiderstandsreduktion,“ 2022.

[2] M. Hilfer, M. Behn, C. Klein, T. Ahlefeldt, U. Tapken, L. Katzenmeier, L. Koop und L. Enghardt, „Near-field measurements of stationary and rotating in-duct sound sources with pressure sensitive paint,“ 2022, https://doi.org/10.2514/6.2022-3056.

[3] M. Kasai, A. Suzuki, Y. Egami, T. Nonomura und K. Asai, „A platinum-based fast-response pressure-sensitive paint containing hydrophobic titanium dioxide,“ *Sensors and Actuators A: Physical,* 2023, https://doi.org/10.1016/j.sna.2022.114140.

[4] J. W. Gregory, H. Sakaue, T. Liu und J. P. Sullivan, „Fast Pressure-Sensitive Paint for Flow and Acoustic Diagnostics,“ *Annual Review of Fluid Mechanics,* 2014, doi: 10.1146/annurev-fluid-010313-141304.

Mitteilung

Fachgruppe: Aerodynamik bodengebundener Fahrzeuge

Unsteady force measurements on wind tunnel train models using multi-dimensional transfer functions to take into account natural oscillations

Arno Peterka, Klaus Ehrenfried
Institut für Aerodynamik und Strömungstechnik,
Bunsenstr. 10, 37073 Göttingen
arno.peterka@dlr.de

Future high-speed trains must be faster and more lightweight to satisfy increasing demands on personal and freight transportation, as well as on the environmental impact of rail transportation. With higher speeds, the aerodynamics of a train become highly important. Both drag and side wind stability are focused on in research. So far, optimization has been done for stationary cases in quiet wind tunnel flow. However, the real surroundings of a train track like bridges, trees, etc. together with natural wind gusts provide a very unsteady incoming flow to the train.

For automobiles it has been found that an unsteady flow sinusoidally alternating around zero with a certain maximum inflow flow angle can lead to an increase in side force compared to a steady side flow at the same constant maximum inflow angle[1]. The present research investigates if this is also applicable for long bodies like trains, what causes this phenomenon and what potentially can be done to reduce it. The side and drag forces are measured with a four-sensor platform. In order to separate the aerodynamic forces from the inherent oscillations of the model and its supporting structure, the latter oscillations are identified by an impact hammer experiment beforehand. The model and its support are equipped with acceleration sensors and the frequency responses of the impact hammer strikes are recorded.

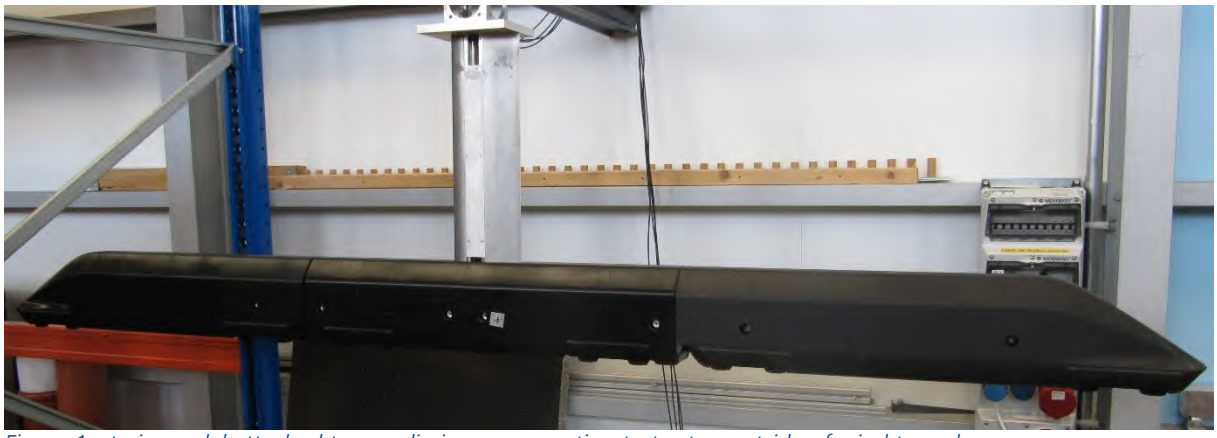

Figure 1 - train model attached to a preliminary preparation test setup outside of wind tunnel

The experiments are conducted in the crosswind simulation facility in Göttingen (SWG). As shown in figure 1, the model is connected to a vertical sting by the force sensor platform. The photo shows the model train with its aerodynamic fairing, however, the beforehand impact hammer measurements are performed on the relevant inner support structure only. For the actual wind tunnel measurements, the impact hammer experiments will be repeated including the fairing. The sensors are applied in such a way that only the acceleration in y-direction is measured, that is the side wind relevant direction. Under wind on conditions, the same acceleration sensor setup is used and – together with the results of the beforehand impact hammer test – can be used to distinguish between wind loads and inherent oscillation loads within the force sensor output.

An FFT is applied to the time signal of the acceleration sensors and impact hammer. The relationship between input (impact hammer, aerodynamic forces) and output signal (acceleration sensors, force sensors) is assumed to be linear.

Figure 2 exemplarily shows the amplitude of the frequency response in the y-direction of a sensor at the far end of the model. The data is an average of five impact hammer strikes at the same end of the model. Resonant frequencies can be identified at about 3 Hz, 5 Hz, 8 Hz and 33 Hz. The multi-dimensional transfer function combines the frequency domain results of all acceleration sensors.

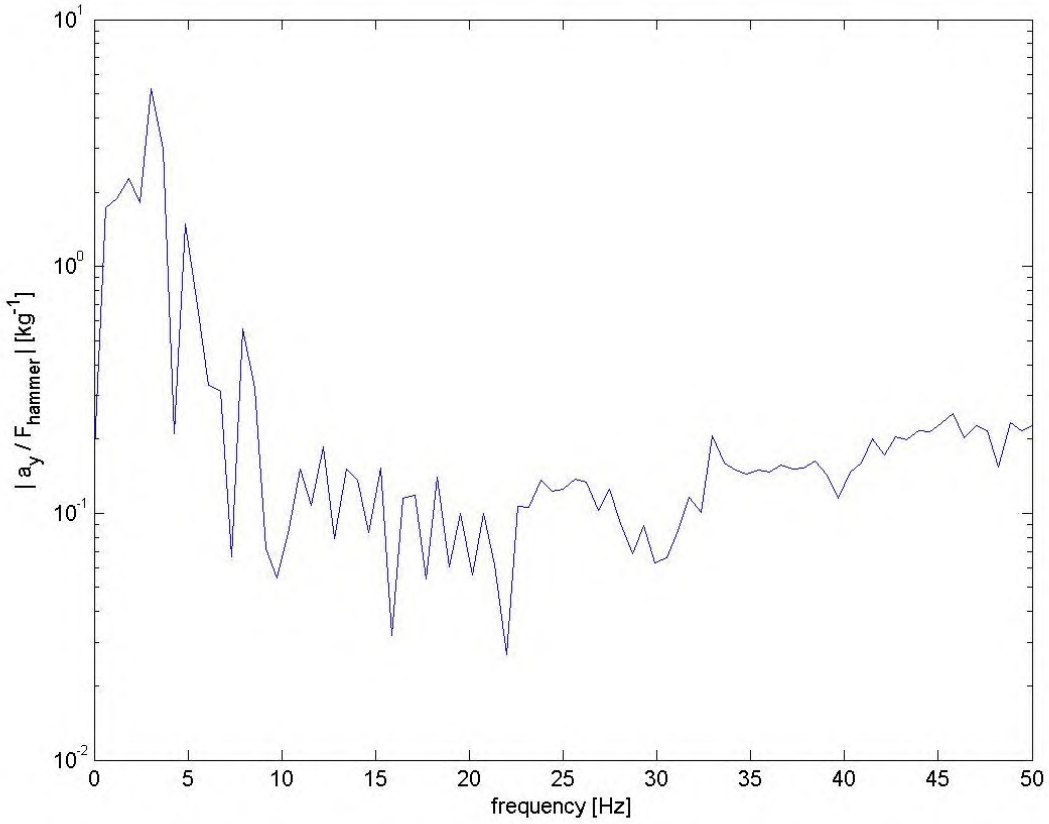

Figure 2 - amplitude of frequency response (acceleration sensor over impact hammer signal)

The influence of the number of acceleration sensors and the number of positions of impact hammer strikes, as well as the number of repetitions of impact hammer strikes on the quality of the transfer function will be investigated.

[1] Schröck, D. - Eine Methode zur Bestimmung der aerodynamischen Eigenschaften eines Fahrzeugs unter böigem Seitenwind, Dissertation, Universität Stuttgart, 2011

Mitteilung

Fachgruppe: Allgemeine Strömungstechnik

Predictions of Exhalation-Induced Particle Dispersion with the Improved Particle Dispersion Models

Ege Batmaz[1, 2], Daniel Schmeling[1], Claus Wagner[1, 2]
[1]German Aerospace Center (DLR). Institute of Aerodynamics and Flow Technology, Bunsenstraße 10, 37073 Göttingen,
[2]Technical University of Ilmenau. Institute of Thermo- and Fluiddynamics, Helmholtzring 1, 98996 Ilmenau,
ege.batmaz@dlr.de

Turbulence plays a decisive role in the dispersion of particles during respiratory events such as breathing or coughing. Computational fluid dynamics (CFD) provides an efficient framework for predicting particle transport, which can be used to asses the risk of SARS-CoV-2 transmission in aircraft cabins or train compartments for example. However, due to their high computational cost, direct numerical simulation (DNS) and large-eddy simulation (LES), which fully or largely resolve turbulence, are not practical. Instead, the most feasible approach is to use Reynolds-averaged Navier–Stokes (RANS) simulations with point-like (Lagrangian) particles. In this context, selecting the appropriate particle dispersion model (PDM) is crutial for accurately capturing the spread of particles in such turbulent environments.

In our previous study [1], we introduced the limited particle–eddy interaction (LPI) model, which improves the prediction of exhalation-induced particle dispersion when applied to an exponentially smoothed DNS velocity field. In the present study, we extend the application of the LPI model to a RANS simulation and evaluate its performance against the commonly used mean particle–eddy interaction time (MPI) model implemented in OpenFOAM using the DNS data from our previous study as a reference.

The steady-incompressible RANS equations coupled with temperature and vapour transport equations via the Boussinesq approximation were solved in OpenFOAM using second-order central differences. Turbulence was modelled using the RNG k–ε model. The computational mesh comprised 4.5 million cells with a maximum size of 1.4 cm and local refinements down to 3 mm near the pipe and the walls. Once the steady velocity field had converged (after 10^4 iterations), particles of various sizes were injected from the mouth and tracked for 5 s in a post-processing step. Three dispersion scenarios were considered: no dispersion model, the MPI model, and the LPI model with an optimal relaxation factor of 4.

As Fig. 1 shows, the RANS simulation without a dispersion model underpredicts the particle spread. In contrast, the MPI model produces erratic overdispersion for 1 µm particles. The LPI model, however, provides the most consistent performance for both small (1 µm) and large (32 µm) particles. To provide a quantitative evaluation, we examined the convex hull volumes (CHVs), which are defined as the smallest convex volume enclosing all particles. As shown in Fig. 2, the MPI model significantly overpredicts the CHV for small particles, but performs well for larger ones. In contrast, the LPI model accurately reproduces the dispersion for both particle sizes. These findings demonstrate that the LPI model achieves performance comparable to that of exponentially smoothed DNS velocity fields when applied in a RANS simulation framework. Furthermore, it is clear that the LPI model improves dispersion prediction relative to the RANS simulation with the MPI model.

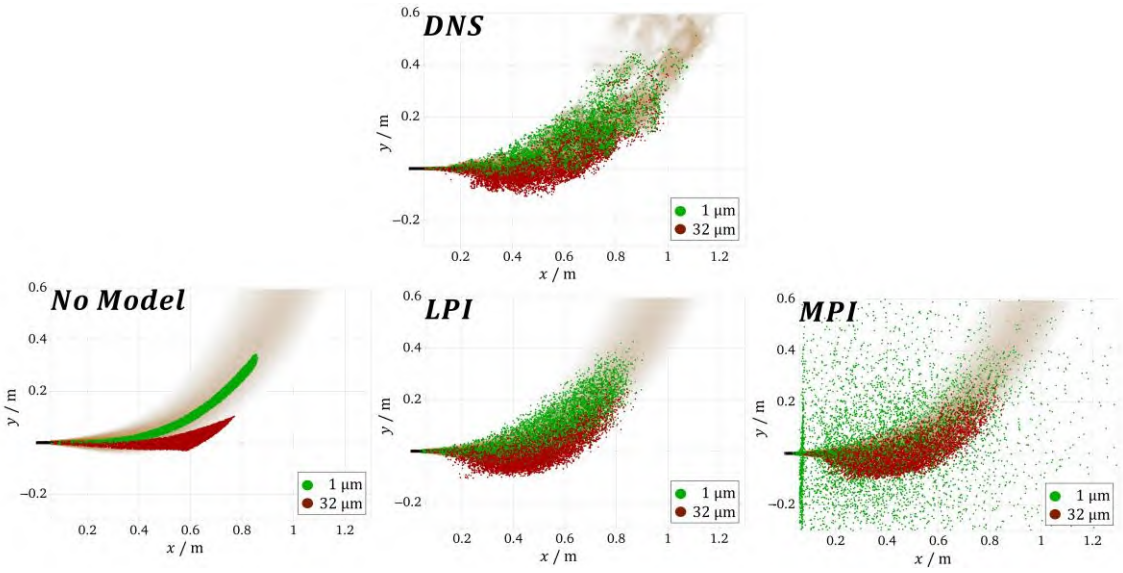

Figure 1: Predicted particle clouds 4 seconds after the start of injection. The DNS results are shown alongside the RANS simulation results obtained without a dispersion model and with the LPI and MPI models, for the particle sizes of 1 µm and 32 µm.

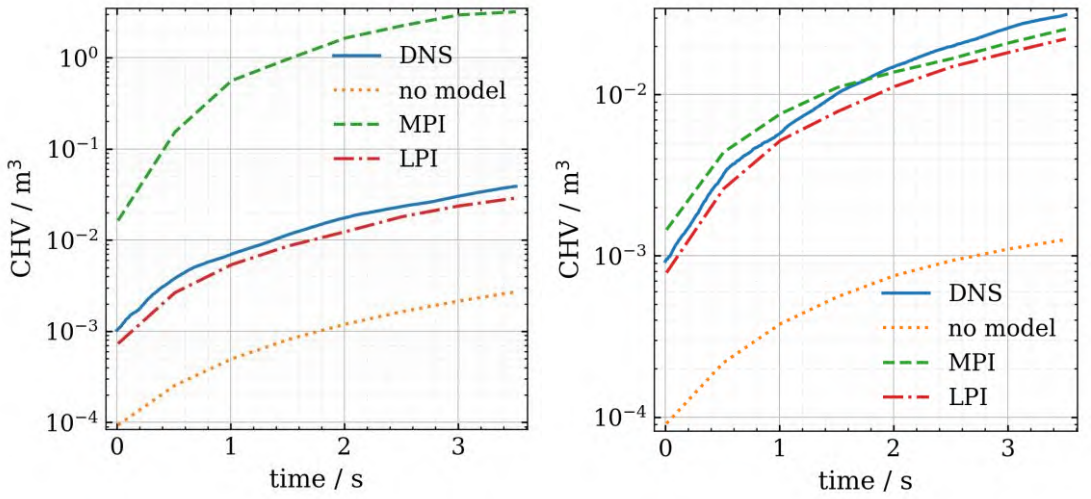

Figure 2: Convex hull volumes (CHVs) of particle clouds as predicted by the RANS simulation using the MPI and LPI models and without a dispersion model, are compared with the DNS results. Results are shown for the particle sizes of 1 µm (left) and 32 µm (right).

References

[1] Batmaz, E., Webner, F., Schmeling, D., & Wagner, C. (2025). Improvements in Turbulent Jet Particle Dispersion Modeling and Its Validation with DNS. Atmosphere, 16(6). https://doi.org/10.3390/atmos16060637

Mitteilung

Fachgruppe: Allgemeine Strömungstechnik

Applying event-based imaging to reconstruct large-scale flow features

Sylvia Brückner, Michael Hilfer, David E. Rival
Institute of Fluid Mechanics, TU Braunschweig, Germany
Hermann-Blenk-Str. 37, 38108 Braunschweig
sylvia.brueckner@tu-braunschweig.de

Understanding micrometeorological phenomena occurring in the lowest atmospheric layer (Arya, 2005) is crucial for a wide range of applications, including agriculture, air pollution, and weather forecasting (Arya, 2001). Early micrometeorological data were often collected using sensors on short stands and towers (Stull, 1988). These Eulerian measurements have advantages but also limitations (Shaughnessy Jr., 2005), for example when investigating coherent structures. Although Eulerian methods have been used for identification of coherent structures, they can fail with flow structures governing transport in unsteady flows for two reasons: First, a feature apparent at one instant can disappear before substantial mixing occurs. Second, Eulerian methods are frame-dependent, whereas genuine transport barriers have to remain invariant under reference frame changes (Peacock and Allshouse, 2015). On the other hand, Lagrangian approaches have become valuable tools for investigating complex flows, and they are particularly well suited to geophysical applications (Bourgoin et al., 2014). Especially due to their high dynamic range and temporal resolution (Gallego et al., 2020), the use of event-based vision for Lagrangian measurements seems to be promising.

The focus of the current work is thus to determine whether high-quality three-dimensional (3D) tracks can be extracted using event-based cameras, and to determine how the cameras can be employed efficiently. Developing a comprehensive methodology for extracting 3D tracks consequently constitutes the objective. To achieve this objective, experimentally generated flows are seeded with centimeter-sized, air-filled soap bubbles (AFSB), and the 3D tracks are obtained through the glare-point particle tracking (GPPT) technique, where glare-point motion is extracted as events using a single event-based camera. If the current work proves successful, it will guide subsequent research toward assessing whether the setup can be used for reconstruction of atmospheric coherent structures.

This work builds on prior studies: Using centimeter-scale soap bubbles dates back to efforts by Rosi et al. (2014) to capture 3D flow patterns in outdoor environments. Conlin et al. (2024) employed multi-camera setups and helium-filled soap bubbles (HFSB) for field measurements in the atmospheric surface layer. Hou et al. (2021) as well as Kaiser and Rival (2023) developed and validated the GPPT technique, and Leister and Rival (2025) refined the technique for field-scale measurements using a drone-based camera and natural illumination.

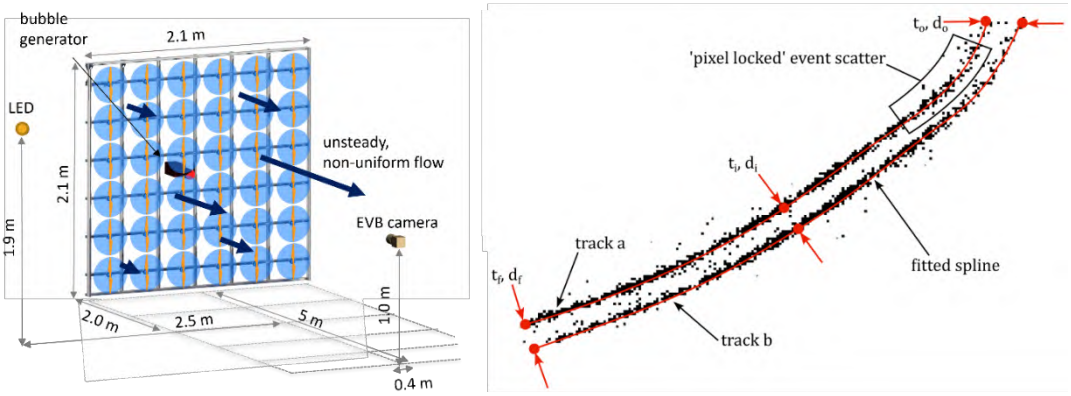

Figure 1: Experimental setup and depth retrieval. Left: Setup with event-based camera extracting GPPT information. The LED array is positioned approximately 90° to the camera. Right: Two tracks pertaining to the same soap bubble, each representing one of the two largest glare points. The distance between the two glare points is used to calculate depth through calibration.

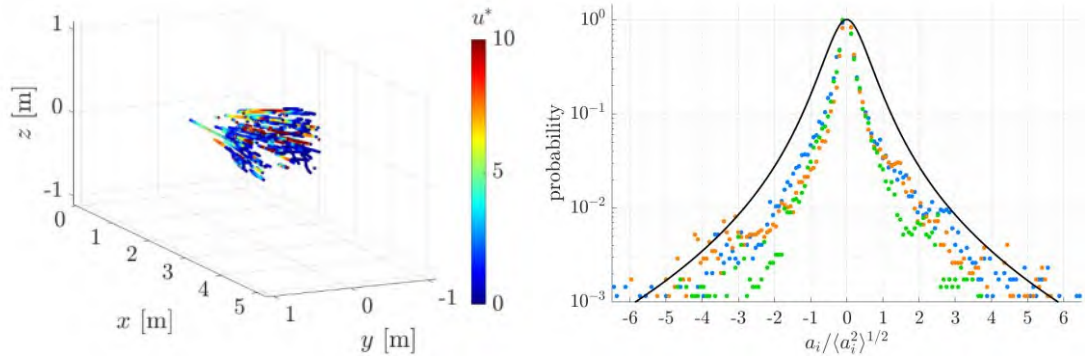

Figure 2: Extracting Lagrangian turbulence statistics. Left: Reconstruction of 3D bubble tracks, including velocity information. Right: Probability distribution functions for a_x, a_y and a_z normalized by their respective standard deviation. The black curve is the parametrization for Lagrangian acceleration from La Porta et al. (2001).

Figure 1 shows the experimental setup and the retrieval of depth information. Different flows are generated via a custom unsteady flow simulator with 36 independently-operated fans, and a measurement volume on the order of 10m^3. Illumination is generated by a LED bank that is positioned approximately 90° to the event-based camera. The camera captures bubble motion by tracking the two largest glare points. The distance between those two glare points is used to retrieve depth information through calibration. This way, a single event-based camera can be used to obtain the 3D information.

Figure 2 displays initial diagrams obtained through data analysis. The Lagrangian tracks, as well as information about there corresponding acceleration and curvature, can be extracted. Analysing such Lagrangian data over a larger measurement volume might have the potential to provide valuable insights well beyond Eulerian-based descriptions.

References

Arya, S. (2001). *Introduction to Micrometeorology.* Academic Press.

Arya, S. (2005). Micrometeorology and Atmospheric Boundary Layer. *Pure and Applied Geophysics*, 162(10), 1721-1745.

Bourgoin, M., Pinton, J.F., & Volk, R. (2014). Lagrangian methods in experimental fluid mechanics. *Modeling Atmospheric and Oceanic Flows: Insights from Laboratory Experiments and Numerical Simulations*, 277-296.

Conlin, N., Even, H., Wei, N.J., Balantrapu, N.A., & Hultmark, M. (2024). Lagrangian particle tracking in the atmospheric surface layer. *Measurement Science and Technology*, 35(9), 095803.

Gallego, G., Delbrück, T., Orchard, G., Bartolozzi, C., Taba, B., Censi, A., Leutenegger, S., Davison, A.J., Conradt, J., Daniilidis, K., Scaramuzza, D. (2020). Event-based Vision: A Survey. *IEEE transactions on pattern analysis and machine intelligence*, 44(1), 154-180.

Hou, J., Kaiser, F., Sciacchitano, A., & Rival, D.E. (2021). A novel single-camera approach to large-scale, three-dimensional particle tracking based on glare-point spacing. *Experiments in Fluids*, 66, 141.

Kaiser, F., & Rival, D. (2023). Large-scale volumetric particle tracking using a single camera: analysis of the scalability and accuracy of glare-point particle tracking. *Experiments in Fluids*.

La Porta, A., Voth, G., Crawford, A., Alexander, J., & Bodenschatz, E. (2001). Fluid particle accelerations in fully developed turbulence. *Nature*, 1017-1019.

Leister, R., & Rival, D. (2025). Escaping the lab: advances in large-scale particle tracking using natural light and uncrewed aerial vehicles. *Experiments in Fluids*, 1-12.

Peacock, T., & Allshouse, M. (2015). Lagrangian based methods for coherent structure detection Available. *Chaos: An Interdisciplinary Journal of Nonlinear Science*.

Rosi, G., Sherry, M., Kinzel, M., & Rival, D. (2014). Characterizing the lower log region of the atmospheric surface layer via large-scale particle tracking velocimetry. *Experiments in Fluids*.

Shaughnessy Jr., E. J., Katz, I. M., & Schaffer, J. P. (2005). *Introduction to Fluid Mechanics.* New York: Oxford University Press.

Stull, R. B. (1988). *An Introduction to Boundary Layer Meteorology.*

MITTEILUNG

Fachgruppe: Allgemeine Strömungstechnik

PTV MEASUREMENT NEAR A PASSENGER MODEL INSIDE THE CABIN OF A SHORT-HAUL AIRCRAFT

Alexander Gluschak*[1,2], Robin Barta[1], Claus Wagner[1,2]

[1] *Institute of Aerodynamics and Flow Technology, DLR, Bunsenstraße 10, Göttingen, 37073, Germany*

[2] *Institute of Thermodynamics and Fluid Mechanics, TU Ilmenau, Helmholtzring 1, Ilmenau, 98693, Germany*

**Corresponding author. E-mail: alexander.gluschak@dlr.de*

In order to enhance cabin ventilation concepts in aircraft, it is crucial to understand the complex interplay between forced convection, driven by the cabin ventilation system, and natural convection resulting from the thermal effects of passengers' body heat. We plan to investigate the interplay between the two flow regimes using particle tracking velocimetry (PTV) in an actual aircraft and compare it with computational fluid dynamics (CFD) simulations.

Mixing ventilation, a common system used in aircraft cabins [1], introduces fresh air above passengers' heads. The passengers' bodies heat the surrounding air, generating rising thermal plumes that interact with the cold supply air, as illustrated in figure 1. Previous studies have demonstrated the complexity of the interaction between natural and forced convection in mixing ventilation, using CFD simulations and experimental techniques such as particle image velocimetry (PIV) and volumetric particle streak velocimetry (VPSV) in cabin models [1, 2]. They have shown that several factors influence the airflow field, including cabin geometry, blockage by seats and passengers, the temperature differential between cabin air, supply air, and rising heat plumes, as well as the interactions of different vents and buoyancy. Subsequent studies, especially in short-haul aircraft, compared mixing ventilation to alternative ventilation systems, demonstrating that improved ventilation concepts can significantly enhance passenger comfort and cabin air quality [3, 4]. Therefore, Bosbach et al. [3] utilized methods such as infrared thermography and PIV measurements, while Schmeling et al. [4] combined CFD simulations and experimental aerosol dispersion measurements to understand pathogen transport.

As far as we know, no study has measured the three-dimensional flow field inside an airplane cabin with mixing ventilation. We use PTV to gain a deeper understanding of the complex three-dimensional flow interactions that occur as a result of mixing ventilation. The measurements take place between two rows of seats, pictured in Figure 2, in the passenger cabin of the Dornier 728, a short-haul aircraft. We replicate the mixing ventilation conditions by introducing cold supply air from above the seats and over the luggage compartment, illustrated in Figure 1. Each seat is equipped with a thermal dummy that continuously uses about 75 watts of electrical power to replicate the heat produced by a real person Particles for PTV are generated using a helium-filled soap bubble generator from LaVision. We place two seeding devices near the two vent openings — one above the luggage compartment, one above the windows. Three high-power LED panels illuminate the measurement area from below. We record the illuminated particles using four high-speed sCMOS cameras (PCO.edge 5.5), which provide high spatial and temporal resolution. For calibration, we record a video of a moving AMOLED display - lacking backlighting and presenting a calibration plate with illuminated marker points - in the focal region of all four cameras. To reduce glare caused by ambient light and thereby improve the accuracy of marker detection, we calibrate in a dark environment. We evaluate our data as in Barta et al. [6] with proPTV, a Python-based tool using the Soloff projection model [5]. At the STAB Symposium, we plan to present the results.

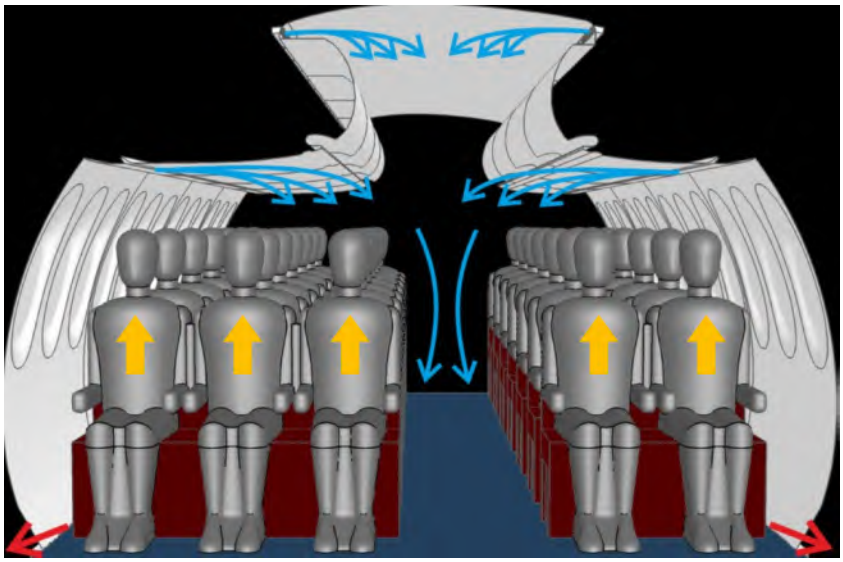

Figure 1. Mixing convection in passenger cabin of the Donier 728. The blue arrows symbolize the fresh, cooled air from the vent openings. Orange arrows symbolize the warm updraft caused by body heat. Red Arrows are the exhaust air on the bottom. Image adapted from Bosbach et. al. [3]

Figure 2. Picture from the measured area of the Donier 728 with a thermal dummie on each seat.

References

[1] Kühn M. et. al.: Experimental parametric study of forced and mixed convection in a passenger aircraft cabin mock-up. *Buildings and Environment* 2009.

[2] Zhang Y. et al.: Experimental characterization of airflows in aircraft cabins, Part II: Results and research recommendation. *ASHRAE Transactions* 111:53–9, 2005.

[3] Bosbach J. et. al.: Alternative ventilation Concepts for aircraft Cabins. *CEAS Aeronautical Journal* 4:3, 2013.

[4] Schmeling D. et. al.: Numerical and experimental study of aerosol dispersion in the Donier 728 aircraft cabin. *CEAS Aeronautical Journal* 14:509, 2023.

[5] Soloff S.M. et. al.: Distortion compensation for generalized stereoscopic particle image velocimetry. *Meas. Sci. Technol.* 8, 1997.

[6] Barta R et. al.: proPTV: A probability-based particle tracking velocimetry. *Journal of Computational Physics* 514, 2024. framework

Mitteilung

Fachgruppe: Allgemeine Strömungstechnik

Large-eddy simulation of wind loads on photovoltaic systems: Comparative open-source CFD study with outlook on urban and aerothermal aspects

Marten Klein*, Hemanth N. Kotra, Marcelin Kabongo, Joseph Gerardi, Heiko Schmidt

Lehrstuhl Numerische Strömungs- und Gasdynamik, Brandenburgische Technische Universität (BTU) Cottbus-Senftenberg, Siemens-Halske-Ring 15A, 03046 Cottbus (*)
E-mail: marten.klein@b-tu.de

The durable operation of photovoltaic (PV) systems is a major design objective that is challenged by wind and thermal loads. At high wind speeds, lift, drag, and torsional forces can lead to panel and cell damage, which is escalated at moderate wind speeds due to reversing loads that can accelerate cracking (e. g. [1, 2]). At low wind speeds, poor ventilation is another that has to be improved to enhance efficiency (e. g. [3]) and reduce environmental impact, especially in urban areas (e. g. [4]). Putting thermal properties aside, the gold standard to obtain robust estimates of wind loads and structural stresses is wind tunnel measurements for both ground-mounted (e. g. [2]) and roof-top (e. g. [5]) PV systems. The experimental approach is cumbersome, expensive, and offers limited insight that depends on the available instrumentation. Advances in computational fluid dynamics (CFD) software and computing hardware have made high-fidelity large-eddy simulation (LES) of entire PV arrays feasible, providing additional insight into the flow organization and flow features that govern unsteady loads (e. g. [1–3, 5]). Simulated wind loads depend not only on solar system geometry, site-specific properties and atmospheric inflow, but also on turbulence modeling and details of the numerical schemes used including the meshes. The challenge for predesign is to obtain robust load estimates at affordable cost as a number of flow conditions and designs parameters (like orientation, tilt angle, row and lateral spacing, and distance from the surface) have to be varied.

The main goal of the present work is to develop a CFD-based workflow for predicting aerodynamic and thermal properties of PV systems. Two aspects are currently in the focus: Uncertainty and solver dependencies. Two different open-source CFD tools are therefore used to address these aspects. The first is the finite-element-based flow solver PVade [1], which includes fluid–structure interaction capabilities tailored to PV applications. The second is the finite-volume-based OpenFOAM library [6] (version 8), which offers multi-purpose simulation capabilities. Both software tools are now applied to the same validation case.

Figure 1 shows a comparison of the instantaneous velocity field in a streamwise–vertical slice for the flow around a ground-mounted PV panel simulated with PVade and OpenFOAM in a half channel with a no-slip wall at the bottom, slip wall at the top, periodic sides and inflow (outflow) boundary at the left (right). Similar unstructured meshes are used with coarse resolution off the panel resulting in visible artifacts in the wake region. The flow separation is qualitatively similar in both simulations, but velocity magnitude and bottom-wall boundary layer representation are significantly different. This is at least partially attributable to the utilization of the Smagorinsky turbulence model [7] in PVade, but the overall better performing wall-adapting local eddy-viscosity (WALE) model [8] in OpenFOAM's *pisoFoam* as in [9].

Figure 2 shows the simulated lift (C_l) and drag (C_d) coefficients for the cases from the previous figure. The systematic difference between the simulated C_l is indicative of not fully matching vertical momentum transport. Preliminary PVade results exhibit onset of grid independence (not shown here) for the selected mesh sizes (characteristic length scale for gmsh is L_{char} = 0.75 m, refined towards the panel), suggesting that the disagreement between the results is a turbulence modeling and/or atmospheric boundary-layer representation issue.

In the talk, ongoing work on the CFD solver intercomparison and the utilization for ground-mounted and roof-top PV applications will be presented, with a discussion of challenges.

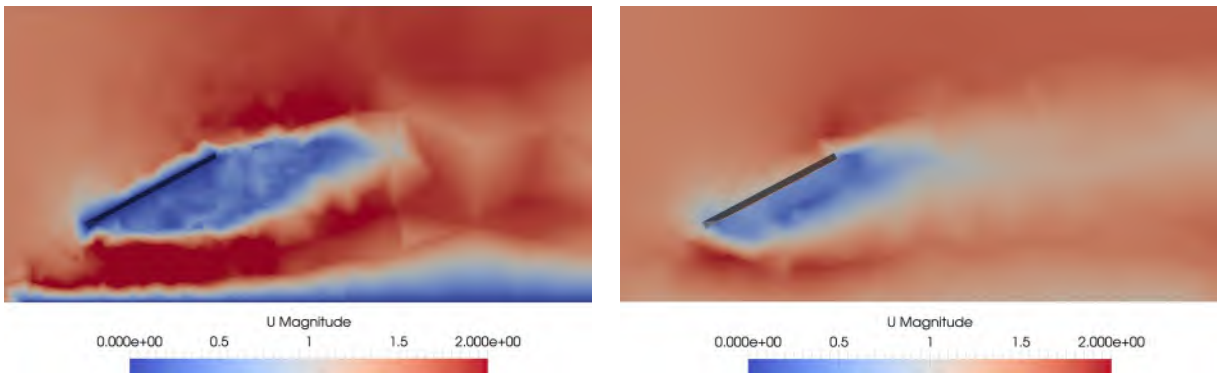

Figure 1: Instantaneous LES velocity magnitude U (m/s) in a streamwise–vertical slice through the flow around the upstream-facing 2 x 2 m PV panel with a thickness of 0.1 m and a tilt angle of −30°. The incoming flow enters the domain on the left. Simulation results from PVade (left) and OpenFOAM (right) are for the same time in the statistically steady state.

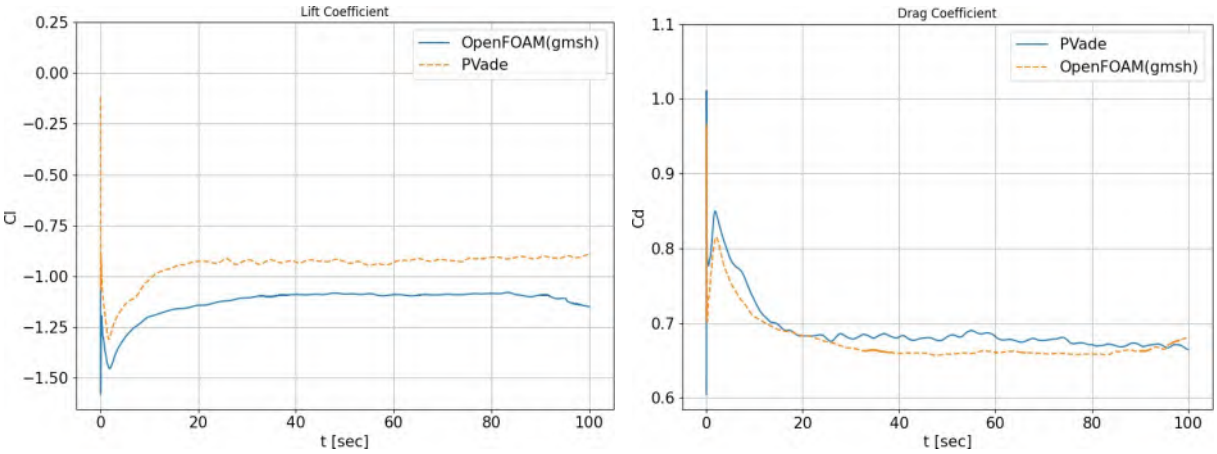

Figure 2: Time series of lift C_l (left) and drag C_d (right) coefficients simulated with PVade and OpenFOAM for the cases from Fig. 1. C_l differs by 30% in magnitude, whereas C_d is found in agreement between the two solvers, except that PVade predicts slightly more fluctuations.

Acknowledgment

This research is supported by the German Federal Government, the Federal Ministry of Research, Technology and Space, and the State of Brandenburg within the framework of the joint project “EIZ: Energie-Innovationszentrum” (project numbers 85056897 and 03SF0693A) with funds from the Structural Development Act for coal-mining regions. The research works of Marcelin Kabongo at LEPOSOL GmbH are co-funded by the European Union through the European Social Fund Plus program “Brandenburger Innovationsfachkräfte 2022” managed by ILB Investitionsbank des Landes Brandenburg (project number 85066437). Fruitful discussion with Richard Meyer (LEPOSOL GmbH), Christoph Glawe (WPD Onshore GmbH & Co. KG), Ethan Young and Brooke Stanislawski (both NREL) are kindly acknowledged.

References

[1] E. Young, X. He, R. King, D. Corbus, *J. Renew. Sustain. Energy* **12**(6):063503, 2020.
[2] A. R. Wittwer, J. M. Podestá, H. G. Castro, J. L. Mroginski, J. O. Marighetti, M. E. De Bortoli, R. R. Paz, F. Mateo, *Sol. Energy* **240**:315-328, 2022.
[3] B. J. Stanislawski, T. Harman, T. J. Silverman, R. B. Cal, M. Calaf, *J. Renew. Sustain. Energy* **14**:063702, 2022.
[4] E. Hosseini, E. Bou-Zeid, *Energy Build.* **347**(B):116354, 2025.
[5] J. Wang, P. Van Phuc, Q. Yang, Y. Tamura, *J. Wind Eng. Ind. Aerodyn*. **198:**104096, 2020.
[6] H. G. Weller, G. Tabor, H. Jasak, C. Fureby, *Comput. Phys.* **12**(6):620, 1998.
[7] J. Smagorinsky, *Mon. Weather Rev.* **91** (3):99–164, 1963.
[8] N. Franck, F. Ducros, *Flow Turbul. Combust.* **62**:183–200, 1999.
[9] M. Klein, R. W. Kessler, H. Schmidt, *Proc. Appl. Math. Mech.* **24**:e202400178, 2024.

Mitteilung

Fachgruppe: Allgemeine Strömungstechnik

Aerosol Particle Transport through an Air Curtain: Influence of Particle Stokes Number and Jet Reynolds Number

Andreas Kohl, Daniel Schmeling, Claus Wagner
Deutsches Zentrum für Luft- und Raumfahrt e.V. (DLR),
Institut für Aerodynamik und Strömungstechnik
Bunsenstraße 10, 37073 Göttingen, E-mail: andreas.kohl@dlr.de

Air curtains have the potential to reduce the airborne transmission of pathogens, for instance in passenger cabins of aircraft [1] or in train compartments. Prior to their implementation in a future passenger cabin, it is important to understand the particle transport processes through the planar turbulent air curtain jet. To this end, we set up an experimental chamber divided by an adjustable and well-defined planar air curtain jet entering through a nozzle at the top (see Figure 1). A monodisperse aerosol generator (FMAG1520, TSI) was implemented to produce a horizontal aerosol jet against the air curtain to mimic constant human exhalation. We analyzed the spread of particles with diameters between 1 µm and 12 µm, which can be produced by humans when breathing or speaking. To achieve sufficient light refraction for our camera setup, DEHS was selected as particle material and a laser light sheet illumination was used.

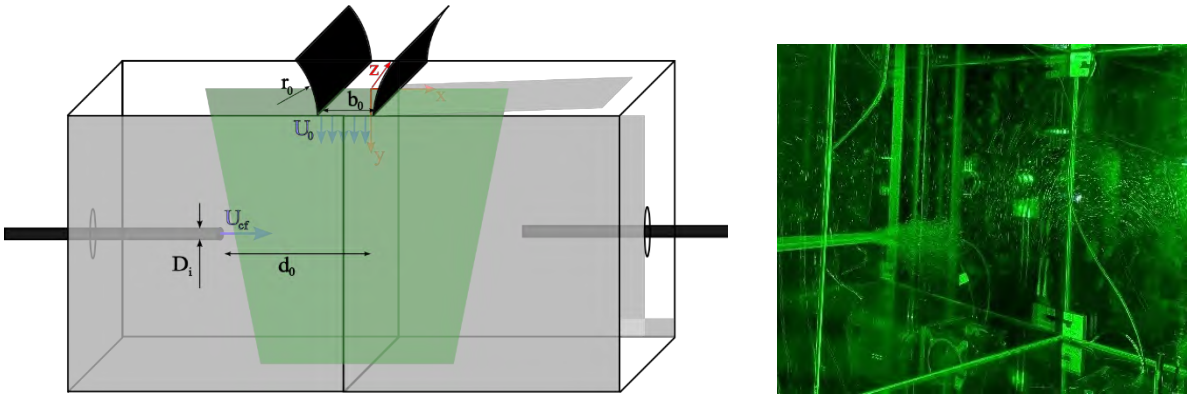

Figure 1 : 3D sketch of the experimental setup (left) and an image of a laser visualization of the aerosol jet inside the measurement chamber, interacting with the air curtain jet (right).

In our study, we systematically investigated the effects of two important parameters on the particle transport through the air curtain : the particle diameter D_p and the two-dimensional momentum flux ratio (γ) between the two jets in the measurement plane, as defined in [2] as

$$\gamma = \frac{\rho_0 \, b_0 U_0^2}{\rho_{cf} D_i U_{cf}^2},$$

where U_{cf} is the velocity of the pressure-driven isothermal ($\rho_0 = \rho_{cf}$) crossflow through a pipe with the inner diameter D_i resulting from the aerosol generator. U_0 is the velocity of the air curtain jet at the nozzle with the width b_0. In this study, we varied the parameter γ by changing the Reynolds number of the air curtain (Re_{ac}) and the aerosol jet ($Re_{ae\text{-}jet}$). We selected the range of $0 \leq \gamma \leq 2.5$, since preliminary studies have shown that the aerosol jet (temporarily) breaks through the air curtain within this range of γ. We used the particle detection tools of a PTV algorithm [3] to count the individual aerosol particles in the laser light sheet and to calculate a two-dimensional particle concentration map (see Figure 2b). Two-dimensional particle image velocimetry (PIV) was employed to measure the flow fields and to visualize the interaction between the two jets, using the same experimental setup, with the addition of DEHS seeding through the air curtain nozzle.

Figure 2a) shows the time-averaged absolute velocity $\overline{U}$ in the laser light sheet ($z = 0$), for a momentum flux ratio of $\gamma = 0.68$ (Re_{ac} = 1146, $Re_{ae\text{-}jet}$ = 1525, St_p < 0.22). The aerosol jet enters the measurement domain at a distance of 25 b_0 downstream of the air curtain nozzle. After propagating horizontally, the jet is deflected downwards due to the momentum of the air curtain jet, at a position of $x <$ -5 b_0. Both jets exit the measurement domain at $x \approx 5\ b_0$. Therefore, installing an air curtain with $\gamma = 0.68$ in an aircraft cabin, would prevent potentially infectious exhaled aerosols from propagating forward towards the other seat rows.
The mean jet propagation path described above is also shown in Figure 2b), which illustrates the instantaneous particle concentration in the laser light sheet, calculated as particles per pixel (PPP). The highest concentrations were found at the position where the aerosol jet enters the domain. The particle concentration remains high along the trajectory of the aerosol jet (see Figure 2a)). For this instantaneous snapshot of the particle concentration, we observed a significant decrease in concentration following the horizontal dotted centerline of the jet, approaching zero before reaching the center plane of the air curtain ($z = 0$, marked by a dashed line). Further downstream, for increasing y and $x < 0$, the particle concentration also decreases. This is due to the mixing of the aerosol jet with the particle-free air from the air curtain, which transports the aerosol downwards. Both jets are expected to hit the floor and spread in the positive and negative x-directions. Unfortunatly we have not yet been able to investigate this area yet due to the very high level of laser light reflection.
At the conference, we are going to compare the velocity and concentration results for all investigated momentum flux ratios and particle diameters to the measured particle concentrations at two distinct locations on the center plane ($z = 0$) in front of the air curtain ($x < 0$) and behind it ($x > 0$). This comparison will allow us to specify air curtains more accurately and to assess their effectiveness in tems of preventing particle dispersal in indoor ventilation scenarios such as passenger cabins.

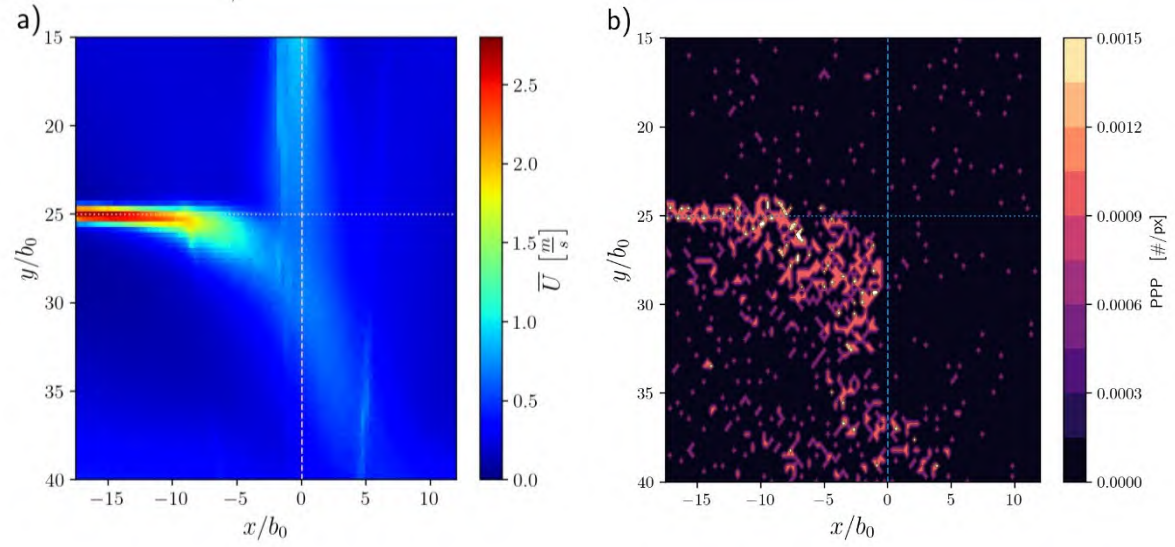

Figure 2: a) Time-averaged absolute velocity $\overline{U}$ obtained from the PIV measurements and b) Instantaneous particle concentration in the planar laser ligth sheet in particles per pixel (PPP) for an instantaneous snapshot of the time series for $\gamma = 0.68$.

[1] Kurec, K., Olszański, B., Gumowski, K., Klamka, M., Remer, M., Piechna, J., Kubacki, S.: Air curtain as a SARS-CoV-2 spreading mitigation method in a small aircraft cabin. Proceedings of the Institution of Mechanical Engineers, Part G: Journal of Aerospace Engineering. 237, 2480–2504 (2023).

[2] Khayrullina, A., Blocken, B., Magalhães De Almeida, M.O., Van Hooff, T., Van Heijst, G.: Impact of a wall downstream of an air curtain nozzle on air curtain separation efficiency. Building and Environment. 197, 107873 (2021).

[3] Barta, R., Bauer, C., Herzog, S., Schiepel, D., Wagner, C.: proPTV: A probability-based particle tracking velocimetry framework. Journal of Computational Physics. 514, 113212 (2024).

Mitteilung

Fachgruppe: Allgemeine Strömungstechnik

Towards a Fully-Coupled Incompressible Two-Phase Flow Solver

Deepak Kunhappan[1], Moritz Ertl[1]

[1]) Deutsches Zentrum für Luft- und Raumfahrt, Bunsenstr. 10, 37073 Göttingen
Institut für Aerodynamik und Strömungstechnik,
deepak.kunhappan@dlr.de
moritz.ertl@dlr.de

1 Introduction

Two-phase flows are common in aerospace and transportation industries. They can occur in several different scenarios, ranging from the injection and combustion of fuel in engines, hydrogen storage, to the motion of large container ships in the sea. Modelling these challenging flows with complex geometries require a robust and accurate two-phase flow solver. This abstract outlines the ongoing development of a two-phase solver within the finite volume framework of the CFD Software by ONERA, DLR and Airbus (CODA). For modelling the two phases we have chosen the well established Volume of Fluid (VOF) method [2]. This method introduces an additional scalar, the VOF variable α which represents the volume fraction of the liquid phase within a cell ($\alpha = 1.0$), and for the cells containing the gas phase, $\alpha = 0.0$. A cell is considered to be an interface cell when $0 < \alpha < 1.0$. The scalar α is advected with the following transport equation

$$\frac{\partial \alpha}{\partial t} + \vec{u}\ \nabla \cdot \alpha = -\nabla \cdot \left[\vec{u}_r\, \alpha\ (1-\alpha)\right], \tag{1}$$

In order to keep the free surface sharp, the advection of α requires a reduction of the numerical diffusion. We use an implementation of the interface compression scheme (IC) based on the work of Weller as described in [1]. The RHS of (1) introduces an anti-diffusion term to the VOF transport from the IC scheme, thereby reducing the numerical dissipation arising from the transport of α, based on a relative velocity ($\vec{u}_r$) between the two phases, $\vec{u}_r = \vec{n}\ C_\alpha\ |\vec{u}_f|$, where $\vec{n}$ is the interface normal vector and C_α a parameter for the strength of the compression scheme.
Equation (1) is coupled with the incompressible solver in CODA to provide the required numerical accuracy and computational efficiency for flows with velocities much smaller that the speed of sound. The discretization is based on a fully-coupled finite-volume spatial discretization (with appropriate linearization) leading to a linear system of block coupled-equations. Within such a system the VOF transport equation and the incompressible Navier-Stokes equations (both pressure and momentum) are solved simultaneously. Further details on the formulation and implementation of the incompressible solver in CODA can be found in [3].

2 Preliminary results

The current implementation was validated against two basic test cases. The first test case is the well known Zalesak's disc problem. In this test case, a slotted disc shown in figure 1(a) undergoes a solid body rotation, and the resulting configuration after two rotations is shown in figure 1(b), indicating that the slotted disc's initial configuration was fairly well preserved, and was similar to what has been found in other studies using the IC scheme.

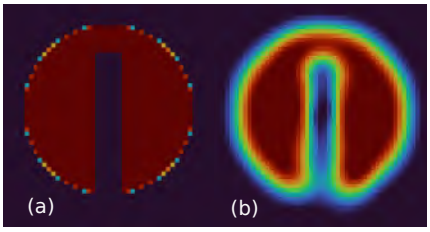

Figure 1: (a) Initial configuration of Zalesak disc, (b) Configuration of the disc after 2 rotations.

The 2D inviscid two-phase flow over a ramp was chosen as the second test case. This simple test case involves several flow phenomena which commonly arise in maritime applications: such as the presence of a distinct free surface, high density ratio ratio between the two phases ($\rho_l/\rho_g = 1000.0$), and gravity effects. The height of the free-surface at the outlet can be obtained analytically, and this quantity was used to validate the simulation. Further details on this case can be found in [4].

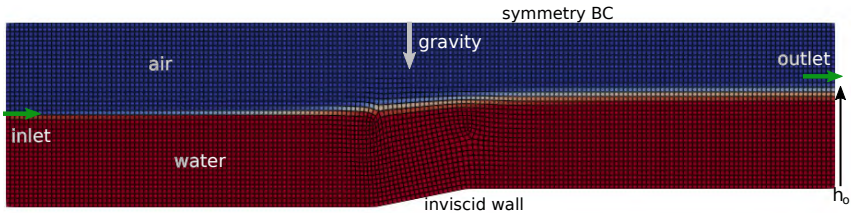

Figure 2: Contours of the phase fraction/VOF variable α (after convergence), with boundary conditions for the 2D ramp case. h_o is the height of the free-surface at the outlet.

Figure 2 shows the converged volume fraction contour and the boundary conditions. Symmetry boundary condition was set at the top (at the air-phase), and inviscid wall boundary condition was set at the bottom (water phase). The free surface height h_o at the outlet was used to validate the case, and it was found to be $1.1m$ whereas the height from the analytical solution was $1.09m$.

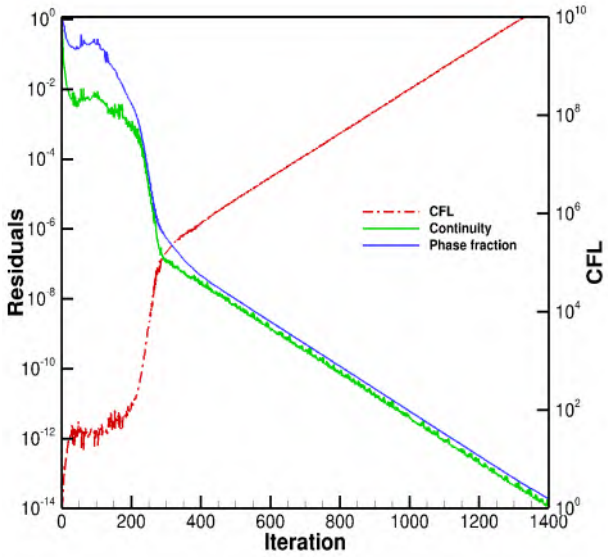

Figure 3: Residual convergence history, 2D ramp case

Furthermore smooth steady state convergence up to machine precision was obtained for both the VOF and continuity equations as shown in figure 3. Future work will include turbulence modelling and simulation of complex two-phase flows relevant to maritime applications.

CODA is the computational fluid dynamics (CFD) software being developed as part of a collaboration between the French Aerospace Lab ONERA, the German Aerospace Center (DLR), Airbus, and their European research partners. CODA is jointly owned by ONERA, DLR and Airbus.

References

[1] Suraj S Deshpande et al. "Evaluating The Performance of the Two-Phase Flow solver InterFOAM". 2012.

[2] C.W Hirt et al. "Volume Of Fluid (VOF) Method for the Dynamics of Free Boundaries". 1981.

[3] Deepak Kunhappan et al. "Development of a Coupled Implicit Incompressible Flow Solver in CODA". In "New Results in Numerical and Experimental Fluid Mechanics XIV", pp. 241–251. Springer Nature Switzerland, Cham, 2024.

[4] Petteri Peltonen et al. "The Ghost Fluid Method for OpenFOAM: A Comparative Study in Marine Context". 2020.

Mitteilung

Fachgruppe: Bio- und Mikrofluidmechanik

Experimental Investigation of Shear-Induced Generation of Respiratory Aerosol: Simultaneous Measurements of Particle Quantities and Wave Topology

Johanna Michel, Lars Krenkel
OTH Regensburg, Labor für Biofluidmechanik, Regensburg Center of Health Sciences and Technology (OTH Regensburg) and Regensburg Center of Biomedical Engineering (OTH and University Regensburg), Galgenbergstr. 30, 93053 Regensburg,
Email: johanna.michel@oth-regensburg.de

In recent years, respiratory aerosol has gained much attention as a carrier of infectious diseases. While the flow mechanics of aerosol spreading and containment are mostly well researched, less is known about the flow mechanics of how the aerosol forms inside the respiratory system. In our work, we focus on the aerosol formation during coughing, which is mostly triggered by large shear air flow velocities in the larger airways. The associated large velocity differences between the wall-lining mucus film and the air trigger Kelvin-Helmholtz waves in the mucus film, from which particles detach (Pöhlker et al. 2023).

Computational modelling could be a valuable tool to improve our understanding of aerosol formation and transport inside the respiratory system. In current literature, among others, the Eulerian wall film model in Ansys Fluent has been used to predict the aerosol formation (Anzai et al. 2022; Khoa et al. 2023). However, as we have shown in previous work (Michel and Krenkel 2025), the particle prediction in this model depends on both the chosen simulation time step and on the local mesh resolution. For an improved model implementation, experimental validation data is highly needed.

In our work, we perform model experiments of shear-induced aerosol generation under simplified flow conditions to provide the necessary validation data for computational models. As such, our goal is to deduct an empirical model of the quantity and size distribution of generated particles depending on the mucus rheology and on the local air flow.

As human mucus is difficult to sample for the experiments, we developed a synthetic hydrogel based on EGDMA, HEMA and SBMA. By varying the concentration of the components, the hydrogel can be tuned to cover the large range of rheological properties of human physiological mucus as recorded in our previous work (Tauwald et al. 2023).

Figure 1a) shows a schematic view of our experimental setup. Building on our previous work, where we triggered shear-induced aerosol generation successfully at a low shear air flow of 9.5 L/min (Michel and Krenkel 2025), we now present a method to increase the achievable air flow range. The main part of the setup was the measuring chamber, which consisted of a rectangular channel (25 x 70 x 2 mm). The bottom wall of the rectangular channel encompassed a trough, in which a mucus mimetic film with an initial thickness of 1 mm was applied. To trigger shear-induced aerosol generation, filtered pressurized air was guided over the fluid film. A computer-controlled valve controlled the air flow to a range of 0 to 200 L/min. To record only the particles detaching from the fluid film, a good seal towards the ambient air was detrimental. To achieve this, the measuring chamber was placed inside a closed, transparent chamber. Air exchange into or from the closed chamber was only possible via a HEPA filter. An optical aerosol spectrometer (RespAerMeter, Palas) recorded the quantity and size distribution of generated particles in real time.

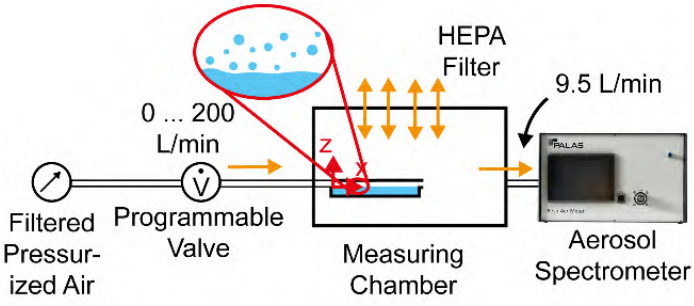

a) Experimental setup for triggering shear-induced aerosol generation at different air flow velocities

b) Exemplary wave profile captured at an air flow of 96 L/min

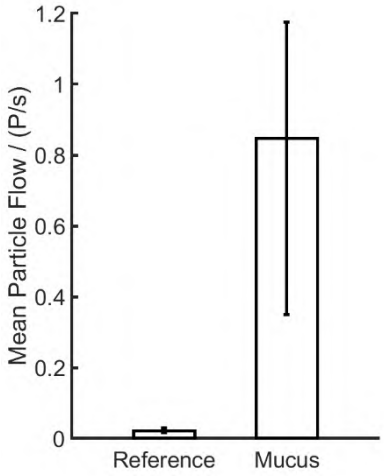

c) Mean particle flow created at an air flow of 48 L/min (data from three repeated measurements)

Fig. 1: Experimental setup for triggering shear-induced aerosol generation at different air flow velocities and exemplary mean particle flow and wave profile

Figure 1c illustrates the mean particle flow created by a shear air flow of 48 L/min in three repeated measurements. Compared to our previous results measured at a shear flow of 9.5 L/min (Michel and Krenkel 2025), a significantly higher mean particle flow was observed. However, there was a large variation between the three individual measurements, which could be caused by differences in how the waves emerged spontaneously from instabilities.

To enable linking particle quantities to wave topology, we integrated a non-invasive optical measurement system into our experimental setup. For this, we used a 532 nm continuous wave laser to illuminate a vertical plane along the streamwise midline of the channel. The intersection of the laser plane with the fluid film including any waves was recorded by a high-resolution camera, which was tilted at an angle of 25°. To eliminate reflections, we dyed the mucus mimetic gels with fluorescent dyes and equipped the camera with a filter. Figure 1b shows an exemplary wave profile captured at an air flow of 96 L/min.

At the workshop, we will present measurements of particle quantities and wave topologies at different mucus mimetic properties and air flows. Further, we develop optical measurement techniques to capture 3D wave profiles.

Anzai, Hitomi, Yugo Shindo, Yutaro Kohata, et al. 2022. “Coupled Discrete Phase Model and Eulerian Wall Film Model for Numerical Simulation of Respiratory Droplet Generation during Coughing.” *Scientific Reports* 12 (1): 14849. https://doi.org/10.1038/s41598-022-18788-3.

Khoa, Nguyen Dang, Kazuki Kuga, Kiao Inthavong, and Kazuhide Ito. 2023. “Coupled Eulerian Wall Film–Discrete Phase Model for Predicting Respiratory Droplet Generation during a Coughing Event.” *Physics of Fluids* 35 (11): 112103. https://doi.org/10.1063/5.0174014.

Michel, Johanna, and Lars Krenkel. 2025. “Towards Experimental Validation of Models of Shear-Induced Aerosol Generation in the Human Respiratory System.” Paper presented at DGLR STAB Symposium 2024. *New Results in Numerical and Experimental Fluid Mechanics XV*.

Pöhlker, Mira L., Christopher Pöhlker, Ovid O. Krüger, et al. 2023. “Respiratory Aerosols and Droplets in the Transmission of Infectious Diseases.” *Reviews of Modern Physics* 95 (4): 045001. https://doi.org/10.1103/RevModPhys.95.045001.

Tauwald, Sandra Melina, Johanna Michel, Marie Brandt, Veronika Vielsmeier, Christian Stemmer, and Lars Krenkel. 2023. “Experimental Studies and Mathematical Modeling of the Viscoelastic Rheology of Tracheobronchial Mucus from Respiratory Healthy Patients.” *Multidisciplinary Respiratory Medicine* 18 (October). https://doi.org/10.4081/mrm.2023.923.

Mitteilung

Fachgruppe: Bio- und Mikrofluidmechanik

Parametrical Investigation of the Aerodynamics of Maple Seeds in Controlled Autorotation Condition in a Vertical Wind Tunnel

Korbinian Neumeier, Florian Erzinger, Lars Krenkel

OTH Regensburg, Biofluid Mechanics, Galgenbergstr. 30, 93053 Regensburg, Germany,
Regensburg Center of Biomedical Engineering (OTH und Universität Regensburg),
E-Mail: korbinian.Neumeier@st.oth-regensburg.de

Understanding the aerodynamics of diaspore flight, such as that of maple samaras and Dipterocarpus, provides valuable insights into natural systems and has important implications for the design of small flying devices and drones. These diaspores use autorotation to disperse over wide areas. The balance between mass distribution, wing morphology, and aerodynamic forces that enable stable autorotation offers a compelling model for biomimetic engineering. Progress in this area can impact robotics and environmental science where efficient and stable flight at low Reynolds numbers is crucial. Prior studies have highlighted the importance of mass distribution and inertia in stable autorotation and identified a leading edge vortex that produces relatively large lift. Numerical work has further emphasized the role of the seed's mass distribution and described the governing vortical structures. A common limitation is that specimens are either observed in free flight without control over variability or are characterized under restricted autorotation, and many simulations rely on simplified geometries without surface microstructure. We address these gaps by establishing a reproducible platform that combines a vertical wind tunnel with directionally conditioned laminar flow and standardized, optically trackable biomimetic replicas. A central feature is template based morphology control. Interchangeable templates enable specific curvature and wave profiles with high repeatability, and a defined wing twist can be introduced in the spanwise direction (**Figure 1**).

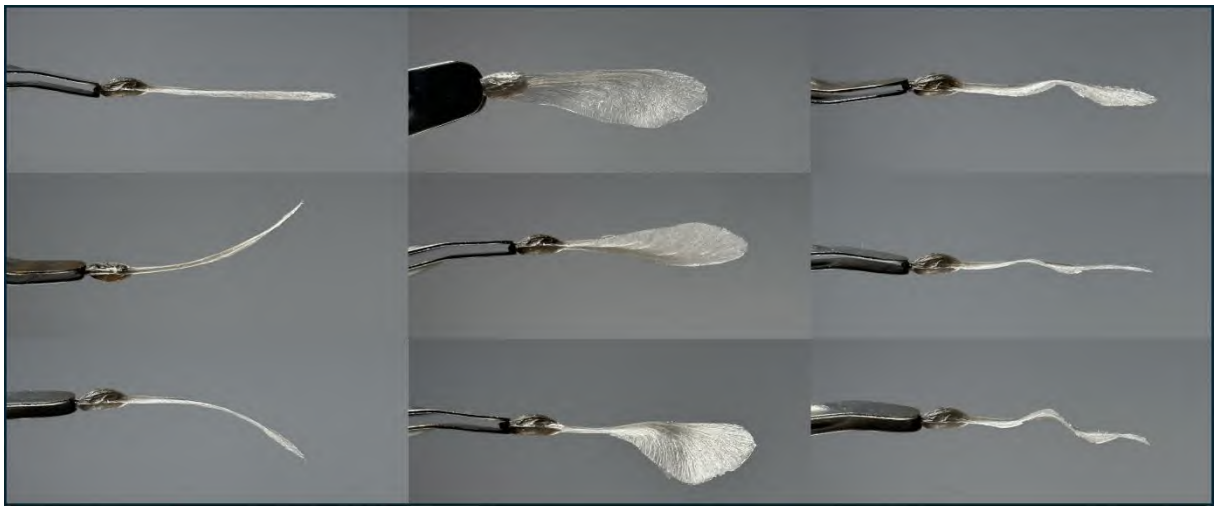

Figure 1: UV resin replica with different curvature profiles produced by thermoplastic reshaping via templates

Figure 2: Mikrostructure of the replica (left) vs the original (right)

Using thermally reconfigurable replicas enables systematic parameter sweeps of wing morphology under fully unrestrained free flight. Three material pathways were evaluated, namely Polyvinylalcohol / Carboxy-methylceluloses, Polycaprolacton, and a UV curable acrylate. The UV resin provided the best microstructure fidelity together with tuneable optics and a suitable stiffness to mass ratio and is used as the reference replica (**Figure 2**). Flow surveys in the test section showed high uniformity and low turbulence intensity. Hover control was stable and repeatable, and for the same seed the power required for hover was reproduced within about one percent over ten repetitions. Motion was quantified by dual view high speed imaging with marker based optical tracking [2500 fps, Photron Fastcam AX mini].

Wind tunnel flight experiments revealed two distinct flight modes. A stable mode with nearly constant rotation frequency and minimal lateral drift (**Figure 3a**), and an unstable mode with circular drift, flatter angle of attack, and higher rotation frequency (**Figure 3b**). The sense of rotation and the mode could be selected by an initial spin at launch. First morphology sweeps indicate that wing curvature and surface undulations affect the flightmode selection.

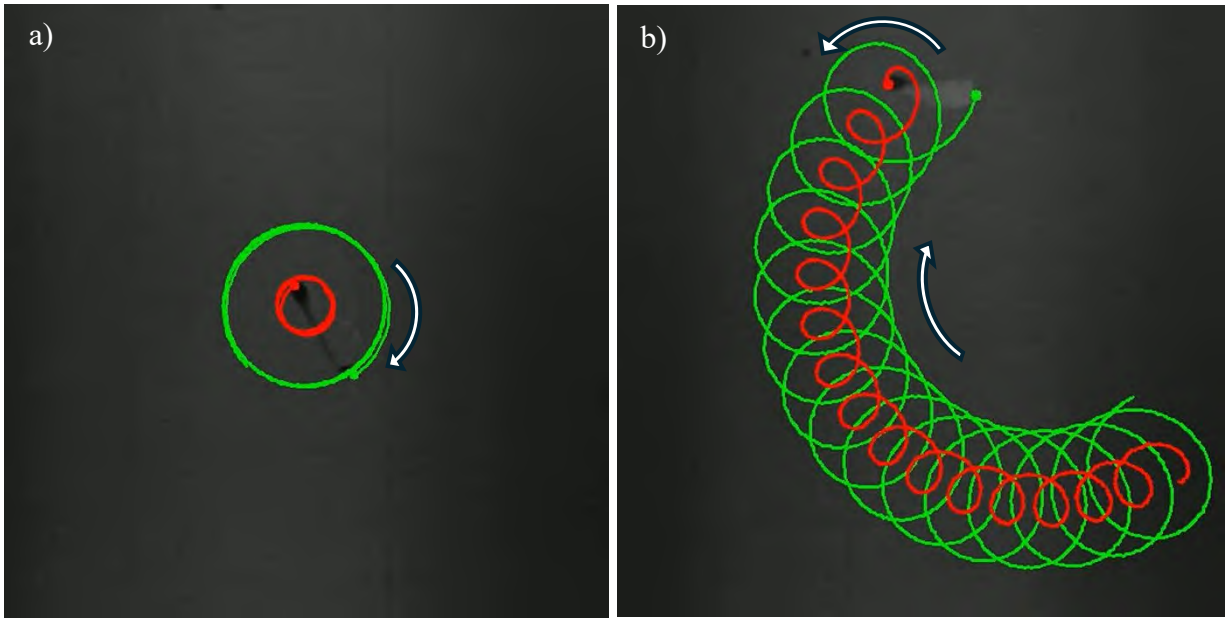

Figure 3: Tracked Wingtip (green) / Wingbase (red) of: (a) The pathing of the stable flighmode; (b) The pathing of the instable flightmode showing circular drift

The wind tunnel control allows programmed flow profiles including steady plateaus, prescribed velocity ramps, and short gusts of adjustable strength and duration. This enables different inflow scenarios up to pseudo free fall. The platform enables quantitative mapping of these regimes in follow up work and supports applications in micro flyers, turbomachinery, and targeted drug delivery while also sharpening our understanding of natural seed dispersal.

Mitteilung

Fachgruppe: Bio- und Mikrofluidmechanik

ML-assisted analysis of flow patterns in artificial membrane lungs

Daniel Pointner, Lars Krenkel
OTH Regensburg, Department of Biofluid Mechanics, Seybothstraße 2, 93053 Regensburg
daniel.pointner@oth-regensburg, lars.krenkel@oth-regensburg.de

Extracorporeal membrane oxygenation (ECMO) is a technique used to support patients with severe respiratory or cardiac failure by means of externally oxygenating the blood. A central component of ECMO is the membrane lung (MemL), which facilitates gas exchange. Despite the continuous advancement of MemL design and ECMO technology, complications such as coagulation disorders and thrombus formation within the MemL persist as significant clinical challenges. The underlying causes of thrombosis – whether driven by flow dynamics, cellular interactions, or a combination of both – are not yet fully understood. It is therefore critical to gain deeper insight into fluid dynamics within the MemL in order to improve ECMO performance and reduce the risk of thrombotic events.

Computational Fluid Dynamics (CFD) can be a powerful analytical tool to investigate the blood flow in complex systems, such as the MemL. The MemL consists of densely packed hollow fibers through which oxygen circulates, while blood flows around these fibers to enable gas exchange. This intricate architecture, in combination with the non-Newtonian behaviour of blood, poses significant challenges for accurate CFD modelling. As illustrated schematically in Figure 1A, a complete MemL is presented, while Figure 1B highlights a representative fiber stack section, illustrating the orientation and arrangement of the hollow fibers. Furthermore, the coagulation process dynamically alters both the fluid properties and the geometry of the system, thereby further complicating simulations. Existing models frequently simplify or neglect these factors, leading to an insufficient consideration of critical geometric and physiological influences that are essential for realistic flow analysis.

Our research uses an integrated approach that combines CFD simulations and machine learning (ML) to investigate blood flow patterns between the fibers in MemL. As shown in Figure 1C, we define a representative fluid domain of the MemL to simulate realistic blood flow. Due to the complex geometry, it is not feasible to compute blood flow throughout the entire MemL using conventional CFD methods. For the MemL section, we utilise the HemoCell framework and an Ansys Fluent implementation of an Euler-Euler (EE) model. The simulation data generated from these models (see Figure 2 for exemplary results of the EE-model and according microfluidic experiments) will be used to train a neural network capable of predicting blood flow patterns across diverse geometries. This data-driven approach enables efficient interpolation across various fiber configurations, eliminating the need for computationally intensive meshing and simulation for each individual case. By integrating CFD with ML, we aim to facilitate flow analysis within the complex MemL geometry. Ultimately, this hybrid CFD-ML framework will contribute to a deeper understanding of flow-induced coagulation mechanisms—an essential step toward enhancing ECMO performance and improving patient safety.

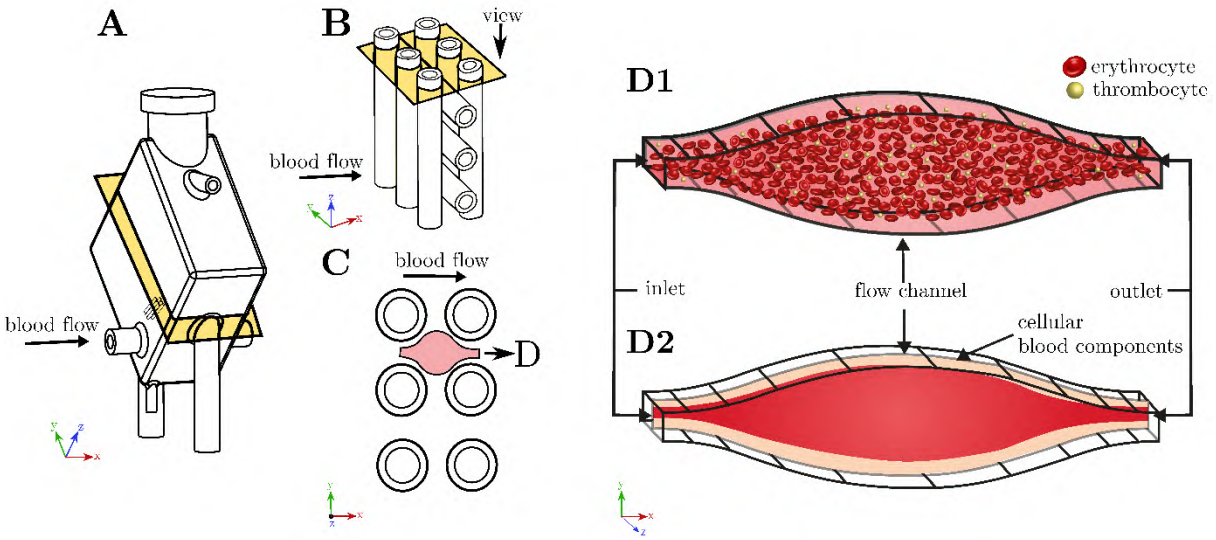

Figure 1 – **A** Overview of a MemL, blood flow in positive x-direction. **B** Side view of fiber bundle. **C** Definition of fluid domain between fibers. **D1** Fluid simulation using HemoCell. **D2** Comparable fluid simulation using Ansys Fluent (EE) model.

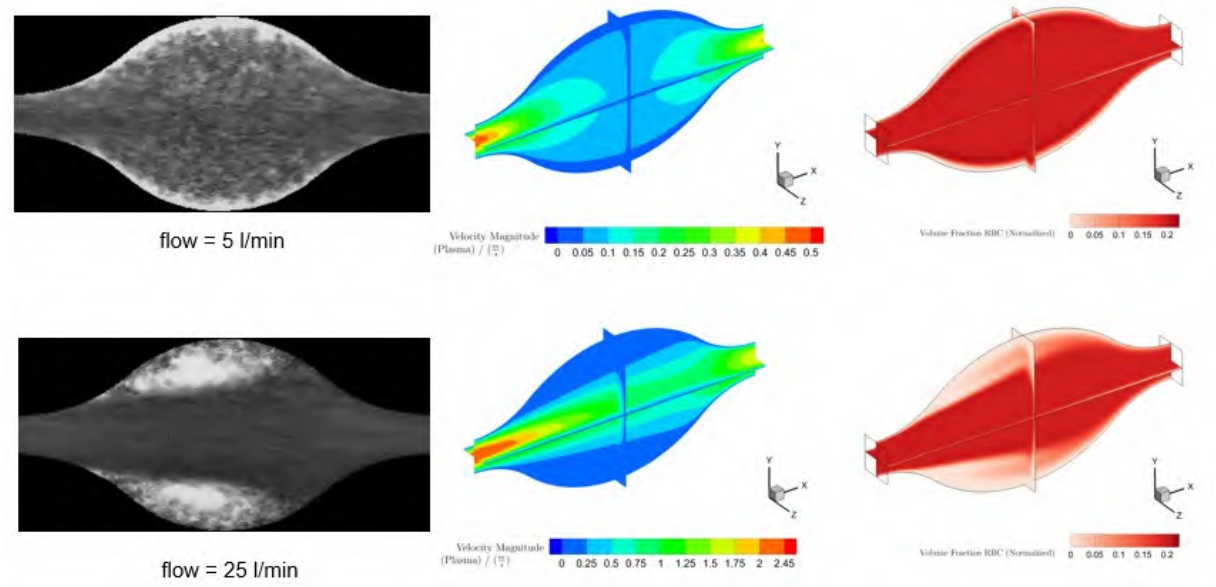

Figure 2 – Exemplary microfluidic experimental data and numerical results from the ANSYS Fluent (EE) model of velocity magnitude and red blood cell (RBC) volume fraction for two flow rates.

Mitteilung

Fachgruppe: Drehflügler

Modal Analysis of Volumetric Flow Fields around a Quadcopter from Experimental Shake-The-Box Results

Alexander Fenk[1], C. Christian Wolf[2] and Gudrun Thäter[1]
[1]Karlsruhe Institute of Technology, Kaiserstr. 12, 76131 Karlsruhe
[2]German Aerospace Center, Bunsenstr. 10, 37073 Göttingen, Germany
alexfenk00@gmail.com, Christian.Wolf@dlr.de, gudrun.thaeter@kit.edu

Introduction

Unmanned aerial vehicles experience a rapid rise in various industries as well as in the private sector. This motivates the investigation of their wake in free flight, to allow understanding and development of efficient, safe and silent vehicles. Therefore, a Shake-the-Box experiment of a quadcopter with an overall span of approximately 0.5 m in free flight was conducted at the DLR site in Göttingen, covering a variety of operating conditions, such as flight in ground effect (IGE) and out of ground effect (OGE) [1]. A momentum analysis neglecting the unknown pressure terms was performed on the volumetric, time resolved velocity data from an OGE-case, yielding an estimate of the quadcopter's thrust. The result exhibits strong fluctuations and a systematic deviation to the expected value derived from the vehicle's weight (see Figure 1). Large scale flow structures, going along with pressure gradients, might be responsible and can be identified by a modal analysis. This presentation features the use of a Proper Orthogonal Decomposition (POD) code on the STB-data of both IGE and the OGE cases to investigate the modal structure of the flow around a free flying helicopter.

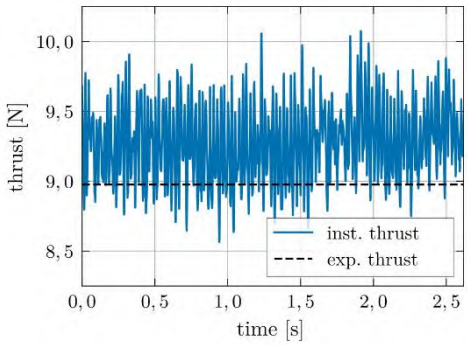

Figure 1: Expected thrust and by momentum analyzation calculated instantaneous thrust.

Applied Method

POD was chosen for a modal analysis due to its optimality with respect to the variance and an assumed stochastic stationarity of the drone centered flow fields. POD in the implemented version decomposes a time and space variant field $u(x,t)$ according to

$$u(x,t) = \overline{u}(x) + \sum_{n=1}^{Z} \alpha_n(t)\phi_n(x),$$

where $\overline{u}(x)$ is the time averaged mean, Z the number of used time steps, $\alpha_n(t)$ the time dependent coefficients and $\phi_n(x)$ the orthogonal and normalized modes, ranked according to their contribution to the overall variance of the flow [2]. The variance can be interpreted as two times the spatially integrated turbulent kinetic energy [3]. For flow fields discretized in time and space, the velocity data for each time step are assembled in a vector $\boldsymbol{q}^{(i)} = \left[u'^{(i)}_1, \ldots, u'^{(i)}_M, v'^{(i)}_1, \ldots v'^{(i)}_M, w'^{(i)}_1, \ldots, w'^{(i)}_M\right]^T$ and summarized in a matrix $\boldsymbol{Q} = [\boldsymbol{q}^{(1)}, \ldots, \boldsymbol{q}^{(Z)}]$. The identified modes are then the solution of the eigenvalue equation

$$\boldsymbol{C\Phi} = \boldsymbol{\Lambda\Phi},$$

with the spatial covariance $\boldsymbol{C} = \boldsymbol{Q}\boldsymbol{Q}^T$, the matrix of modes $\boldsymbol{\Phi} = [\boldsymbol{\phi_1}, \dots, \boldsymbol{\phi_Z}]$ and the matrix of eigenvalues $\boldsymbol{\Lambda} = \mathrm{diag}(\lambda_1, \dots, \lambda_Z)$. The eigenvalues mark the contribution of a mode to the overall variance and thus indicate its energy. To reduce the computational costs, the method of snapshots was applied [3].

Results and Discussion

The spatially continuous experimental STB-data were discretized by evenly spaced regular cartesian grids with a spacing of 1 cm. In the OGE case a drone centered coordinate system was applied, removing a residual position drift of the drone similar to the approach in [1]. The IGE case was investigated from the perspective of a fixed global observer.

The modes 5 and 6 of the OGE case both contributed 1.14% of the overall energy and presented a similar but slightly shifted spatial structure (see Figure 2) indicating travelling structures [4]. Figure 3 shows the result of an FFT analysis of the calculated thrust as well as the coefficients of the modes 5 and 6. In all cases, the most prominent peak is at around 40 Hz. The flow structures represented by the combination of modes 5 and 6 most likely go along with pressure gradients, explaining the fluctuations in the calculated thrust when neglecting the pressure terms.

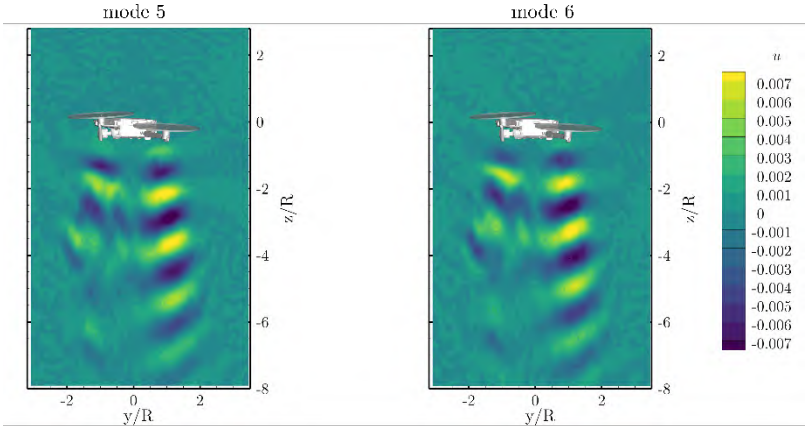

Figure 2: Non-dimensional u-component of modes 5 (left) and 6 (right) of OGE case. Slice through longitudinal axis. Rotor radius R = 0.11 m.

Similarly, for the IGE case, the coefficients of modes 6 and 7, containing 1.10% and 1.09% of the energy respectively, showed related spectra (see Figure 3). They contain a mixture of frequencies, with the most relevant ones being smaller than 20 Hz. Again, the close relation indicates travelling structures.

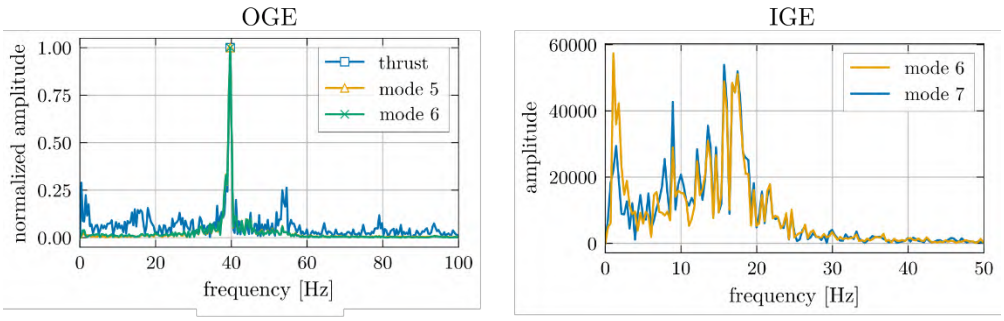

Figure 3: FFT of calculated thrust, modes 5 and 6 OGE case (left) and modes 6 and 7 IGE case (right).

In both the OGE and IGE case the travelling structures are suspected to have aerodynamic reasons such as shear layer instabilities. The other high-ranking modes showed a generally transient behavior, being most likely caused by positional drift and other large-scale effects during the experiments.

[1] C. C. Wolf *et al.*, "Volumetric wake investigation of a free-flying quadcopter using Shake-The-Box Lagrangian particle tracking," *Exp. Fluids*, vol. 65, no. 10, p. 152, Oct. 2024, doi: 10.1007/s00348-024-03880-3.

[2] C. Howard, S. Gupta, A. Abbas, T. A. G. Langrish, and D. F. Fletcher, "Proper Orthogonal Decomposition (POD) analysis of CFD data for flow in an axisymmetric sudden expansion," *Chem. Eng. Res. Des.*, vol. 123, pp. 333–346, Jul. 2017, doi: 10.1016/j.cherd.2017.05.017.

[3] O. T. Schmidt and T. Colonius, "Guide to Spectral Proper Orthogonal Decomposition," *AIAA J.*, vol. 58, no. 3, pp. 1023–1033, Mar. 2020, doi: 10.2514/1.J058809.

[4] K. Taira *et al.*, "Modal Analysis of Fluid Flows: An Overview," *AIAA J.*, vol. 55, no. 12, pp. 4013–4041, Dec. 2017, doi: 10.2514/1.J056060.

Mitteilung

Fachgruppe: Drehflügler

Wind Tunnel Experiments on Rotor Blade Tip Vortices using Hot-Film Anemometry

Laura Mezzoli [1 2], Hauke T. Bartzsch [1], Alex Zanotti [2], C. Christian Wolf [1], Markus Raffel [1]

[1] German Aerospace Center, Bunsenstr. 10, 37073 Göttingen
[2] Politecnico di Milano, Piazza Leonardo da Vinci 32, 20133 Milano

laura.mezzoli@dlr.de, hauke.bartzsch@dlr.de, alex.zanotti@polimi.it, christian.wolf@dlr.de, markus.raffel@dlr.de

Introduction

Helicopter rotors produce helical vortex systems originating from the blade tips (Fig. 1), which affect the aerodynamic performance, vibrational loads and acoustic emissions of the rotorcraft.

Vortex properties include vortex core size, convective trajectory, and swirl velocity distribution. Phenomena linked to blade tip vortices include vortex pairing and blade vortex interaction (BVI). Previous research shows that the vortex properties are strongly influenced by the vortex Reynolds number. Galli et *al.* [2] investigated blade tip vortex characteristics at high Reynolds numbers (profile Reynolds number $\mathrm{Re}_{c,75\%R}$ up to $5 \cdot 10^5$) in a high-pressure wind tunnel. Using the same two-bladed rotor, the present study analyzes vortex evolution at lower Reynolds numbers ($\mathrm{Re}_{c,75\%R} = 6 \cdot 10^4$). To reduce vortex–vortex interactions, a specially designed single-bladed rotor was also tested.

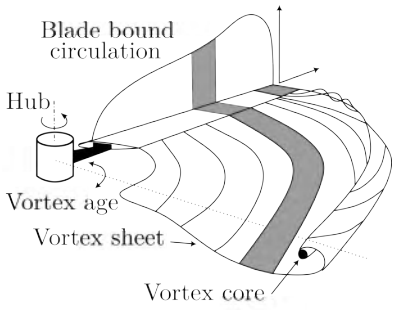

Figure 1: Sketch of bound circulation on a blade and its corresponding wake, after Martin and Leishman [1].

Experiments were conducted in the closed-loop 1-meter wind tunnel (1MG) at the German Aerospace Center (DLR) in Göttingen. Constant-temperature anemometry (CTA) with a hot-film probe was used to resolve the small-scale, high-frequency blade tip vortex structures.

Experimental setup

The test section of the 1MG has a width of 1.0 m, a height of 0.74 m and a length of approximately 2.5 m. The wind tunnel fan was only used for probe calibration, and was blocked during the vortex measurements for a low inflow velocity into the rotor plane, creating a flow structure as similar to hover condition as possible.

The rotor was mounted on a tube-like housing (Fig. 2) with a length of 0.7 m, attached to a vertical support. Tests comprised an Aeronaut CAMcarbon Light 12 × 4.5" rotor and an in-house-manufactured single-bladed aluminum rotor with a rotor radius of $R = 0.15$ m. The latter features a pitch distribution specifically designed for wind-tunnel testing at medium- and high-Reynolds numbers.

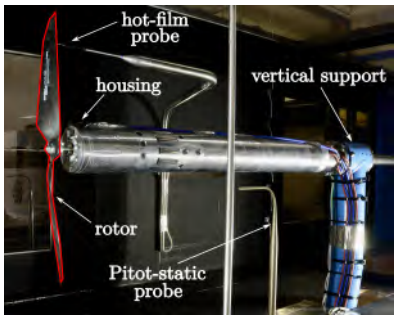

Figure 2: Side view of the test section, Aeronaut CAMcarbon Light 12 × 4.5" rotor, hot-film probe close to the blade tip.

The tube-like housing contains the motor, a piezoelectric balance for thrust measurements, and three accelerometers and temperature sensors to monitor vibrations and temperature gradients across the balance. A light barrier and an encoder with a resolution of 1024 counts per revolution tracked the rotor position, thus allowing a measurement of the vortex age Ψ (defined as the azimuthal angle the rotor has moved since the production of the vortex segment). The rotational speed of the rotor was then maintained at 4000 rpm by a PID controller integrated into the data-acquisition system.

The hot-film probe was positioned in the wake of the rotor by means of a two-axis traversing system, which allowed operation from 0 R to 1.6 R in rotor axial and 0.5 R to 1 R in rotor radial direction.

Measurements

The hot-film sensor was set-up to measure the velocity magnitude in the rotor's axial-radial plane, and calibrated against a Pitot-static probe at 18 calibration points with velocities from 1 to 36 $\mathrm{m\,s^{-1}}$. Following Bruun [3], several fits were tested, including King's law, an extended power law—adding a linear term to King's model—and a fourth-order polynomial. From the comparison, King's law proved to fit the data best, with a maximum deviation between fitted and measured velocity below 3%. Including a temperature correction, the calibration law reads: $\frac{E^2}{T_w - T_a} = A + B\,U^n$, where E and U are the measured signal and corresponding velocity, A, B and n are calibration parameters, and $T_w = 250\,^\circ\mathrm{C}$ and T_a are the hot-film and ambient temperature.

For the investigation of the rotor blade tip vortices, 14 axial stations were sampled from $z = 0.02\,R$ to 1.20 R. At each location, the signal was inspected, looking for the vortex signal shape, as shown in Fig. 3. The mean vortex radial position was initially estimated by observation of the time signal. Measurements were then taken at nine radial positions spanning $\pm 1 \cdot \sigma$ around the estimated mean, with σ (standard deviation of the vortex position in rotor radial direction) estimated mathematically from prior measurements. For increasing vortex age, the number of radial sampling points was successively increased from 9 to 16. This enabled a better tracking where the radial variation increased, for example, due to vortex pairing events for successive blade passes. To gain the expectation value and standard deviation of the radial vortex position, a Gaussian distribution was applied and fitted to the data. The results allowed insights into the vortex trajectories and, hence, vortex interactions.

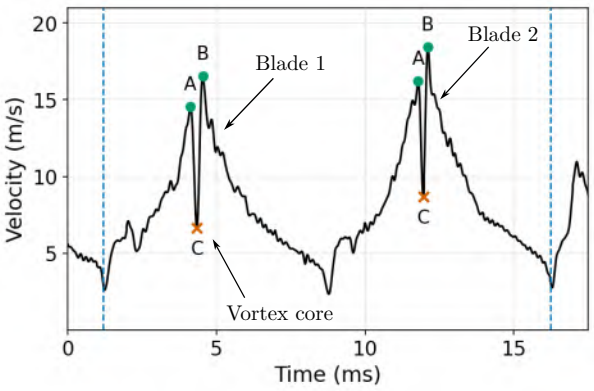

Figure 3: Sample measurement of velocity over time, hot-film probe, at a vortex age of $\Psi = 75°$.

Figure 3 shows the hot-film signal over time at a vortex age of $\Psi = 75°$ (dashed line: 1/rev blade trigger). The signal was low-pass filtered at 5 kHz (sampling rate: 50 kHz) through a fourth-order Butterworth filter to remove high frequency noise. The velocity-time signal shows the distinct footprint of a tip vortex: The peaks (A) and (B) in Fig. 3 are related to the passage of the vortex core radius, with local maxima of the tangential (swirl) velocity. In between, the dip (C) marks the vortex center with zero tangential velocity but non-zero convection velocity. The vortex core radius is computed from half the peak-to-peak time difference multiplied by the local convection speed, which is derived from the computed vortex trajectories. These data are then analyzed over vortex age and compared to the findings of Galli et *al.* [2] and Bartzsch et *al.* [4], and to analytical vortex models.

References

[1] P. B. Martin and J. G. Leishman. "Trailing vortex measurements in the wake of a hovering rotor blade with various tip shapes". In: *Proceedings of the 58th AHS International Annual Forum*. 2003.

[2] E. Galli, H. T. Bartzsch, A. Zanotti, C. C. Wolf, and A. D. Gardner. "Hot-film measurements of rotor tip vortices in a high-pressure wind tunnel". In: *Proceedings of the STAB Symposium*. 2024.

[3] H. H. Bruun. *Hot-Wire Anemometry. Principles and Signal Analysis*. Oxford: Oxford University Press, 1995.

[4] H. T. Bartzsch, C. C. Wolf, E. Galli, M. Raffel, M. Braune, and M. Löhr. "BOS and HWA measurements on rotor tip vortices in a high-pressure wind tunnel". In: *Vertical Flight Society's 81st Annual Forum and Technology Display*. 2025, pp. 1–17. DOI: 10.4050/F-0081-2025-0253.

Mitteilung

Fachgruppe: Drehflügler

Out of Ground Effect Blade Tip Vortex Study of a Single Bladed Rotor in Hover

Marlene Neef, Alexander Heintz, Hauke T. Bartzsch, Clemens Schwarz, C. Christian Wolf, Markus Raffel
German Aerospace Center, Bunsenstr. 10, 37073 Göttingen,
marlene.neef@dlr.de, alexander.heintz@dlr.de, hauke.bartzsch@dlr.de, clemens_a.schwarz@web.de, christian.wolf@dlr.de, markus.raffel@dlr.de

The wake of a helicopter is strongly influenced by rotor blade tip vortices, which govern the wake's shape and dynamics. These vortices are associated with several adverse effects, including blade–vortex interactions, increased noise, and energy loss. Improving models of blade tip vortices is crucial for more accurate predictions of the flow field around rotorcrafts in order to mitigating these adverse effects. The formation of blade tip vortices can be explained by considering the static pressure difference between the suction side (upper surface) and the pressure side (lower surface) of the 3D airfoil. This pressure difference, along with a span-wise pressure gradient, causes streamlines on the suction side to curve inboard and those on the pressure side to curve outboard. As a result, air flows around the blade tip, since no solid barrier prevents the opposing pressure areas from seeking equilibrium. The blade tip vortex then moves downward from the rotor plane and decays. Along its trajectory the flow field can be visualized using Particle Image Velocimetry (PIV) as illustrated in Fig.1.

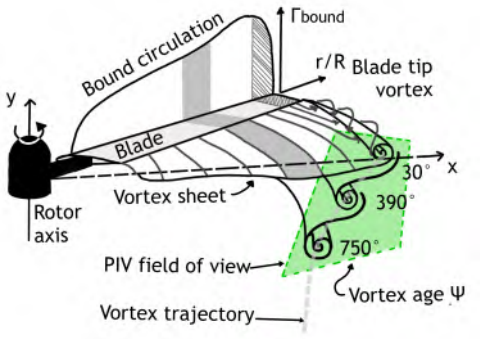

Figure 1: Schematic explaining the formation of a blade tip vortex of a single bladed rotor system and outlining a PIV field of view.

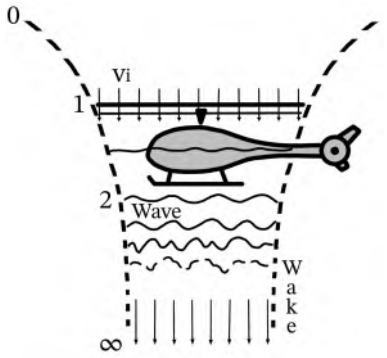

Figure 2: Helicopter diagram illustrating long-wave instabilities and wake contraction over wake age

The following analysis is based on data acquired at the Hover Test Stand (HVG) of the German Aerospace Center (DLR) in Göttingen. Three-component, two-dimensional (3C-2D) PIV measurements were conducted to capture the flow field around a rotor with a radius of 0.76 meters. From this data, vortex characteristics were extracted and systematically analyzed to investigate rotor wake dynamics in hover out of ground effect.

During the analysis of the vortex core radius r_c over varying vortex ages Ψ, the data revealed deviations from expected behavior. While a continuous growth of the vortex core with increasing vortex age was anticipated—consistent with typical vortex diffusion theory—the measurements showed a contraction of the vortex core beginning at approximately 850 degrees of vortex age. This can be seen in Fig.3, where vortex core radius starts to contract between 750-1000 degrees vortex age. This unexpected trend suggests the presence of additional aerodynamic effects influencing vortex development beyond the initially assumed mechanisms.

Wave and wake stretching

A plausible explanation for changes in vortex core size are stretching and contraction of the vortex tube caused by wave and wake stretching, depicted in Fig.2. The change in length of the vortex tube and the vortex core radius have an inverse relationship resulting from the law of conservation of mass.

Wake contraction as described by Landgrebe[1] is one factor that shortens the vortex tube and increases the core radius and directly follows the momentum theory. A second factor causing stretching of the vortex tube are long-wave instabilities, which grow as the vortex ages and moves down the wake. This is based on an idea of Ananthtan and Leishman (2004).

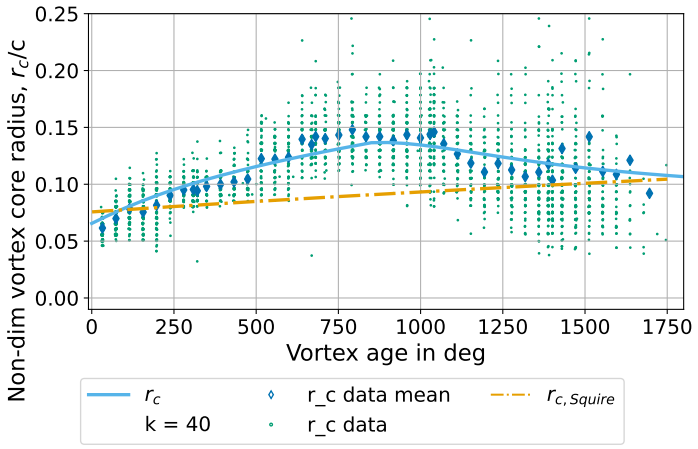

Figure 3: Measured mean vortex core radius with standard deviation over vortex age, and vortex core growth models after Squire's finite-radius version of the Lamb-Oseen model and r_c

Vortex model

The Lamb-Oseen blade tip vortex model, is derived from the 2D Navier-Stokes equations, describes the growth of a laminar vortex through viscous diffusion. Its strong grounding in fundamental physics makes it a suitable basis for the improved vortex model. To include these two factors quantitatively in a blade tip vortex model, the wake contraction and the harmonic long-wave instabilities need to be quantified. The wake contraction can be derived from the vortex trajectory, while the long-wave instability can be quantified through the wave number k and the amplitude a. The amplitude of these disturbances may be estimated from the positional standard deviation of the vortex in the y-direction, the wave number needs to be measured or estimated. Through integration the stretching factor of the long-wave instability can be found to be:

$$L = \int_{\Psi_1}^{\Psi_2} \sqrt{1 + (ak\,\cos(k\Psi))^2} \quad d\Psi. \tag{1}$$

The influence of the wake contraction can be approximated long the wake as the local wake radius contraction C_{WS}^{-1}. Incorporating these into the Lamb-Oseen model $r_{c(\mathrm{Lamb\text{-}Oseen})} = \sqrt{4\alpha_L \nu t}$ we get:

$$r_c = \sqrt{r_0^2 + 4\alpha_L \nu t \cdot C_{\mathrm{WS}}^{-1} L_{\mathrm{sin}}^{-1}}, \tag{2}$$

with Lamb's constant $\alpha_L = 1.25643$ and the fluid's kinematic viscosity ν and r_0 the initial vortex core radius. For this we estimated the wave number to be 40 and derived the amplitude and wake contraction from the positional data of the vortices. The modified Lamb-Oseen model called r_c is depicted in Fig.3. The curve of r_c captures the overall shape of the measurements well, including the initial rise, and the decline at higher vortex ages. In contrast, Squire's finite-radius version of the Lamb-Oseen model, $r_{c\,\mathrm{Squire}}$ remains nearly flat across all vortex ages and fails to reproduce the observed variation in the data. This demonstrates that the modified Lamb-Oseen model fits the empirical data's shape much more accurately.

Concludingly, the close agreement between the r_c fit and the measured data indicates that models rooted in the Lamb–Oseen formulation can capture the true behaviour of the vortex core radius accurately, using physical modulations. Since the Lamb–Oseen model is strongly grounded in fundamental physical laws, its further investigation and refinement may be well worth pursuing to achieve both improved predictive capability and a solid theoretical basis.

[1] Landgrebe, Anton J. "The wake geometry of a hovering helicopter rotor and its influence on rotor performance." Journal of the American Helicopter society 17.4 (1972): 3-15.

Mitteilung

Fachgruppe: Drehflügler

Test Stand for Measurements on Lateral Stability of Rotorcraft in Ground Effect

Julien Schwalbe, Felix Schreiner, Anthony D. Gardner, C. Christian Wolf, Hauke T. Bartzsch, Alexander Heintz, Johannes N. Braukmann
German Aerospace Center, Bunsenstr. 10, 37073 Göttingen,
julien.schwalbe@dlr.de, felix.schreiner@dlr.de, tony.gardner@dlr.de, christian.wolf@dlr.de, hauke.bartsch@dlr.de, alexander.heintz@dlr.de, johannes.braukmann@dlr.de

Introduction

The unique capability of helicopters to hover close to the ground offers significant operational advantages. However, hover flight in ground effect (IGE) involves complex aerodynamic phenomena that decrease power demands while simultaneously introducing stability challenges. These effects arise from interactions among blade tip vortices, detachment vortices, and wandering stagnation point flows with recirculating regions beneath the rotorcraft. Given the proximity to the ground, even minor instabilities can cause uncomfortable motions and, in extreme cases, safety risks. Despite its importance, the transient flow topology and stability characteristics of rotorcraft operating IGE remain insufficiently understood, particularly regarding root cutout, fuselage design, trimming, and crosswind conditions. Consequently, high-quality experimental data are required to better understand the flow mechanisms and improve helicopter safety and performance during IGE operations.

Experimental Setup

The experiment is conducted in an Eiffel Wind Tunnel at DLR Göttingen, used to generate defined crosswind. The tunnel has a 1.60 m × 1.60 m nozzle and achieves wind speeds up to 10 m/s. As Fig. 1 visualizes, the entire setup is inverted, positioning the rotorcraft in an upside-down orientation. This enables the use of a Pitch-Yaw-Unit (PYU) while minimizing aerodynamic interference caused by the setup itself - a critical consideration given the ground effect's sensitivity to disturbances. The rotor and fuselage are mechanically decoupled to enable the measurement of forces on both systems independently. The fuselage is mounted via a sting connected directly to the sled of the PYU. This configuration allows for rotation around the Z-axis (Yaw) and trimming adjustments via rotation around the Y-axis (Pitch). The rotor assembly is affixed to the PYU and comprises the motor, clutch, shaft, bearings, and a 75 mm diameter tube housing. The motor is equipped with water cooling to ensure continuous operation and prevent overheating.

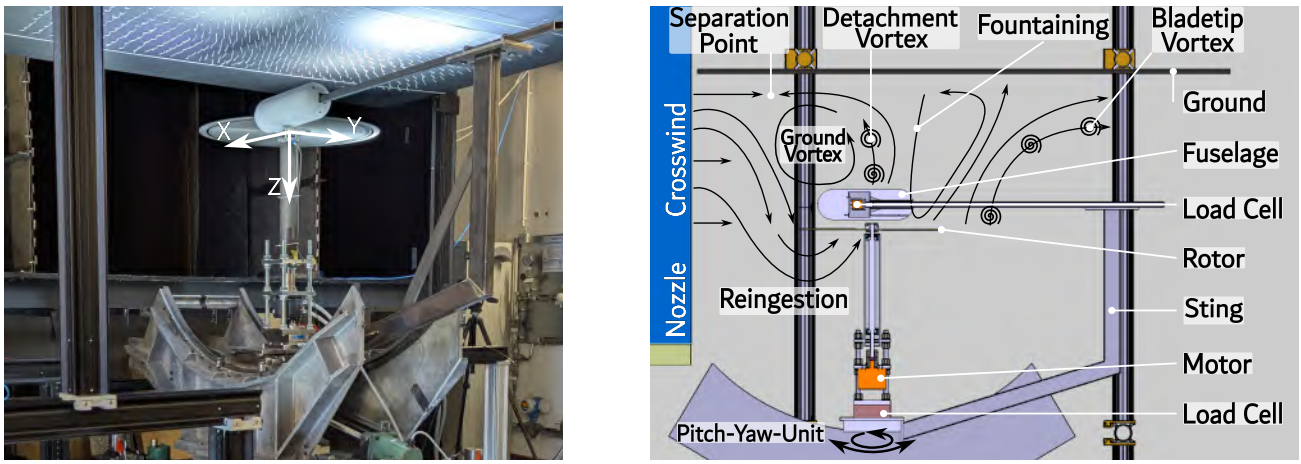

(a) Photographic overview of the experimental setup.

(b) Cross-sectional schematic showing the expected flow field and outwash phenomena.

Figure 1: Experimental setup for the investigation of lateral stability of helicopters in ground effect.

Two six-component load cells are installed to measure forces and moments separately on both the fuselage and the rotor system. The rotor system utilizes a robust piezoelectric balance, while the fuselage forces are measured using a compact strain gauge balance integrated within the fuselage. Different fuselages are designed and 3D-printed to investigate the influence of their geometry on stability. As showcased in Fig. 2, the geometries are chosen to be generic, providing a flexible baseline with the option to adapt to more realistic shapes in future studies. A total of 32 pressure probes are distributed across the fuselage cross-section,

to obtain detailed pressure distribution measurements.

The blades used are the commercially available SpinBlades BlackBelt 320 and BlackBelt 350 models, both featuring an identical symmetric airfoil profile. These blades are mounted on a custom-made rotor hub, which ensures a fixed and consistent pitch angle. To maintain a constant rotor diameter of 751 mm, the shorter BlackBelt 320 blades are fitted with adapters compensating for their reduced length, enabling the study of different root cutouts without altering the overall rotor diameter. The ground, covering an area of 2.5 m × 2.5 m, is suspended from an X95-structure, allowing height adjustments via a pulley.

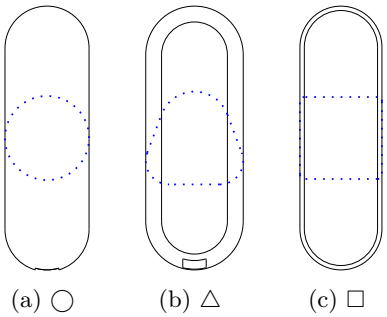

(a) ◯ (b) △ (c) □

Figure 2: Visualization of generic fuselage geometries. Solid black: plan view; dotted blue: cross section.

Sample Results and Discussion

To obtain an initial qualitative understanding of the flow behavior, selected areas of the ground surface were instrumented with tufts, and recorded using pco.Panda 26 sCMOS cameras. Following the calibration procedure of optical rectification, the recorded tuft movements were analyzed using a semi-automated image processing algorithm. A schematic overview of the algorithm is presented in Fig. 3. The images were captured during a trial run conducted at 2200 RPM without any fuselage installed.

a) **Preprocessing** To ensure consistent analysis, a brightness calibration was performed and non-informative regions were removed. The region of interest was manually defined to normalize the visible area across all frames. Subsequently, a grid of anchor points was imposed on the images to support the accurate localization of tuft base positions.

b) **Processing** The preprocessed images were converted to binary format, and an edge detection algorithm was applied. Based on the identified edges the tufts were detected and characterized by their geometric features. Each tuft was fitted with a spline to accurately capture its curved shape, and both the base and tip of the tuft were automatically located. To quantify the tuft orientation, a linear polynomial was fitted by a least-square method to the extracted spline. The fitted tuft direction was subsequently translated to originate at the tuft base.

c) **Postprocessing** The obtained vectors were compiled into a discrete vector field, representing the local flow directions across the observed area. Based on this vector field, a preliminary flow field was computed, providing an initial qualitative estimate of the flow field.

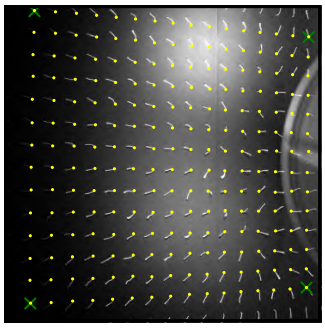

(a) Raw image of tufts: Rotor appears on the right, yellow markers show anchor points and crosses indicate the field of interest for further analysis.

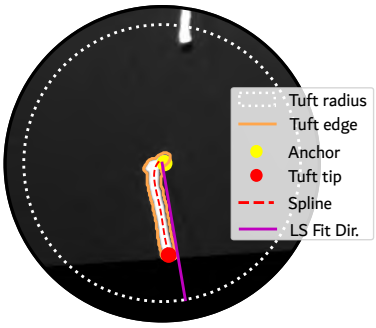

(b) A single tuft is presented, displaying its image alongside selected detected geometric features.

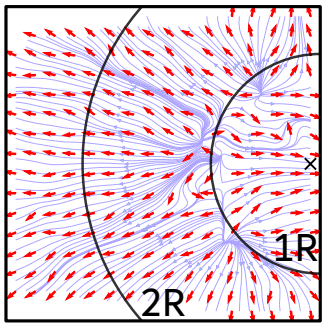

(c) Resulting vector field with related streamplot visualization. Rotor radii are marked for reference, a cross indicates the rotor hub position.

Figure 3: Visualization of the tuft processing algorithm.

Outlook

The next steps include a series of initial tests with the test stand, where data from the six-component balances will provide insights into the magnitude and reproducibility of expected lateral forces. Building on these findings, pressure distributions on the fuselage geometries will be investigated. Upon successful completion of these preliminary tests, an optical measurement technique such as Particle Image Velocimetry (PIV) will be employed to obtain detailed information on the highly transient flow topology.

Mitteilung

Fachgruppe: Experimentelle Aerodynamik

Experimental Study of Turbulent Boundary Layer Separation Induced by a Backward-Facing Ramp

M. Costantini[1]*, C. Klein[1], A. De Vincenzo[1], R. Geisler[1], J. Lemarechal[1], D. Schanz[1], A. Schröder[1], T. Knopp[1], C. Grabe[1], S. Sattler[2], M. Miozzi[3]

[1]DLR, Institute of Aerodynamics and Flow Technology, DLR, Bunsenstrasse 10, D-37073 Göttingen, Germany

[2]TU Braunschweig, Institute of Fluid Mechanics, Hermann-Blenk-Str. 37, D-38108 Braunschweig, Germany

[3]CNR, Institute of Marine Engineering, via di Vallerano 139, I-00128 Rome, Italy

*corresponding author: marco.costantini@dlr.de

Introduction and experimental setup

The importance of turbulent separated flow is undoubted for a wide range of applications, and in particular at the borders of the aircraft flight envelope. At the same time, turbulence modeling in Reynolds-Averaged Navier-Stokes equations still requires improvements to correctly predict the shape and size of turbulent separation bubbles (TSBs). For reliable turbulence model validation and modeling extensions, high-quality experimental data are necessary. A new experiment, focusing on geometry-induced separation of a turbulent boundary layer at quasi-zero pressure gradient, was designed and conducted within the DLR project *ADaMant* [1] to provide such validation data.

The measurements were performed in the Large Water Tunnel of TU Braunschweig (GWB) on a flat-plate configuration featuring a 25° Backward-Facing Ramp (BFR). The model configuration is shown in Figure 1. The BFR had a height h = 8 mm and was located at a streamwise distance x_h = 1.134 m from the plate leading edge; it was designed to induce a TSB but no secondary recirculation, following the findings of a preliminary wind-tunnel experiment [2].

The measurements were conducted using Lagrangian Particle Tracking by Shake-The-Box (STB) [3] and Temperature-Sensitive Paint (TSP) [4]. The application of these measurement techniques was enabled by a modular model design: a module with a glass insert was used for the STB measurements (STB module in Figure 1, left), whereas a module with TSP coating and integrated electrical heating was used for the TSP measurements (TSP module in Figure 1, right). The glass in the STB module allowed a minimization of light reflections at the wall during the STB measurements, while the integrated heating in the TSP module enabled an enhancement of the flow-induced thermal signatures at the surface, which were captured via TSP. As can be seen in Figure 1, the flat plate was installed vertically in the GWB test section, spanning the whole test-section height. The laser-optical arrangement for the STB measurement system (5 high-speed cameras and a dual-head laser illuminating two measurement subvolumes) is sketched in Figure 1 (left). The high-speed camera for the TSP measurements was also mounted at the same position as the central STB camera, whereas the TSP was excited by three high-power LED systems.

Results

The experiments were conducted at four different freestream velocities (in the range U_∞ = 1.2–2.6 m/s), corresponding to Reynolds numbers $\mathrm{Re}_{xh} = x_h U_\infty/\nu$ = 1.2–2.7 · 10^6, where ν is the fluid viscosity. The present work focuses on the results obtained at the lowest Reynolds number (Re_{xh} = 1.2 · 10^6) in the region downstream of the BFR.

Figure 2 (left) shows instantaneous particle tracks over 10 time-steps reconstructed by STB, color-coded by the streamwise component of the velocity, for two wall-parallel slices at different distances from the surface downstream of the BFR. Figure 2 (right) shows an instantaneous temperature distribution (map of temperature fluctuations T' downstream of the BFR). Both STB and TSP results indicate recirculating flow characteristic of a TSB up to approximately $X = x - x_h$ = 40 mm from the BFR. Furthermore, a streaky pattern is visible in both datasets. These streamwise-oriented streaks are the focus of current analysis, aiming at the improvement of the understanding of the structure of a turbulent boundary layer in the presence of geometry-induced TSB.

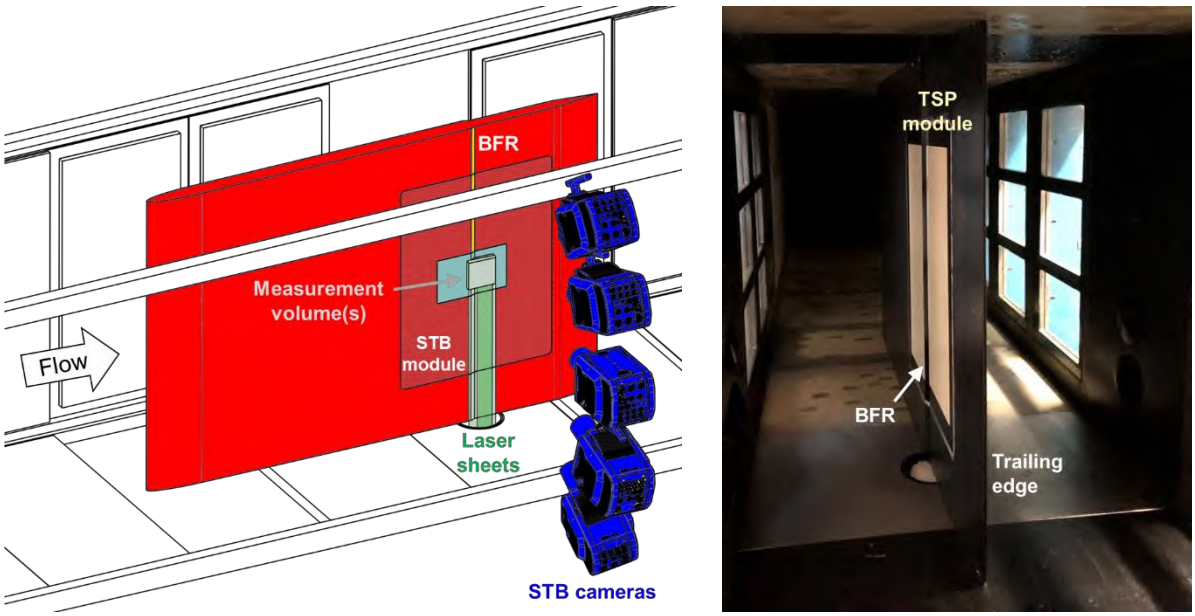

Figure 1. Left: sketch of the experimental setup for the STB measurements. Right: picture of the flat-plate model with TSP module installed in the GWB test section, as seen from a downstream location.

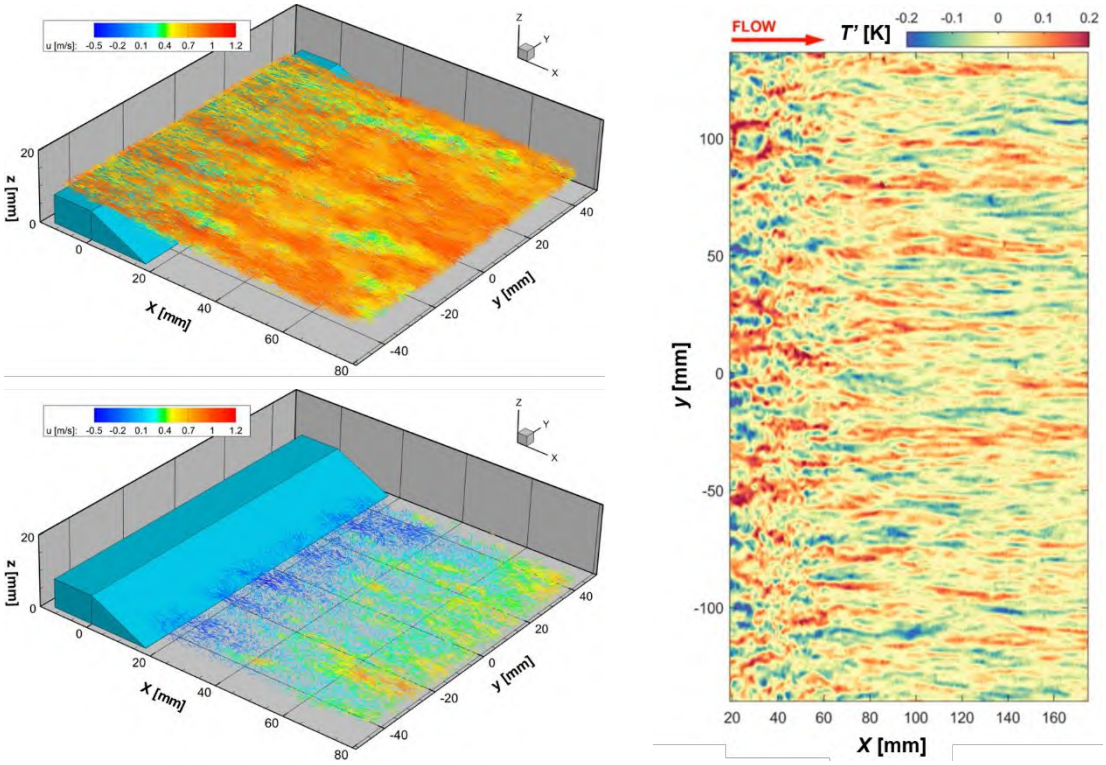

Figure 2. Results obtained at $Re_{xh} = 1.2 \cdot 10^6$, where $X = 0$ corresponds to the BFR location x_h, $y = 0$ to the mid-span location, and $z = 0$ to the vertical location of the plate surface downstream of the BFR. Left: particle tracks reconstructed by STB, color-coded by the streamwise component of the velocity u, for wall-parallel slices close to the model surfaces upstream (top, left) and downstream (bottom, left) of the BFR. Right: instantaneous distribution of the surface temperature fluctuations, obtained from the TSP data downstream of the BFR.

References

[1] Grabe C. (2022) DLR-Project ADaMant: Adaptive, Data-driven Physical Modeling towards Border of Envelope Applications. DLRK 2022, Dresden, Germany, 27–29 Sept. 2022.

[2] Costantini M., Schanz D., Geisler R., Schröder A., Knopp T., Dormoy C., Grabe C., Miozzi M. (2023) Experimental and numerical study of geometry-induced separation of a turbulent boundary layer. DLRK 2023, Stuttgart, Germany, 19–21 Sept. 2023.

[3] Schröder A., Schanz D. (2023) 3D Lagrangian Particle Tracking in Fluid Mechanics. Annu. Rev. Fluid Mech. 55: 511-540.

[4] Liu T., Sullivan J.P., Asai K., Klein C., Egami Y. (2021) Pressure and Temperature Sensitive Paints, 2nd ed., Springer International Publishing.

Mitteilung

Fachgruppe: Experimentelle Aerodynamik

Exploring Lagrangian flow-separation criteria using back-illuminated Temperature Sensitive Paint (TSP) and Lagrangian Particle Tracking (LPT)

Michael Hilfer, Richard Braun, David E. Rival
TU-Braunschweig, Institut für Strömungsmechanik, Hermann-Blenk-Strasse 37, 38108, Braunschweig
michael.hilfer@tu-braunschweig.de

Common Eulerian criteria, such as Prandtl's definition of the vanishing wall shear stress ($\tau_w = 0$), are insufficient for all unsteady flow [1, 2, 5]. An alternative is offered by the Lagrangian perspective,as shown in Fig. 1, which allows for a reference-frame-independent observation of the flow, fixed to fluid parcels. The goal of this study is to instantaneously detect and describe flow separation using both TSP [4] and LPT to explore the Lagrangian criterion [1]. Determining the instantaneous position of the flow separation on the model surface is necessary to make the separation criteria based on Lagrangian flow theory measurable.
The separation is detected via the instanteniou surface temperature, which is measured with high temporal resolution on a cylinder in cross-flow using TSP, shown in Fig. 3. The experimental setup developed specifically for this purpose integrates all the equipment within the cylinder, Fig. 2, which requires a new, transparent measurement setup. Based on the repulsion rate introduced by Haller [3], Sadr and Vétel [2] developed a separation criterion for turbulent flows that is applicable in practice. This criterion is illustrated in Fig. 1: It shows the transport of fluid parcels upstream of the separation point defined by Prandtl (PS). The particles converge towards a curve whose origin (LS) is located on the surface far upstream of the PS point. In an unsteady flow, there may not necessarily be a point with vanishing wall shear stress ($\tau_w = 0$), whereas an LS point is always expected.

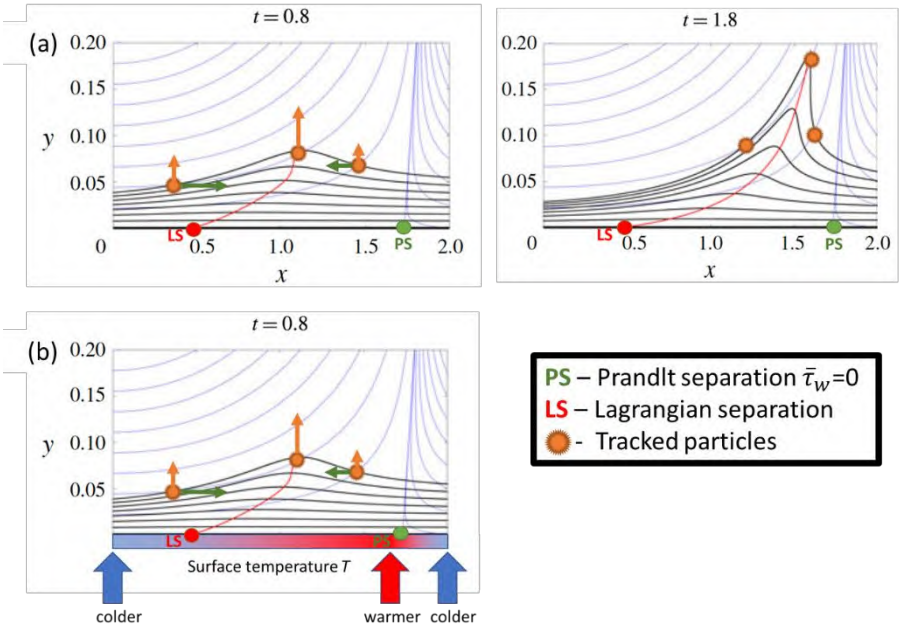

FIgure 1: Serra et al. (2018), J. Fluid Mech., modified:
(a) Transport of fluid parcels, (b) Expected instantenious temperature distribution on the surface

Since temperature determination using TSP requires the calculation of an intensity ratio between measurement and reference images, it is crucial that these images are perfectly aligned during the division. Relative movements between the TSP, the optical components, and the camera lead to image shifts. Although these can be partially corrected in post-processing, it is of great importance to minimize these relative movements through the design of the measurement setup. Additionally, the setup can be used to track particles in the near-wall flow. Because the camera's focal plane is on the model surface, it is possible to track the position of the particles in the boundary layer. Furthermore, by using defocusing, the particle's distance normal to the surface can be determined. From this, conclusions can be drawn about the instantaneous position of the particles inside and outside the boundary layer. The presented model-integrated approach also enables measurements on maneuvering bodies.

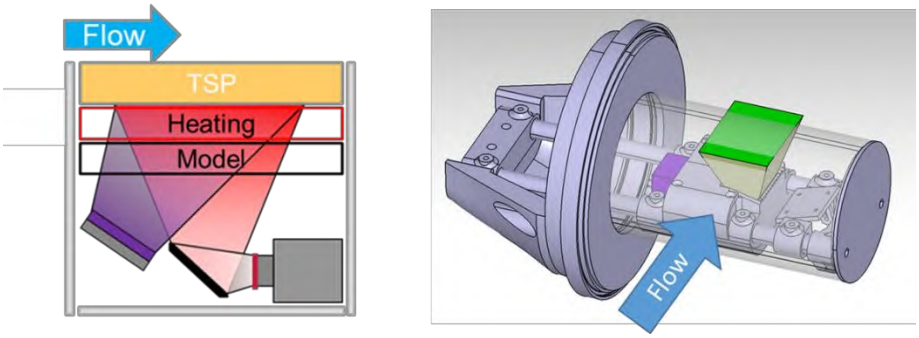

FIgure 2: Schematic of the measurement setup: The camera and excitation light are located inside the model.

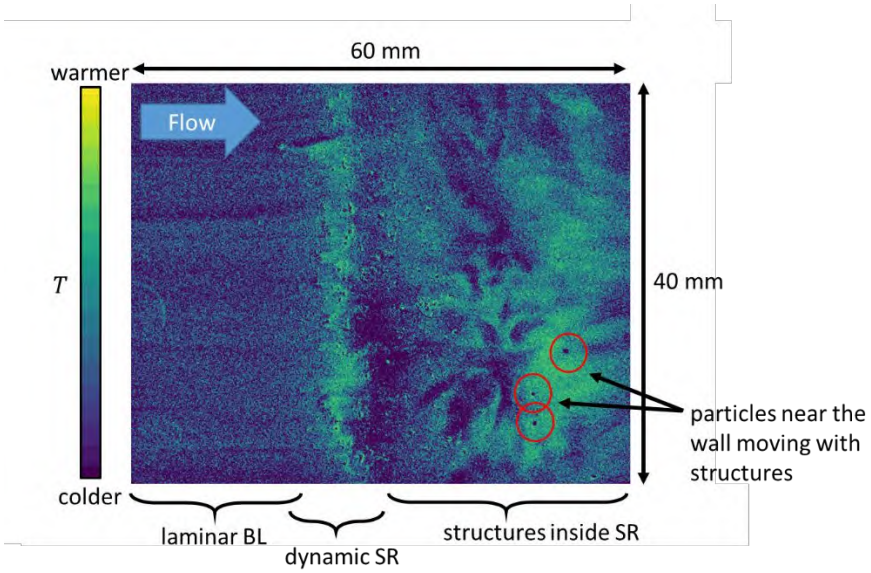

FIgure 3: Cylinder in cross-flow and instantaneous temperature distribution.

Refernces :
[1] M. Serra, J. Vétel, and G. Haller. Exact theory of material spike formation in flow separation. Journal of Fluid Mechanics, 845:51–92, 06 2018.
[2] M. Sadr and J. Vétel. Turbulent separation detection based on a lagrangian approach. In Proceedings of the 13th International Symposium on Turbulence and Shear Flow Phenomena (TSFP13), page Paper 80, Montréal, Canada, 2024
[3] G. Haller. A variational theory of hyperbolic lagrangian coherent structures. Physica D: Nonlinear Phenomena, 240(7):574–598, 2011.
[4] Liu, T., & Sullivan, J. P. (2005). Pressure and temperature sensitive paints. Berlin, Heidelberg: Springer Berlin Heidelberg.
[5] R. L., Simpson. Turbulent Boundary-Layer Separation. In Annual Review of Fluid Mechanics, Volume 21, 1989

Mitteilung

Fachgruppe: Experimentelle Aerodynamik

Experimental Investigation of Aerodynamic Effects in Wing Coupling

Angelique Kolberg, Thomas Grund and Julien Weiss
Institut für Luft- und Raumfahrt, Technische Universität Berlin,
Marchstr. 12-14, 10587 Berlin
angelique.kolberg@tu-berlin.de

High-Altitude Platform Systems (HAPS) are envisioned as a flexible alternative to satellites for telecommunications and related services. Compared to orbital satellites, they offer advantages such as adjustable positioning and the avoidance of both costly launches and space debris after end of life. The main challenge of long-endurance flight at altitudes around 20 km lies in the structural requirements: solar-powered propulsion with batteries imposes significant weight, demanding both minimal structural mass and very high aspect ratios to ensure sufficient aerodynamic efficiency. To alleviate these constraints, a modular concept has been proposed [1] in which several smaller aircraft couple flexibly at their wingtips to form a joint structure in flight.

While structurally promising, the concept introduces aerodynamic challenges during the docking manoeuvre. Previous experimental studies at TU Berlin investigated the aerodynamic effects of in-flight wingtip coupling using rectangular wings with symmetric NACA [2] and laminar flow [3] profiles. Despite differences in Reynolds number (2×10^5 and 7×10^5), both studies revealed consistent trends: decreasing the spanwise gap increased lift and reduced drag, which was primarily attributed to modifications in the tip vortex system and the associated reduction in induced downwash. At small distances, a gap flow developed between the wings, generating suction forces of opposite sign that produced strong lateral forces and rolling moments when the angles of attack were matched. These results highlight that the aerodynamic interaction during wingtip approach is highly sensitive to both gap size and angle of attack configuration, with lift, drag, and side forces strongly coupled.

The present contribution builds upon these findings using a new experimental setup with two laterally aligned wings, which are placed vertically in the measurement section as shown in Figure 1. The lower wing (index 1) is mounted on a six-component balance, while the other one (index 2) is connected to a traversing system for lateral movement, changing the wing tip distance d. The wings are rectangular with square tips and a laminar profile. They can be rotated to change their angle of attack and are equipped with 4 pressure tap rows each. The balanced wing is fitted with an aileron, which can be deflected over a range of angles.

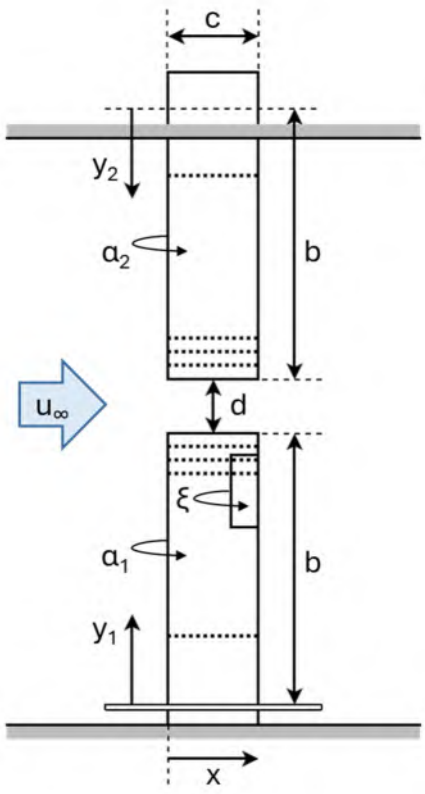

Figure 1 Side view of measurement setup with dotted lines showing chordwise rows of pressure taps

An initial validation step confirmed the consistency of the setup by reproducing the lift and drag trends, which were observed in previous work across different wingtip distances and angle of attack combinations. The obtained lift coefficients are displayed in Figure 2, showing

the described change with gap size. First investigations into the use of aileron deflections for mitigating the rolling moment induced by the asymmetric lift show that for small angles of attack, aileron deflection can effectively counteract the increased lift on the inner wing during approach. At higher angles of attack with strong gap flow, however, the compensation is less effective, as can be seen on the right of Figure 2.

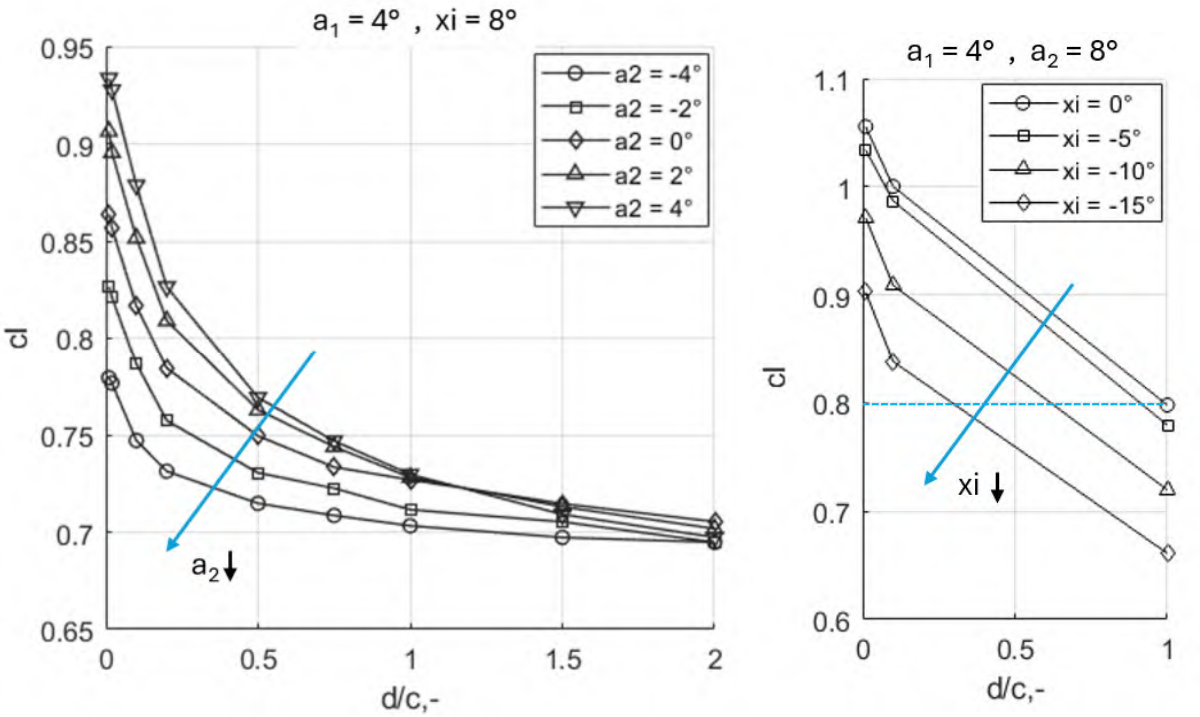

Figure 2 Lift impact of decreasing distances d/c for varying a2 (left) and aileron deflection xi (right)

The current setup will be extended to investigate additional aspects of wing coupling. Planned experiments include streamwise and vertical displacements of the upper wing. Furthermore, the updated setup will enable dynamic measurements during traverse motion and parallel acquisition of balance and PIV data. This combined approach allows aerodynamic loads to be directly related to velocity and vorticity fields in the tip region.

The results to date demonstrate both the challenges and possibilities associated with aerodynamic coupling of high-altitude aircraft. The future setup provides a foundation for developing control strategies that mitigate asymmetric loads, as well as for investigations aiming to capture the unsteady interaction using combined force and flow-field measurements.

This project is funded by the Deutsche Forschungsgemeinschaft (DFG, German Research Foundation) – 511042382.

References:

[1] Köthe, Alexander (2019). Flight Mechanics and Flight Control for a Multibody Aircraft: Long-Endurance Operation at High Altitudes. Doctoral thesis, Technische Universität Berlin, Institute of Aeronautics and Astronautics, Scientific Series. Universitätsverlag der TU Berlin.

[2] Behrens, Alexander, Grund, Thomas, Ebert, Carola, Luckner, Robert, Weiss, Julien (2019). Investigation of the aerodynamic interaction between two wings in a parallel flight with close lateral proximity. CEAS Aeronautical Journal , Vol. 11, No. 2, 553-563.

[3] Grund, Thomas, Weiss, Julien (2022). Experimental Investigation of the Coupling Process of Laminar Wings at Their Tips. Journal of Aircraft , Vol. 60, No. 3, 637-647.

Mitteilung

Fachgruppe: Experimentelle Aerodynamik

Searching for the gust-wing interaction *textbook*

P. Olivucci[1], D. E. Rival[2]

Institut für Strömungsmechanik, TU Braunschweig, Hermann-Blenk-Str. 37, Braunschweig

[1]p.olivucci@tu-braunschweig.de, [2]david.rival@tu-braunschweig.de

We address whether complex aerodynamic phenomena can be investigated through the synergy of automated high-volume experiments and the reduction of large datasets to a concise, representative subset — a *textbook*. As a test case, we explore the unsteady aerodynamics of wing-gust encounters, which is characterized by its rich, high-dimensional physics and is critical in applications such as small autonomous aircraft encountering high-intensity atmospheric disturbances.

Large-amplitude gust-wing interactions remain a challenging subject of research due to their enormous variety including transverse, vortical, and streamwise gusts, in either two-dimensional or even fully three-dimensional configurations [1][2]. This fact supports the case for the use of data-driven computational techniques in the extraction of key gust-wing interaction physics [4][5][6].

Our study takes advantage of a purpose-built gust generator to systematically produce random gust events covering diverse flight conditions. The gust generator consists of an array of individually controlled fans that can bring about a myriad of spatio-temporal unsteady flow patterns by virtue of randomizing its forcing parameters. We measure the pressure signature on an array of sparse sensors and the loads induced by each gust event on a NACA0012 delta wing [3]. This results in a database of over 1,000 distinct gust-wing encounters.

We then employ a data summarization algorithm to identify optimally representative subsets of events of increasing size from the large-scale database [7]. These subsets serve as training data for a machine-learning model predicting aerodynamic loads from sparse pressure measurements. We show how an appropriately selected *textbook* of a few events is sufficient to achieve predictive accuracy comparable to randomly acquired training datasets up to two orders of magnitude larger.

The *textbook* captures essential information of the full-scale data, generalizing well on ordinary and extreme cases. A *textbook* not only enhances modeling efficiency but can lead to improved interpretability of critical gust-load physics. We verify that the *textbook* gust events, which are selected by means of a purely data-driven procedure based on their predictive value, bear a connection to the underlying flow physics. To uncover this connection, we apply tools from statistics and time-series analysis and show how the *textbook* captures the diversity of the full gust ensemble.

Our approach evidences the potential of tackling complex aerodynamics by collecting a large body of observations and compressing it down to maximally informative subsets, with applications in fields requiring efficient prediction, such as autonomous flight, and serving as an interpretable basis to further its physical understanding.

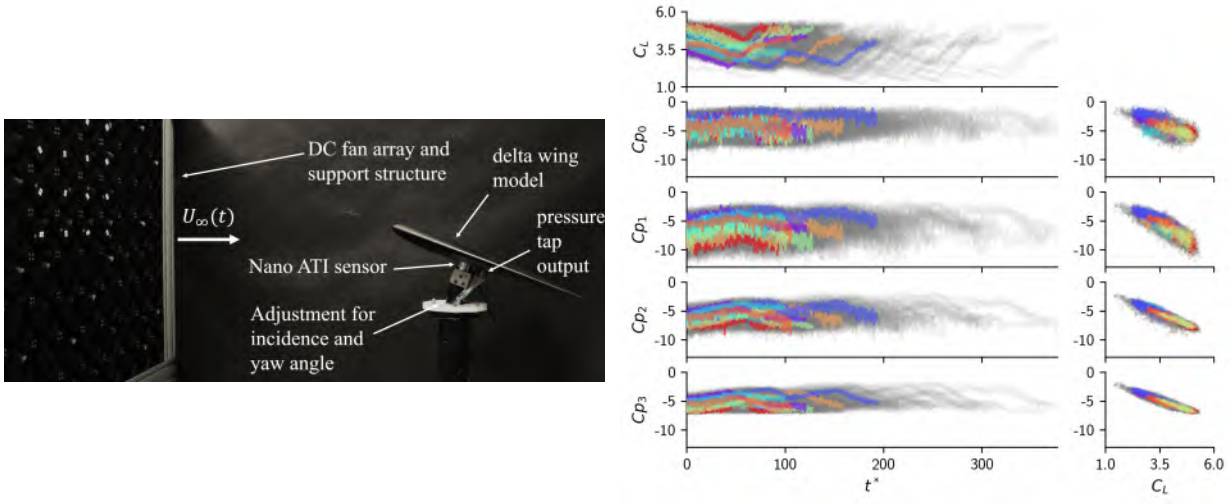

Fig. 1 – **(a)** The random gust generating facility used to collect a database of 1,000 gust-wing interaction events. **(b)** The pressure-lift signatures corresponding to a *textbook* of 10 events are highlighted in colour against the remainder of the database, in grey.

References

[1] Jones, A. R. et al., *Physics and Modeling of Large Flow Disturbances: Discrete Gust Encounters for Modern Air Vehicles*. Annu. Rev. Fluid Mech. (2022)

[2] Burelle, L. A. et al., *Exploring the signature of distributed pressure measurements on non-slender delta wings during axial and vertical gusts*. Phys. Fluids (2020)

[3] Chen, D. et al., *Sparse pressure-based machine learning approach for aerodynamic loads estimation during gust encounters*. AIAA J. (2023)

[4] Fan, D. et al. *A robotic Intelligent Towing Tank for learning complex fluid-structure dynamics*. Science Robotics (2019)

[5] Fukami, K. and Taira, K. *Grasping extreme aerodynamics on a low-dimensional manifold*. Nat. Commun. (2023)

[6] Iacobello G. et al., *Load estimation in unsteady flows from sparse pressure measurements: application of transition networks to experimental data*. Phys. Fluids (2022)

[7] Koh P. W. and Liang, P., *Understanding Black-box Predictions via Influence Functions*. Proceedings of the 34th International Conference on Machine Learning (2017)

Mitteilung

Fachgruppe: Experimentelle Aerodynamik

Characterization of a Phosphor-Based Temperature-Sensitive Paint
for High-Temperature Applications

F. Rosner[1,2], C. Klein[1]*, B. D. Dimond[1], P. Nau[3], D. Surujhlal[1], T. Jüstel[2]
[1]DLR, Institute of Aerodynamics and Flow Technology, DLR, Bunsenstrasse 10,
D-37073 Göttingen, Germany
[2]FH Münster University of Applied Sciences, Stegerwaldstr. 39,
D-48565 Steinfurt, Germany
[3]DLR, Institute of Combustion Technology, DLR, Pfaffenwaldring 38-40,
D-70569 Stuttgart, Germany
*corresponding author: christian.klein@dlr.de

Introduction

Research into the fundamental flow physics of hypersonic regimes, such as shock–shock interactions and vortex dynamics, has increased in recent years. Understanding these flow phenomena is crucial for the development of hypersonic vehicles. However, hypersonic flow conditions pose unique challenges for experimental measurements, for example when extracting surface temperature data with high spatial and temporal resolution from the investigated vehicle. Conventional point-wise methods, such as thermocouples, have been successfully integrated into hypersonic test articles. Nevertheless, it is of great interest to obtain image-based temperature data with both high spatial and temporal resolution on such vehicles, due to their increasingly complex geometries prohibiting point-wise sensor integration into these test articles. Temperature-sensitive paints (TSP) have been employed to measure surface temperatures, and for high-temperature conditions (> 100 °C), phosphor-based TSP can be used [1, 2].

Experimental methods and results

In this study, a complete characterization of a phosphor-based TSP is presented. This TSP enables surface temperature measurements in hypersonic flow conditions up to 500 °C using the intensity method. For such a TSP, it is necessary to combine the phosphor with a binder, forming a suspension that can be applied to the test object with a spray gun. The phosphor, $(Sr_{1-x}Ca_x)AlSiN_3:Eu^{2+}$ [3], provided by the FH Münster, was suspended in different binder materials, all selected for their high heat resistance. In this work, only the results obtained with the so-called Ceramabind 880 [4] binder are reported. The phosphor–binder suspension was coated onto an aluminum plate, resulting in a TSP layer thickness of approximately 50 µm. The temperature-dependent emission spectra of the coated plate are shown in Figure 1 a). The decay behavior (luminescence lifetime) of the phosphor powder is shown in Figure 1 b), respectively. With a measured photoluminescence lifetime of τ = 614 ns, this TSP is in principle capable of resolving temperature fluctuations in the kHz range, extending into the upper-tens-of-kHz regime.
For further temperature calibration tests, an electrically operated muffle furnace [5], which is equipped with an optical window in its front-loading door will be employed. The TSP will be excited with a 405 nm near UV-LED, and the luminescence of the phosphor will be recorded using a 12-bit CMOS camera. Both the LED and the camera is equipped with appropriate bandpass filters. A schematic of the calibration setup is shown in Figure 2. To analyze the thermal stability of the TSP investigated here, the calibration measurements will be carried out during both the heating and cooling processes. This procedure allows possible aging effects or hysteresis of the TSP to be quantified. Such behavior would be unsuitable for later use of the TSP under hypersonic conditions when applying the intensity method. First tests were performed using a temperature-controlled sample holder inside a spectrometer with the coated aluminum plate attached to it, the resulting temperature calibration is presented in Figure 3 a). To further examine potential interactions of the phosphor with oxygen (O_2 quenching), the phosphor was also tested in nitrogen and oxygen environments. No dependence on oxygen was observed, as confirmed by the emission spectra in Figure 3 b). In the next step, the TSP developed here will be tested in the described setup in Figure 2 and applied to further investigations on a heated cylinder in hypersonic flows.

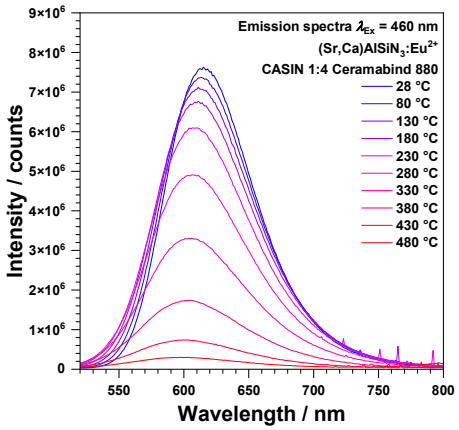

a) Temperature-dependent emission spectra of the coated aluminum plate under 460 nm excitation

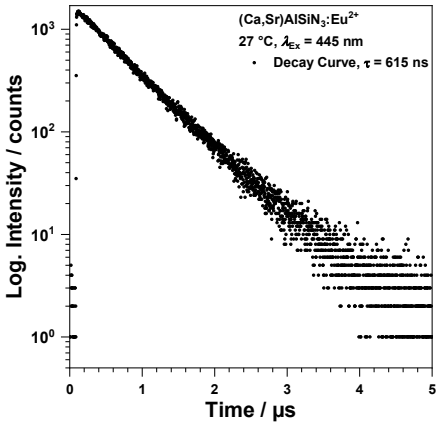

b) Decay curve of $(Sr_{1-x}Ca_x)AlSiN_3:Eu^{2+}$ powder under pulsed 445 nm excitation

Figure 1 Temperature-dependent emission intensity and lifetime (at room temp.) of the investigated TSP.

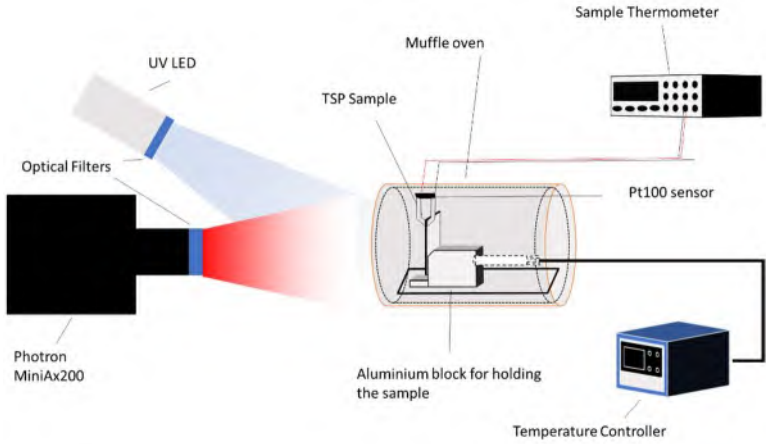

Figure 2 Schematic of the calibration setup, by Aleksandro Budina and Lorenzo Menghini, ITS Umbria.

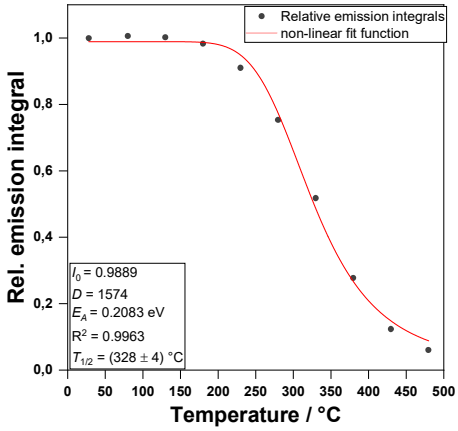

a) Relative emission integrals of the coated aluminum plate over the temp. range of 30 - 480 °C

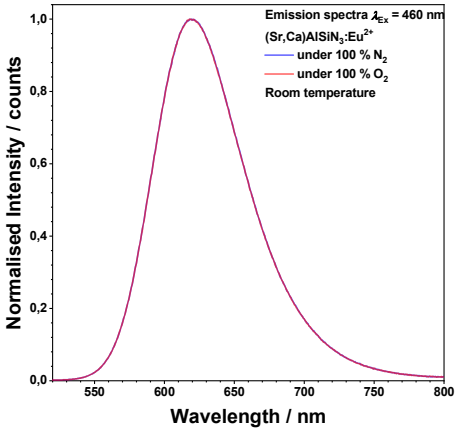

b) Emission spectra in oxygen or nitrogen atmospheres

Figure 3 TSP temperature calibration and emission spectra in oxygen and nitrogen atmospheres.

References

[1] Liu T., Sullivan J.P., Asia K., Klein C., Egami Y. (2021) Pressure and Temperature Sensitive Paints, 2nd Edition, Experimental Fluid Mechanics, ISBN 978-3-030-68055-8.
[2] Dramićanin M. D., Sensing temperature via downshifting emissions of lanthanide-doped metal oxides and salts. A review, Methods Appl. Fluoresc. 4 (2016) 042001, DOI: 10.1088/2050-6120/4/4/042001.
[3] Ueda J., Tanabe S., Takahashi K., Takeda T., Hirosaki N., Thermal Quenching Mechanism of CaAlSiN3:Eu2+ Red Phosphor, Bull. Chem. Soc. Jpn. 91 (2018) 173-177, DOI: 10.1246/bcsj.20170307.
[4] Commercially available from Aremco Products, Inc.
[5] Provided by Karsten Pfeiffer, DLR-AS, Göttingen.

Mitteilung

Fachgruppe: Experimentelle Aerodynamik

Anemometer in Windkanälen – Analyse von strömungsinduzierten Messfehlern

Anemometers in Wind Tunnels –Analysis of Flow-Induced Measuring Errors

Wolfgang Send[1] , Dietmar Pachinger[2]

[1] ANIPROP GbR, Sandersbeek 20, 37085 Göttingen - wsend@aniprop.de
[2] BEV / E+E Elektronik GmbH (Austria)

The starting point for this presentation is a series of new systematic comparisons of flow sensors in various wind tunnels [1, 4], which largely confirm earlier studies [3]. There are systematic measurement errors [2] that can be attributed, on the one hand, to the interaction between the mechanical design of the installation and the surrounding flow (center of Figure 1). On the other hand, little is known about the topology of the flow in a wind tunnel behind the contraction nozzle in the measuring chamber. Contrary to what is shown in many illustrations, the maximum velocity is not located in the center of the channel cross-section, but rather the minimum is located there before the velocity drops with a slight bulge-like increase on all sides in the boundary layer. This is also shown by the contour line in Figure 1 that runs across the sensor. The numerical findings [5] based on CFD calculations have now been confirmed by comparative measurements with LDA in the E+E wind tunnel.

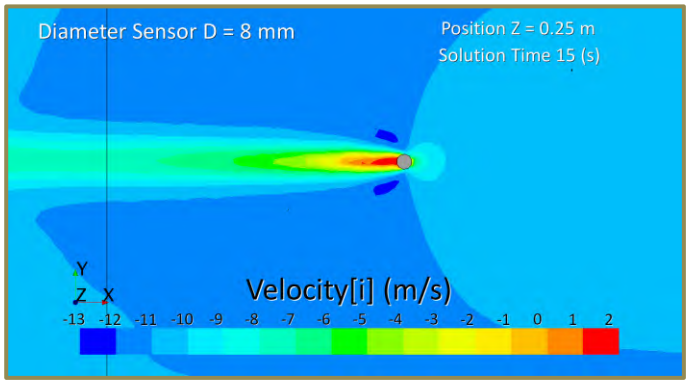

Figure 1. Contour plot of the longitudinal component V_x of the velocity in a wind tunnel (cross-section 0.25 m x 0.16 m) with sensor at a mass flow of 0.5 kg/s. Flow direction to the left.

The presentation will begin with a review of the known findings. Numerical and experimental investigations show that pronounced vertical cross-flows arise in front of and behind a sensor mount, reaching up to 10% of the main flow (at 11 m/s). Figure 2 shows the vertical component behind a sensor with a complex contour image. A drastic reduction in disturbance is achieved by a classic solution in the form of a symmetrical airfoil covering the holder (Figure 3). However, this solution has yet to prove itself in practice. Naturally, it is not possible to simply change the immersion depth of the sensor. Any change would also mean a change in the height of the covering.

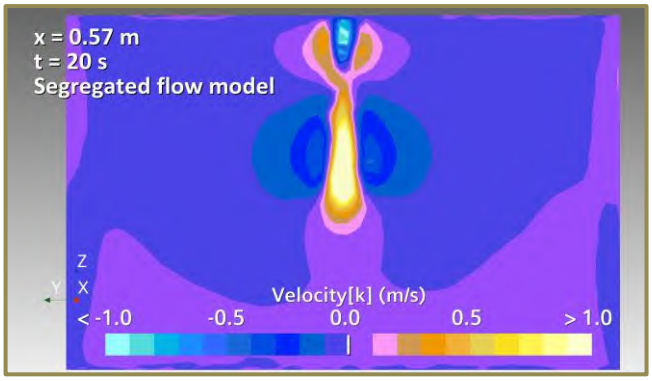

Figure 2. Contour image of the vertical component V_z of the velocity downstream of the sensor as in Figure 1.

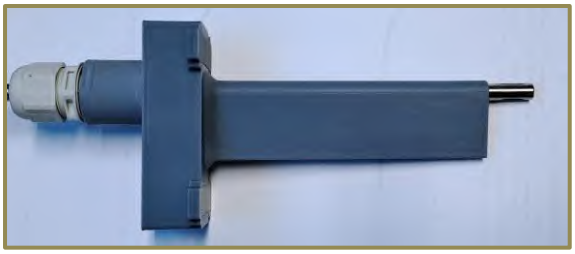

Figure 3. Sensor with aerodynamic fairing.

mains constant across the cross-section and decreases in the wall boundary layer. However, as the findings show, this assumption is not justified. This raises the question of how to determine wind speed according to metrological standards that take these findings into account.

The E+E wind tunnel is a Göttingen-type tunnel with an open measuring section and a speed of up to 40 m/s. The round nozzle has a diameter of D = 255 mm. The length of the measuring section is 300 mm. The tunnel is temperature-stabilized for calibration purposes. CFD calculations and LDA measurements (Figure 5) were performed for this tunnel

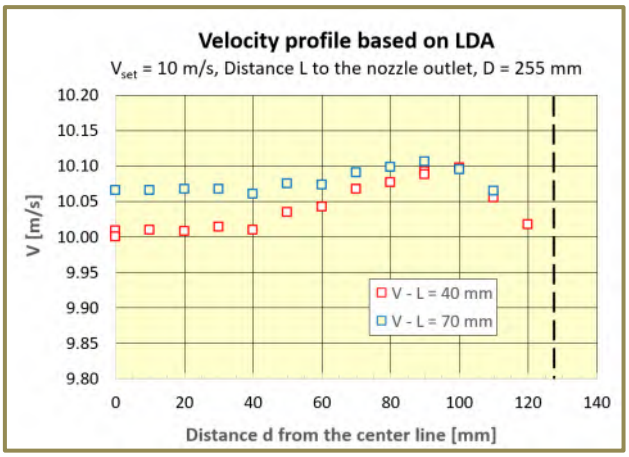

Figure 5. Velocity profile of the LDA measurements for two different distances L from the end of the nozzle.

One of the **aims of the presentation** is to stimulate discussion about the possibilities of physically determining wind speed in a wind tunnel. The metrological standard is to determine the speed on the geometric central axis of a wind tunnel as a measure of the flow velocity of the entire tunnel. It is assumed that this speed re-

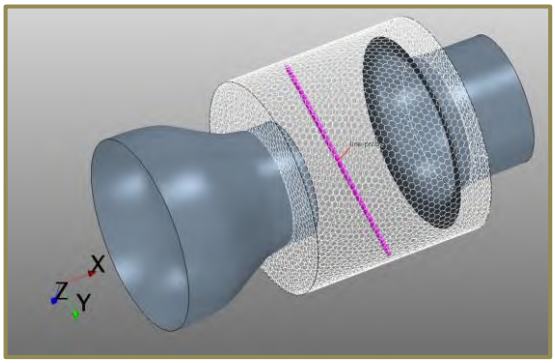

Figure 4. Simple modeling of the open measuring section. The white mesh describes the boundary for the laboratory air at environmental pressure. The red line illustrates a data path for comparison with the LDA measurements.

using a simple CFD model (Figure 4). The dashed line in Figure 5 marks the position of the nozzle edge. Calculations and measurements show the same trend and thus the fundamental significance of the comment in the last paragraph. The velocity profile with the minimum in the center of the channel and the bulge-like increase in velocity before the drop into the boundary layer can also be found in an open measuring section.

At d = 130 mm (outside the extent of the nozzle at d = 127.5 mm) and L = 40 mm, the velocity measured with LDA is still around 5.4 m/s (data point outside the graph axes).

[1 Geršl J., Sluše J, Pachinger D., Kampe J., Roß A., Kouba P., *Effect of the insertion depth on calibration results of vane anemometers,* Measurement 222 (2023) 113630. https://www.sciencedirect.com/science/article/pii/S0263224123011946

[2] Send W., Speed of a Betz wind tunnel using laser triangulation – comparative measurements, DLRK2021, Document ID: 550282. https://www.dglr.de/publikationen/2021/550282.pdf

[3] Pachinger D., contributing to *CCM.FF-K3.2011 CIPM Key Comparison of Air Speed, 0.5 m/s to 40 m/s Final Report*

[4] Kampe J., Hornig J., Taube A., Comparison Report DKD-V 11-4: *National Ring Comparison of Flow Velocity in the Range from 1 to 35 m/s Using a Vane Anemometer*, Issue 03/2025, Revision 0, Physikalisch-Technische Bundesanstalt, Braunschweig and Berlin. DOI: 10.7795/550.20250312, https://oar.ptb.de/rsources/show/10.7795/550.20250312

[5] Send W., *Wind Tunnel with Sensor - Comparison of Experiment and CFD Calculation*, 24th DGLR STAB Symposium – November 13-14, 2024 – Regensburg, revised and accepted for publication in the Springer series "New Results in Numerical and Experimental Fluid Mechanics." Currently available is the submitted, but not yet revised paper: https://aniprop.de/sites/default/files/Stab2024_WSend_paper_preprint.pdf, with differences to the accepted version.

Mitteilung

Fachgruppe: Experimental Aerodynamics

Investigation of ice formation on unmanned aerial vehicles at low Reynolds numbers

Kübra Soy, Mariachiara Gallia
Institute of Fluid Mechanics (ISM)
Technische Universität Braunschweig
Hermann-Blenk-Str. 37, 38108 Braunschweig, Germany
kuebra.soy@tu-braunschweig.de

The applications of unmanned aerial vehicles (UAVs) have broadened from military uses to civil and commercial markets, including urban air mobility, package delivery, and search and rescue operations. However, these systems are highly vulnerable to performance deterioration due to ice accumulation. The formation of ice influences aerodynamic profiles, reduces lift, increases drag, and can induce significant vibrations [1]. In cold conditions, these factors greatly restrict the operation of UAVs. Recent research has demonstrated that ice can significantly influence lift and torque; yet, these studies mostly focused on large systems with high Reynolds numbers, neglecting the differing flow characteristics of small UAVs. Thus, ice accumulation on small UAVs remains poorly understood. In low Reynolds number regimes ($Re < 5\times10^5$), the aerodynamic and thermodynamic behavior differs significantly. In these regimes, the boundary layer tends to remain laminar over a larger portion of the surface, making it more sensitive to disturbances but less prone to immediate transition [2-4]. As a result, ice-induced surface roughness may not trigger turbulent transition as predictably as in high Reynolds number flows, complicating efforts to model heat transfer, surface shear, and subsequent ice accretion [2-4]. Furthermore, the formation of laminar separation bubbles, which is not present at higher Reynolds numbers, can become an important factor for low-Re studies influencing pressure distribution and flow stability [4-5]. Therefore, low Reynolds number icing studies are essential for designing reliable anti-icing systems and ensuring flight safety in the expanding sector of UAVs [6-7].

In this study, we investigated the impact of low Reynolds numbers on ice formation in UAVs experimentally. To isolate the effect of the Reynolds number, we kept ice scaling factors constant such as the accumulation parameter (A_c) and freezing fraction (n_0). A_c is the total potential volume of water that can accumulate on an airfoil over a given icing time, normalized by the ice density and a characteristic length of the model (nose radius of a leading edge) [8].

$$A_c = \frac{LWC\ V\ t}{\rho\ d}$$

LWC is the liquid water content of the cloud, *V* is the free stream velocity, *t* is the icing time, *d* is the nose radius of the model, and ρ is the ice density. By keeping A_c constant, we ensure that the total amount of ice accreted relative to the model size is consistent between tests. On the other hand, the freezing fraction (n_0) is the dimensionless ratio of the mass of impinging water that freezes on impact to the total mass of impinging water at the stagnation point [8].

$$n_0 = \frac{1}{b}\left(\frac{\theta}{\Lambda} + \frac{\Phi}{\Lambda}\right)$$

Φ is the drop energy transfer parameter, representing the heat gain from the kinetic energy and sensible heat of the impinging water drop, θ is the air energy transfer parameter, representing the heat transfer due to convection and evaporation from the air, Λ is the latent heat of freezing [8]. *b* is the relative heat factor, which relates the total heat capacity of the impinging water to the surface's ability to convect heat. It is defined as

$$b = \frac{LWC\ V\ \beta_0\ c_{p,ws}}{h_c}$$

Maintaining a constant n_0 ensures that the thermal conditions governing the ice accretion process are similar, which is critical for reproducing equivalent ice shapes, especially for glaze ice.

Experiments were performed at Braunschweig Icing Wind Tunnel [9]. Two velocities were used 25 m/s and 40 m/s, with three different chord lengths of the RG15 model. The models were produced using a 3D printer using PLA material. All models had a 50 cm span, while the chord lengths were 10 cm, 20 cm, and 30 cm. Reynolds number was kept in between 1.8-8.8 × 10^5 among 11 cases. Each case will be presented at the workshop.

The shadowgraphy method was used to evaluate the 2D ice shape [10]. One camera was placed perpendicular to the right side of the test section to observe the cross-section of the model and the ice accumulated on the leading edge, Figure 1, while another camera was positioned on top of the test section to double-check the ice thickness. LED light sources were placed for each camera to provide shadow imaging. One LED light was positioned on the left side of the tunnel, while the other was placed at the bottom. Each case was repeated three times to ensure repeatability. All data is processed using the in-house shadowgraphy code [10], with post-processing explained in detail later.

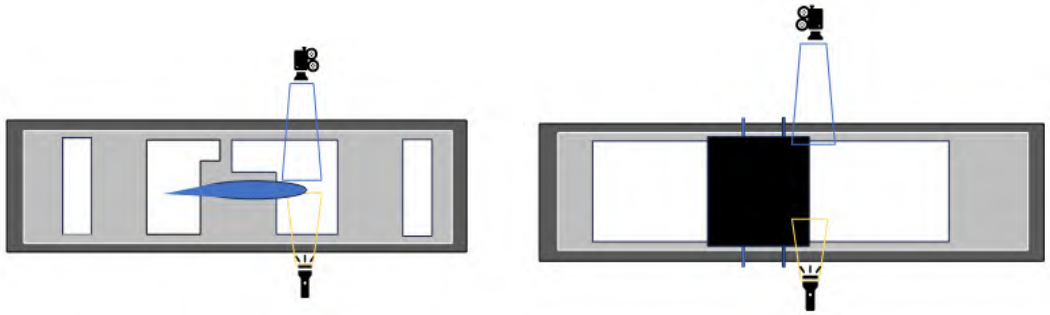

Figure 1: Right side view and top side view of the test section with shadowgraphy setup

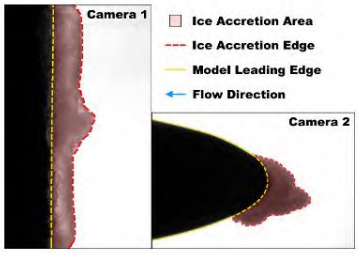

Figure 2: Example of ice shape detected by the shadowgraphy code [10]

The aim is to study how the ice formation changes on UAVs within the low Reynolds number range (1.8-8.8 × 10^5) if icing conditions are kept constant. Preliminarily, results show that the glaze ice accreted qualitatively similarly due to constant accumulation parameter and freezing fraction in most of the cases. As the heat transfer is not sufficient to freeze all impinging droplets in glaze ice conditions (-5°C), water runback occurred along the airfoil surface during the test campaigns. It is visually observed that the runback region is longer at smaller Reynolds numbers due to reduced convective heat transfer coefficient, less efficient freezing of impinging water droplets, late laminar to turbulent transition. The final results and related detailed discussion will be presented at the workshop.

References

[1] Cebeci, T., Kafyeke, F., Aircraft Icing, Annu. Rev. Fluid Mech., 35:11-21, 2003.
[2] Oo, N.L., *Low Reynolds number aerodynamics of a UAV under icing condition*, 2020, The University of Auckland
[3] Samadani, S., *Aerodynamic and heat transfer correlations for smooth and rough airfoils*, 2022, Montreal.
[4] Zhou, Y., Wang, Z. J., *Effects of Surface Roughness on Laminar Separation Bubble over a Wing at a Low-Reynolds Number,* AIAA, 2011, Orlando.
[5] Muhammed, M., & Virk, M. S. (2024). On the Fidelity of RANS-Based Turbulence Models in Modeling the Laminar Separation Bubble and Ice-Induced Separation Bubble at Low Reynolds Numbers on Unmanned Aerial Vehicle Airfoil. Drones, 8(4), 148.
[6] Szilder, K. and McIlwain, S., In-Flight Icing of UAVs - The Influence of Reynolds Number on the Ice Accretion Process, SAE Technical Paper 2011-01-2572, 2011,
[7] Hann, R., Johansen, T. A., Unsettled Topics in Unmanned Aerial Vehicle Icing, SAE Technical Paper, 2020.
[8] Anderson, D. N., Manual of Scaling Factors, NASA/CR—2004-212875, 2004
[9] Bansmer, S. E., Baumert, A., Sattler, S., Knop, I., Leroy, D., Schwarzenboeck, A., Jurkat-Witschas, T., Voigt, C., Pervier, H., and Esposito, B.: Design, construction and commissioning of the Braunschweig Icing Wind Tunnel, Atmos. Meas. Tech., 11, 3221–3249, https://doi.org/10.5194/amt-11-3221-2018, 2018.
[10] Malik, Y., Bennani, L.,Vorgias, A., Trontin, P., Villedieu, P., Experimental and Numerical Investigation of Ice Crystal Icing on a Heatable NACA0012 Airfoil. AIAA AVIATION 2022 Forum, Jun 2022, Chicago, United States. pp.AIAA 2022-3534.

Mitteilung

Fachgruppe: Experimentelle Aerodynamik

Optical deformation measurement for load monitoring on a scaled flight test vehicle

J. Wagner*, T. Kirmse*,
O. Luderer† , F. Thielecke†,
W. Gropengießer‡, S. Adden‡

* German Aerospace Center, Institute of Aerodynamics and Flow Technology, Bunsenstr. 10, Göttingen, Germany
† Hamburg University of Technology, Institute of Aircraft Systems Engineering, Nesspriel 5, 21129 Hamburg, Germany
‡ IBK Innovation GmbH & Co. KG, Butendeichsweg 2, Hamburg, Germany
jan.wagner@dlr.de

Various measurement parameters, such as acceleration, strain, pressure data, and deformation, can be used to monitor loads on aircraft wings. Here, deformation is recorded optically using a stereo camera system. Two different measurement systems are used for this purpose:
The Image Pattern Correlation Technique (IPCT) is an established, well-proven method for measuring 2.5D surface deformations based on a random distribution of points on the surface. This method achieves high accuracy (~ 0.2 pixels), but is computationally intensive and not suitable for real-time applications. (Boden et al. 2013)
In contrast, marker-based measurement is fast and efficient and can also be performed with a single camera. The four corners of the marker enable the position in space to be determined using a separate marker coordinate system, but only at discrete points. Here, a further development (Enhanced ArUco Marker) of the widely used ArUco markers is used, which provide better subpixel accuracy thanks to their checkerboard frame (Garrido-Jurado et al. 2014; Kedilioglu et al. 2021), see Fig. 1. Preliminary tests have shown that a stereo camera system offers greater accuracy than a mono camera marker recognition system. (Kedilioglu et al. 2021).

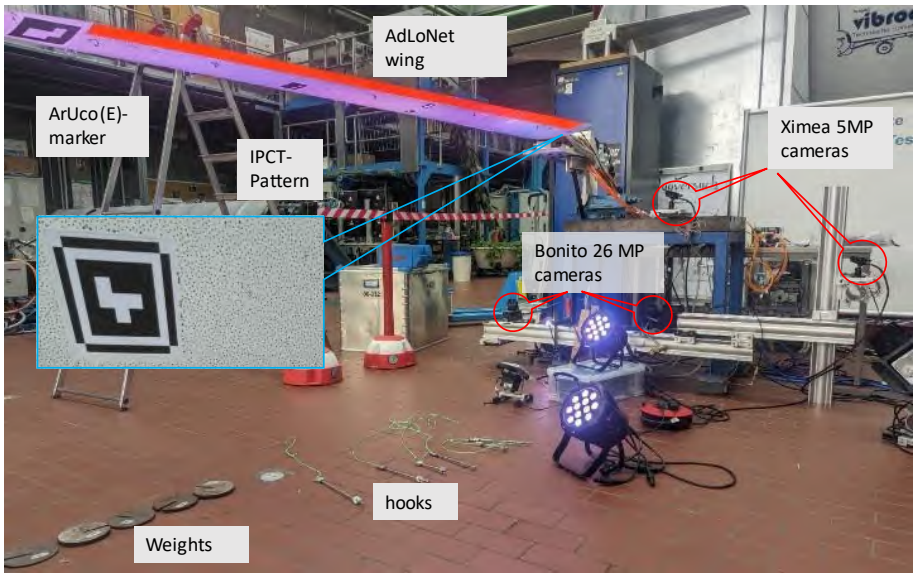

Fig. 1: Calibration setup with the two stereo camera systems (26 Mpx Bonito, 5 Mpx Ximea), as well as the IPCT pattern and the Aruco(E) markers. The weights for the wing loading are on the floor.

The aircraft used is the AdLoNet-Dimona, a scaled test aircraft from the TUHH with a wingspan of 2.5 m and a payload of approx. 4 kg at a total weight of 25 kg, whose right wing is equipped with strain gauges and acceleration sensors for load monitoring. (Luderer et al. 2023)

The aim is to compare the two optical measurement systems with each other and with the other sensor results, and to assess their suitability for use in measurement environments with severe restrictions in terms of optical accessibility, installation space, weight, and electrical power. For this purpose, the data from the static calibration test will be used, as well as the wind tunnel measurement, which was also carried out, but where only the 5 Mpx Xiema cameras were used for optical measurements, see Fig. 2.

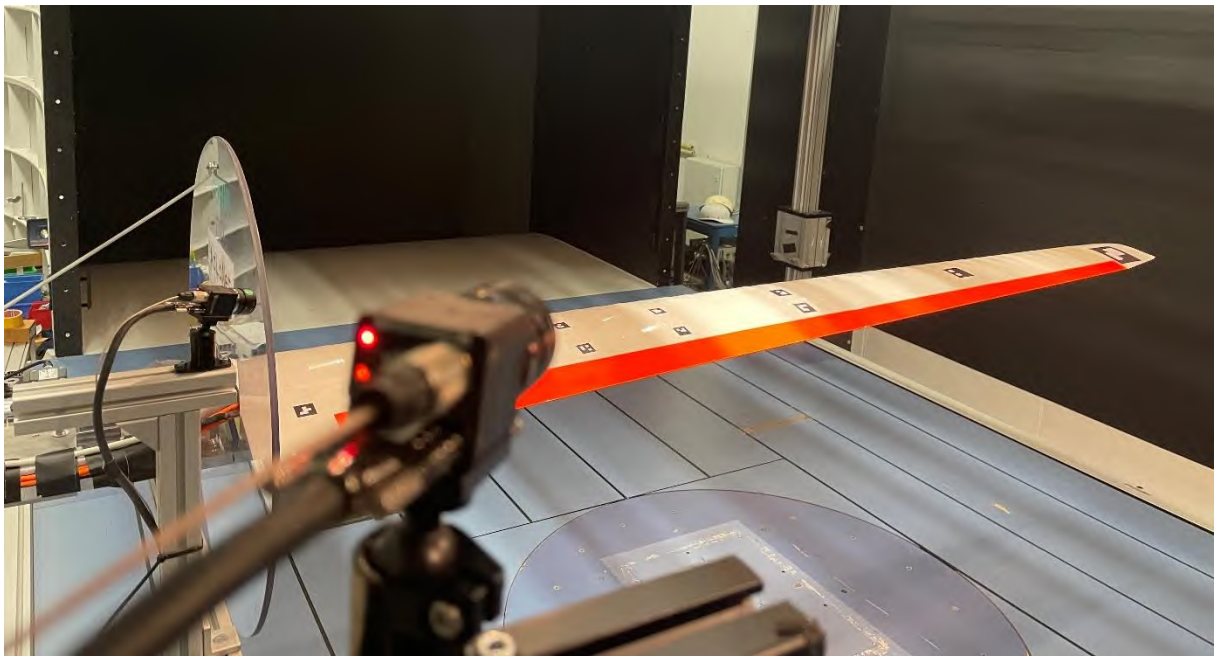

Fig. 2: Wing in the wind tunnel with the markers and the two Ximea 5 Mpx cameras. The other sensors are installed in the wing.

Literaturverzeichnis

Boden, Fritz; Kirmse, Tania; Jentink, Henk (2013): Image pattern correlation technique (IPCT). In: AIM² Advanced Flight Testing Workshop-HANDBOOK of ADVANCED IN-FLIGHT MEASUREMENT TECHNIQUES. BoD-Books on Demand, Norderstedt, S. 63–85.

Garrido-Jurado, S.; Muñoz-Salinas, R.; Madrid-Cuevas, F. J.; Marín-Jiménez, M. J. (2014): Automatic generation and detection of highly reliable fiducial markers under occlusion. In: *Pattern Recognition* 47 (6), S. 2280–2292. DOI: 10.1016/j.patcog.2014.01.005.

Kedilioglu, Oguz; Bocco, Tomas Marcelo; Landesberger, Martin; Rizzo, Alessandro; Franke, Jorg (2021): ArUcoE: Enhanced ArUco Marker. In: 2021 21st International Conference on Control, Automation and Systems (ICCAS). 12-15 Oct. 2021. 2021 21st International Conference on Control, Automation and Systems (ICCAS). Jeju, Korea, Republic of, 10/12/2021 - 10/15/2021. Piscataway, NJ: IEEE, S. 878–881.

Luderer, O.; Thielecke, F.; Wagner, J.; Kirmse, T.; Gropengießer, W.; Adden, S. (2023): Development and Testing of a Complementary Sensor Network for Robust Estimation of Maneuver and Gust Loads.

Mitteilung

Fachgruppe: Hochagile Konfigurationen

From Gaussian Process Regression to Bayesian Neural Networks: Uncertainty Quantification for High-Dimensional Aerodynamic Datasets

Ferdinand Dunkes[1], Hans-Jörg Steiner[2], Christian Breitsamter[1]
[1]Technical University of Munich, Boltzmannstr. 15, 85748 Garching, ferdinand.dunkes@tum.de
[2] Airbus Defence & Space GmbH, Rechliner Str., 85077 Manching

Introduction

For modern high-agility aircraft configurations, employing a Flight Control System (FCS) to offer carefree handling qualities in the presence of inherently unstable aircraft dynamics, detailed knowledge of the aircraft aerodynamics is of paramount importance. An accurate aerodynamic model allows the FCS to be designed as close as possible to the limits and capabilities of the aircraft. The generated aerodynamic model is required by numerous other customers, including e.g., flight-performance, -mechanics, -simulation, -testing, air data systems, and loads. Wind-tunnel testing is typically conducted to generate a continuous model of the aircraft's aerodynamic characteristics. This and other possibilities for data acquisition, such as flight testing or numerical simulations, are resource, time, and cost-intensive. Thus, introducing a comprehensive surrogate modelling framework for the continuous and accurate prediction of aerodynamic stability and control quantities from high-dimensional and non-linear input data is beneficial. While simultaneously providing uncertainty quantification capabilities, the Bayesian paradigm, e.g., Bayesian Neural Networks (BNN) and Gaussian Process Regression (GPR), is evaluated on data of the Unmanned Aerial Vehicle DLR-F17, commonly referred to as the Stability and Control Configuration (SACCON), alongside DLR-F19. This work aims to treat the following aspects:

- Introduction of a BNN and GPR setup for the high-fidelity prediction of high-dimensional aerodynamic stability and control data.
- Comprehensive comparison and assessment of the limits and capabilities of both methods with varying model setups, including uncertainty quantification.

Data and Experimental Setup

To evaluate the performance and accuracy of selected Bayesian surrogate models, training and test data from DLR-F17 and F19 are employed [1].

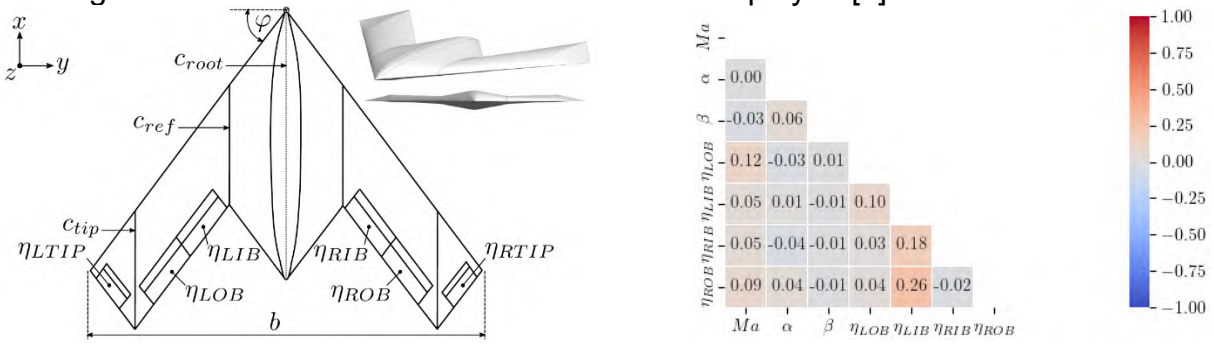

Figure 1: (left)Planform and control surfaces of the highly-swept, flying wing delta configuration SACCON; adapted from [2]. (right) Weak or non-linear correlations can be observed from the diagonal correlation matrix.

This aircraft concept exhibits a tailless flying-wing, lambda-shaped configuration. All lift and control functions are integrated into the main wing without a separate empennage. The highly swept planform with sharp leading edges features three control surfaces at each wing's trailing edge and tip. In addition to three quantities describing the flight condition, ten features are included overall in the dataset with ~30,000 qua-

si-static wind-tunnel samples. Figure 1 illustrates the aircraft's control surfaces, overall shape, and the diagonal correlation matrix of the design space.

Methodology

The subject of comparison are above mentioned probabilistic models. A BNN trained via mean-field Variational Inference (VI), a BNN sampled with the No-U-Turn Sampler (NUTS) in Hamiltonian Monte Carlo, and Gaussian Process Regression (GPR) with a Radial Basis Function (RBF) kernel were implemented. For the VI-BNN, we maximize the evidence lower bound $ELBO = E_{q(w)}[\log p(D|w)] - KL(q(w)||p(w)$ with $q(w) = \prod_i N(w_i|\mu_i, \sigma_i^2)$. The NUTS-BNN directly approximates the posterior by drawing samples via the adaptive Hamilton Monte Carlo (HMC) method. The GPR model employs a zero mean and RBF kernel $k(x, x') = \sigma_f^2 \exp\left(-\left||x - x'|\right|^2/(2l^2)\right)$, yielding predictive mean $\mu_* = k_*^T(K + \sigma_n^2 I)^{-1} y$ and variance $\sigma_*^2 = k(x_*, x_*) - k_*^T(K + \sigma_n^2 I)^{-1} k_*$.

Results

Figure 2 directly compares VI-BNN and GPR, visualizing uncertainties alongside predictive outputs.

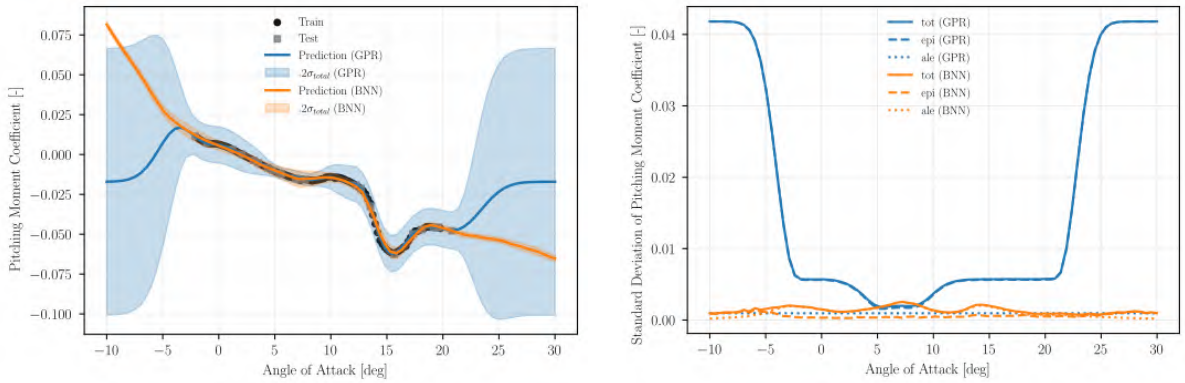

Figure 2: Comparison of prediction accuracy (left) and standard deviations (right) for BNN-VI and GPR. BNN frameworks generally outperform GPR capabilities, limited by stiffer means and reduced uncertainty decomposition capabilities.

Gaussian process regression with an RBF kernel exhibited a poorer performance on high-dimensional datasets compared to BNN approaches, proving effective only on small-scale, low-feature-count problems outside the transonic regime, as previously noted in scalability analyses of GPR by [3] and [4] for smaller design spaces. Moreover, RBF kernels without an explicit constant white-noise term cannot represent aleatoric uncertainty. In contrast, BNNs inherently decompose epistemic and aleatoric components, offering a more comprehensive uncertainty quantification framework.

Acknowledgements

The funding of all research activities by Airbus Defence & Space GmbH and the scientific guidance by the Chair of Aerodynamics and Fluid Mechanics at the Technical University of Munich is gratefully acknowledged. The authors want to thank Kai Richter and Andreas Schütte from Deutsches Zentrum für Luft- und Raumfahrt for providing valuable training data from SACCON.

References

[1] A. Schütte, K. C. Huber, N. T. Frink, and O. J. Boelens, "Stability and Control Investigations of Generic 53 Degree Swept Wing with Control Surfaces," *Journal of Aircraft*, vol. 55, no. 2, pp. 502–533, 2018, doi: 10.2514/1.C033700.

[2] G. Suarez, E. Özkaya, N. R. Gauger, H.-J. Steiner, M. Schäfer, and D. Naumann, "Nonlinear Surrogate Model Design for Aerodynamic Dataset Generation Based on Artificial Neural Networks," *Aerospace*, vol. 11, no. 8, p. 607, 2024, doi: 10.3390/aerospace11080607.

[3] L. Li, J. Chang, A. Vakanski, Y. Wang, T. Yao, and M. Xian, "Uncertainty quantification in multivariable regression for material property prediction with Bayesian neural networks," *Sci Rep*, vol. 14, no. 1, p. 10543, 2024, doi: 10.1038/s41598-024-61189-x.

[4] M. Anhichem, S. Timme, J. Castagna, A. Peace, and M. Maina, "Bayesian Approaches for Efficient and Uncertainty-Aware Prediction of Pressure Distributions," in *AIAA SCITECH 2024 Forum*, Reston, Virginia, 2024.

Mitteilung

Fachgruppe: Hochagile Konfigurationen

Sabot separation of a group of finned slender projectiles in Mach 4.5 flow

Oskar Grudziński, Robert Hruschka

Deutsch-Französisches Forschungsinstitut Saint-Louis, 5 Rue du Général Cassagnou, 68300 Saint-Louis, Frankreich, Oskar-Filip.GRUDZINSKI@isl.eu

To improve the counter-capabilities of ground and naval forces against fast airstrikes by drones and hypersonic threats, a novel concept of a high rate-of fire, high-velocity munition is considered, where each shot consists of a several arrow-shaped submunitions, also known as fléchettes. The high ballistic coefficient of such a finned slender projectile is favourable for long-range shots. However, when destabilized by the muzzle outflow during the transitional ballistic phase, these densely packed fléchettes tend to tumble erratically. As a result, they rapidly loose kinetic energy, effective range, and their terminal ballistic effectiveness. This shortcoming can be overcome by using a cup sabot that carries the arrows through the transitional flow near the muzzle in a stable manner, while separating later when the package is in steady free flight, i.e outside the muzzle blast.

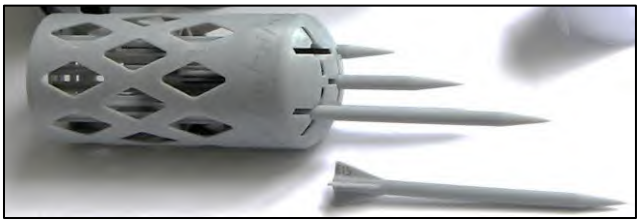

Figure 1: Flechette models and the sabot.

The separation of such a bundle of arrows from the sabot is a complex process, involving supersonic aerodynamic interference, multiple conical shock wave diffractions, free-flight interbody collisions, and dynamics of motion of multiple bodies in all degrees of freedom. It is investigated how aerodynamics, separation stability, and arrow dispersion are influenced by the relevant parameters of the system for a long-distance shot.

The study focused on a separation of 5 parallel, symmetrically arranged projectiles with no axial stagger. Previous studies by Chaplin et al. [1] showed experimentally that the impinging shockwave generated by a nearby-flying body can significantly shift the centre of pressure of the aerodynamically-stabilized projectile, potentially resulting in a temporal loss of its static stability. Therefore, the location of the centre of gravity was the first parameter varied in the study, affecting the arrow's stability margin.

Three sets of projectile models of $4mm$ shaft diameter, or calibre, were additively manufactured using UV-curable engineering resin, with their centre of gravity (CG) adjusted by the location of an embedded tungsten rod. The chosen reference location of the CG was the volumetric centre of the projectile (CG_{ref}).

From there, the CG was shifted forward by 2 (CG_{ref}+2cal) and by 4 calibres (CG_{ref}+4cal). The projectiles were placed in a lightweight 3D-printed sabot, and weakly suspended in the evacuated test chamber aft of the Ludwieg tube nozzle exit. Two perpendicular cameras filmed the separation and flight of the projectiles at 20000 frames per second, and 1024p greyscale resolution. A double Z-schlieren setup was used for high-contrast shock visualization. The optical setup was augmented with 4 strong LED lights to illuminate the surface of the models to facilitate capturing their motion in all six degrees of freedom. During their transit of the Mach cone of the nozzle, projectiles experienced a steady-state free stream condition of $p_\infty = 51\ mbar, T_\infty = 48K$ at $Ma_\infty = 4.5$, verified by the nozzle pressure measurements.

These first experimental investigations revealed CG-location-dependent behaviour of the group of parallel arrows after launch. In case of the reference CG location, the shockwave system generated by the sabot and interfering arrows appears to significantly impact the separation dynamics of the arrow bundle, usually leading to collisions and resulting in unstable, non-deterministic trajectories. Shifting the CG forward by two calibres significantly improved the overall stability of the separation, providing more damping to the interference-induced pitching motion, which was enough to prevent chaotic projectile collisions due to impinging shockwaves. Placing the CG farther forward at $CG_{ref} + 4cal$ further improved stability.

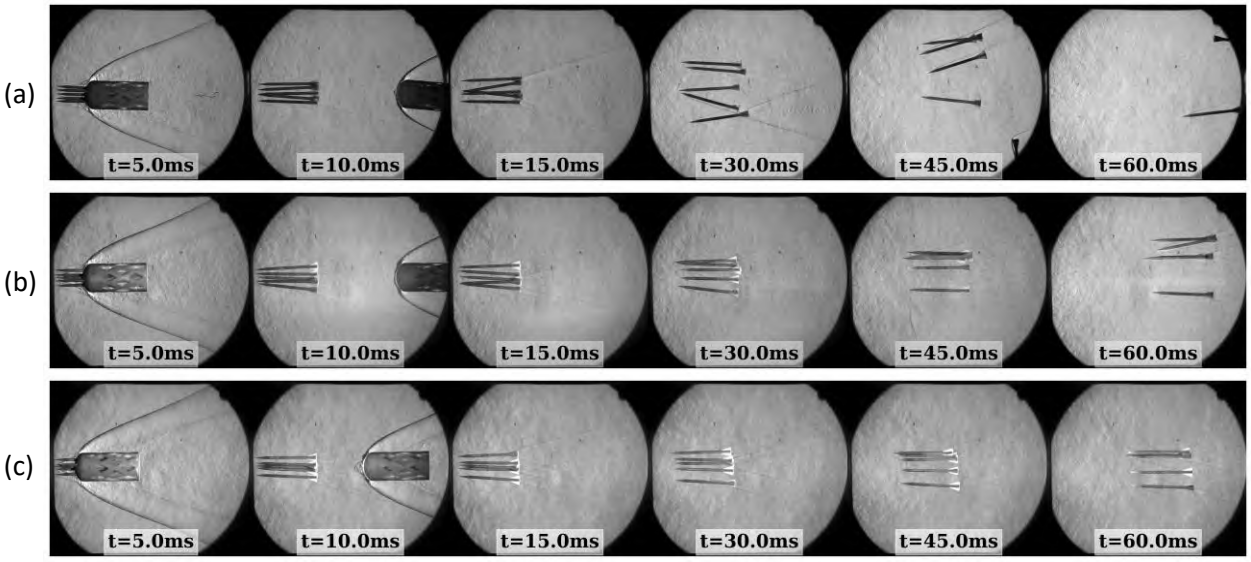

Figure 2(a,b,c): A sequence of frames from the free flight test of the arrows with (a) CG_{ref}, (b) $CG_{ref} + 2cal$, and $CG_{ref} + 4cal$.

The system of monolithic finned slender projectiles launched into the supersonic stream from the sabot exhibits a non-deterministic behaviour. The arrows collide with each other, and scatter in an unstable manner. The separation stability can be significantly improved by shifting the centre of gravity forward, thereby increasing the stability margin. In practice, a trade-off has to be made, as the gain in stability margin is made at a loss of the maximum possible ballistic coefficient of the projectile. More refined studies and also the investigation of alternative means of assuring a stable separation and deterministic scatter will follow.

[1] Chaplin 2009 – Aerodynamic interference between high-speed slender bodies, PhD thesis.

Mitteilung

Fachgruppe: Hochagile Konfigurationen

Semi-Empirical and Numerical Analysis of the Aerothermal Heating of a Hypersonic Sounding Rocket

Sebastian Michalski[1], Felix Lamnek[1]
Diehl Defence GmbH & Co. KG
[1]Department of Aerodynamics and Propulsion,
Alte Nußdorfer Straße 13, 88662 Überlingen, Germany

Rockets and missiles that fly at hypersonic speeds are subject to severe aerothermal heating. This aerothermal heating is a key aspect, which influences the design process with regard to the overall geometry, the selection of appropriate high-temperature materials, or the implementation of active and passive cooling solutions. Within this design process it is useful to apply aerothermal prediction methods of increasing fidelity – and therefore of increasing computational effort – to give predictions adequate for the progressively refined design. In practice, the application of semi-empirical methods is the low fidelity / low computational effort approach, while the application of computational fluid dynamics (CFD) methods with different levels of approximations for the flow physics and the fluid chemistry represents the other end of the spectrum.

The current study presents the underlying principles of a semi-empirical and a CFD prediction method and demonstrates their validity by application to a hypersonic sounding rocket experiment conducted by the German Aerospace Center (DLR) [1, 2]. Both methods are used for the analysis of the transient heating of the nose-ogive structure, which was instrumented with temperature probes during the free-flight experiment.

The semi-empirical approach is based on inviscid flow solutions, which are used as input for approximate boundary layer solutions, which again yield the local aerothermal heat flux at the surface. The inviscid flow solutions are based on the oblique shock relations, the modified Newtonian theory, and the conical flow theory by Taylor-Maccoll [3, 4]. The boundary layer approximations follow the approaches of van Driest [5] for the flat plate and the stagnation point cases. Furthermore, this semi-empirical approach approximates the local laminar-turbulent boundary layer state as a function of the Mach number as well as the unit and local Reynolds numbers at the boundary layer edge. The evaluation of the thermal heat transfer also considers a one-dimensional radial heat conduction into the structure and radiative cooling at the surface.

The CFD method uses a two-dimensional axisymmetric computational grid, which includes the fluid and the solid structure domain. Two-dimensional heat transfer within the structure, under the assumption of isotropic heat conductivity, and radiative cooling at the surface are also accounted for by the CFD method. The gas is modeled either as thermally perfect or as chemically reacting, considering five gas species, as given by Park [6]. However, steady-state test cases showed negligible influence of the chemical reactions and thus the less computationally expensive thermally perfect gas model was used for the transient trajectory calculations. Depending on the Reynolds number for the half-length of the ogive, the flow over the whole ogive is switched between a fully laminar or a fully turbulent state with use of the k-ω-SST turbulence model [7]. Figure 1 shows exemplarily the temperature distribution in the forward part of the ogive structure.

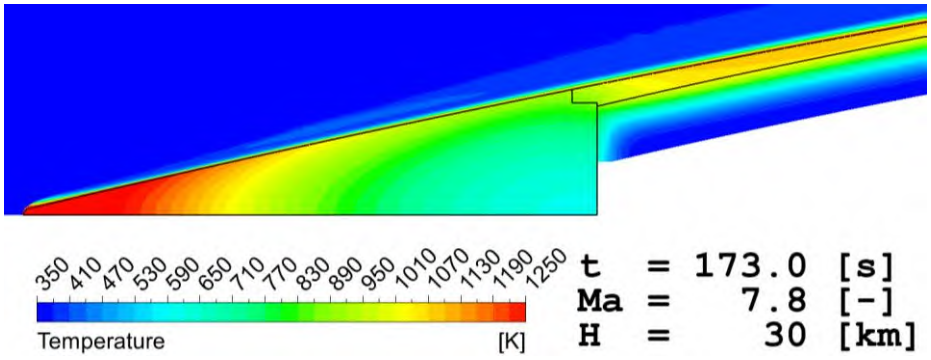

Figure 1: Temperature field of the nose section extracted from the transient CFD solution.

Figure 2 presents the results regarding the temperature profiles within the structure obtained by both prediction methods. The comparison of the fully turbulent assumption and the deployment of laminar-turbulent switching for the CFD solution highlights the necessity of adequate transition modeling in order to obtain satisfactory predictions over the whole trajectory. For the $x = 40\ \mathrm{mm}$ position, the global switch between fully laminar and fully turbulent modelling of the CFD method, which considers the Reynolds number of the half-length of the ogive, predicts a biased turbulent state for the low Reynolds numbers at the tip of the ogive. Hence, an overprediction by the CFD

method is expected. The semi-empirical method yields a good qualitative agreement, but an underprediction is apparent. Most likely, this is due to the neglection of the axial heat flux from the nose tip by the semi-empirical method. Because the temperature gradient generally decreases downstream along the structure, the axial heat flux is most significant for the upstream sections. As a consequence, the prediction quality of the semi-empirical method improves for the further downstream probes, e.g., $x = 230\ mm$, $x = 550\ mm$, and $x = 1480\ mm$. The data for the position of $x = 230\ mm$ is an example for the possible sensitivity of local predictions to the laminar-turbulent transition parameters. The semi-empirical method results in quantitative good agreement, only if the initially predicted transition Reynolds numbers are reduced by 20 % ($Re_t * 0.8$). In contrast, this scaling of the transition Reynolds numbers has very little influence on the predictions for the other positions.

Despite their respective limitations – which are most relevant for the nose region – both methods yield satisfactory results. The CFD method results in higher-fidelity predictions, while the semi-empirical method yields predictions still well suited for engineering purposes with the use of little computational and pre-processing resources.

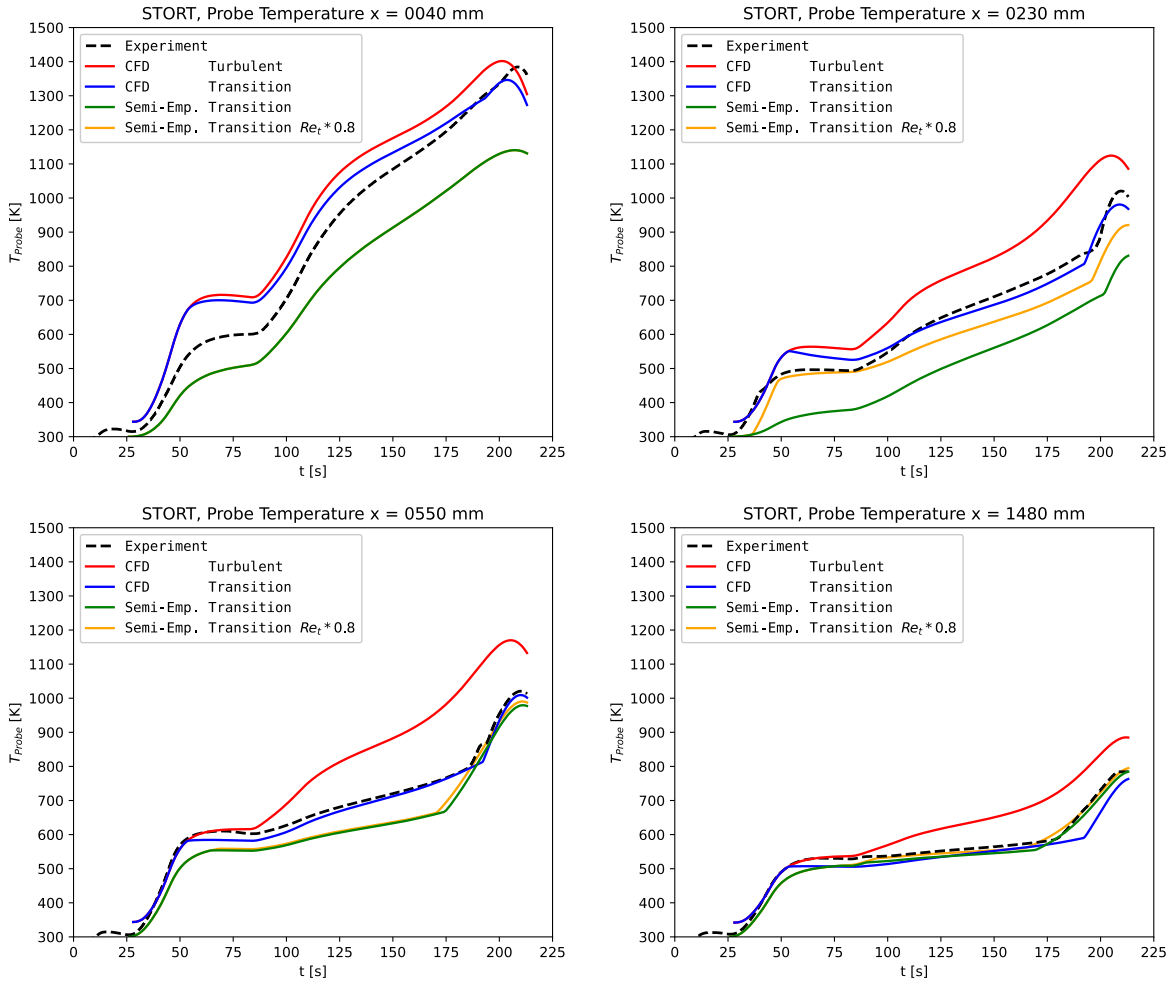

Figure 2: Comparison of the results regarding the temperature within the structure.

References

[1] A. Gülhan, D. Hargarten, M. Zurkaulen, F. Klingenberg, F. Siebe, S. Willems, G. Di Martino and T. Reimer, *Selected Results of the Hypersonic Flight Experiment STORT,* Acta Astronautica, Vol. 211, pp. 333-343, 2023.

[2] T. Reimer, G. Di Martino, I. Petkov, L. Dauth, L. Baier and A. Gülhan, *Design, Manufacturing and Assembly of the STORT Hypersonic Flight Experiment Thermal Protection System*, 25th AIAA International Space Planes and Hypersonic Systems and Technologies Conference, AIAA 2023-3089, Bengaluru, India, 2023.

[3] J. D. Anderson, *Hypersonic and High-Temperature Gas Dynamics*, 3rd. ed., AIAA, Reston, USA, 2019.

[4] J. D. Anderson, *Modern Compressible Flow: With Historical Perspective*, 2nd. ed., McGraw-Hill Publishing, New York, USA, 1990.

[5] E. R. van Driest, *The Problem of Aerodynamic Heating*, Aeronautical Engineering Review, Vol. 15, No. 10, pp. 26-41, 1956.

[6] C. Park, *Review of Chemical-Kinetic Problems of Future NASA Missions, I: Earth Entries*, Journal of Thermophysics and Heat Transfer, Vol. 7, No. 3, pp. 385-398, 1993.

[7] F. R. Menter, *Two-Equation Eddy-Viscosity Turbulence Models for Engineering Applications*, AIAA Journal, Vol. 32, No. 8, pp. 1598-1605, 1994.

Mitteilung

Fachgruppe: Hochagile Konfigurationen

Numerical Investigations on Vortex-Vortex and Vortex-Shock Interactions at Hybrid-Delta-Wing Configurations

Yasin Özdemir, Christian Breitsamter
Chair of Aerodynamics and Fluid Mechanics, Technical University of Munich
Boltzmannstr. 15, 85748 Garching b. München, yasin.oezdemir@tum.de

Leading-edge vortices (LEV) dominate the flow topology around delta wing planforms, providing a nonlinear lift contribution that yields a smoother post-stall characteristic, which is an essential tool for maneuverability [1]. However, as the angle of attack (α) increases, LEVs become unstable and vortex breakdown takes place, which may ultimately impair the flight stability characteristics. Modern high-agility aircraft feature multi-swept delta wing or strake-wing configurations, where multiple vortices yield a higher nonlinear contribution to the lift force [2]. Vortex-vortex and vortex-shock interactions lead to a highly intricate flow field, while the latter potentially triggers the vortex breakdown and, thus, degrades the aerodynamic characteristics and flight stability [3].

The objective of this study is to deliver a comprehensive analysis of the flow field at various Mach numbers (Ma) in the transonic flow regime. Two multi-swept generic wing-fuselage configurations with sharp leading edges (r_n/c_r = 0) are investigated. The double-delta wing features a highly swept strake and a moderately swept main wing element with sweep angles of $\varphi_2 = 75°$ and $\varphi_3 = 52.5°$, respectively. The triple-delta-wing configuration is further equipped with a LEV controller (LEVCON) segment with a sweep angle of $\varphi_1 = 52.5°$. Additionally, the influence of the leading-edge radius r_n on the vortex flow physics is studied with relative values referring to the wing root chord c_r of r_n/c_r to 0.25% and 0.50%.

Computational Fluid Dynamics (CFD) simulations are carried out using the TAU Code developed by the German Aerospace Center (DLR). Unsteady Reynolds Averaged Navier-Stokes (URANS) computations employ the one-equation Spalart-Allmaras turbulence model in its negative formulation with rotation correction (SARC-neg). Computations are carried out at Ma = 0.75, 0.85, and 0.95, with α ranging from 16° to 32° in 4° increments for both symmetric (β = 0°) and asymmetric (β = 5°) flow conditions. Time-step size of $\Delta t = 2 \times 10^{-4}\ s$ is used for URANS calculations. For higher fidelity, hybrid RANS/LES (IDDES) simulations based on the URANS results are performed using the same turbulence model. A time-step sensitivity study shows that $\Delta t = 2 \times 10^{-5}\ s$ provides the best compromise between computational cost and accuracy. The applied numerical setup is validated by comparing the computational results with data of the wind tunnel measurements in the transonic wind tunnel Göttingen (TWG) provided by DLR and Airbus Defence and Space.

Figure 1 illustrates iso-surfaces of the non-dimensional Q criterion, $Q^* = \frac{Q{l_\mu}^2}{{U_\infty}^2} = 50$, colored by local Mach number values at freestream Mach numbers of Ma = 0.75, 0.85, and 0.95 for symmetric flow conditions. Additionally, iso-surfaces of axial pressure gradients of 2.5×10^5 are depicted to identify the shocks. At Ma = 0.75, a narrowing of the Q*-Isosurface and a decrease in the local Mach number above the wing indicate the breakdown of the Inboard Vortex (IBV), whereas the Midboard Vortex (MBV) remains

stable, Fig. 1a. At Ma = 0.85, the first shock disturbs the flow field and causes a reduction in the local Mach number associated with the IBV, however, the interaction with the second shock results in a complete breakdown of the IBV, Fig. 1b. The MBV is still developed until the trailing edge despite its interaction with the shock. For Ma = 0.95, a single shock occurs on the fuselage and the IBV bursts above the main wing, Fig. 1c. The MBV gets energized along the entire leading edge and extends to the trailing edge, where a strong shock forms and reduces the flow velocities. As shown in Figure 1d, the IBV increases in size and features higher local Mach numbers at higher α, yet starts bursting upstream of the second shock. Further, the MBV-shock interaction results in breakdown.

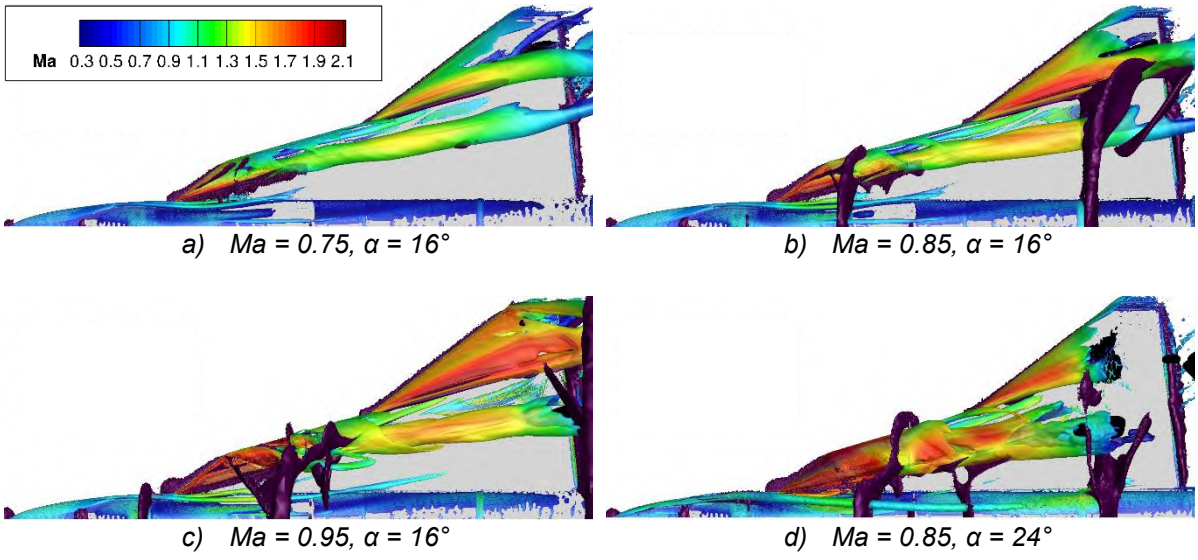

a) Ma = 0.75, α = 16° *b) Ma = 0.85, α = 16°*

c) Ma = 0.95, α = 16° *d) Ma = 0.85, α = 24°*

Figure 1: Isosurfaces of the non-dimensional Q-criterion of 50 for a triple-delta wing configuration at Re = 1.06 × 10⁷, Ma = 0.75; Re = 1.20 × 10⁷, Ma = 0.85; and Re = 1.34 × 10⁷, Ma = 0.95, under symmetric flow conditions.

Acknowledgments

The authors gratefully acknowledge the funding of the project by the Deutsche Forschungsgemeinschaft (DFG, German Research Foundation) – project number DFG BR1511/13-2. The DLR is appreciated for providing the flow simulation software DLR TAU Code. Additionally, both DLR and Airbus Defence and Space are acknowledged for the provision of experimental data, utilized for comparative analysis with the numerical results in this study. The authors also thank the Gauss Center for Supercomputing e.V. for funding this project by providing computing time at the Leibniz Supercomputing Center (LRZ, www.lrz.de).

References

[1] Christian Breitsamter, Turbulente Strömungsstrukturen an Flugzeugkonfigurationen mit Vorderkantenwirbeln. Aerodynamik. München: Utz, Wiss., 1997.

[2] P. E. Olsen and R. C. Nelson, “Vortex interaction over double delta wings at high angles of attack,” in 7th Applied Aerodynamics Conference, 1989, American Institute of Aeronautics and Astronautics Inc, AIAA, Seattle,1989. doi: 10.2514/6.1989-2191.

[3] M. Werner, A. Schütte, S. Weiss, and A. Senior, “Turbulence Model Effects on the Prediction of Transonic Vortex Interaction on a Multi-Swept Delta Wing,” AIAA Scitech Forum, San Diego, CA, 2022.

Mitteilung

Fachgruppe: Hochagile Konfigurationen

Pitch Recovery Investigations on a Generic Fighter Aircraft Configuration

Andreas Schütte
Institute of Aerodynamics and Flow Technology, Lilienthalplatz 7,
38108 Braunschweig, andreas.schuette@dlr.de

Anirvin Puttur
US Air Force Academy, Colorado, USA

Introduction

The design of modern fighter aircraft configurations is mainly driven by constrains of low observability, high maneuverability and good supersonic flight characteristics. The aerodynamic requirements of modern fighter aircraft can be fulfilled by delta wing planforms. The medium to high leading edge sweep angles of these configurations lead to a complex vortical flow field and challenging aerodynamic behavior. Fig. 1 shows on the left the current configuration, the DLR-FFD 2nd Generation fighter configuration and on the right an example of the complex vortical flow topology around the DLR-FFD (Future Fighter Demonstrator).

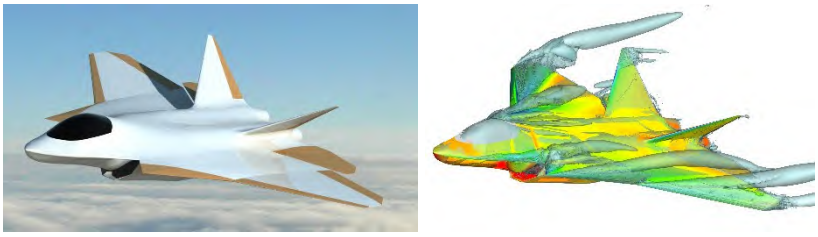

Fig. 1 : DLR FFD 2nd Generation Fighter Configuration (Future Fighter Demonstrator)

The DLR project Diabolo [1] and the follow-on project WingMates focuses on the development capabilities for the design and assessment of modern fighter aircraft. One of the aerodynamic tasks is to provide aerodynamic data sets for the overall design assessment, to evaluate the flow physics and to enhance the aerodynamic performance. Based on the initial DLR-FFD planform (1st Generation) in Diabolo, aerodynamic studies have been conducted to find potential enhancement of the aerodynamic roll stability behavior. Previous investigations have been performed looking at the influence of wing and strake leading edge sweep angle, wing leading edge slats, strake flaps and different vertical stabilizer settings. The results have been published by Schütte and Hummel [2], Alt and Schütte [3] and finally by Schütte and Hummel [4]. Within WingMates the follow-up task is to map the planform study finding towards a 2nd generation of the DLR-FFD and to assess if the gained enhancements in aerodynamic performance remains.

Objectives

The presented investigations analyses the vortical flow physics and aerodynamic performance of DLR-FFD 2nd Gen. aircraft configuration. The work focuses on the aerodynamic task to determine the pitching moment performance and in particular the ability to provide the requested pitch recovery moment. The numerical investigations have been performed with the DLR RANS solver TAU.

Results

Fig. 2 shows the size of pitching moment coefficient C_m for different inclination angles of the horizontal tail plane (HTP) versus AoA α for flight conditions at Mach 0.5. The configuration shows a stable pitching moment behavior for $C_m < 0$ where the configuration shows a rear loading behavior. It can be observed that for higher angle of attack a higher HTP inclination is needed to provide stable conditions. Fig. 3 shows the lift, pitching moment and drag coefficient versus AoA for the entire configuration and the contribution of the HTP only. It can be seen that with the given MRP (Moment Reference Point) the configuration shows an unstable pitching moment behavior. However, the inclination of the HTP is providing a desired rear loading pitching moment for almost the entire AoA range. In addition, it can be seen that for inclination angles of η_{HTP} = 0° and 10° degrees the rear loading increases with increasing AoA. Whereas for η_{HTP} = 20° the characteristics is almost stagnating with increasing AoA.

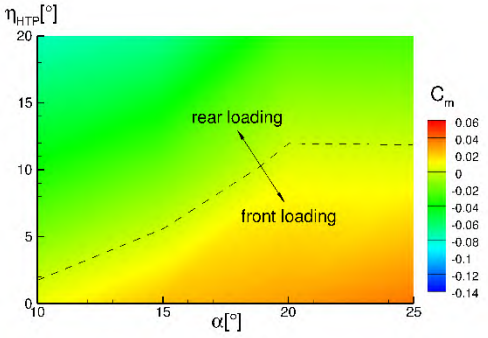

Fig. 2 : Horizontal tail plane (HTP) inclination versus AoA α, colored by the pitching moment coefficient C_m, M = 0.5.

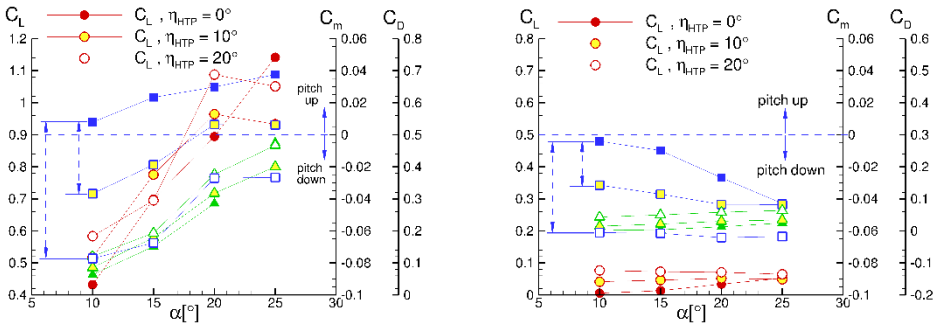

Fig. 3 : Lift, pitching moment and drag coefficient versus AoA for the entire configuration (left) and the contribution of the HTP only (right).

Further results will be provided for a lower Mach number of 0.2 and it will be presented how the pitching moment behavior changes with changing MRP and if the required pitch recovery moment can be achieved with the current setup of the DLR-FFD.

References

[1] Liersch, C., Schütte, A., Moerland, E., and Kalanja, K.: DLR Project Diabolo: An Approach for the Design and Technology Assessment for Future Fighter Configurations. AIAA Paper 2023-3515, 2023. https://doi.org/10.2514/6.2023-3515

[2] Schütte, A., and Hummel, D.: Numerical Design Studies on the Roll Stability of a Multi-Delta-Wing Configuration. AIAA Journal of Aircraft, Vol. 60, No. 3, 2023, pp. 898–914. https://doi.org/10.2514/1.C037128

[3] Alt, K., and Schütte, A.: Influence of the Vertical Stabilizer on the Aerodynamics and Roll Stability of a Generic Multiple Delta Wing Aircraft Configuration. In: New Results in Numerical and Experimental Fluid Mechanics XIV, Springer, 2023, p. 637–646. https://doi.org/10.1007/978-3-031-40482-5_60

[4] Schütte, A., and Hummel, D.: Numerical Mach number studies on a multi-delta wing configuration with vertical stabilizers. AIAA Journal of Aircraft, 2024. https://doi.org/10.2514/1.C038163

Mitteilung

Fachgruppe : Hyperschallaerothermodynamik

Investigation of the Ablation of Fins in Hypersonic Flows

L. Barbiche, F. Denis, B. Sauerwein, M. Bastide, A. Runser, R. Kempf
Institution : ISL – French-German Research Institute of Saint-Louis
5 rue du Général Cassagnou, 68300 Saint-Louis, France
Mail: Laureen.BARBICHE@isl.eu

***Index Terms*—Hypersonic, Shock tunnels, Ablation, Heat-flux**

I. Introduction

THE ablation phenomenon describes the removal of material, by melting [1], pyrolysis oxidation, gas blowing, etc. In our study, we focus specifically on ablation driven by melting and oxidation on metallic surfaces — the fins of a generic model of an armor-piercing fin-stabilized projectile fig.1, the EMI-Finner, with a slenderness ratio of 21.25 [2][3]. When subjected to hypersonic flow, i.e, above Mach 4–5, shock waves form at the projectile's nose and leading edges. Within the shock layer, between the projectile surface and the shock wave, a significant temperature rise occurs, mainly due to adiabatic gas compression and the conversion of kinetic energy which increases the wall heat flux ($\dot{q}_w \propto v^3$). The metallic surface is heated beyond the melting point and advected downstream by the flow.

Understanding this phenomenon is becoming increasingly important with the emergence of new hypersonic applications - for instance, in modern battle tanks equipped with anti-armor weapons or for electromagnetic railgun, in which future projectiles could reach hypersonic speeds and extended ranges. For these systems, the integrity of the fins is essential to ensure stable flight and accurate targeting, while maintaining high speed and long range to effectively penetrate armored targets.

This is what investigate in this study, by identifying the regions affected by ablation and quantifying it.

Fig. 1. Photographs of the model: it consists of three separable parts that are screwed together. The fin assembly is cast in gallium, whereas the remaining sections are manufactured from steel.

II. Shock Tunnel simulations

Ablation is experimentally investigated in a high-enthalpy shock tunnel [4], which generates a hypersonic flow directed toward a fixed model, simulating flight conditions at Mach 4.5 hypersonic speeds flow and ground-level equivalent altitude with a stable flow regime lasting about two milliseconds. We use nitrogen as test gas to prevent oxidation reactions.

To observe ablation over the short timeframes, the fins were molded from gallium around a central rod. The mold was CAO-designed and 3D printed. Gallium, a non-toxic metal with a 302.91K melting point, was melted, injected into the mold, and solidified by freezing. The rest of the projectile was machined from steel and designed so that the three main parts — the nose, the shaft, and the tail assembly- can be separated if needed to add a sabot threaded section as found on armor-piercing fin-stabilized discarding-sabot projectiles (APFSDS-projectiles).

An optical setup enables direct visualization of the flow through two windows positioned on either side of the test section, providing a clear view of the model. On one side, light diffusor covers the window, and a flash is triggered as the flow reaches the projectile. On the opposite side, a Photron SA-X high-speed camera, operating at 2400 frames per second with

a 0.29-microsecond exposure time, producing a sequence of black-and-white images. Equipped with a 300 mm f/2.8 lens and featuring a decoupled optical system to increase the zoom, the camera records images at a resolution of 1024 × 512 pixels, enabling precise observation of ablation on the fin surface.

III. POST-PROCESSING AND RESULTS

A dedicated Python code is used for post-processing the images and quantifying ablation by comparing the fins contours at the beginning and end of the stable flow phase fig.2.

The raw images are first realigned with reference to the first image of the steady flow to correct the vibrations caused by the flow on the model. We use the OpenCv library to do a cross correlation by selecting the region of interest (ROI) on the first image, which serves as a reference for the following images. For optimal results, we first need to unify the shades of gray that vary from one image to another as the flash weakens. Thus, we successively apply a contrast stretching towards black and white , a bilateral filter and an Otsu threshold, which produce a black and white image with a unified background and cleared fin edges. The different contours can eventually be extracted and compared between the first and last image to quantify the ablation and identify regions affected.

Preliminary observations show a material removal that tends to smooth the surface, making it appear shinier, which suggests a localized polishing effect due to ablation. However, what we measured is on the order of a few tenths of a millimeter which is not yet conclusive considering optical and numerical uncertainties, although this results open up several experimental perspectives.

IV. CONTINUATION

At the date of writing this paper, we want to add a chamfer to the edge of the fins, in accordance with what already exists for this type of projectile, for a second campaign in shock tunnel. This will also reduce the fins surface area to be ablated. A higher magnification will also be performed.

As this PhD project progresses, we will study how a sabot thread on the shaft affects the fins, and the heat fluxes at the fins surface will be characterized. Based on these results, numerical studies will subsequently be carried out and numerical model for the aerodynamic heating will be developed by using OpenFoam.

REFERENCES

[1] **Flavien Denis**, *Study of the ablation by melting in hypersonic flow. Fluid mechanics [physics.class-ph].* Université de Strasbourg, 2022. English.ffNNT : 2022STRAD004ff.fftel-03885516f

[2] **Sebastian Michalski**, *Doctoral Thesis : Aerodynamics of High-Slenderness Finned Projectile in Super- and Hypersonic Flows with Boundary Layer Transition and Surface Roughness Effects*, p.12-16 **https://doi.org/10.24405/17342**

[3] Fraunhofer Institute for High-Speed Dynamics, Ernst-Mach-Institut, EMI

[4] **P.Gnemmi, J.Srulijes, F.Seiler, B.Sauerwein, M.Bastide, C.Rey, P.Wey, B.Martinez, H.Albers, G.Schlöffel, R.Hruschka, T.Gauthier** "Shock Tunnels at ISL". Experimental Methods of Shock Wave Research,2016,p. 131 to 179

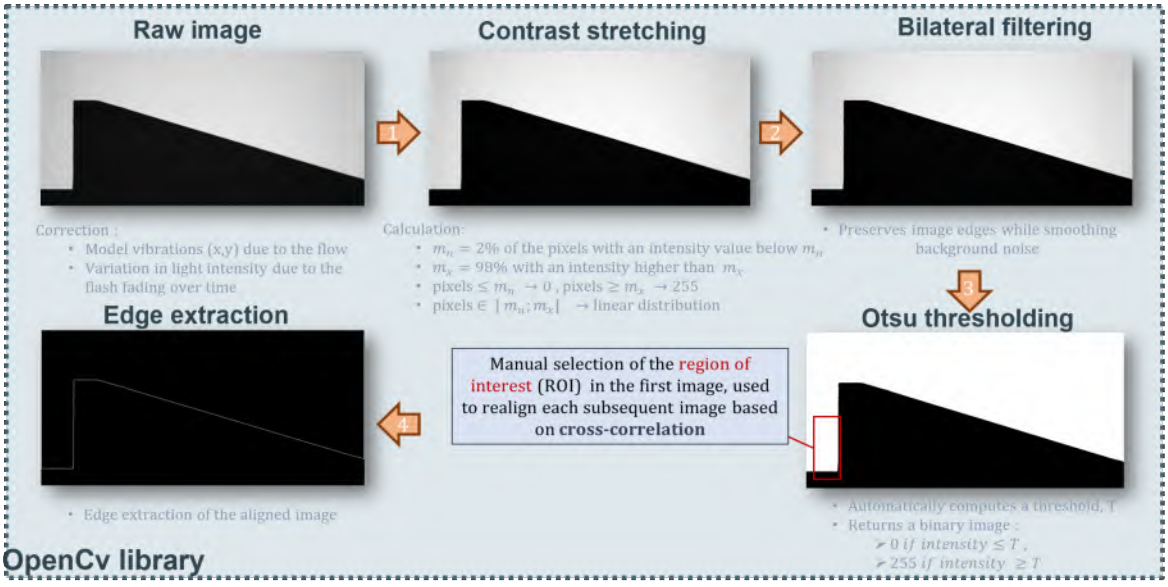

Fig. 2. Scheme of the steps for processing a raw image until the extraction of the fin outline

Mitteilung

Fachgruppe: Hyperschallaerothermodynamik

Boundary-layer investigation of the MORABA sounding research rocket at hypersonic speeds

Lennart Bott, Christian Stemmer
Lehrstuhl für Aerodynamik und Strömungsmechanik, Technische Universität München,
Boltzmannstr. 15, 85748 Garching b. München
lennart.bott@tum.de

The high-speed aerodynamics group at the Chair of Aerodynamics and Fluid Mechanics (Technical University of Munich) employs the Direct Numerical Simulation (DNS) code NSMB (Navier-Stokes Multi-Block) to investigate laminar-turbulent transition at the ogive/conical front section of DLR's micro-gravity research rocket VSB-30 for Mach-numbers ranging from 4 – 6. The goal is to determine the influence of three-dimensional isolated roughness, discontinuities as well as roughness patches on the stability of the boundary layer extending the work of Chiapparino and Stemmer [1, 2] for the flow over a ramp.
The prediction and description of transition presents a challenging task as it highly depends on the flow conditions and geometry. Hence, flight experiments, like HiFire [3] or BOLT [4, 5], are needed, where the latter employed a rounded leading edge with concave surfaces. This configuration leads to a complex flow pattern exhibiting small longitudinal vortices that cause local instabilities. However, an increase in surface roughness at Ma = 3.45 inside NASA's Langley Probe Calibration Tunnel showed only minor influence on the transition as it is dominated by the vortices [6]. Boundary layer stability investigations considering ogive geometries have not been conducted so far, as such a detailed approach exceeds the needs for most technical applications. In addition, flows around ogive bodies exhibit a negative pressure gradient and hence, flow acceleration leading to a more stable boundary-layer flow.
Current work is devoted to achieving a laminar, two-dimensional, axis-symmetrical, high-resolution base flow to be analyzed for stability. Hence, a fourth-order central scheme is employed, and strong gradients, like in the shock or boundary layer, are well resolved. For a free-stream Mach number of 6, Fig. 1 shows the Mach-number distribution in the flow domain. The formation of a detached shock upstream of the blunted nose, as well as the flow acceleration downstream, are clearly observable. The accelerated nature of the flow can also be identified in Fig. 2, which compares the boundary layer profiles at nose-tip angles of 30° and 60° as well as at x = 50 mm and x = 500 mm.
As a next step, the influence of high-temperature effects on the post-shock flow field will be assessed and three-dimensional DNS simulations will be conducted accounting for the rocket's exact surface characteristics, different pitch angles, and atmospheric disturbances. The addition of localized roughness or patches will be decided upon the result of the stability analysis and the obtained flow results will be further investigated and compared to experimental data gathered by DLR's MORABA group in cooperation with the research group of Prof. Ingo Jahn (University of Southern Queensland, USQ) during the ascent phase of the upcoming MAPHEUS mission in Esrange, Sweden. In addition, shock tube experiments will be conducted at USQ, also allowing a comparison to wind tunnel data.

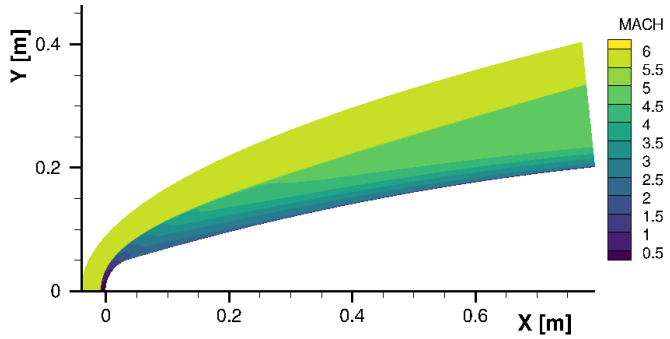

Fig. 1: Mach-number distribution in flow domain for Ma = 6

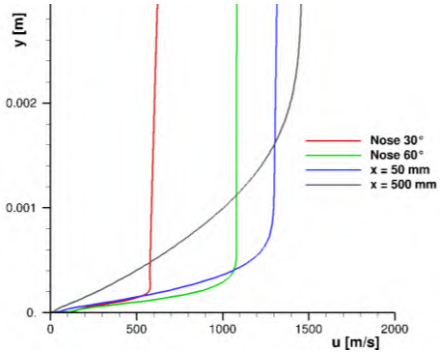

Fig. 2: Boundary-layer profiles at nose angles of 30° and 60° and x = 50 mm and 500 mm

Acknowledgements

The authors gratefully acknowledge the Deutsche Forschungsgesellschaft (DFG) and the International Graduate School of Science and Engineering (IGSSE) for funding this project, as well as the Leibniz Supercomputing Center for providing the computational capabilities and data. The authors would also like to thank their project partners at USQ and DLR and in particular the campaign team of MAPHEUS for the opportunity to gather free flight data.

References

[1] G. Chiapparino and C. Stemmer. DNS of a hypersonic flow on a ramp geometry with isolated roughness. 2nd International Conference on Flight Vehicles, Aerothermodynamics and Re-entry Missions and Engineering (FAR), 2022. URL https://mediatum.ub.tum.de/node?id=1664027.

[2] G. Chiapparino and C. Stemmer. Numerical investigation of a Mach 6 laminar shock-wave/boundary layer interaction on a two-dimensional ramp with 3d controlled surface roughness. International Journal of Heat and Fluid Flow, 103:109193, 2023. doi: 10.1016/j.ijheatfluidflow.2023.109193.

[3] R. Kimmel, D. Adamczak, and S. Stanfield. HIFiRE-1 boundary layer transition measurements. In 28th international congress of the aeronautical sciences ICAS 2012, 2012.

[4] Z. M. Johnston and G. V. Candler. Hypersonic boundary layer transition of the BoLT-2 flow field at flight conditions. AIAA paper 2023-0084, 2023.

[5] C. S. Butler, N.P. Bitter, and B.M. Wheaton. Initial bi-global stability analysis of the bolt ii flight experiment. AIAA paper 2023-0291, 2023

[6] J. Davami, T. J. Julian, A. Chou, and A. Leidy. Effect of roughness on transition on the bolt-1a geometry in supersonic flow. AIAA paper 2023-3441, 2023.

Mitteilung

Fachgruppe: Hyperschallaerothermodynamik

Influence of wall temperature distribution on hypersonic flow stability

Capecchi Cosimo[1], Christian Stemmer[2]

Lehrstuhl für Aerodynamik und Strömungsmechanik, Technische Universität München
Boltzmannstr. 15, 85748 Garching b. München
[1] MSc., email: cosimo.capecchi@tum.de
[2] Prof. Dr.-Ing. habil., email: christian.stemmer@tum.de

Abstract

Hypersonic boundary-layer laminar-turbulent transition strongly influences aerodynamic heating, drag, and overall vehicle operability. Transition leads to increased heat transfer, requiring stronger or more advanced thermal protection systems (TPS), as well as higher viscous drag. These effects highlight the importance of understanding the transition process in hypersonic regimes. This study investigates the impact that wall-temperature variations have on the transition onset, by means of surface strips with different wall temperature, mimicking the use of cooling/heating strategies in TPS. The influence of such patterns is first assessed on a clean geometry to isolate thermal effects, and subsequently in combination with localized roughness patches to capture the coupled role of surface irregularities. The results provide insight into transition mechanisms and potential means for passive control in hypersonic vehicle design. Following the approach of *Zhao et al.* [7], various wall-temperature patches are applied to a flat plate. The study considers uniformly cold and uniformly hot wall conditions as baselines to represent localized cooling and heating effects. In parallel, collaborators from the University of Queensland (UQ) [1] are preparing an experimental campaign to investigate the influence of wall-temperature strips on flow stability in a high-enthalpy wind tunnel.
The final aim of the study is to extent the work from *Chiapparino et al.* [2, 3], to include the effect of wall temperature distribution in the study of the Shock-Wave Boundary-Layer Interaction (SWBLI) and perform Linear Stability Theory (LST) simulations as in Ref. [5, 6]. Finally, the use of chemical and thermal non-equilibrium models is going to be included in the stability analysis, as in [4], to assess the impact of non-equilibrium condition of the flow.

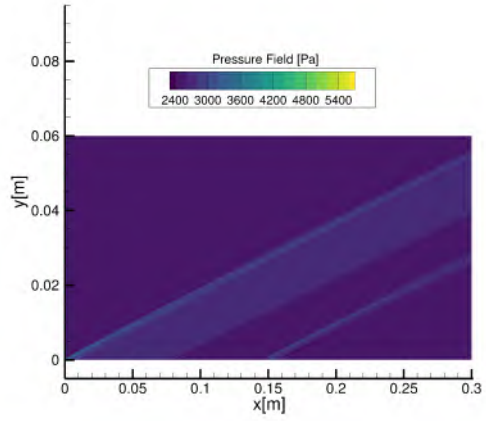

Figure 1: Pressure contour with heated strip

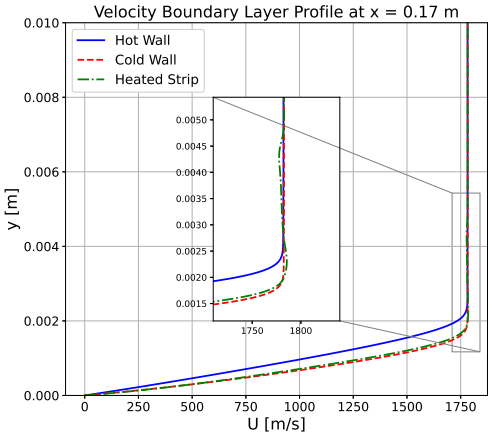

Figure 2: Velocity Boundary-Layer Profile comparison at $x = 0.17m$

Simulation Setup

In this study, Direct Numerical Simulations (DNS) are performed using the Navier-Stokes Multi-Block (NSMB) code. The current state of the project is obtaining a laminar two-dimensional high-resolution flow, at Mach 6, with wall temperature distributions, that is going to be analyzed using the LST. The DNS are solved using a 4^{th} order skew-symmetric central scheme in order to properly resolve the shocks present in the flow field.
Figure 1 shows the pressure contour in the domain where a high-temperature strip is present in $[x_{min}, x_{max}] = [0.15m, 0.16m]$: the constant T_w is $300K$ while the heated strip is at $700K$. The zero-order effect of the heating patch is underlined by the presence of a compression wave first followed by a set of expansion waves, as reported by [7].
Figure 2 reports the velocity boundary-layer profile at $x = 0.17m$, i.e. after the heating patch, of the uniformly-cold ($T_w = 300K$), uniformly-hot ($T_w = 700K$) and the cold-wall with heated strip.

Acknowledgments

The authors gratefully acknowledge the International Graduate School of Science and Engineering (IGSSE) for funding this project, as well as the Leibniz Supercomputing Center for providing the computational capabilities. The authors would also like to thank their project partners at University of Queensland (UQ) for the exchange of insight.

References

[1] R. Ananthapadmanaban, A. Veeraragavan, T. McIntyre, V. Wheatley, and D. Mee. Measurements of free stream density fluctuations in the t4 stalker tube. In *25th AIAA International Space Planes and Hypersonic Systems and Technologies Conference*, 2023.

[2] G. Chiapparino and C. Stemmer. Dns of a hypersonic flow on a ramp geometry with isolated roughness. In *2nd International Conference on Flight Vehicles, Aerothermodynamics and Reentry Missions Engineering (FAR)*, 2022.

[3] G. Chiapparino and C. Stemmer. Numerical investigation of a mach 6 laminar shock-wave/boundary-layer interaction on a two-dimensional ramp with 3d controlled surface roughness. *International Journal of Heat and Fluid Flow*, 103:109193, 2023.

[4] M. Hudson, N. Chokani, and G. Candler. *Linear stability of hypersonic flow in thermochemical nonequilibrium.* PhD thesis, Graduate Faculty of North Carolina State University, 1996.

[5] F. Oz, T. E. Goebel, J. S. Jewell, and K. Kara. Local wall cooling effects on hypersonic boundary-layer stability. *Journal of Spacecraft and Rockets*, 60(2):412–426, 2023.

[6] F. Oz and K. Kara. Hypersonic boundary-layer stability with local cooling and local metasurface treatment. In *AIAA SCITECH 2023 Forum*, 2023.

[7] R. Zhao, C. Wen, X. Tian, T. Long, and W. Yuan. Numerical simulation of local wall heating and cooling effect on the stability of a hypersonic boundary layer. *International Journal of Heat and Mass Transfer*, pages 986–998, 01 2018.

Mitteilung

Fachgruppe: Hyperschallaerothermodynamik

Electron density measurement in a high-enthalpy shock tunnel at Mach 10

N. COURVALIN*, F. DENIS, C. REY, B. SAUERWEIN,
M. BASTIDE, R. KEMPF, A. RUNSER

ISL, 5 rue du Général Cassagnou, BP 70034,
68301 SAINT-LOUIS Cedex, France

**nicolas.courvalin@isl.eu*

Characterization of plama in hypersonic flow is essential because it interacts with radio waves and radar signals. This study aims to experimentally measure and then to simulate the ionisation around hypersonic bodies. The plasma model will be used to better understand the variation in projectile radar signatures caused by the hypersonic flow. The first part of this project is to develop a measuring instrument for the characterization of the electron density in the ISL high-enthalpy shock tunnel.

In hypersonic flow, behind the bow shock, the kinetic energy of the gas is converted into internal energy. This energy is described by different temperatures. The first is the translational temperature, which measures the translational velocity of the molecules and atoms relative to each other. The second is the rotational temperature which measures the rotational energy of the molecules. The third is the vibrational temperature which represents how much the molecules will vibrate. If the energy exceeds a certain value, the molecules will dissociate. If the collisions between molecules and/or atoms are strong enough, their electrons will receive enough energy to escape. The flow becomes an ionized flow. It is this ionization that will be of interest to us in our study. We will determine the amount of free electrons as well as the electron temperature, which represents the kinetic energy of the electrons.

First, a copper Langmuir probe is developed [1]-[3] in order to measure the electron density (Fig. 1). It is used to compute the electron density, the electron temperature and the plasma potential by measuring simultaneouly the current and voltage in the probe (Fig. 2). Knowing that the plasma is composed of charged particles, the electrons and ions are attracted or repelled depending on the voltage imposed on the probe. Thus, by measuring the current and voltage of the probe we can deduce the quantity of captured electrons, their temperature and the plasma potential. By calculating the slope of the curve in zone A, the ionic current is determined and subtracted from the measured current in order to determine the electronic current. By calculating the slope of the curve in zone B the electron temperature is computed. By calculating the intersection of the tangent of zone B with that of zone C, the plasma potential and the electron saturation current are determined. Using these electron temperature, the electron saturation current and the probe surface, the electron density can be computed considering a Maxwellian’s distribution for the electron velocity.

A plasma characterization around a sphere of 15 cm in diameter is performed at Mach 10 at an equivalente altitude of 40 km. Several probe architectures are tested in order to determine the materials, lengths and diameters of the wires to be used. Measurement issues were identified. For example, the probe insulation and/or the probe itself may ablate or even melt. Another example is that a calibration step was inaccurate. Solutions to these issues were identified. In the futur, Teflon insulation and tungsten wire will be used in order to resolve these issues of ablation and melting. Futhermore a new calibration procedure has been defined. Measurement uncertainties are also determined. The length and diameter measurements of the wires were taken using a digital microscope and Photron FASTCAM Viewer 4 software. An error of ten pixels equivalent to 8 µm is estimated occurs during measurement. These

measurements were confirmed by measurements taken with a micrometer and a digital caliper. The uncertainty in the electron temperature and electron saturation current is determined by calculating the slopes, taking into account more or fewer measurement points in the areas of interest. Another part of the uncertainty in the electron saturation current comes from the calibration and accuracy of the measuring instrument.

Only part of the data has been analysed yet. However, an electron density of $(1.2 \pm 0.6) \cdot 10^{17}$ m^{-3} is measured. Langmuir probe measurement is an intrusive technique as it can disrupt the flow. In the videos, we can see that the probe radiates the thermal energy it has received from the flow, and we can also see a trail coming from the probe and the grounds, which could be caused by ablation of the probe. However, these phenomena only appear after the measurement range, so they do not influence the measurement results. More detailed analyses must be carried out to determine the influence of the probe on the flow in order to ascertain whether the measurement is representative. The first analysis to be carried out will be to check the influence of the length and diameter of the probe and grounds wires. The second analysis will consist of taking measurements with a surface Langmuir probe. A surface probe will therefore be developed. CFD simulations will then be performed to simulate the electron density and the flow. Finally, the last analysis will be the development of a spectroscopic measurement technique in order to compare it with the results from the Langmuir probe. This measurement technique is non-intrusive.

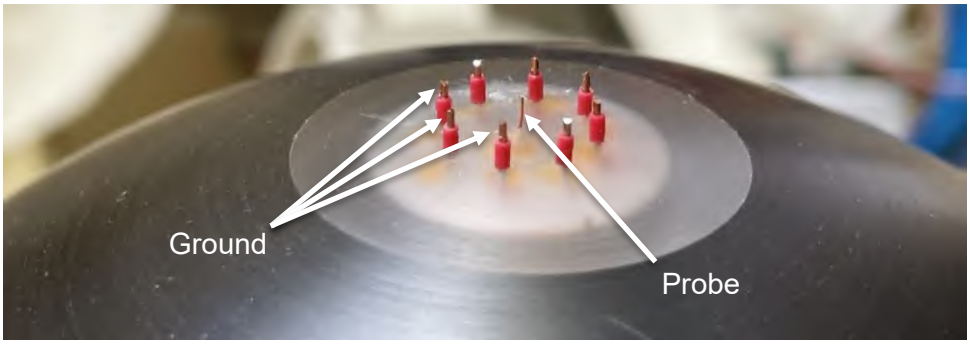

Fig. 1: Model with the Langmuir probe mounted on the stagnation point

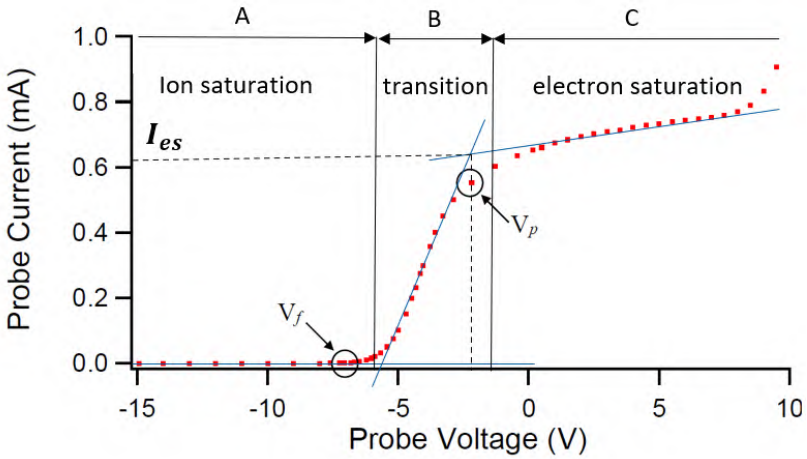

Fig. 2: A representative Langmuir probe trace with different regions of interest indicated [3]

References :
[1] F. F. Chen, Lecture Notes on Langmuir Probe Diagnostics, University of California, 2003
[2] H. M. Mott-Smith and I. Langmuir, The theory of collectors in gaseous discharges, Physical review 28.4, Research Laboratory General Electric Company Schenectady New York, 1926
[3] J. Williams, A simple, inexpensive Langmuir Probe Experiment, Wittenberg University, 2014

Mitteilung

Fachgruppe: Hyperschallaerothermodynamic

Flow Field Analysis of a Blended-Wing-Body Re-entry Vehicle in Different Speed Regimes

Spartaco Massimo Giannino*, Chiara Amato†, Tim Horchler†, Tobias Ecker†

*Università degli Studi della Campania, Luigi Vanvitelli, †German Aerospace Center (DLR)

spartacomassimo.giannino@unicampania.it, Chiara.Amato@dlr.de, Tim.Horcler@dlr.de, Tobias.Ecker@dlr.de

The need to perform effective space operations in Low Earth Orbit (LEO), including support and servicing missions for the International Space Station (ISS), has led to a growing demand for aerodynamic configurations that offer good performance throughout the entire atmospheric re-entry phase. In this framework, the research work addressed the design of a reusable Blended Wing Body (BWB) configuration capable of withstanding the extreme conditions faced during re-entry and landing as a glider on a conventional runway. For this purpose, a Multidisciplinary Design Optimization (MDO) procedure was employed, accounting for constraints on maximum normal load factor, heatshield allowable temperature, dynamic pressure, landing velocity, *etc.* Additionally, the minimization of mass was considered as the objective function. The multidisciplinary analyses were performed using Low-Order Fidelity (LOF) methods, with the ultimate aim of validating the results through high-fidelity Computational Fluid Dynamics (CFD) simulations. The CFD simulations presented in this work were conducted under both subsonic and hypersonic flow regimes for the configuration NM0, one of the six optimized aeroshapes obtained from the MDO procedure [1].

For the subsonic case, the flow field numerical results were obtained by solving the incompressible three-dimensional Reynolds Averaged Navier Stokes (RANS) equations. The coupled pressure-based solver available in ANSYS Fluent was employed, and the closure of the RANS equations was achieved using the Shear-Stress Transport (SST) k - ω model. The numerical results (Figure 1) refer to the configuration at sea level altitude (in symmetric flight condition) and at a freestream velocity of 30 m/s, reproducing the Mach (M_∞=0.09) and Reynolds number (Re_∞=1.2e6) of the experimental test conducted in the 4 ft X 3 ft low-speed Wind Tunnel (WT) at the University of Sydney [2]. As can be observed, the configuration is statically stable with a trimmed Angle of Attack (AoA) close to 15°, where the linear trend of the lift coefficient (C_L) is no longer preserved and an increase in the slope of the C_L curve (typical of the vortex lift phenomenon) is noticeable. This is precisely the effect the authors aim to achieve: leveraging the enhanced lift resulting from the vortex flow development to improve the landing capability of the aircraft.

The hypersonic CFD (RANS) simulations were conducted using the DLR TAU-Code. A fully turbulent flow was simulated accounting for thermochemical nonequilibrium effects, employing the Spalart-Allmaras in negative form (SA-neg) as the turbulence model. Air was modeled as a five-species mixture consisting of nitrogen (N_2), oxygen (O_2), atomic nitrogen (N), atomic oxygen (O), and nitric oxide (NO), with chemical reactions described according to the model of Gupta et al. [3]. The numerical simulations were performed at six distinct points along the configuration's re-entry trajectory, spaced at 5 km intervals over an altitude range of 40 km-65 km. The optimization procedure used to determine the trajectory is described in the work of Aprovitola et al. [4]. For the sake of brevity, only the results corresponding to an altitude of 50 km (M_∞=13.4, Re_∞=2.5e6, AoA=16.6°), where the maximum heat flux is expected, are presented in this work. In particular, Figure 2 (left side) shows the streamline and the shock wave forming in the vicinity of the aircraft, while Figure 2 (right side) illustrates the heat flux distribution at the vehicle midsection. As expected, the maximum heat flux occurs at the nose of the configuration (stagnation point) with a peak value of approximately 340 kW/m^2, consistent with the heat-flux constraint of 600 kW/m^2 imposed in the trajectory optimization procedure.

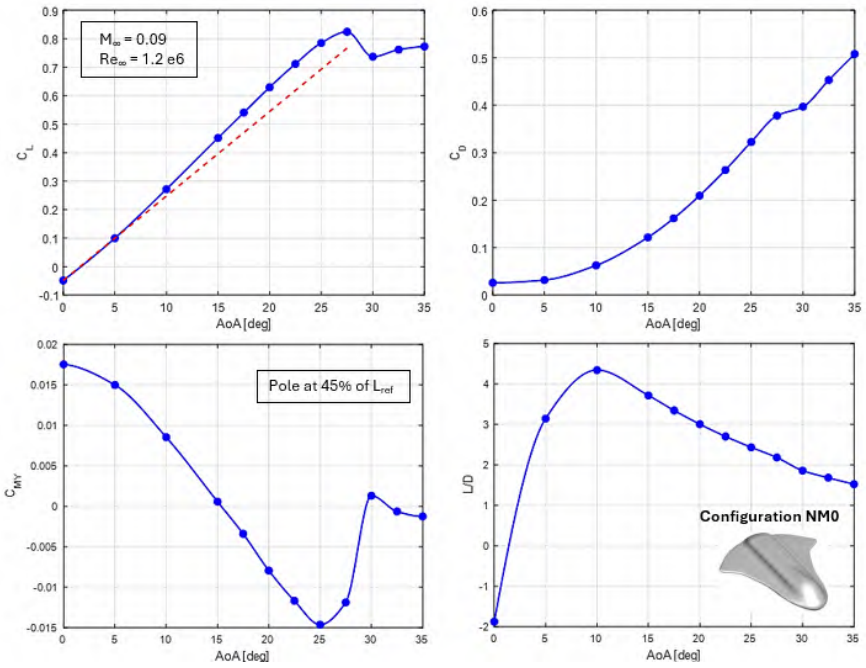

Figure 1: Lift,drag,pitching moment coefficient and lift-to-drag ratio.

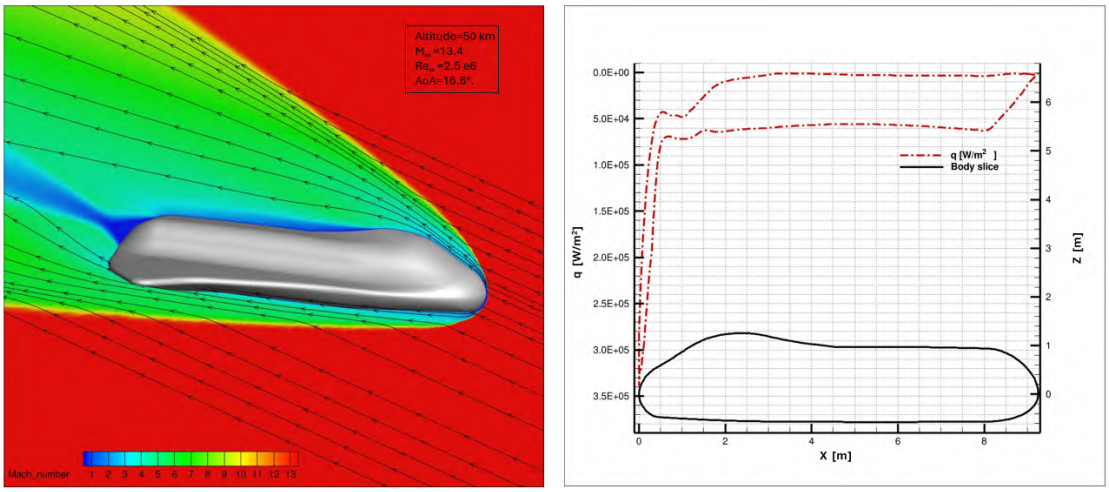

Figure 2: Mach and streamline (left side) - Heat flux distribution (right side).

References

[1] Montella, N., Iuspa, L., Vio, G. A., Aprovitola, A., Pezzella, G., and Viviani, A., "Aeroshape design and low speed aerodynamic analysis of a crew return vehicle," *Aerospace Science and Technology*, Vol. 158, 2025, pp. 109876.

[2] Montella, N., Vio, G., Iuspa, L., Aprovitola, A., Pezzella, G., and Viviani, A., "Wind Tunnel Analysis of a Space Re-Entry Vehicle at Low-Speed Conditions," *34th Congress of the International Council of the Aeronautical Sciences*, 2024.

[3] Gupta, R. N., Yos, J. M., Thompson, R. A., and Lee, K.-P., "A review of reaction rates and thermodynamic and transport properties for an 11-species air model for chemical and thermal nonequilibrium calculations to 30000 K," 1990.

[4] Aprovitola, A., Montella, N., Iuspa, L., Pezzella, G., and Viviani, A., "An optimal heat-flux targeting procedure for LEO re-entry of reusable vehicles," *Aerospace Science and Technology*, Vol. 112, 2021, pp. 106608.

Mitteilung

Fachgruppe: **Multidisziplinäre Optimierung**

Aeroshape optimization of a UAV configuration for Mars exploration

Gennaro Barbato*, Chiara Amato†, Tim Horchler†, Tobias Ecker†

*Università degli Studi della Campania, Luigi Vanvitelli

†German Aerospace Center (DLR)

gennaro.barbato@unicampania.it, Chiara.Amato@dlr.de, Tim.Horchler@dlr.de, Tobias.Ecker@dlr.de

During the last five decades, international space agencies have significantly increased their operations on Mars. Planetary exploration has advanced through various methods, including orbiters, flyby spacecraft, landers, and rovers. Unmanned Aerial Vehicles (UAVs) have also made remarkable progress, becoming increasingly attractive for planetary exploration, as they can bridge the gap between high-resolution local data (from landers and rovers) and regional-scale observations (from orbiters and flyby spacecraft) [1, 2]. This research proposal is framed within this context, focusing on the conceptual design of a non-conventional **eVTOL** (electric Vertical Take-Off and Landing) system.

The proposed concept is a propeller-driven Blended Wing Body (**BWB**) powered by solar panels and batteries (Figure 1a). A coaxial rotor is integrated into the central body-covered during the cruise phase-enabling vertical take-off and hovering capabilities [3]. This configuration aims to combine the advantages of both rotary- and fixed-wing platforms: rotorcraft can perform multiple flights but are limited in range (e.g., Ingenuity has a maximum range of approximately 1 km), whereas fixed-wing aircraft can cover significantly longer distances (on the order of 100 km) but are generally restricted to a single flight, as suitable horizontal take-off and landing areas cannot be guaranteed on the Martian surface.

The research objective is to develop a Multidisciplinary Design Optimization (**MDO**) procedure for determining the optimal UAV aeroshape. The procedure is implemented within a wrapped environment (ANSYS APDL) that enables batch execution of the CAD modelling tool (OpenVSP) and the low-fidelity aerodynamic solver (VSPAERO). The optimization algorithm is based on the Subproblem Approximation Method (SAM), aiming to maximize aerodynamic efficiency while ensuring static longitudinal stability and trimmability under the nominal cruise regime ($M = 0.2$, $Re = 97{,}000$). In addition, a planform-based constraint is applied to ensure that the configuration's gross mass does not exceed 26 kg. The aeroshape is parameterized through 13 design variables: nine for the planform, two for the winglets, and two for the body and wing twist. The ranges of the design variables are defined such that the configuration with folded wings can fit inside a Viking-like aeroshell (4 m in diameter). The configuration integrates three custom airfoils for the body, fillet, and wing sections, while a four-digit NACA airfoil is employed for the winglets. The resulting optimized CAD model is shown in Figure 1b.

In the optimization procedure, aerodynamic performance is evaluated using a Panel Method (**PM**) with an uncoupled viscous correction [4]. Computational Fluid Dynamics (CFD) analyses provide off-loop validation of both efficiency and stability requirements. Specifically, the DLR-TAU Code is used to perform fully turbulent Reynolds-Averaged Navier-Stokes (**RANS**) simulations, employing both the Spalart-Allmaras (SA) and the k-ω Shear Stress Transport (SST) turbulence models. As illustrated in Figure 2, the efficiency trend predicted by the low-fidelity PM tool aligns well with the RANS simulations. The predicted maximum efficiency, corresponding to the optimization objective function, is approximately 5% higher than the RANS values. The pitching moment, computed at 48% of the centerline chord, indicates that the proposed configuration is longitudinally stable, with
a trim Angle of Attack (AoA) of approximately 6°.

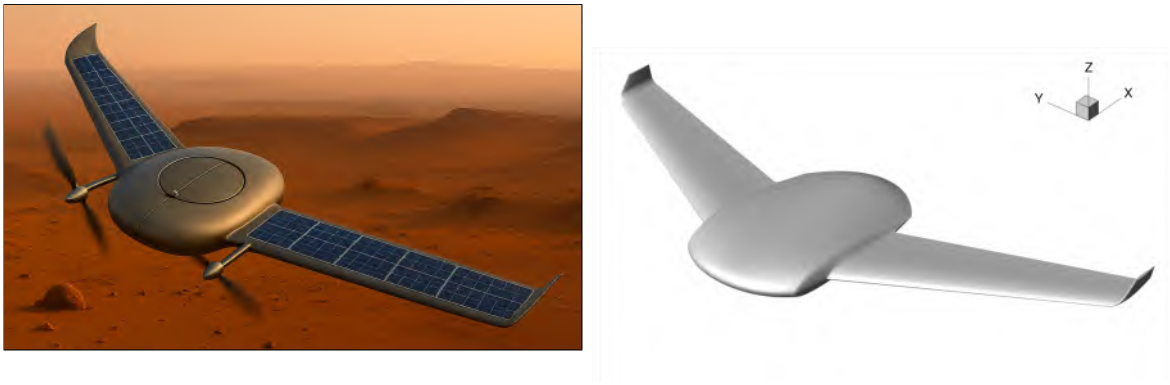

(a) Conceptual view (b) CAD model

Figure 1: Optimized UAV aeroshape in cruise closed configuration

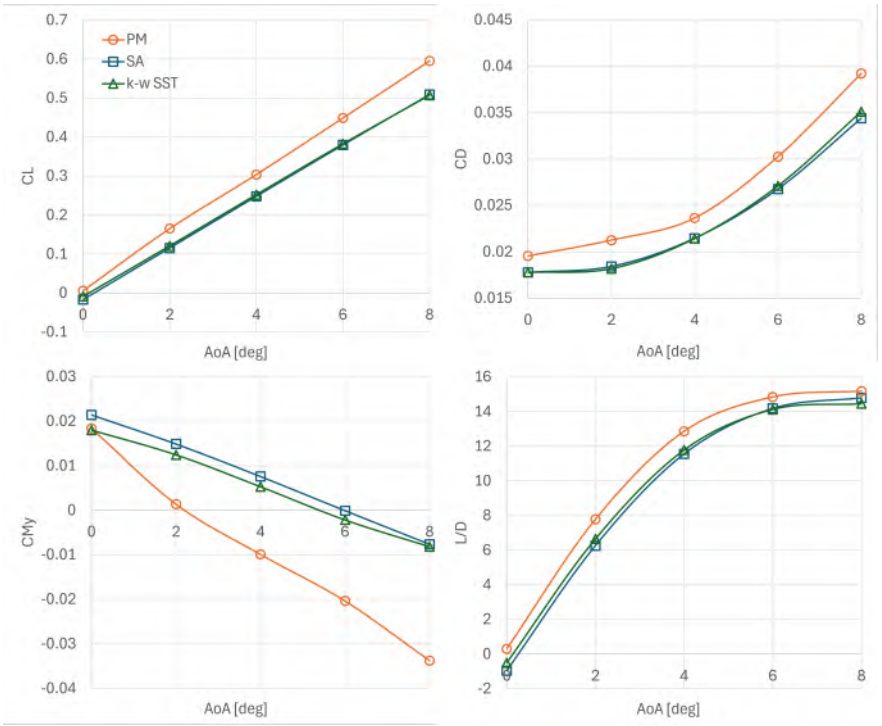

Figure 2: Lift, drag, pitching moment coefficients and lift-to-drag ratio comparing PM, RANS SA, and RANS k-ω SST (M = 0.2, Re = 97,000)

References

[1] Aprovitola, A., Iuspa, L., Pezzella, G., and Viviani, A., "Aerodynamic optimization of airfoils shape for atmospheric flight on Mars planet," *Acta Astronautica*, Vol. 212, 2023, pp. 580–594.

[2] Barbato, G., Pezzella, G., Viviani, A., et al., "Phase-A design of a Mars exploration aerial vehicle," *75th International Astronautical Congress (IAC-2024)*, 2024.

[3] Collins, N. S., *System design and nonlinear state-dependent riccati equation control of an autonomous Y-4 tilt-rotor aerobot for martian exploration*, University of Surrey (United Kingdom), 2016.

[4] Aprovitola, A., Iuspa, L., Pezzella, G., and Viviani, A., "Optimization procedure for wings flying in the Martian atmosphere," *Acta Astronautica*, 2025.

Mitteilung

Fachgruppe: Multidisziplinäre Optimierung

Variational Flow-State Estimation and Sensor Placement Optimization from Discrete Measurements

Mathias Lemke
Institute of Fluid Dynamics and Technical Acoustics (ISTA), TU Berlin
Müller-Breslau-Str. 8, 10623 Berlin, Germany
mathias.lemke@tu-berlin.de

Vincenzo Citro
Department of Industrial Engineering, University of Salerno
Via Giovanni Paolo II, 132, 84084 Fisciano (SA), Italy
vcitro@unisa.it

We present a variational data assimilation framework designed to reconstruct complete flow fields from a limited set of discrete point measurements. The approach combines the compressible Navier–Stokes equations with a continuous adjoint formulation and includes a systematic optimization of sensor locations. As a reference case we investigate the wake of a circular cylinder in the subcritical regime at Mach number 0.28. The results demonstrate that a surprisingly small number of velocity probes is sufficient to achieve accurate reconstructions of the unsteady wake dynamics, provided that the sensors are placed in regions of high sensitivity or along directions of strong observability. Sensor placement guided by adjoint-based sensitivities and empirical observability Gramians leads to a improvement in robustness, numerical conditioning, and convergence speed.

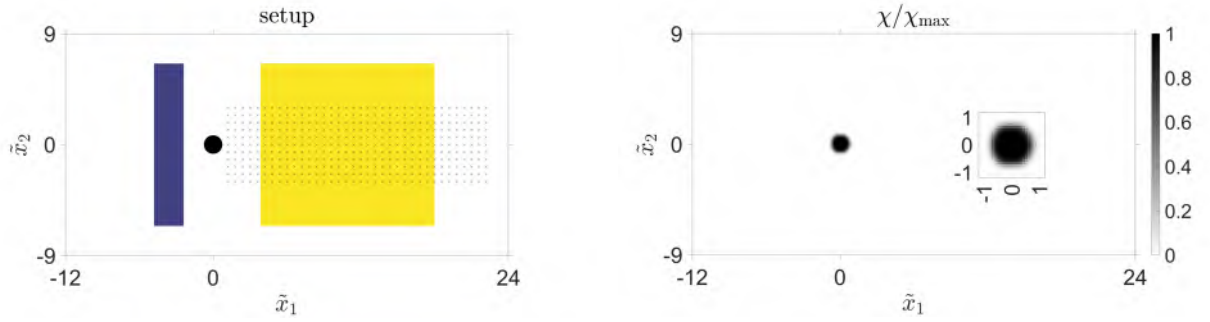

(Left) Numerical setup with a circular cylinder; the dark area on the left marks the actuation region, the yellow area on the right the measurement region for the continuous case. Black dots indicate candidate discrete sensor positions. (Right) Cylinder modeled with the immersed boundary method using a Darcy approach; the inset shows the smooth mask transition.

The methodology builds on a compressible solver with volume penalization to represent solid boundaries. A localized momentum source term acts as the assimilation forcing, distributed over an action region chosen to avoid direct overlap with sensors. The cost functional measures the misfit between simulated and measured data, localized through a (spatial) sensor mask. By integrating the adjoint system backward in time, gradients with respect to the forcing are obtained and used in an iterative optimization loop. Discretization employs high-order finite differences and explicit Runge–Kutta time integration with non-reflecting boundary

conditions. Smooth transitions in the penalization field guarantee numerical stability and suppress spurious oscillations.

Beyond direct sensitivity maps, we evaluate sensor configurations using an empirical observability Gramian constructed from adjoint impulse responses. A singular value decomposition of the resulting snapshot matrix highlights observable directions in the system state space and helps identify sensor sets that provide complementary information rather than redundant coverage. This combination of local sensitivity maxima with Gramian-based global measures ensures that the chosen sensors resolve both the dominant instability mechanisms and the long-range wake dynamics.

The cylinder wake study confirms the effectiveness of this strategy. In the uncontrolled simulation, the mean streamwise velocity is underpredicted and vortex shedding exhibits a phase shift compared with the target data. Introducing variational assimilation corrects both issues: the mean flow recovers the correct velocity deficit, and the vortex phase is locked to the reference. The cost function decreases by more than 60 % within about 150 iterations, while the assimilation forcing rapidly decays after the initial transients. When relying on discrete probes, reconstructions with as few as six sensors capture the amplitude, frequency, and phase of vortex shedding. Twelve sensors further enhance robustness against model uncertainties and noise, though the marginal gain in near-wake accuracy is limited, indicating that the essential flow dynamics are already well observed with fewer probes.

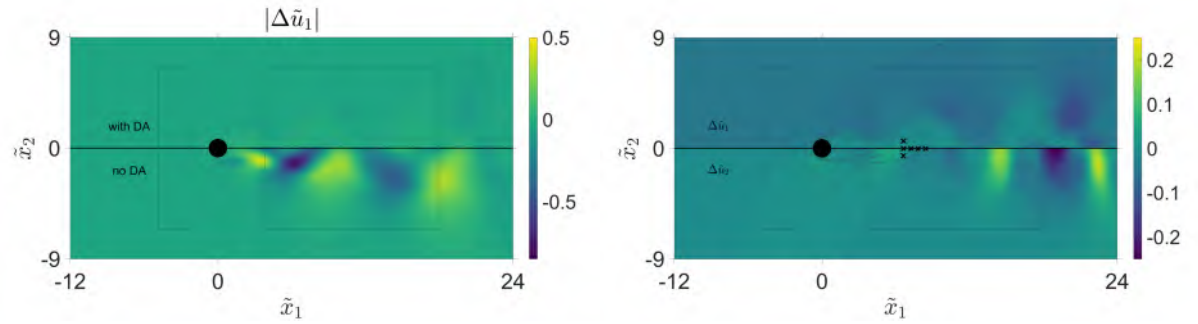

(Left) Velocity difference in u_1 with (top) and without (bottom) adjusted forcing. (Right) Velocity magnitude in u_1 and u_2 from data assimilation with six sensors, each normalized by the inflow velocity.

Overall, the study highlights three findings: First, variational assimilation with localized momentum forcing can reconstruct unsteady cylinder wakes from sparse data. Second, the combination of adjoint sensitivities and Gramian-based analysis provides a principled strategy for placing sensors in a way that balances accuracy, robustness, and efficiency. Third, the proposed framework is modular and adaptable, allowing different measurement types or geometries to be incorporated with minimal modification. The contribution will focus on methodological details of the adjoint formulation, on a comparison of sensor placement strategies, on quantitative error analyses for the cylinder wake, and on an outlook toward more complex geometries and flow regimes, such as bluff bodies with separation control or multibody configurations.

Mitteilung

Fachgruppe: Multidisziplinäre Optimierung

Improvements on Robust High-Fidelity Dataset-Based Optimization for Aircraft Design

Markus Maier[1,2], Kaare Sørensen-Libik[2], Christian Breitsamter[1]

[1] **Technical University Munich**
Boltzmannstr. 15, 85748 Garching bei München
GERMANY
markus.v.maier@tum.de

[2] **Airbus Defence and Space GmbH**
Rechliner Str, 85077 Manching
GERMANY

Introduction

Automatic numerical optimization is playing an increasingly central role in the aircraft development for both the civil and military sectors.
Due to computational limitations, especially in aerodynamic simulations, current optimization approaches typically focus on a limited number of performance points within the flight envelope. Even though this multi-point approach reduces computational cost and enables reasonable industrial time scales, it can lead to flight envelope limitations or the discarding of the design since not all parts of the flight envelope are considered, thus eliminating the potential performance increases that may result from the optimization.
Recent developments in the efficient production of complete aerodynamic datasets [1], have however made more robust optimization processes feasible. In such a process, the entire flight envelope is taken into account during the optimization, ensuring that the resulting designs meet stability and control requirements, as well as giving a clear picture of the performance at all relevant points. In addition, by including the entire flight envelope in the analysis, a complete set of load conditions is produced, allowing for a structural analysis where no a-priori assumptions have to be made on which parts of the flight regime are driving the design. This reduces structural design risks significantly and enables robust coupled optimizations of aerodynamics and structures, also allowing for the influence of deformation effects on performance, stability and control to be included in the optimization.

Optimizations where only aerodynamic effects in the parameter variations are taken into account have often proven to be of reduced value due to the fundamental coupling of many parameters to several disciplines [2].
A typical example of such a parameter is the wing profile thickness, to which aerodynamic drag, structural weight and available fuel volume are strongly connected. If such fundamentally multi-disciplinary parameters are present in the optimizations, it is necessary to at least include low-order influences of all relevant aspects to ensure a relevant outcome. With time, the fidelity in the treatment of these different disciplines should be increased to improve the accuracy of the predictions, with the end result being a highly accurate Model Based Systems Engineering (MBSE) design environment.
Capable optimization tools will result in more accurate predictions and thus better products, as well as the reduction of required person-hours and thus the costs of the design process. The usage of highly accurate predictive numerical tools also reduces the risks in a project and resolves problems at early stages that would otherwise result in expensive corrections at later phases in the design.

State of the art

In previous work, the authors have demonstrated the feasibility of high-fidelity dataset-based optimization for aircraft design using a simplified yet physically meaningful test case – the Optimization Test Interceptor with ducted Fan (OTIFAN) [3]. The applied framework leverages existing capabilities for aerodynamic dataset generation and gradient-based multi-point optimization, enabling a robust high-fidelity treatment of the aerodynamic characteristics. Other disciplines are currently included at lower fidelity, reflecting a pragmatic multi-disciplinary approach.

Recent advancements

The computational costs involved in dataset-based optimizations are typically very high for a basic implementation of the toolchain where a fixed raster of polars is computed for each design baseline as well as the incremental geometries needed for the computation of sensitivities. Several approaches can significantly reduce the overall cost of the optimization process while still assuring a complete and accurate coverage of the flight envelope. Such approaches are related to evaluating the impact of envelope regions on the evolution of the design, taking the disciplines of performance, stability and control, loads and all other design drivers into account, and adapting the local resolution accordingly. This adaptation can be applied both on the dataset breakpoint level and on the mesh resolution for the computational fluid dynamics simulations. The resolution of the sensitivity datasets will be dependent on the particular design parameter considered and requiring a flexible dataset generation to minimize the overall cost of the process. Additionally, restart techniques are being investigated to further enhance efficiency. An illustration of the efficiency improvements under development within the optimization framework is given in *Figure 1* and will be presented as basis for discussion.

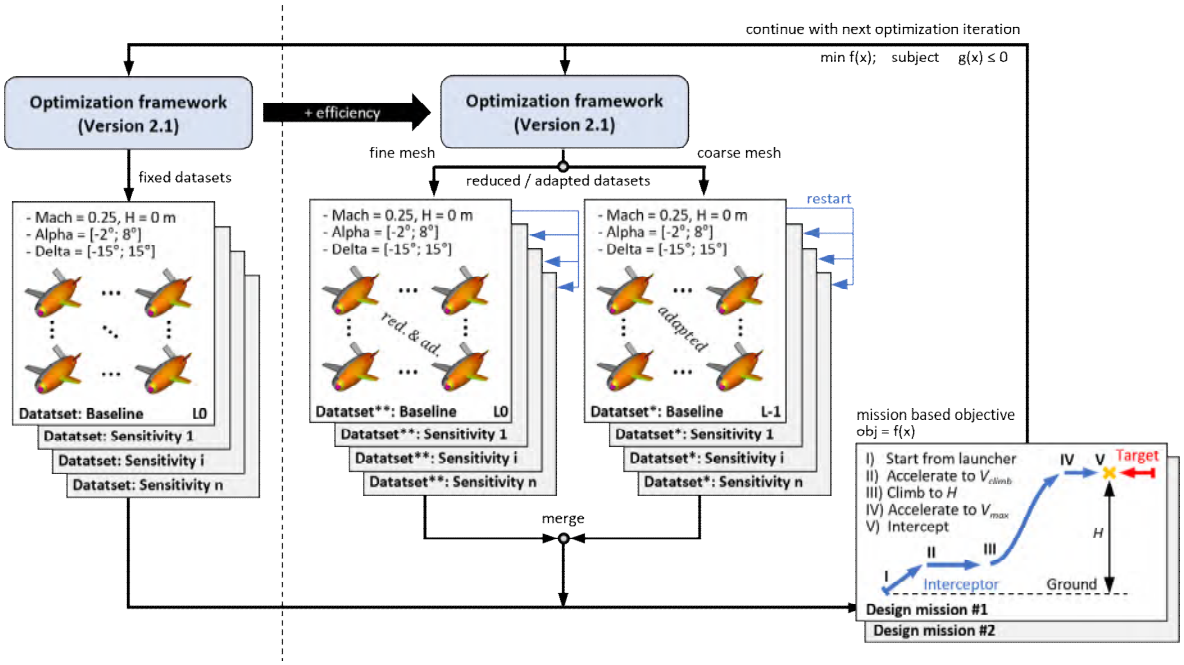

Figure 1: Efficiency improvement methods for high-fidelity dataset-based optimization

References

[1] Kaare Sørensen-Libik. Overview and Results of Subproject VitAMIn-ABC. In: Heinrich, R. (eds) Advanced Aircraft Understanding via the Virtual Aircraft Model. Notes on Numerical Fluid Mechanics and Multidisciplinary Design, vol 155. Springer, Cham. DOI: 10.1007/978-3-031-69425-7_7.

[2] Jun-xue Leng, Zhen-guo Wang, Wei Huang, Yang Shen, and Kai An. Multidisciplinary design optimization processes for efficiency improvement of aircraft: State-of-the-art review. International Journal of Aeronautical and Space Sciences 26, 2020–2042, Jul 2025.DOI: 10.1007/s42405-024-00811-8.

[3] Markus Maier, Kaare Sørensen-Libik, Christian Breitsamter (2025): Robust High-Fidelity Dataset-Based Shape Optimization for Aircraft Design. Deutscher Luft- und Raumfahrtkongress 2025, Augsburg, Deutsche Gesellschaft für Luft- und Raumfahrt - Lilienthal-Oberth e.V., Bonn, 2025. DOI: *pending*

Acknowledgements

The funding of the activities by Airbus Defence and Space GmbH (www.airbus.com) and the scientific guidance by the Chair of Aerodynamics and Fluid Mechanics at the Technical University of Munich (AER, www.epc.ed.tum.de/aer) is gratefully acknowledged. The authors want to thank the German Aerospace Center (DLR, www.dlr.de/en) for providing the computational fluid dynamics solver TAU, Airbus Defence and Space GmbH for providing the additional software as well as the Gauss Centre for Supercomputing e.V. (GCS, www.gauss-centre.eu) for funding this project by providing computing time on the Linux Cluster and the SuperMUC NG at Leibniz Supercomputing Center (LRZ, www.lrz.de).

Mitteilung

Fachgruppe: Multidisziplinäre Optimierung

An MDAO-Framework Approach enabling
Adjoint Sensitivity Analyses in Unsteady Multidisciplinary Problems

Florian Roß, Sebastian Gottfried, Arthur Stück
German Aerospace Center (DLR)
Institute of Software Methods for Product Virtualization
Nöthnitzer Straße 46b, 01187 Dresden
florian.ross@dlr.de, sebastian.gottfried@dlr.de, arthur.stueck@dlr.de

The adjoint method is a key ingredient to efficiently compute sensitivity derivatives for gradient-based optimization in conjunction with large-scale multidisciplinary problems. For steady-state multidisciplinary problems, MDAO frameworks like OpenMDAO [1] automate the processing of coupled adjoints to a large extent. RKOpenMDAO [2] was developed to bridge the gap towards unsteady problems, enabling the baseline version of OpenMDAO for higher-order time-stepping via diagonally-implicit Runge-Kutta (DIRK) schemes. The time integration is driven by RKOpenMDAO, which delegates the repeated processing of time stages to a single instance of the baseline framework OpenMDAO. The baseline framework remains agnostic to the time integration process; RKOpenMDAO, in turn, is currently being prepared to also support other steady-state MDAO frameworks beyond OpenMDAO, e.g. GEMSEO. The steady-state capabilities of the baseline MDAO frameworks are systematically carried over to the unsteady domain. The DIRK time integration in RKOpenMDAO is fully differentiated in forward and reverse mode, allowing the computation of unsteady sensitivities, provided the involved disciplinary adjoint operators are available for the involved implicit or explicit components.

The adjoint framework capabilities for unsteady problems are demonstrated for a CFD example integrating the algorithmically differentiated CFD software CODA, which is being developed as part of a collaboration between the French Aerospace Lab ONERA, the German Aerospace Center (DLR), Airbus, and their European research partners [4]. With $R(W)$ representing the steady-state residual contributions, the semi-discrete equation system governing the flow state W is extended by a momentum source term $Q(t)$. The latter was introduced to control the flow in an unsteady, target-oriented way:

$$\frac{\partial}{\partial t} W + R(W) + Q = 0 \,.$$

A functional in the form of drag C_D integrated over time was considered for the optimal control problem:

$$J = \int_0^T C_D(W(t))\, dt \,.$$

The framework extension RKOpenMDAO was used to integrate these equations in time. The equation system solved each stage of the Runge-Kutta scheme reads

$$\begin{aligned} \frac{W_n^i - W_n - \Delta t\, s_i^W}{\Delta t\, a_{ii}} + R\left(W_n^i\right) &= 0 \,, \\ k_i^W - \frac{W_n^i - W_n - \Delta t\, s_i^W}{\Delta t\, a_{ii}} &= 0 \,, \\ k_i^J - C_D\left(W_n^i\right) &= 0 \,, \end{aligned}$$

where W_n^i and W_n represent the flow state during the stage and at the start of the time step, k_i^W and k_i^J are the updates of W and J respectively, s_i^W is an accumulation of previous stage updates consistent with the used Butcher tableau, Δt represents the used step size and a_{ii} is

a parameter defined in the Butcher tableau of the considered DIRK scheme. The framework solves these equations to proceed in the time integration, and uses linearized versions to compute and verify the sensitivities $\frac{dJ}{dQ}dQ$ (forward) and $\left(\frac{dJ}{dQ}\right)^T \bar{J}$ (reverse), respectively. The unsteady functional derivatives computed in reverse were successfully verified against finite differences for the CRM/DPW-5 configuration in fully turbulent flow, cf. Figure 1. The computation of forward-mode sentitivities is straight-forward, as it can be done in tandem with the primal time integration. The reverse-mode sensitivity analysis is more involved, since the time trajectory has to be traversed in reverse. Pure recomputation (restoring) of intermediate stage quickly becomes prohibitive in runtime (memory). By means of checkpointing, runtime can be traded for memory. An optimum achieving the least number of recomputations given a fixed number of checkpoints is the binomial checkpointing algorithm REVOLVE [5]. Efficiency aspects of the unsteady framework approach will be discussed in the presentation together with an outlook to unsteady sensitivity analyses for multidisciplinary problems.

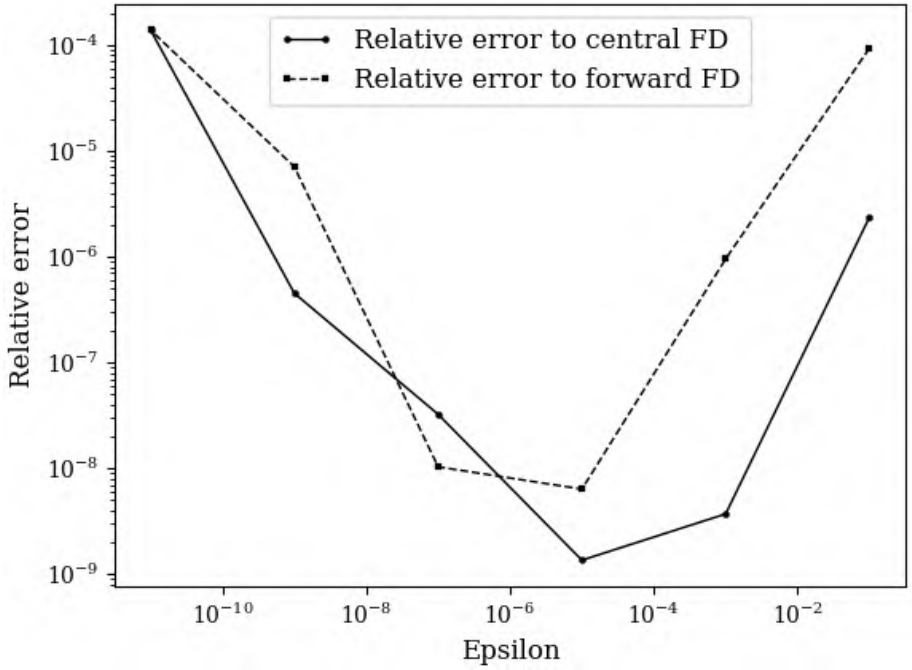

Figure 1: Comparison of reverse-mode derivatives against finite-differences for the DPW-5/CRM wing-body configuration [6].

[1] J. Gray, J. Hwang, J. Martins, K. Moore, and B. Naylor. OpenMDAO: An Open-Source Framework for Multidisciplinary Design, Analysis, and Optimization. *Structural and Multidisciplinary Optimization*, 04/2019. doi:10.1007/s00158-019-02211-z.

[2] F. Roß, A. Büchner, S. Gottfried, and A. Stück. A High-Fidelity Framework Approach Enabling High-Order Implicit Time Stepping for MDAO. *9th European Congress on Computational Methods in Applied Sciences and Engineering*, 2024. doi:10.23967/eccomas.2024.196.

[3] Gallard, F., Vanaret, C., Guénot, D, *et al.*, GEMS: A Python Library for Automation of Multidisciplinary Design Optimization Process Generation. *2018 AIAA/ASCE/AHS/ASC Structures, Structural Dynamics, and Materials Conference*. 2018. p. 0657.

[4] T. Leicht, D. Vollmer, J. Jägersküpper, A. Schwöppe, R. Hartmann, J. Fiedler, and T. Schlauch. DLR-Project Digital-X: Next Generation CFD Solver ’flucs’. DLRK 01/2016

[5] A. Griewank and A. Walther. Algorithm 799: revolve: An Implementation of Checkpointing for the Reverse or Adjoint Mode of Computational Differentiation. *ACM Trans. Math. Softw.*, 26(1):19–45, 03/2000. doi:10.1145/347837.347846.

[6] NASA. Common Research Model. http://commonresearchmodel.larc.nasa.gov/, 2012.

Mitteilung

Fachgruppe: Numerische Aerodynamik

A High-Order Galerkin-Type 3D Panel Method – Current Status and Perspective

Karsten Bock
German Aerospace Center (DLR)
Institute of Software Methods for Product Virtualization (SP)
Helmholtzstraße 10, 01069 Dresden
karsten.bock@dlr.de

Introduction

Particularly in preliminary aircraft design and early optimization phases, which require vast numbers of aerodynamic simulations, quick turnaround times are mandatory. Although, high-fidelity CFD methods are readily available, computational costs are often prohibitive and limit the evaluation of the design space, e.g. in the context of massive dynamic load analyses and multidisciplinary design. Commonly, low-fidelity potential flow methods like the vortex-lattice (VLM) or doublet-lattice method (DLM), which omit the thickness of the bodies in the flow, are employed when fast evaluation is key. Panel methods include the thickness of the body and, hence, can capture three-dimensional effects that VLM and DLM neglect. The present work presents the design and development status of an innovative 3D *Galerkin*-type panel method of higher order, which puts special emphasis on modern numerical and software design. Additionally, results produced with a work-in-progress version of the code are presented.

Description of the Panel Method

A panel method solves the boundary integral equation, which can be derived from the *Laplace* equation by distributing source and doublet singularities, i.e. fundamental solutions of the *Laplace* equation, on the body which is submerged in the flow. The implemented panel method represents the surface geometry using linear shape panels, currently supporting triangular and quadrangular elements. The code supports low-order, i.e. element-wise constant, singularity distributions and also high-order ones. A well-known disadvantage of low-order panel methods are spurious vortex velocities caused by jumps in doublet strength at the panel boundaries cause. In subsonic cases this merely affects the local fulfilment of

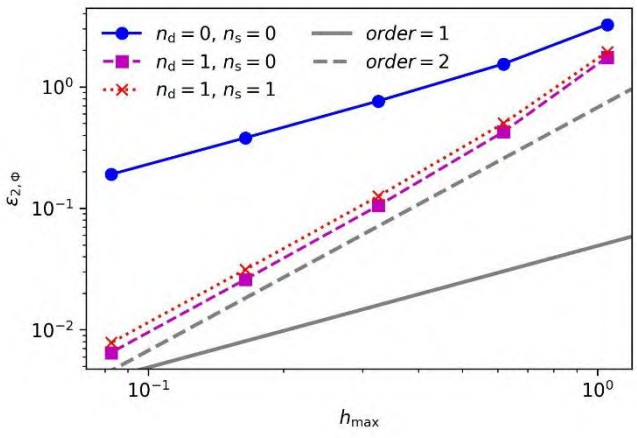

Figure 1: Convergence of the L_2-error the of surface potential $\varepsilon_{2,\Phi}$ with respect to the maximum mesh spacing $h_{\max}$ for the unit sphere.

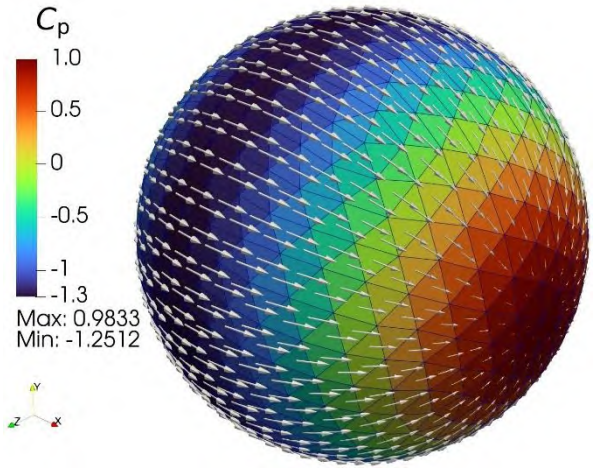

Figure 2: Surface pressure coefficient and velocity vectors for a sphere with quasi-equidistant spacing $h \approx 0.325$.

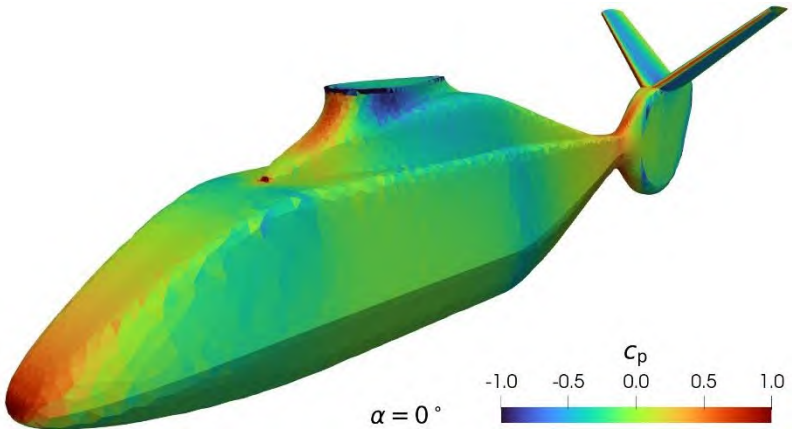

Figure 3: Surface pressure coefficient for level flight. Underlying mesh of the "Fast Rescue" fuselage and tail courtesy of DLR-AS-HEL [3]

boundary conditions [1]. For supersonic flows however, the problem is "frequently serious enough to produce a totally incorrect solution for the flow" [2]. In contrast, smooth higher-order panel methods achieve continuous doublet distributions.
Numerically, the presented method is of the *Morino* type and utilizes a *Dirichlet* boundary condition. Hence, the equation system is directly built and solved for scalar potentials, where more traditional panel method implementations often resort to *Neuman*n boundary conditions and solve systems for velocities. The boundary condition is enforced in a weighted residual sense choosing the basis functions as test functions, hence yielding a *Galerkin* method. It is worth noting, that *Galerkin* and collocation methods yield equivalent equation systems for element-wise constant singularity distributions, when the *Galerkin* method is applied with one quadrature point in the numerical integration. However, *Galerkin*-type panel methods allow for the solution of higher-order distributions, where more traditional collocation methods are usually restricted to element-wise constant distributions.
The code is designed as a *C++* library with a *Python* interface. This design targets ease of use, integration with existing frameworks, straightforward installation as well as flexible adaptation and expansion, while offering the performance of the *C++* library core.

Results

A convergence study for the flow around the unit sphere was conducted using quasi-equidistant meshes. Results are presented in Figures 1 and 2 and show accordance with the potential theory exact solution. The convergence orders are as expected (Figure 1): Linear doublets lead to better convergence in comparison to more traditional constant doublet distributions. Figure 2 shows exemplary pressure and surface velocity distributions for a medium grid spacing mesh of the sphere, which consists of 320 triangles. For this example, the extreme values of the pressure coefficient agree with the analytical solution. The pressure ranges between $c_{\mathrm{p,\,min}} = -1.25$ and $c_{\mathrm{p,\,max}} = 1$ in the stagnation points. Additionally, the pressure distribution for a fuselage and tail of the "Fast Rescue" helicopter is illustrated in Figure 3. Future work will continue towards the implementation of a free wake, time-stepping unsteady solutions and integration into a modular framework.

References

[1] K. Bock, "Towards a 3D Galerkin-Type High-Order Panel Method: A 2D Prototype," in *Notes on Numerical Fluid Mechanicsand Multidisciplinary Design*, 2021.

[2] L. L. Erickson, "Panel methods: An introduction," Techreport NASA-TP-2995, 1990.

[3] H. Inac and T. Schwarz, "Validation of a turbulent boundary layer method for fuselages of helicopters," in *50th European Rotorcraft Forum 2024*, 2024.

Mitteilung

Fachgruppe: Computational Aerodynamics

Towards rapid flow reconstruction using surface observations: Exploring data-assimilation strategies on a toy problem

Ángel González Villatoro, Mariachiara Gallia, David Rival
Institut für Stromüngmechanik TU Braunschweig
Hermann-Blenk-Straße 37, 38108 Braunschweig
angel.gonzalez-villatoro@tu-braunschweig.de

Reconstructing the flow field around complex bodies using only surface-based observations remains a fundamental challenge. Data assimilation provides a framework to address this by fusing sparse observations with physical models for accurate flow estimation (Sciacchitano, 2025). Surface observations such as wall pressure and shear stress have been shown to capture near-wall dynamics (Shah and Tang, 2025; Özbay & Laizet, 2022), especially with optimized sensor placement (Bidar et al., 2024; Sciacchitano et al., 2025). In parallel, studies by Cooper (2025) demonstrate that surface temperature can enhance reconstruction in complex or under-resolved flows.

Despite these advances, the specific effectiveness of different physical quantities (i.e. pressure, temperature or shear stress) as observations remains underexplored. This study addresses that gap resolving 2D Navier–Stokes equations for a flat plate suddenly accelerated inside a static flow with an imposed pressure gradient (beta) to induce separation, shown in Figure 1. A high-resolution simulation provides reference data, from which surface observations are extracted and assimilated into a coarse-grid for reconstruction. Four DA strategies are tested (nudging, Kalman Filter, EnKF, 4D-Var) to assess reconstruction of temperature, pressure, and wall shear stress fields.

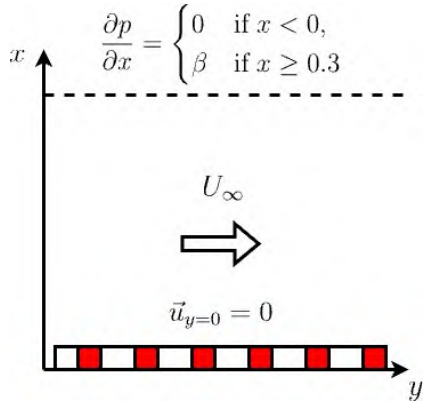

Figure 1: Test case sketch

Results, shown in Figure 2, provide preliminary evidence that wall temperature alone enables surprisingly accurate reconstruction across all fields. Among the tested methods, nudging yields the best trade-off between accuracy and computational efficiency, likely due to its simplicity and low reliance on uncertainty modeling. These findings suggest that temperature is not only a robust observable but also an efficient one for flow reconstruction. At least in cases, as this toy problem, where the influence of the variation of temperature is relatively more significant than the other parameters. Further work is required to validate these findings in more realistic and turbulent flow configurations, where the interplay between thermal and dynamic effects may differ significantly.

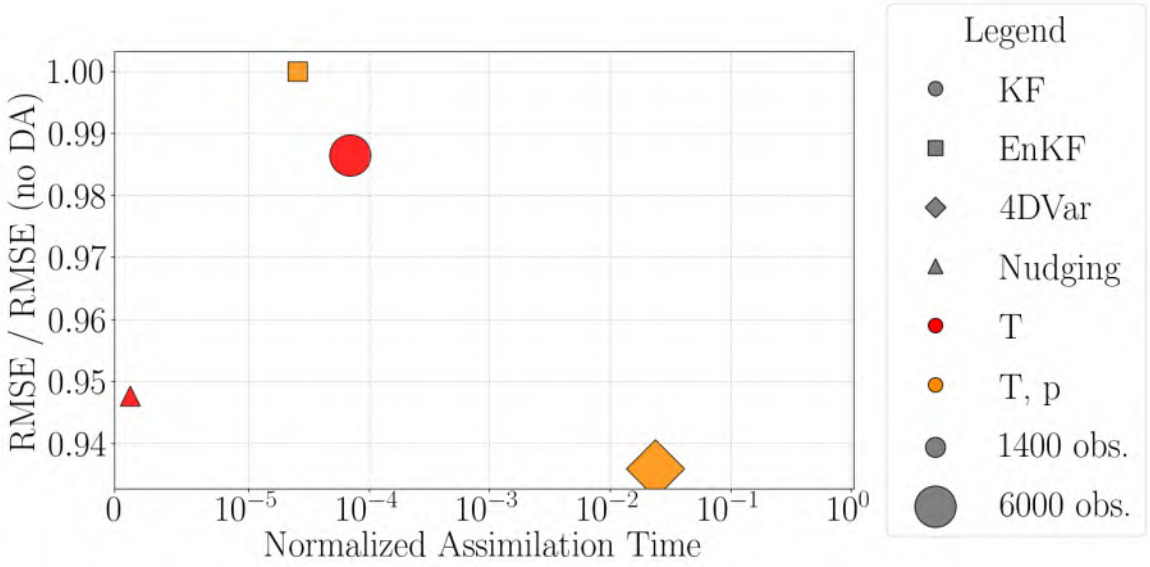

Figure 2: Comparison of data assimilation strategies in terms of reconstruction accuracy and computational cost (best case for each method)

Sciacchitano, A., Leclaire, B., & Schröder, A. (2025). On the accuracy of data assimilation algorithms for dense flow field reconstructions. https://doi.org/10.1007/s00348-025-03969-3

Shah, A., & Tang, D. (2025). Turbulent boundary layer and heat transfer over an aerodynamic body of revolution. https://doi.org/10.1063/5.0281560

Özbay, E., & Laizet, S. (2022). Deep learning for wall-based reconstruction of turbulent flows.https://doi.org/10.1063/5.0087488

Bidar, O., Anderson S. R., Qin N. (2024). Sensor placement for data assimilation of turbulence models using eigenspace perturbations. https://doi.org/10.1063/5.0182080

Cooper, V. T. (2025). Monthly Sea-Surface Temperature, Sea Ice, and Sea-Level Pressure from Coupled Data Assimilation. https://doi.org/10.1175/JCLI-D-25-0021.1

Mitteilung

Fachgruppe: Computational Aerodynamics

VERIFICATION AND EFFICIENCY STUDY USING THE TIME-SPECTRAL METHOD (TSM) FOR FAST PREDICTIONS OF GUST ENCOUNTER IN VISCOUS FLOW

Raphael Haupt[1], Christoph Kaiser[2] and Arthur Stück[1]

[1] German Aerospace Center (DLR), Institute of Software Methods for Product Virtualization, raphael.haupt@dlr.de, arthur.stueck@dlr.de

[2] German Aerospace Center (DLR), Institute of Aeroelasticity, christoph.kaiser@dlr.de

A time-spectral Reynolds-Averaged Navier-Stokes method (RANS) is presented and evaluated for efficient predictions of gust-encounter scenarios of aircraft. The TSM was integrated into the computational fluid dynamics (CFD) software CODA being developed as part of a collaboration between the French Aerospace Lab ONERA, the German Aerospace Center (DLR), Airbus, and their European research partners. CODA is jointly owned by ONERA, DLR and Airbus [2]. For a time-periodic prediction of N harmonics, the TSM results in a nonlinear block-equation system, in which 2N + 1 time-instances – each of the size of a standard RANS equation system on the given spatial mesh – are coupled via a time-spectral operator. This space-time equation system requires strong implicit solution procedures to be efficiently and reliably solved for complex, turbulent flow problems. To achieve a strong coupling in time, we followed an element-implicit formulation suggested by Mundis and Mavriplis [1]. All time-instances per space-time element are being block-inverted by means of direct solution methods provided by the linear algebra library Spliss [4]. The implementation in CODA allows to combine the element-implicit TSM with line-implicit block-Jacobi preconditioning based on the Thomas algorithm, which is an important ingredient for the numerical solution of high Reynolds-number flows. The TSM preconditioner is used inside a flexible GMRES solver which, in turn, is embedded in an implicit-Euler pseudo-time stepping scheme with local time steps. Thus, the steady-state solution capabilities of the baseline CFD software CODA are systematically carried over to the TSM solver.

In this study, the TSM was applied to viscous, aerodynamic CFD problems including gust-encounter scenarios. Previous investigations are presented by Mundis et al. [3] for inviscid aeroelastic and gust encounter cases in 2D. We used a standard 2nd-order finite-volume (FV) discretization in space. The implementation also supports higher-order spatial Discontinuous-Galerkin discretizations. The TSM is verified against reference solutions generated from implicit Runge-Kutta time-stepping.

Figure 1 depicts a time evolution of the lift coefficient for a periodic gust encounter on an NACA64A010 at a Mach number $Ma = 0.8$ and a Reynolds number of $Re = 1.25 \times 10^7$. The vertical gusts of (1 - cos)-type have a span of two cord lengths and has a peak velocity of 0.0013 x v_∞ . The distance between the periodic gust encounters is six times the cord length. The underlying spatial mesh is depicted in the top right corner of Figure 1. TSM time instances being the collocation points for the harmonic ansatz are represented by black markers. The reconstructed time trajectory of the TSM solution is represented by a solid line. Figure 1 also illustrates how the agreement of the TSM prediction converges with the number of time instances 2N + 1. Whereas 5 harmonics (i.e. 11 time instances) lead to a significant deviation of the lift evolution, the time-stepping reference is well represented with a TSM of 15 harmonics, where only small discrepancies at the extrema can be recognized. These tend to disappear with 25 harmonics, resulting no visible difference between time-stepping and TSM.

In the presentation, detailed verification and solver-efficiency studies will be provided for gust-encounter scenarios. Key features of the nested implicit solver stack for the TSM will be discussed together with important solver settings and numerical parameters.

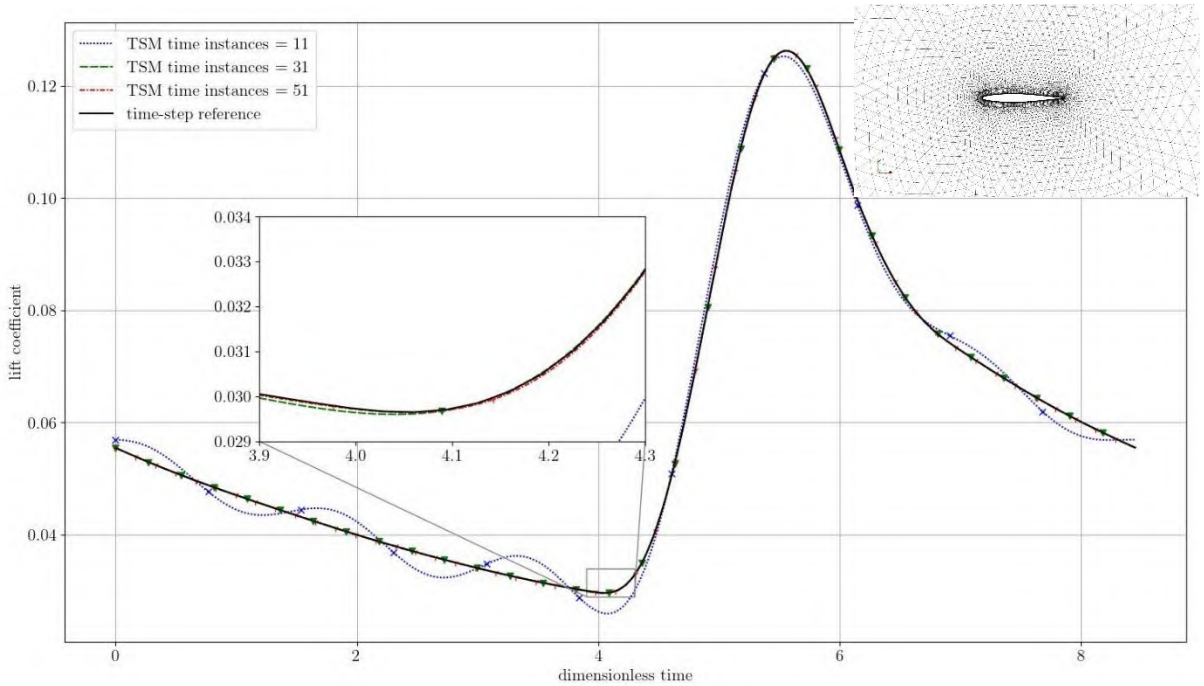

Figure 1: Time histories of the lift coefficient predictions by the TSM using 5, 15 and 25 harmonics for a gust encounter of a NACA64A010 section in turbulent flow. The TSM prediction is compared against a reference solution obtained by an implicit standard time-stepping method (DIRK-2). The underlying spatial mesh is shown in the top right corner.

Run-time and memory efficiency of the implicit TSM solver in CODA will be discussed to reliably converge the space-time block-equation systems resulting from the TSM. The systematic studies for 2D cases will be complemented by selected 3D simulation cases for wing/wing-body configurations in fully turbulent flows.

References

[1] N. L. Mundis and D. J. Mavriplis. Toward an Optimal Solver for Time-spectral Solutions on Unstructured Meshes. AIAA 2016-0069. https://doi.org/10.2514/6.2016-0069

[2] Leicht, T. et al. DLR-Project DIGITAL-X – Next Generation CFD Solver FLUCS, DLRK2016, Braunschweig, Germany, 13—15 September 2016

[3] Mundis, Nathan L., Dimitri J. Mavriplis, and Jay Sitaraman. "Quasi-periodic time-spectral methods for flutter and gust response." *69th Forum of the American Helicopter Society, AHS International, Alexandria*. 2013.

[4] Olaf Krzikalla et al. “Spliss: A Sparse Linear System Solver for Transparent Integration of Emerging HPC Technologies into CFD Solvers and Applications”. In: *22nd STAB/DGLR Symposium on New Results in Numerical and Experimental Fluid Mechanics XIII*. Notes on Numerical Fluid Mechanics and Multidisciplinary Design. Springer International Publishing, July 2021, pp. 635–645. DOI: https://doi.org/10.1007/978-3-030-79561-0_60

Mitteilung

Fachgruppe: Numerische Aerodynamik

Impact of the entropy fix at no-slip wall boundaries

Jesús Miguel Sánchez Gil[1], Markus Fertig[1], Ralf Hartmann[1], Tobias Knopp[2], Stefan Langer[1], Tobias Leicht[1], Axel Schwöppe[1]
DLR, Institute of Aerodynamics and Flow Technology
[1]Lilienthalpl. 7, 38108 Braunschweig, jesus.sanchezgil@dlr.de, markus.fertig@dlr.de, ralf.hartmann@dlr.de, stefan.langer@dlr.de, tobias.leicht@dlr.de, axel.schwoeppe@dlr.de
[2]Bunsenstraße 10, 37073 Göttingen, tobias.knopp@dlr.de

The CFD Software by ONERA, DLR and Airbus (CODA) [1] uses the Riemann solver of Roe to compute the convective flux of the Navier-Stokes or RANS equations. Although Roe´s scheme [2] can capture discontinuities such as shock and contact waves, it is known to produce entropy-violating shocks in expanding flows when one of the acoustic eigenvalues approaches zero. Harten's entropy fix [3] was therefore introduced to displace the eigenvalues away from zero hereby modifying the coefficients of the dissipation term in the Roe flux. Hence, the entropy condition is satisfied, but artificial viscosity is added to the convective flux. Mavripilis [4] reported that the amount of artificial viscosity influences the boundary integral quantities such as lift (C_L) and drag (C_D) coefficients. Furthermore, the results of the skin friction (c_f) coefficients computed with CODA have shown to vary significantly when adding artificial viscosity by means of Harten's entropy fix to the convective flux. Concretely, this effect has been observed to be prominent at boundaries on coarse meshes when imposing adiabatic no-slip wall boundary conditions, as the addition of artificial viscosity would decrease on finer grids. Due to the fact that CODA is a cell centered code in which a weakly imposed boundary condition formulation is used as described by Hartmann et al. [5], both states entering the convective flux at the boundary have in general non-zero velocities. As the difference between these states does not vanish, artificial viscosity is added on the boundary due to non-zero eigenvalues. Instead of using a cut-off based on a fixed fraction of the largest eigenvalue, Kermani and Plett [6] proposed a more local approach based on the difference between eigenvalues on the left and right sides of the face in comparison to the values for the face-averaged state. As a third option, CODA offers a wave-based entropy fix, which inherently does not add artificial viscosity at the boundary and thus prevents the entropy fix from affecting the results. Overall, these alternative entropy fixes add less dissipation to the convective flux at boundaries compared to Harten's entropy fix at the cost of a potential robustness reduction. Due to the described effects of the entropy fix at no-slip wall boundaries, an investigation of the impact of

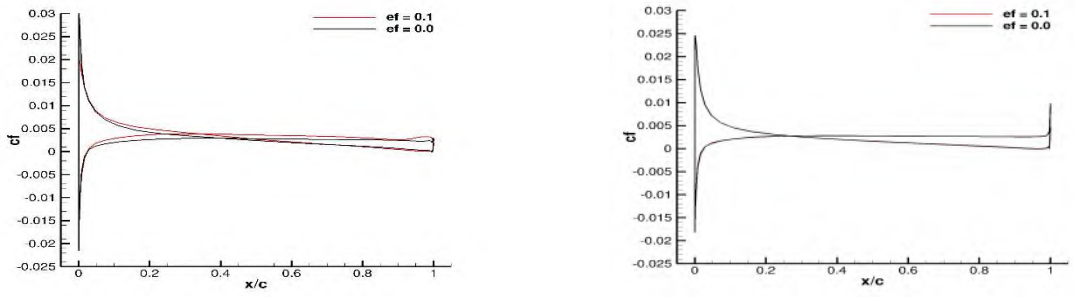

(a) FV (a) DG

Figure 1. The skin friction coefficient (c_f) for the FV and DG discretizations when varying the amount of artificial viscosity for a NACA 0012 airfoil at Ma = 0.15, Re = $6x10^6$ and AoA = 10°

the entropy fix on the results of the skin coefficient (c_f) has been pursued.

Figure 1 shows the skin friction coefficient (c_f) with and without artificial viscosity (ef = 0.1 and 0.0) for a NACA0012 airfoil at a Mach number of 0.15, a Reynolds number of 6x10^6 and an

angle of attack of 10 degrees for the Finite Volume (FV) and the Discontinuous Galerkin (DG) discretizations. The FV discretization shows a significant sensitivity to the addition of artificial viscosity through the entropy-fix (ef = 0.1), in contrast to the behavior observed for the DG discretization. This effect is attributed to the fact that the FV discretization uses a gradient-based piecewise linear reconstruction which relies on the neighbor and neighbors-of-neighbor cell values to compute a solution on a single degree of freedom. In contrast, the DG discretization employs more compact polynomial functions on multiple degrees of freedom. As a result, the DG discretization matches the weakly imposed boundary conditions better due to the reduced dependency on the cell neighboring values. Due to this, the difference between the values on both sides of the boundaries becomes smaller and thus less dissipation is added to the convective flux. When using a gradient-based piecewise linear reconstruction in FV, the effect of artificial viscosity at the boundary becomes more pronounced under grid metric changes. This arises because gradient computations (e.g., via least squares [4]) depend on weighting coefficients that vary with the relative positions of neighboring cells. Consequently, the boundary condition may exert weaker influence, altering the reconstructed state across the boundary and often leading to higher amounts of artificial viscosity.Therefore, a gradient computation that applies a stronger weighting on the boundary conditions is suggested to be investigated in order to reduce its impact at the wall boundaries.

In order to asses how to minimize the effect of the entropy fix at boundaries, the deactivation of Harten's entropy fix directly at boundaries was investigated. This investigation was also compared against the Kermani and Plett method [6] and the wave-based entropy fix. The results obtained with this modification of the Roe scheme at boundaries showed an impact on the results of the skin friction (c_f) similar to the one shown by the Kermani and Plett method and the wave-based entropy fix whose modification of the eigen values results in less dissipation at wall boundaries. However, the deactivation of Harten's entropy fix at boundaries is not recommended, as it leads to a flux computation which is inconsistent between inner and boundary faces. Furthermore, the entropy fix has shown to contribute to the overall viscous effects. This means that the viscous effects coming from the viscous flux are balanced with the artificial viscosity added to the convective flux via the entropy fix. This explains the observed changes in the skin friction coefficient (c_f) when the entropy-fix is activated. As CODA currently uses a post-processing to compute the skin friction coefficient (c_f) based only on the viscous fluxes, a consistent approach is proposed in which the contribution of the convective and viscous fluxes are included. With this approach, the results using FV discretizations varied less under the activation of the entropy fix.

According to the described effects of Harten's entropy fix at boundaries, it is suggested to use an entropy fix that reduces the addition of artificial viscosity at boundaries, a consistent flux-based post-processing in order to minimize the effects of the entropy fix at boundaries and to investigate a gradient computation with stronger weighting on the boundary conditions.

Bibliography

[1] P. Stefanin Volpiani, J.-B. Chapelier, A. Schwöppe, J. Jägersküpper and S. Champagneux, "Aircraft Simulations Using the New CFD Software from ONERA, DLR, and Airbus," *Journal of Aircraft,* vol. 61, pp. 857-869, 2024.

[2] P. L. Roe, "Approximate Riemann solvers, parameter vectors, and difference schemes," *Journal of Computational Physics,* pp. 357-372, 1981.

[3] A. Harten, "High Resolution Schemes for Hyperbolic Conservation Laws," *Journal of Computational Physics,* pp. 357-393, 1983.

[4] D. Mavriplis, "Revisiting the Least-Squares Procedure for Gradient Reconstruction on Unstructured Meshes," in *16th AIAA Computational Fluid Dynamics Conference*, 2003.

[5] R. Hartmann and T. Leicht, "Generalized adjoint consistent treatment of wall boundary conditions for compressible flows," *Journal of Computational Physics,* vol. 300, pp. 754-778, 2015.

[6] M. Kermani and E. Plett, "Modified entropy correction formula for the Roe scheme," in *39th Aerospace Sciences Meeting and Exhibit*, 2001.

Mitteilung

Fachgruppe: Computational Aerodynamics

A Hybrid Differentiation Approach towards Performance-Improved Discrete Adjoint CFD Computations

Büşra Sert[*], Adam Büchner[†], Franziska Kasielke[‡], Anton Schmid[§], Arthur Stück[¶]

German Aerospace Center (DLR e.V.)
Institute of Software Methods for Product Virtualization
Nöthnitzer Straße 46b, 01187 Dresden

Due to recent advances in the development of algorithmic differentiation (AD) software [1], many CFD methods and multiphysics software packages have started to incorporate AD tools for computing sensitivities (see for example [3] and [4]) in different ways in order to accelerate the time-consuming and error-prone process of manual discrete differentiation, cf. [2]. Numerous AD libraries are available under various license models that can be considered for incorporation in such CFD software. Different AD implementation strategies come with different up- and downsides depending on the specific use case (for more information on AD tools visit autodiff.org). Therefore, the implementation of AD-tool based differentiation capabilities of a CFD software requires more flexibility to allow better performance optimization.

In this paper, we present a hybrid approach to discrete differentiation pursued in the development of the adjoint methods in the computational fluid dynamics (CFD) software CODA, which is being developed as part of a collaboration between the French Aerospace Lab ONERA, the German Aerospace Center (DLR), Airbus, and their European research partners. The AD framework of CODA supports the usage of different operator-overloading (OO) AD libraries via an AD abstraction interface. Therefore, it allows the choice of the best-fitting AD library for a given use case.

In a so-called compact-tape approach, the reverse-mode differentiation is applied using AD tools locally on the level of face- and element-wise operations for the residual function differentiation. It leads to very small fixed-size tapes for local stencil operations.

The hybrid differentiation approach is embedded within the compact-tape approach. The tool-based algorithmic differentiation was replaced by hand-coded discrete differentiation for selected parts in the computational graph of the code from the CFD software to achieve a performance-improved adjoint implementation.

Accordingly, these approaches are considered for the function computing the Green–Gauss gradient $G(U)$ as a function of the flow state U. It is called within the computation of the residual R of the finite volume (FV) discretization. It leads to the primal dependency chain of the residual function, $R(U, G(U))$. The corresponding discrete forward and reverse differentiation reads

$$\frac{\mathrm{d}R}{\mathrm{d}U} = \left[\frac{\partial R}{\partial U}\right] + \left[\frac{\partial R}{\partial G}\right]\left[\frac{\partial G}{\partial U}\right] \qquad \text{and} \qquad \overline{U} \mathrel{+}= \left(\left[\frac{\partial R}{\partial U}\right]^T + \left[\frac{\partial G}{\partial U}\right]^T \left[\frac{\partial R}{\partial G}\right]^T\right)\overline{R}\,,$$

[*]buesra.sert@dlr.de
[†]adam.buechner@dlr.de
[‡]franziska.kasielke@dlr.de
[§]anton.schmid@dlr.de
[¶]arthur.stueck@dlr.de

respectively. Whereas the reverse-mode differentiation of the residual is fully AD-tool-based in the base-line version, the discrete-adjoint Green–Gauss computation, i.e., $[\partial G/\partial U]^T \overline{G}$ with $\overline{G} = [\partial R/\partial G]^T \overline{R}$, is partially hand-differentiated in the hybrid approach. Due to its simplicity, the Green–Gauss operator is deemed a natural choice for incorporating hand differentiation. For such operations it can be expected that the use of AD libraries would involve a high relative overhead.

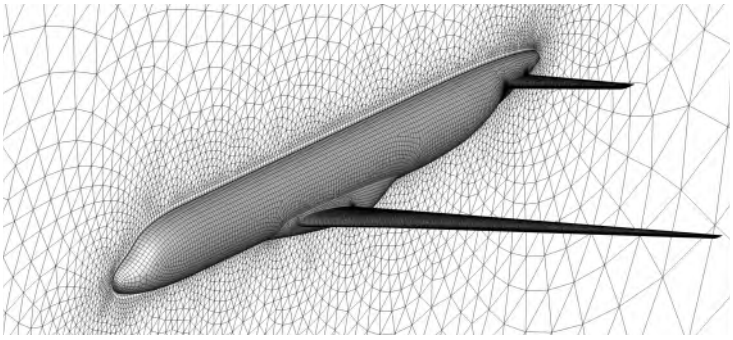

Figure 1: F25 full aircraft test case with 2.5M cells.

Numerical experiments are carried out using the DLR-F25 configuration in cruise conditions at a Mach number $Ma = 0.78$ and a Reynolds number $Re = 5.9 \times 10^6$. The aircraft is considered in fully turbulent Reynolds-averaged Navier–Stokes (RANS) flow in combination with the negative extension of the Spalart-Allmaras turbulence model (SA-neg). A second-order finite-volume discretization is applied in combination with a standard Green–Gauss scheme used for the computation of spatial gradients. In the presentation, the performance of fully AD-library-based and hybrid residual and Green–Gauss gradient computations will be investigated and compared. Moreover, we will study the performance of the two approaches in MPI-parallel execution using different AD libraries, such as ADOLC, dco/c++ and CoDiPack. Based on the presented experiences with the hand-differentiated Green–Gauss operator an outlook will be given on further promising application areas of the hybrid approach and its potential in CODA.

References

[1] Margossian, Charles C. “A review of automatic differentiation and its efficient implementation.” Wiley interdisciplinary reviews: data mining and knowledge discovery, 9.4 (2019).

[2] Stück, Arthur. “Dual-consistency study for Green-Gauss gradient schemes in an unstructured Navier-Stokes method. Journal of Computational Physics, 350, 530–549 (2017).

[3] Banović, Mladen, et al. “Algorithmic differentiation of the Open CASCADE Technology CAD kernel and its coupling with an adjoint CFD solver.” Optimization Methods and Software, 33.4–6, 813–828 (2018).

[4] Maugars, Bruno, et al. “Algorithmic Differentiation for an efficient CFD solver.” ECCOMAS 2022 – 8th European Congress on Computational Methods in Applied Sciences and Engineering. 2022.

Mitteilung

Fachgruppe: Computational Aerodynamics

Multidisciplinary Higher-Order Time Integration Towards Adaptive Time-Stepping

Imri Shuvi, Florian Roß and Arthur Stück

German Aerospace Center (DLR)
Institute of Software Methods for Product Virtualization
Nöthnitzer Str. 46b, 01187 Dresden
imri.shuvi@dlr.de, florian.ross@dlr.de, arthur.stueck@dlr.de

Multidisciplinary Design Analysis and Optimization (MDAO) frameworks like OpenMDAO [1] or GEMSEO offer a number of multidisciplinary (implicit) solution and optimization algorithms to facilitate the set-up and processing of large-scale MDAO cases. Multidisciplinary forward- and reverse-mode gradient accumulation are automated by the frameworks. Today, MDAO is well-established for steady-state type of applications, cf. [2]. MDAO frameworks enjoy a growing user community. However, comparable MDAO solutions and capabilities for the processing of time-dependent problems are not available. In order to support unsteady MDAO problems, the open-source extension RKOpenMDAO [3] to OpenMDAO, has been developed to support time integration using Runge-Kutta (RK) schemes. The time integration is performed by successively modeling time stages as multidisciplinary inner problems of quasi steady-state type. We take advantage of the baseline steady-state MDAO capabilities of the framework. In the time-stepping process, the inner problem is repeatedly being reused to avoid re-allocation over time steps and stages. Currently, explicit and Diagonally-Implicit RK (DIRK) schemes of higher order are implemented in RKOpenMDAO. The compressible CFD Software by ONERA, DLR and Airbus (CODA) was integrated into the MDAO framework approach via the FlowSimulator HPC ecosystem [3].

Based on the gradient-enabled MDAO framework environment described above, an adaptive *multidisciplinary* time-stepping was developed, implemented and evaluated in this study. It allows for dynamically adjusting the time-step size based on the evolving requirements of the simulation. The time-adaptive approach, well-known on the disciplinary level in the context of CFD [4], is systematically carried forward to the multidisciplinary level. Thus, effects on the discretization error in time stemming from the multidisciplinary coupling can be considered in the choice of the optimal time step for transient MDAO problem. A well-chosen time step homogeneizes the computational error over time, can help to keep the simulation stable and effectively capture important transient phenomena. We expect that – depending on the use case – the multidisciplinary adaptive time stepping can increase computational efficiency and accuracy of the time integration.

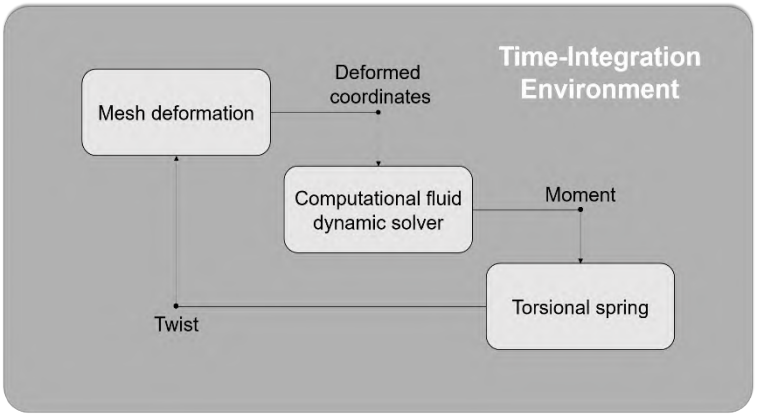

Figure 1: Coupled CFD-Spring problem

Numerial experients were carried out to systematically investigate key numerical parameters and asses the framework-based adaptive multidisciplinary time-stepping approach. A NACA0012 section connected to a torsional spring was considered in inviscid flow at a Mach

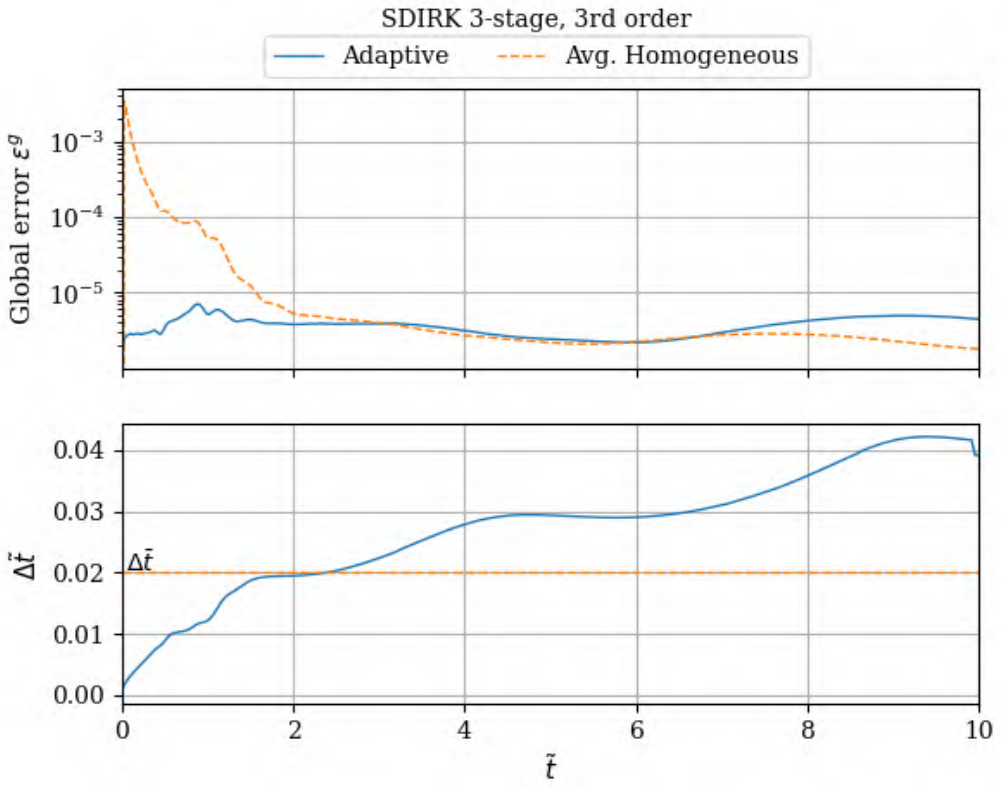

Figure 2: Coupled CFD-Spring problem: global error comparison between adaptive and homogeneous time-stepping methods

number of Ma = 0.1 using CODA. The multidisciplinary coupling is sketched in Figure 1. The performance of the adaptive method was compared against a homogeneous (fixed time step) method. The global error and the time step size are compared for both adaptive and homogeneous time-stepping in conjunction with a 3rd-order SDIRK scheme, cf. Figure 2. As expected, the adaptive scheme successfully achieves a more uniform distribution of the error over time than the latter.

By construction, the multidisciplinary adaptive time-stepping accounts for interdisciplinary coupling effects, which is a key advantage over a disciplinary time-step adaptation. Selected analytical and numerical problems will be considered in the presentation to study and quantify the advantages of the suggested multidisciplinary adaptive time-stepping method – and its prerequisites to be successful.

References

[1] J. S. Gray, J. T. Hwang, J. R. Martins, K. T. Moore, and B. A. Naylor. Openmdao: An opensource framework for multidisciplinary design, analysis, and optimization. *Structural and Multidisciplinary Optimization*, 59(4):1075–1104, 2019.

[2] J. Sobieszczanski-Sobieski and R. T. Haftka. Multidisciplinary aerospace design optimization: survey of recent developments. *Structural optimization*, 14:1–23, 1997.

[3] F. Roß, A. Büchner, S. Gottfried, and A. Stück. A high-fidelity framework approach enabling high-order implicit time stepping for mdao. In *ECCOMAS Congress 2024 - 9th European Congress on Computational Methods in Applied Sciences and Engineering*, Oktober 2024

[4] V. John and J. Rang. Adaptive time step control for the incompressible Navier-Stokes equations. *Computer Methods in Applied Mechanics and Engineering*, 199(9):514-524, 2010

Mitteilung

Fachgruppe: Computational Aerodynamics

Impact of Spectral Element Polynomial Order on
Large-Eddy Simulations of a Thick Flatback-Airfoil

Tinto Thomas[1], Johannes Nicolaas Theron[2], Neeraj Paul Manelil[3], Bernhard Stoevesandt[4], Philipp Schlatter[5]
Fraunhofer IWES, Küpkersweg 70, 26129 Oldenburg, Germany[1,2,3,4]
Friedrich – Alexander – Universität (FAU) Erlangen – Nürnberg, Germany[1,4]
ForWind – Center for Wind Energy Research, University of Oldenburg, Germany[3]
tinto.thomas@iwes.fraunhofer.de[1]

The aerodynamic performance of thick airfoils is strongly influenced by separated flow structures and turbulent wake dynamics. Capturing these complex phenomena requires accurate numerical approaches that can resolve both near-wall features and turbulent structures. The Spectral Element Method (SEM) offers a high-order discretization strategy, enabling refinement through polynomial order increase without altering the underlying mesh. In this study, Wall-Resolved Large-Eddy Simulation (LES) is employed to investigate the flow around thick flatback-airfoil. The influence of spectral polynomial order on LES predictions was studied, using the NEKO code, and validated against OpenFOAM simulations and experimental measurements. The objective is to evaluate the accuracy and computational efficiency of varying spectral element polynomial orders in wall-resolved LES of thick airfoils, thereby highlighting the potential benefits and limitations of high-order SEM for simulations.

Increased midspan thickness with flatback airfoils enhance both structural and aerodynamic efficiency. Flatback airfoils provide advantages over conventional sharp trailing-edge profiles, such as higher lift coefficients and steeper lift curve slopes, they also introduce complex flow features, including stronger adverse pressure gradients, flow separation, and wake interactions, which are difficult to capture accurately [1]. Hence, the simulation demands high-fidelity methods like wall-resolved LES combined with high-order Spectral element numerical schemes to resolve turbulent structures and separation phenomena precisely. SEM offer substantial benefits like spectral convergence compared to traditional finite volume or finite difference approaches [2]. SEM-based NEKO is a non-dimensional solver, an evolution of NEK5000, is a modern high-performance CFD code written in object-oriented Fortran to optimize memory management and enable multi-tier solver abstractions. NEKO has been validated against experimental data and demonstrated good agreement [3]. Designed for HPC environments, it efficiently exploits diverse hardware architectures and accelerators for large-scale simulations [4].

High-order methods are particularly sensitive to mesh quality and therefore require carefully structured and smoothed grids. In this study, the mesh is generated using Gmsh, which provides precise control over element quality, while additional smoothing with NEK5000's mesh utility enhances accuracy through nodal displacement. The 2D structured mesh from Gmsh is exported in binary format to NEK5000, where it is smoothed and extruded to 2.5D with a span length of 5% chord and six layers. Polynomial orders are chosen to yield approximately 20-30 inner nodes in the spanwise direction, consistent with typical wall-resolved LES simulations [5]. The thick flatback-airfoil considered has a 35% chord thickness at

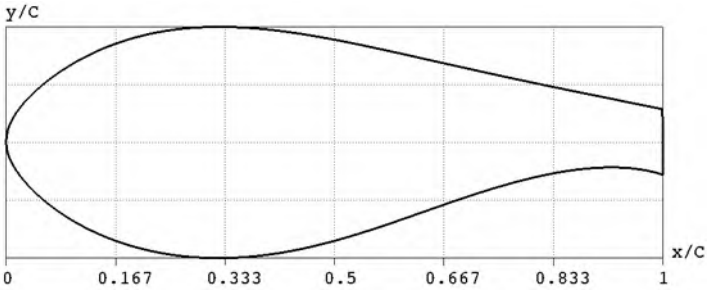

Fig. 1: Airfoil profile with 35% max and 10% flatback thickness

33% chord length and a 10% trailing-edge thickness [Fig. 1], simulated at a Reynolds number of one million and an angle of attack of four degrees. Employing a wall-resolved mesh at such high Reynolds numbers poses significant challenges, as the first elements must remain within the laminar sublayer. $y^+<1$ with $z^+\sim30$ and $5<x^+<40$ resulting in element sizes on the order of 10^{-4} and about 50,000 SEM elements in 2D with added polynomial inner grids. With six spanwise layers, the mesh contains roughly 300,000 SEM elements, corresponding to a total of ~ 8.5, 20, and 38 million inner nodes for polynomial orders 3, 4, and 5, respectively. Separate simulations are conducted for each order, where the degrees of freedom scale with the product of the SEM element and the cube of the polynomial order. The computational domain was defined with an upstream length of four chord lengths, a downstream length of eight chord lengths, and a far-field extent of eight chord lengths. Standard boundary conditions were applied, with a DONG condition [6] at the pressure outlet to suppress artificial wave reflections and enhance stability. The top and bottom boundaries employed a 'normal_outlet' condition, maintaining the horizontal velocity component while allowing normal flow exit at the outermost layer. Spanwise boundaries were treated as periodic, and a no-slip condition was imposed on the airfoil surface.

A uniform unit-velocity inflow was prescribed at the inlet and the field is initiated with the same. The CFL number was maintained constant around 0.6 using an adaptive timestep, and simulations employed third-order time IMEX scheme. Krylov solvers with Preconditioners are used with Projections, the vector spaces which accelerates the solution procedure. Identical simulation setups were tested with polynomial orders 3, 4, and 5, all satisfying boundary-layer resolution requirements, to evaluate the impact of spectral order. The solver computes aerodynamic forces, generates turbulence statistics, and time & space averaged flow quantities. These data can be extracted to compute lift and drag coefficients and pressure distributions provide an overall assessment of our result accuracy. The velocity field from the WR-LES with polynomial order 5, reveals well-resolved turbulent eddy structures [Fig. 2]. Results obtained with NEKO were cross-compared against OpenFOAM simulation and experimental data to establish a benchmark for simulations.

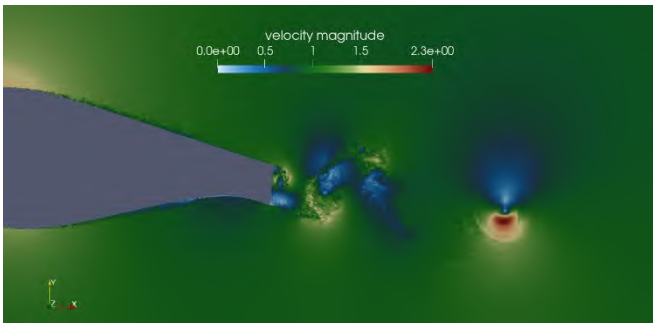

Fig. 2: Velocity field from the WR-LES

This work contributes to the understanding of SEM by evaluating its advantages and limitations in CFD. The performance of NEKO's newly implemented LES module is examined, with emphasis on its ability to resolve turbulence and complex flow behavior. The influence of polynomial order on accuracy and computational performance is evaluated, providing insights into the trade-off between resolution and computational cost. To ensure reliability, the simulations are validated against both OpenFOAM results and experimental data, providing a robust benchmark for assessing the predictive capability of high-order SEM-based solvers in comparison to conventional CFD approaches and physical measurements. This validation not only confirms the accuracy of high order methods in LES framework but also highlights its potential to serve as a reliable tool for investigating aero-fluid dynamic problems.

References :

[1] Mehdi Doosttalab et al. Vortex generator effects on dynamic stall of thick airfoils - Renewable Energy - 255 (2025) 123746
[2] Francesco Capuano et al. Cost vs Accuracy: DNS of turbulent flow over a sphere using structured immersed-boundary, unstructured finite-volume, and spectral-element methods - European Journal of Mechanics - B/Fluids - 102 (2023) 91–102
[3] Filipe F. Buscariolo et al. Spectral/hp element simulation of flow past a Formula One front wing: Validation against experiments - Journal of Wind Engineering and Industrial Aerodynamics - 221 (2022) 104832
[4] Niclas Jansson et al. Neko: A modern, portable, and scalable framework for high-fidelity computational fluid dynamics - Computers & Fluids - 275 (2024) 106243
[5] A. Frere et al. High Reynolds Number Airfoil: From Wall-Resolved to Wall-Modeled LES - Flow, Turbulence and Combustion (2018) 101: 457–476
[6] S. Dong et al. Accurate low-dimensional modeling of pressure-driven flows via proper orthogonal decomposition - Journal of Computational Physics 217.1 (2006): 40-58

Mitteilung

Fachgruppe: Strömungsbeeinflussung

Numerical Evaluation of Adaptive Dropped-Hinge Flap Kinematics on High-Lift Wing Performance

Paloma García-Guillén[1,a *] and Christian Breitsamter[1,b]
[1]Chair of Aerodynamics and Fluid Mechanics, Technical University of Munich,
Boltzmannstr. 15, 85748 Garching bei München, Germany
[a]p.garcia-guillen@tum.de, [b]christian.breitsamter@tum.de

Achieving the emission reduction goals established by the Flightpath 2050 [1] requires innovations across a wide range of disciplines. In the field of aerodynamics, improving the performance of high-lift systems is essential for enhancing the operational efficiency of modern civil aircraft, particularly during low-speed flight phases such as takeoff and landing. In this context, improving high-lift performance has led to growing interest in active flow control (AFC) systems as an extension to conventional devices such as slats and flaps. These concepts can alleviate adverse effects related to the aeromechanics of lifting surfaces, such as by delaying stall in fixed-wing aircraft. Among various AFC methods, the potential of oscillating trailing-edge flaps to increase the maximum lift and the associated flow physics is the subject of ongoing fundamental research but requires further investigation. Ruhland and Breitsamter [2] and García-Guillén et al. [3] conducted numerical studies showing that an oscillating dropped-hinge flap (DHF) can significantly influence the separation topology of the flow, and flow separation can be suppressed beyond the maximum static flap deflection angle. It was also shown that a longitudinally oscillating DHF yields higher increases in lift compared to a purely rotational flap motion [2]. This approach can be realized by leveraging the existing infrastructure of modern fly-by-wire aircraft equipped with systems such as adaptive dropped-hinge flaps (ADHF) in combination with an adapted actuator concept.

The current research, conducted as part of a joint project between ILR RWTH Aachen and TUM-AER, investigates the potential of AFC using an oscillating ADHF through numerical and experimental methods, with particular focus on its influence on flow separation topology and lift enhancement. The examined high-lift configuration is representative of real-world civil transport aircraft and is based on the LR-270 geometry developed by RWTH Aachen and TUM [2]. The midboard section of the LR-270 is defined by the NASA SC(2)-0711 airfoil. The used configuration consists of a four-element airfoil, comprising a leading-edge slat, a deflectable spoiler, and a single-segment trailing-edge flap as high-lift devices. The geometry is implemented as a rectangular wing with quasi-two-dimensional flow characteristics.
This paper presents a numerical analysis of the specified geometry featuring an oscillating ADHF, with focus on the influence of the longitudinal motion component, which is expected to affect the boundary layer development by imposing unsteady flow conditions.
It is assumed that the flap oscillation leads to a more favorable pressure recovery, delayed separation and increased lift under certain conditions. In addition, the ADHF setup allows independent deflection of the spoiler element, enabling investigation of how the gap and overlap between spoiler and flap affect separation control and lift performance.
To establish reference performance metrics and define the operating condition and relevant parameter space, initial numerical investigations are carried out without active flow control, considering various steady spoiler and flap deflection settings. Building on these results, the subsequent analysis focuses on the aerodynamic behavior of the high-lift configuration with a harmonically oscillating ADHF. Key design parameters in this study include the reduced frequency k and the flap oscillation amplitude $\Delta\delta$, whose influence on boundary layer development, gap flow characteristics, and global aerodynamic coefficients is systematically evaluated. To constrain the complexity of the parameter space, the position of the ADHF hinge point is held constant. From the numerical data, characteristic regions of the flow field are identified and analyzed in detail. Time-resolved pressure coefficient distributions, force

coefficients, and flow field visualizations are examined to assess the effect of flap motion on flow control effectiveness.
In addition, the influence of the Reynolds number is addressed by performing simulations at both low and high Reynolds number regimes. For validation purposes against ongoing experimental efforts, simulations are conducted at a Reynolds number of $Re = 0.5 \times 10^6$, consistent with subscale conditions in the water tunnel facility at RWTH Aachen. Complementary analyses are performed at $Re = 30 \times 10^6$, representative of full-scale landing conditions for a modern commercial aircraft.
Numerical simulations are performed using ANSYS Fluent with unsteady Reynolds-averaged Navier-Stokes (URANS) and hybrid URANS and large-eddy simulation (LES) approaches. Meshes are generated using ANSA by BETA CAE Systems. A high-resolution block-structured grid, shown in Fig.1, is used. The mesh consists of appproximately one million cells and is refined near the flap gap and trailing edge to accurately resolve flow separation, reattachment, and vortex dynamics. Figure 2 shows the chordwise pressure distribution for the reference high-lift setup for low Reynolds number conditions.

Overall, the intended findings contribute to bridging current gaps in the understanding of unsteady aerodynamic effects associated with AFC via oscillating flaps and support the development of future high-lift systems.

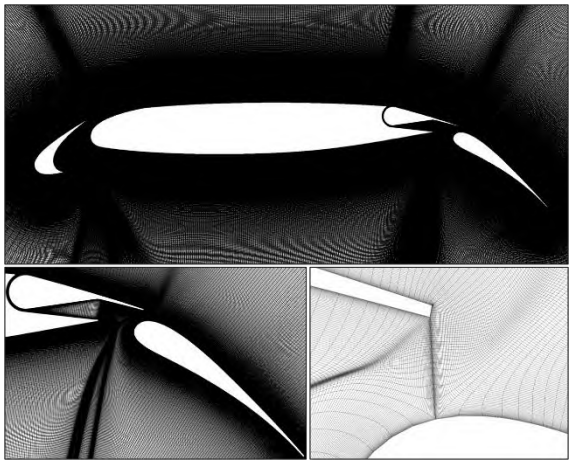

Figure 1: Block-structured grid with detailed views of the refined mesh around the flap and gap regions.

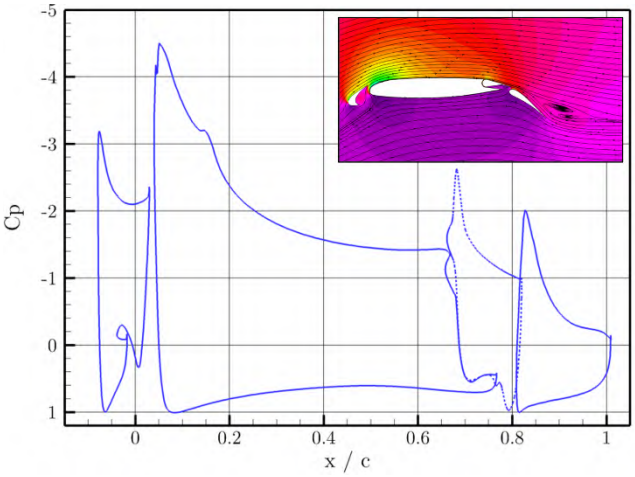

Figure 2: Chordwise pressure coefficient distribution at $Re = 0.5 \times 10^6$ and $\alpha = 8^o$ (water tunnel conditions) of the reference configuration.

References

[1] Flightpath 2050: Europe's vision for aviation: maintaining global leadership and serving society's needs. Luxembourg: Publications Office of the European Union, 2011. DOI: 10.2777/50266.

[2] Ruhland, J. and Breitsamter, C. Numerical analysis of high-lift configurations with oscillating flaps. CEAS Aeronautical Journal 12.2, pp. 345–359, 2021. DOI: 10.1007/s13272-021-00498-7.

[3] García-Guillén, P., Kärner, J. K., and Breitsamter, C. Numerical study for active flow control on high-lift configurations by oscillating dropped-hinge flaps. Forthcoming in: New Results in Numerical and Experimental Fluid Mechanics XV: Contributions to the 24th STAB/DGLR Symposium, Regensburg, Germany, 2024. Notes on Numerical Fluid Mechanics and Multidisciplinary Design, Springer. Accepted for publication.

Acknowledgement

This research was funded by the Deutsche Forschungsgemeinschaft (DFG, German Research Foundation) in the framework of the project *Active Flow Control through Oscillation of a Dropped-Hinge Flap* (BR 1511/19-1). Special thanks are addressed to ANSYS for providing the flow simulation software. Furthermore, the authors gratefully acknowledge the Gauss Centre for Supercomputing e.V. (www.gauss-centre.eu) for funding this project by providing computing time on the GCS Supercomputer SuperMUC at Leibniz Supercomputing Centre (www.lrz.de).

Mitteilung

Fachgruppe: Strömungsbeeinflussung

Bayesian minimisation of energy consumption in turbulent pipe flow via unsteady driving

Felix Kranz[1], Daniel Morón[1] and Marc Avila[1,2]
[1]University of Bremen, Center of Applied Space Technology and Microgravity, Am Fallturm 2, 28359 Bremen, Germany.
[2]University of Bremen, MAPEX Center for Materials and Processes, Am Biologischen Garten 2, 28359 Bremen, Germany.

Correspondence: Felix Kranz, felix.kranz@zarm.uni-bremen.de

Turbulent pipe flows are ubiquitous in engineering, ranging from large-scale oil or gas pipelines to small-scale applications like heating pipes or fresh water supply. Pumping systems are recognized as major energy consumers globally, contributing to an estimated global energy share of nearly 20 % (Frenning, 2001). In certain industrial plant operations, pumping systems even account for up to 50 % of the energy usage. When compared to the laminar regime, in turbulent conditions, the multi-scale eddying motion is responsible for a major part of the total friction and the comparably large energy consumption associated with pumping (Blasius, 1913). Therefore, many strategies have been developed to reduce drag and control turbulence. These range from passive methods, such as riblets (García-Mayoral & Jiménez 2011), to active approaches like body forcings (Marensi et al., 2019; Kühnen et al., 2018). Oscillatory forcing is particularly promising, including spanwise wall oscillations (Quadrio & Ricco, 2004; Auteri et al., 2010) and unsteady pressure gradients. Both, simulations (Foggi Rota et al. 2023a,b; Scarselli et al. 2023) and experiments (Souma et al. 2009, Scarselli et al. 2023) demonstrate that pulsatile forcings can achieve notable drag reduction and energy savings. Nonetheless, the space of possible flow parameters and — most importantly — pulsation waveforms capable of achieving such improvements is vast and remains only partially explored.

Here, we follow up on the work of Scarselli et al. (2023) and aim to devise periodic bulk velocity waveforms $U(t)$ that (at Reynolds numbers $Re \in \{5160, 8600\}$ and a Womersley number of 10) either minimize the n-cycle-averaged drag or energy consumption while delivering a desired time-averaged mass flux $\overline{U}_d$. In contrast to Scarselli et al. (2023) and Foggi Rota et al. (2023a,b), we use optimisation algorithms in order to minimize an objective functional $\mathcal{J}$ (the turbulent drag or energy consumption), that is

$$min_{U(t)} \mathcal{J}(U(t)) \text{ subject to } \overline{U} = \overline{U}_d. \quad (1)$$

Equation (1) is a complex optimisation problem for multiple reasons: (i) it is constrained by a partial differential equation (the Navier–Stokes equations have to be fulfilled), (ii) it features state constraints ($\overline{U} = \overline{U}_d$), and (iii) it is of infinite dimensions (seeking functions $U(t)$).

As there is no analytic framework to map different waveforms to values of the objective $\mathcal{J}$ (in other words, $\mathcal{J}$ is a black-box) evaluating it requires for direct numerical simulation (DNS), making it expensive to access, though, eliminating difficulty (i). We consider two finite-dimensional waveform designs $U_\eta(t), \eta \in \mathbb{R}^d$ that, by design, realize the desired time-averaged flux (i.e. fulfill (ii) and (iii)), reducing the optimization problem to $min_{\eta \in \mathbb{R}^d} \mathcal{J}$.

First, we consider triangular waveform designs (figure 1(a)), inspired by the work of Scarselli et al. (2023). Here, we aim to identify drag- or energy-optimal acceleration phase length (T_a in figure 1(a)). Second, we used a truncated Fourier series to express the waveform and aim to determine the energy-optimal Fourier coefficients.

These seemingly simple optimisation problems conceal a significant challenge, arising from the chaotic nature of turbulence. Figure 1(b) shows the wall stress τ_w and energy input P for three periods of a pulsatile run as in figure 1(a), unveiling that per-period quantities show significant noise. The noise amplitude is inversely proportional to the square root of the number of periods considered in the DNS, making accurate evaluations of $\mathscr{J}$ computationally expensive and rendering gradient-based optimisation algorithms infeasible.

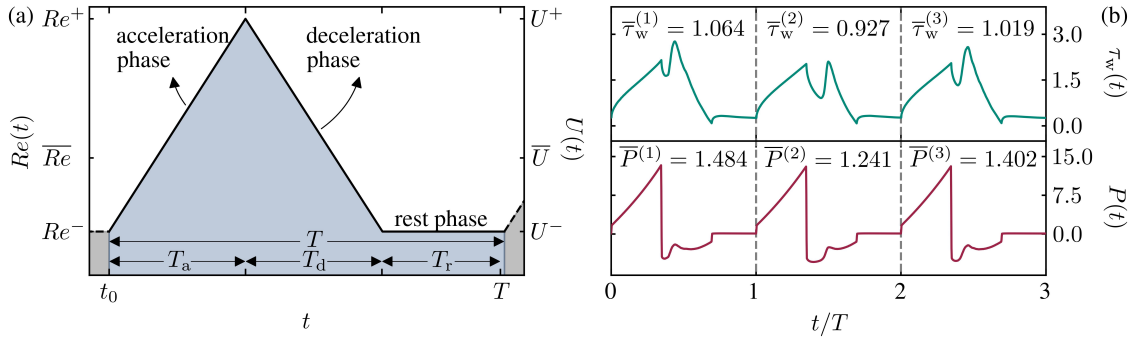

Figure 1: (a) Schematic description of the considered triangular waveforms in terms of the time variant Reynolds number $Re(t)$ or bulk velocity $U_\eta(t)$. (b) The wall shear stress $\tau_w(t)$ and power input $P(t)$ over three periods of a pulsatile run driven as in (a) where $T_a = 0.35T$.

We show that Bayesian optimisation — a global data-driven optimisation technique for black-box functions that feature stochastic noise — is a valuable tool for our problem and possibly for other optimisation problems where the objective results from finite-time-averaging of turbulent flows.

At $Re = 5160$, energy-optimal waveforms reduce the total energy expenditure by up to 12 % while reducing drag by up to 22 %, when compared to steady driving. At elevated Reynolds numbers ($Re = 8600$) energy consumption is decreased by up to 23 %, while drag is reduced by 37 %. After modifying our optimal waveforms with different techniques, we show that the drag and energy reductions are rooted in two physical mechanism: (1.) the delayed onset of turbulence caused by low minimum velocity and steep acceleration and (2.) wall-distant localization of turbulence. Our results pinpoint that the predominant, steady operation mode of pumping fluids through pipes is far from optimal.

References

FRENNING, L., 2001: *Pump life cycle costs — a guide to LCC analysis for pumping systems.* Brussels, Belgium: Hydraulic Institute & Europum, ISBN: 978-1-935762-89-8.

BLASIUS, H., 1913: *Mitteilungen über Forschungsarbeiten auf dem Gebiete des Ingenieurwesens – das Ähnlichkeitsgesetz bei Reibungsvorgängen in Flüssigkeiten.* Springer Berlin Heidelberg 131, 1–41.

GARCÍA-MAYORAL, R. & JIMÉNEZ, J., 2011: *Drag reduction by riblets.* Philosophical Transactions of the Royal Society A: Mathematical, Physical and Engineering Sciences 369 (1940), 1412–1427.

MARENSI, E, WILLIS, A. P. & KERSWELL, R. R., 2019: *Stabilisation and drag reduction of pipe flows by flattening the base profile.* Journal of Fluid Mechanics 863, 850–875.

KÜHNEN, J. SONG, B., SCARSELLI, D., BUDANUR, NAZMI B., RIEDL, M., WILLIS, A. P., AVILA, M. & HOF, B., 2018: *Destabilizing turbulence in pipe flow*. Nature Physics 14 (4), 386–390.

QUADRIO, M. & RICCO, P., 2004: *Critical assessment of turbulent drag reduction through spanwise wall oscillations.* Journal of Fluid Mechanics 521, 251–271.

AUTERI, F., BARON, A., BELAN, M., CAMPANARDI, G. & QUADRIO, M., 2010*: Experimental assessment of drag reduction by traveling waves in a turbulent pipe flow*. Physics of Fluids 22 (11).

FOGGI ROTA, G., MONTI, A., ROSTI, M. E. & QUADRIO, M., 2023a: *On–off pumping for drag reduction in a turbulent channel flow.* Journal of Fluid Mechanics 966.

FOGGI ROTA, G., MONTI, A., ROSTI, M. E. & QUADRIO, M., 2023b: *Saving energy in turbulent flows with unsteady pumping*. Scientific Reports 13 (1).

SCARSELLI, D., LOPEZ, J. M., VARSHNEY, A. & HOF, B., 2023: *Turbulence suppression by cardiac-cycle-inspired driving of pipe flow.* Nature 621 (7977), 71–74.

SOUMA, A., IWAMOTO, K. & MURATA, A., 2009: E*xperimental investigation of pump control for drag reduction in pulsating turbulent pipe flow.* In Proceeding of Sixth International Symposium on Turbulence and Shear Flow Phenomena, pp. 761–765. Begellhouse.

Mitteilung

Fachgruppe: Strömungsbeeinflussung

DNW-NWB Wind Tunnel Experiments for Efficient Sequential Suction

H. Lüdeke (Heinrich.luedeke@dlr.de)
R. von Soldenhoff (Richard.vonSoldenhoff@dlr.de)

DLR, Institut für Aerodynamik und Strömungstechnik
Lilienthalplatz 7, 38108 Braunschweig

Investigations of multiple suction surfaces for the laminarization of future aircraft fuselages are carried out on a flat-plate model in the DNW-NWB wind tunnel facility. Different configurations of multiple suction panels are arranged on the five meter long flat plate for extended laminarization. Up to four sequential suction panels are installed simultaneously and operated at reference Reynolds numbers of up to 20 million. The fundamental approach for fuselage laminarization consists in suction walls for boundary layer stabilization and alternating regions without suction, where the flow field is kept laminar until the next suction wall starts.

Former DNW-NWB experiments are conducted on the modular flat-plate model (see Fig. 1) between 2019 and 2025 to demonstrate the efficiency of different suction concepts under various inflow conditions and suction rates. Based on an aerodynamically shaped nose and an adjustable trailing edge flap for adjusting the surface pressure distribution, the total chord length of the model is 5m.
The modular approach allows an exchange of single wall elements, called panels, with suction surface or closed heated wall for infrared thermography. Instrumented panels with hot wire traversing or hot films are optional for detailed investigations of boundary layer instabilities.
While suction panels in the front part have an 1.3m extent, the rear middle area allows smaller 500mm wide panels (see Fig. 1). The streamwise panel-dimensions are 200mm, 400mm or 600mm for both, heated closed panels or suction walls [1].

Streamwise pressure distributions can be adjusted by the trailing edge flap or the angle of attack to ensure transition on the 4m flat part for all flow conditions between 20m/s and 60m/s without suction. The suction rates are determined either by using a Laminar Flow Meter for single panels, or a rotary flow meter for multiple large 1.3m panels. For all suction regions, dimensionless volume rates up to $c_Q = 1 \cdot 10^{-3}$ are reached by this setup.

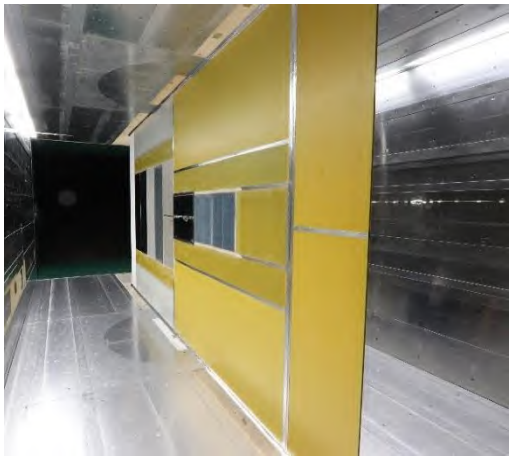

Abbildung 1: Model with various suction walls in the DNW-NWB

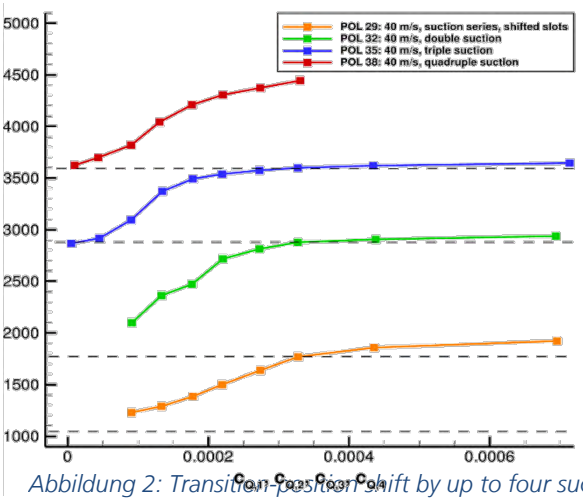

Abbildung 2: Transition-position shift by up to four suction surfaces

Past experiments have successfully shown capacities of different slotted or laser drilled suction surfaces at 50 micron suction diameter, as well as 3D printed panels or different etched TSSD concepts using a 50 micron metal foil. The current setup allows up to five successive porous panels for boundary layer laminarization along the complete model downstream to the trailing edge at high Reynolds numbers [1].

The results of this campaign answer important questions, like how to keep a complete fuselage laminar by using a large number of suction walls, alternating with closed smooth walls [2]. Fig. 2 shows transition positions from infrared thermography on the heated panels at varying c_q on the last suction panel. It confirms the previous question positively, since every added porous wall shows approximately the same growth of the laminar region, even by using in total four suction panels. Consequently, the chosen setup seems to be applicable for fuselage laminarization.

After previous NWB investigations have shown a generally shorter laminar region than predicted by the classical linear stability theory at a constant critical amplification rate for all c_q [3], the results of this campaign allow additional suction surfaces along the whole model chord to laminarize large areas of a near zero pressure gradient boundary layer [4].

Another important result, concerning the distance between suction panels, is the fact, that laminar regions have to extend large parts of the following suction panel. This will allow the damping of boundary layer instabilities by this next suction surface and is essential in practice to keep the downstream area laminar for adding the next stabilizing surface-part.

This work is part of the multi-disciplinary project LamTA (Laminar Tailored Aircraft) which aims to investigate the maximum potential of laminar technologies to reduce the energy consumption in flight. We would like to acknowledge the funding by the Deutsche Forschungsgemeinschaft (DFG, German Research Foundation) under Germany's Excellence Strategy EXC 2163/1 - Sustainable and Energy Efficient Aviation Project-ID390881007.

Literatur:

[1] R. von Soldenhoff: Overview of the Wind Tunnel Tests with Suction in the DNW-NWB, in New Results in Numerical and Experimental Fluid Mechanics XIV - Contributions to the 23rd STAB/DGLR Symposium, Berlin. Springer Verlag, 2023

[2] R. von Soldenhoff, H. Lüdeke, et.al.: Hot-Wire Measurements in sequentially sucked Boundary Layers, 24th STAB/DGLR Symposium, 13.-14.11.2024 Regensburg

[3] H. Lüdeke, R. von Soldenhoff, P. Weigmann, K. Thamm: Critical N-Factor behavior in HLFC applications, 24th STAB/DGLR Symposium, 13.-14.11.2024 Regensburg

[4] K. Thamm, R. von Soldenhoff, et.al.: Experimentelle Untersuchung Sequentieller Absaugung. In: Deutscher Luft- und Raumfahrtkongress 2024, 30.9.-2.10.2024 Hamburg

Mitteilung

Fachgruppe: Strömungsbeeinflussung

Onset of Turbulence in Particle-laden Pulsatile Pipe Flow Experiments with a Physiological Waveform

Larissa Richter[1,2], Bastian Bäuerlein[1,2] und Kerstin Avila[1]
[1] Institute of Physics and ForWind, University of Oldenburg, Ammerländer Heerstrasse. 114-118, 26129 Oldenburg, Germany
[2] Center of Applied Space Technology and Microgravity (ZARM), University of Bremen, Am Fallturm 2, 28359 Bremen, Germany
kerstin.avila@uni-oldenburg.de

Particle-laden flows are present in many engineering processes and biological systems. In the case of the human cardiovascular network the unsteady (pulsatile) nature of the flow raises the complexity even further. Irregular flow patterns or turbulent structures can locally elevate the shear stress at the inner layer of the blood vessels, potentially connecting high turbulence levels with the occurrence of cardiovascular diseases. This hypothesis is supported by atherosclerosis, which tends to occur in regions of arteries that exhibit turbulent blood flow [1] and is one of the main causes of death worldwide [2].

Little is known about the onset of these types of flow structures in pulsatile flow. Recent numerical studies indicate a high susceptibility of the flow to turbulence transition at flow parameters typically found in cardiovascular flows [3]. Small geometric defects at the pipe wall can trigger helical flow patterns during the deceleration phase that collapse and break up into turbulence at certain phases of the period (helical instability) [3,4].

This study expands upon this research by using other types of perturbations and a physiological waveform with an increased range of pulsation frequencies. The pulsation frequency is especially important for physiological flows, since the heart rate may temporarily accelerate or decelerate throughout the day depending on stress level, excitement or activity level. The pulsation frequency changes the intrinsic time scale of the flow, thus the time that is available for turbulence to develop in each pulsation period. Due to viscous forces, a change of the pulsation frequency also changes the flow profile (Sexl-Womersley profile). At certain frequencies, inflection points appear in the Sexl-Womersley profile (see figure 1). Recent numerical studies indicate that the presence of inflection points makes the flow susceptible to instabilities, like the aforementioned helical instability [3].

Our findings indicate a strong dependency of the transition scenario in pulsatile flow on the type and intensity of the perturbation. We distinguish between low amplitude perturbations, where turbulence develops from a helical instability in the deceleration phase, and large amplitude perturbations, where our results reveal a distinctly different mechanisms for turbulence transition compared to previous studies. To investigate the influence of strong amplitude perturbations, we use two specific types of perturbations: a (local) geometric bending of the pipe wall or alternatively the introduction of suspended particles into the flow. We observe that both the strong amplitude perturbation from Dean-vortices in the bending, and the vortices in the particle wake (see figure 2) expedite the turbulence onset, causing a turbulent patch to appear already during the acceleration phase.

To analyse the flow field, we use 3D Lagrangian particle tracking with the Shake-The-Box algorithm [5]. We observe in both cases that the turbulence completely disrupts the Sexl-Womersley profile and its inflection points, thereby inhibiting any growth of a helical instability in the deceleration or low-velocity phase. In contrast to the phase-locked helical instability, this second transition scenario is dominated by the pulsation frequency, with longer pulsation

periods showing an earlier onset with larger turbulence structures of higher magnitudes. Especially in physiological flows with naturally strong perturbation levels, such as the aortic arch, this mechanism might be the most relevant for the turbulence production.
Our results reveal distinctly different mechanisms for turbulence transition in pulsatile pipe flow compared to previous studies and further highlight the importance of considering various instability mechanisms in the analysis of pulsatile flows with a cardiovascular waveform.

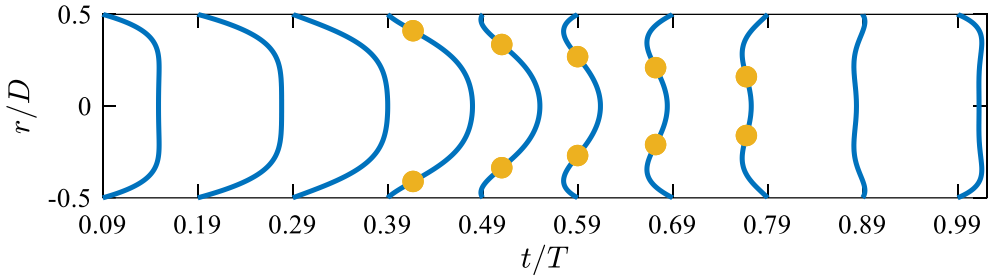

Figure 1: Sexl–Womersley velocity profiles for pulsatile flow with a harmonic waveform with $(Re)^{-} = 2500$, Wo=5.6 and A=1. The inflection points in the velocity profiles are marked by circles.

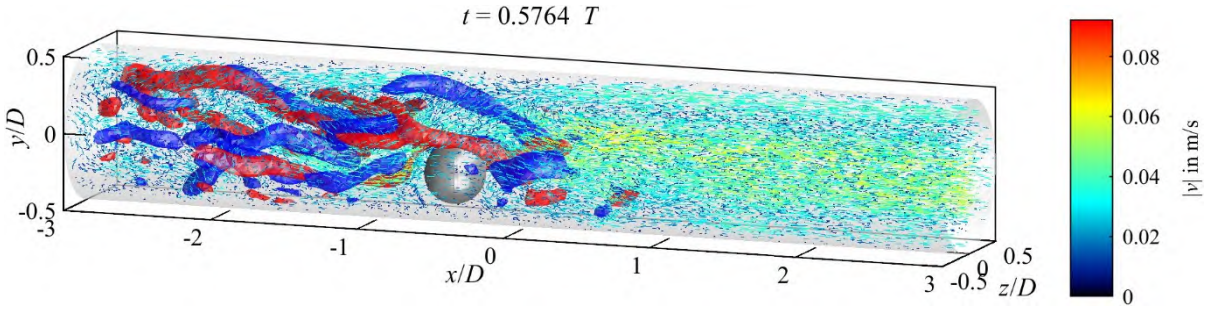

Figure 2: Emerging turbulence patches in pulsatile flow with a physiological waveform in the wake of a large particle with Lagrangian particle tracking measurements. Red/blue structures indicate streaks of the streamwise vorticity.

References

[1] Björkegren, J. L. M., & Lusis, A. J. (2022). Atherosclerosis: Recent developments. *Cell, 185* (10), 1630–1645. https://doi.org/10.1016/j.cell.2022.04.004

[2] Kim, H., Kim, S., Han, S. et al. (2019). Prevalence and incidence of atherosclerotic cardiovascular disease and its risk factors in Korea: a nationwide population-based study. *BMC Public Health 19*, 1112. https://doi.org/10.1186/s12889-019-7439-0

[3] Morón, D., Feldmann, D., & Avila, M. (2022). Effect of waveform on turbulence transition in pulsatile pipe flow. *Journal of Fluid Mechanics*, *948*, A20. https://doi.org/10.1017/jfm.2022.681

[4] Xu, D., Varshney, A., Ma, X., Song, B., Riedl, M., Avila, M., & Hof, B., (2020). Nonlinear hydrodynamic instability and turbulence in pulsatile flow, *Proc. Natl. Acad. Sci. U.S.A. 117* (21) 11233-11239, https://doi.org/10.1073/pnas.1913716117

[5] Bäuerlein, B., Avila, K., (2025). Pulsatile pipe flow experiment to study particle–fluid interactions using Lagrangian flow measurements. *Review of Scientific Instruments, 96* (7): 075204. https://doi.org/10.1063/5.0254258

Mitteilung

Fachgruppe: Strömungsbeeinflussung

Numerical analysis of surface jets for load alleviation on transport aircraft

Florian Siebert[*§], Till Strothteicher[*‡], André Bauknecht[*§]
[*]Cluster of Excellence SE²A - Sustainable and Energy Efficient Aviation
[‡]DLR Institute of Flight Systems, Lilienthalplatz 7, 38108 Braunschweig
[§]Institute of Fluid Mechanics, Technische Universität Braunschweig
Hermann-Blenk-Str. 37, 38108 Braunschweig, Germany
florian.siebert@tu-braunschweig.de

Effective alleviation of aerodynamic peak loads, caused by gusts or manoeuvres, allows significant reductions in wing-structure mass and overall energy consumption. Traditional control surfaces, like trailing edge flaps, are limited by deflection rates [1], whereas fluidic actuators, such as wall-normal surface jets, use pressurized air to achieve a much faster response [2]. The surface-jet actuator chosen for this study consists of a thin, planar air jet that is issued from a slot on the upper side of the wing under a certain angle against the outer flow, thus creating a separation region downstream of the jet location. As shown in the concept sketch in Fig. 1, the flow deflection at the trailing edge is reduced by the separation, which results in an effective de-camber of the wing section and consequently lower lift.

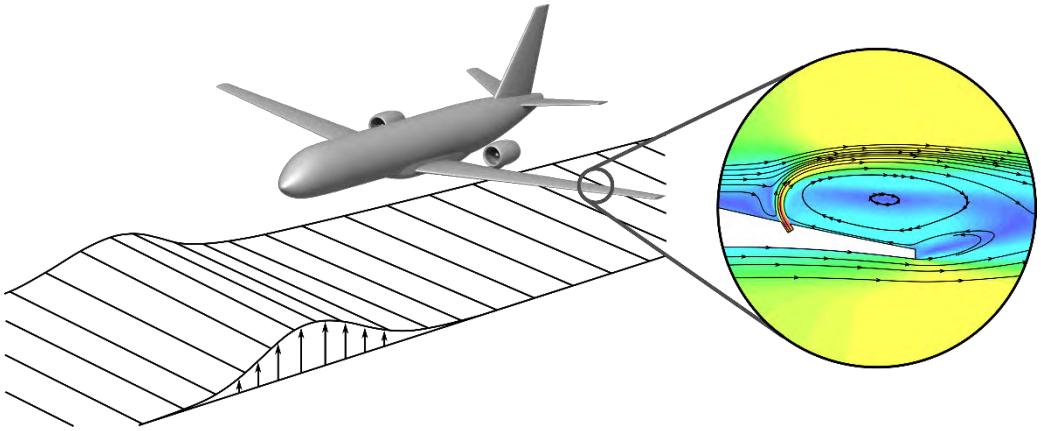

Figure 1 : Concept sketch of a surface jet for gust load alleviation integrated into a transport aircraft wing

Two main objectives are pursued in this work. First, the actuator's mass flow demand for a certain actuation target is to be minimized. Second, actuator integration on a three-dimensional elastic wing is investigated regarding control authority under consideration of aeroelastic effects. A parametric study on 2D actuator design is presented based on RANS simulations on a representative wing section of a medium range transport aircraft. The simulations were carried out using the unstructured finite volume solver DLR-TAU with SA-negative turbulence modelling. Selected actuator geometries were subsequently investigated regarding their performance under various flight conditions. A comprehensive CFD dataset of Reynolds number, Mach number, and angle of attack variation was generated and a reduced order model of actuator performance derived. The model was implemented in a low-fidelity aeroelastic framework featuring aerodynamic airfoil data including transonic flow effects coupled with a linear beam-element model to study aeroelastic effects of the actuator and sensitivities regarding spanwise positioning.

The design study shows the importance of the slot width as a design parameter to balance mass flow against jet velocity and thus compressor power. For a compressor-constrained pressure ratio, the mass flow can be reduced by about $40\ \%$ compared to earlier studies [3] by employing a slot width of $0.05\ \%$ relative to the chord length. A reduction of actuator efficiency regarding jet momentum has to be taken into account for supersonic jet velocities.

Regarding the second objective, a variation of chordwise position (see Fig. 2) shows that an actuator located at $x/c = 80\,\%$ with chord length c provides the highest reductions of lift coefficient c_l under cruise flight conditions but also causes significant nose-up pitching moment $c_{m,y}$. This leads to reduced aeroelastic effectiveness on the flexible wing compared to the actuator located at $x/c = 60\,\%$. This actuator has a significantly lower pitching moment influence at only slightly impaired authority on lift reduction. As shown in Fig. 3, this combination enables it to achieve around 20% reduction of wing root bending moment (WRBM) relative to the cruise value in both subsonic and transonic flight at a mass flow rate below $1.5\ \mathrm{kg/s}$. The actuator at $x/c = 80\,\%$, however, outperforms its upstream counterpart at low blowing rates, especially when located further inboard on the wing. Conventional ailerons yield less wing root bending moment reduction due to their increased pitching moment causing an adverse wing twist. The sensitivity analysis on spanwise positioning shows for both chordwise positions that an optimal location is found at the second most outboard actuator section investigated here (reaching from 69 % to 81 % half-span). This position offers a good balance of, on the one side, a relatively high spanwise lever arm and impact on the lift distribution to reduce the bending moment, and on the other side only moderate performance reduction due to twist deformation and 3D effects towards the wing tip. On-going studies using CFD-CSM coupled simulations further investigate spanwise actuator positioning and sizing for effective alleviation of gust-induced loads.

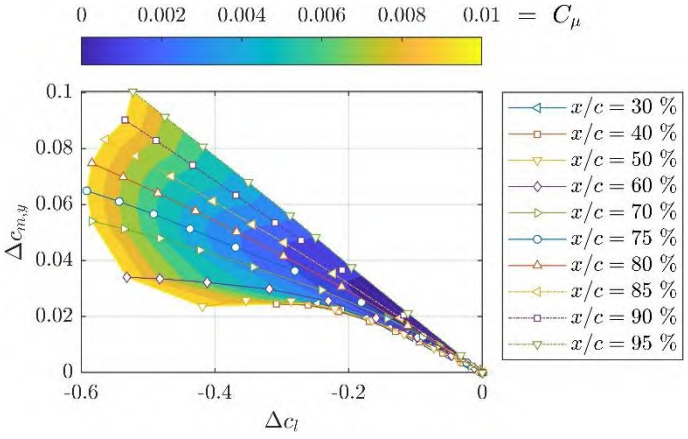

Figure 2: Change of lift and pitching moment for varying jet momentum coefficients C_μ at different chordwise positions

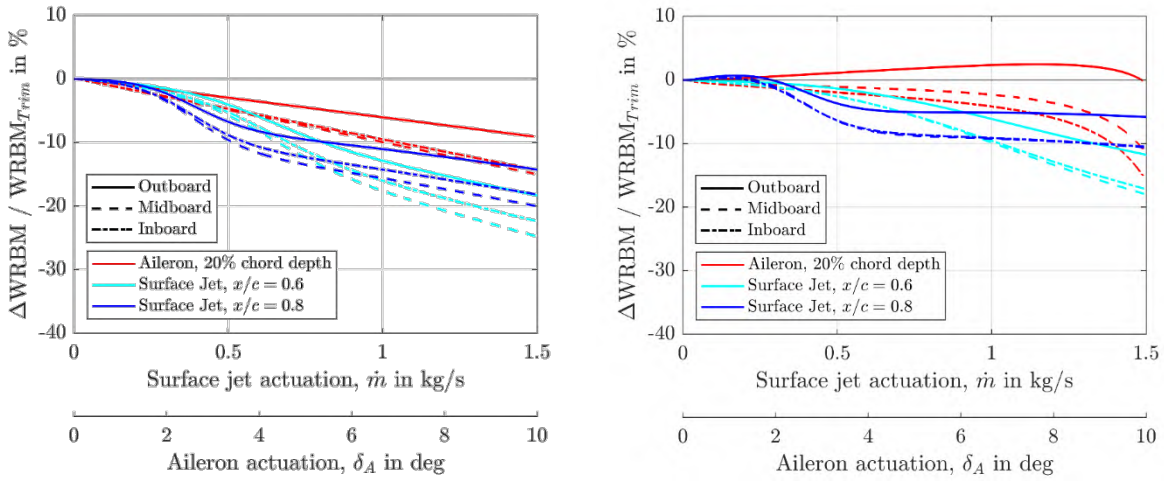

a) $M_\infty = 0.5$ b) $M_\infty = 0.76$

Figure 3: Aeroelastic effectiveness of surface jets compared to ailerons for three wingspan positions

References:

[1] Hillebrand, M., Breitenstein, C., and Lutz, T., "Aeroelastic Effects of a Load Alleviation System on a High Aspect Ratio Wing Based on CFD-CSM Simulations," AIAA Aviation Forum and Ascend 2024, AIAA 2024-3841, 2024.

[2] Asaro, S., Khalil, K., and Bauknecht, A., "Unsteady Characterization of Fluidic Flow Control Devices for Gust Load Alleviation," New results in numerical and experimental fluid mechanics XIII: Contributions to the 22nd STAB/DGLR Symposium, edited by A. Dillmann, G. Heller, E. Krämer, and C. Wagner, 2021, pp. 153–163.

[3] Khalil, K. and Bauknecht, A., "Fluidic Flow Control Devices for Gust Load Alleviation," Journal of Aircraft, Vol. 61, No. 4, 2024, pp. 1–14.

Mitteilung

Fachgruppe: Strömungsbeeinflussung

LES/URANS of heat transfer enhancement due to Kelvin-Helmholtz instability on finned channel

Denis Sotomayor-Zakharov, Peter Scholz
Institute of Fluid Mechanics, TU Braunschweig, Hermann-Blenk-Straße 37, 38106, Braunschweig, d.sotomayor-zakharov@tu-braunschweig.de

Introduction

Finned surfaces are widely used for cooling applications, relying on the enhancement of wetted surface area to increase the heat transfer, although with the consequence of increasing the total drag. Previous research seeking to increase the heat transfer vs. drag ratio RA has shown that Kelvin-Helmholtz instabilities due to velocity gradients at the fin edge can enhance heat transfer with a lower drag increase [1][2]. Since the this research has been performed via DNS, it is of interest to study if LES and URANS approaches can capture such effect, and, therefore, be used for the engineering of fin configurations. This study is performed on a finned channel configuration based on the DNS of Kuwata [1]. URANS and LES are carried at $Re_\tau = 300$ based on the u_τ at $y = 0$, for $Pr = 1.0$ following the original study, and for $Pr = 0.75$, which represents air.

Numerical setup

The numerical domain is a half channel shown in Figure 1, with $L_x = 6h$ and $L_z = 3.3h$. The fins present a height of $h_f/h = 0.67$ and a thickness $w/h = 0.05$. A fin separation of $s/h = 0.2$ was selected since maximum RA is achieved at this value [1]. The cutcell mesh presents $\Delta x^+ = 5 \rightarrow 40$ and $\Delta z^+ = \Delta y^+ = 2.5 \rightarrow 20$, while the fins present a boundary layer mesh with $\Delta y_0^+ = 1$. The study was carried in ANSYS FLUENT 2023R2, having been used before for LES on rough surfaces [3]. The subgrid-scale WALE model is selected for the LES, with $C_w = 0.325$ and $Pr_{sgs} = 0.85$, while for the URANS, the SST k-ω model is used, with a $Pr_t = 0.85$.

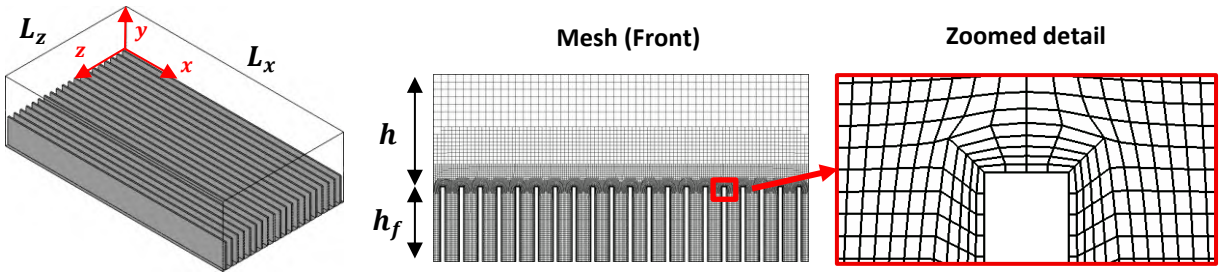

Figure 1: Domain and mesh for finned channel

Results

A comparison of values of u^+ and T^+ vs. y/h is shownin Figure 2. URANS and LES capture the DNS behavior. Still, LES captures the DNS profiles more accurately for $y > 0$.

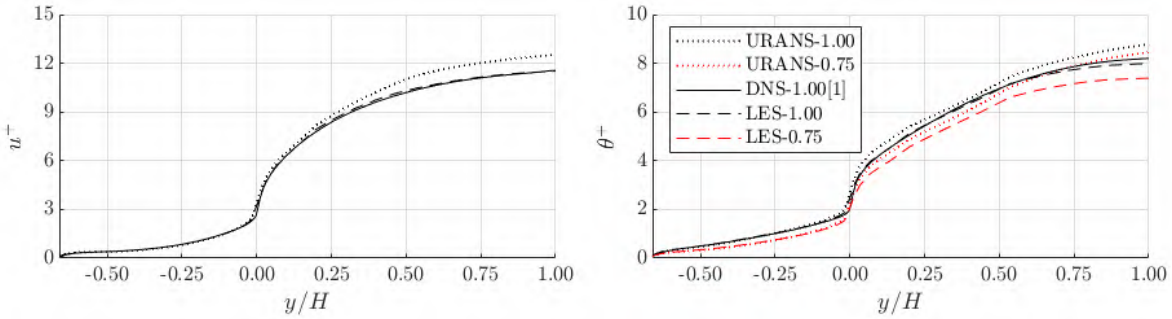

Figure 2: u^+ and θ^+ vs. y/h for all simulated cases.

T^+ vs. y/h shows that cases at $Pr = 0.75$ present higher heat transfer capability. This is seen in table 1, where the values of $RA = 2St/C_f = U_b^+/T_b^+$ are presented. The accuracy of LES and URANS approaches can be noted. An RA increase of 10% can be seen when lowering $Pr = 1$ towards $Pr = 0.75$.

Table 1: Comparison of RA

	DNS Pr = 1	LES Pr = 1	Rel.Err. (%)	URANS Pr = 1	Rel. Err. (%)	LES Pr = 0.75	URANS Pr = 0.75
RA	1.45	1.46	0.53	1.45	0.01	1.59	1.61

Figure 3 displays iso-surfaces of $q_{crit}^+ = 0.002$ of LES and URANS results, as well as contours of instantaneous temperature θ^+. URANS manages to resolve Kelvin-Helmholzt instability-induced rollers.

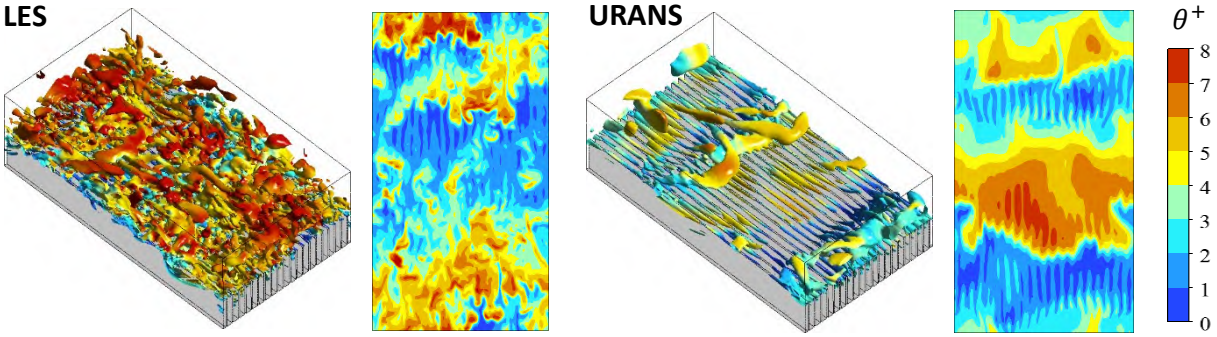

Figure 3: Iso-surfaces of $q_{crit}^+ = 0.002$ and contours of instantaneous θ^+ (xz plane at $y^+ = 10$).

Figure 4 presents a comparison of resolved $-\overline{u'v'}$ and $-\overline{v'\theta'}$, as well as their pre-multiplied cospectra. LES resolves most of the energy exchange present between u, v and T, although at a larger λ_x/H mode. Interestingly, URANS resolves part of the main energy-exchange mode.

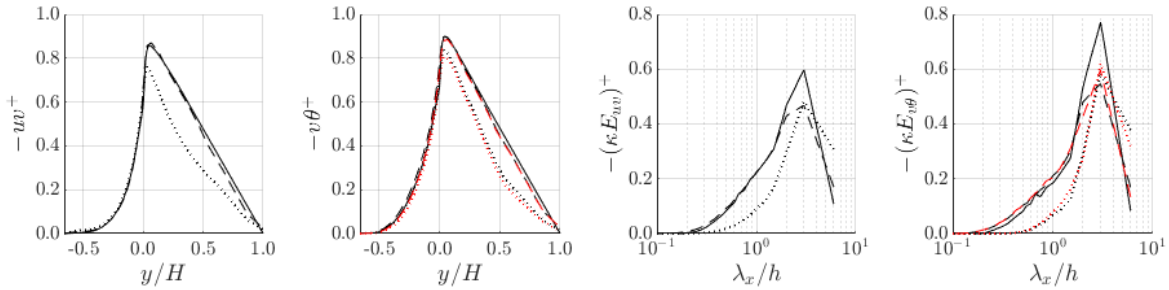

Figure 3: $-\overline{u'v'}$ and $-\overline{v'T'}$ vs. y/h, as well as their pre-multiplied cospectra (legend as of Figure 2).

Conclusions

URANS and LES can be used to capture the heat transfer enhancement of Kelvin-Helmholtz instabilities. Higher values of Re_τ will be tested, as well as on turbulent boundary layers over fins.

Acknowledgment

This project has received funding from the European Union's Horizon Europe research and innovation programme under the Climate, Energy and Mobility grant agreement No 101140559 (FAME). The authors gratefully acknowledge the computing time made available to them on the high-performance computer "Lise" at the NHR Center NHR@ZIB.

References

[1] Kuwata, Y., Dissimilar turbulent heat transfer enhancement by Kelvin–Helmholtz rollers over high-aspect-ratio longitudinal ribs, Journal of Fluid Mechanics 952(A21), 2022. DOI: 10.1017/jfm.2022.915

[2] Rezaei. R.A. et al, *Impacts of passive flow control techniques on Reynolds analogy breakdown*, International Communications in Heat and Mass Transfer 165(B), 2025. DOI: 10.1016/j.icheatmasstransfer.2025.108959

[3] Sotomayor-Zakharov, D., Gaudioso, R., Gallia, M., Embedded LES of a turbulent thermal boundary layer over ice roughness, Computers & Fluids 297, 2025. DOI: 10.1016/j.compfluid.2025.106652

Mitteilung

Fachgruppe: Strömungsbeeinflussung

Influence of Discrete Suction Orifices on Effectiveness of HLFC Surfaces

R. von Soldenhoff (Richard.vonSoldenhoff@dlr.de)
H. Lüdeke (Heinrich.Luedeke@dlr.de)
Deutsches Zentrum für Luft- und Raumfahrt (DLR), Institut für Aerodynamik und Strömungstechnik, Lilienthalplatz 7, 38108 Braunschweig

To effectively apply Hybrid Laminar Flow Control (HLFC) for drag reduction of transport aircraft, it is desirable to achieve the largest possible laminar flow region with given suction power. Therefore, experimental as well as numerical studies are conducted at DLR.

In past wind tunnel tests with a flat plate with suction in the DNW-NWB, differences in the effectiveness of different suction orifice geometries have been found [1,2]. These are investigated in more detail in recent wind tunnel measurements. Two slotted geometries are compared with nearly homogeneous suction through a four-layer wire mesh (see Fig. 1). Transition locations are determined by infrared thermography, hot-wire and hot-film sensors are used to determine amplitudes of Tollmien-Schlichting waves.

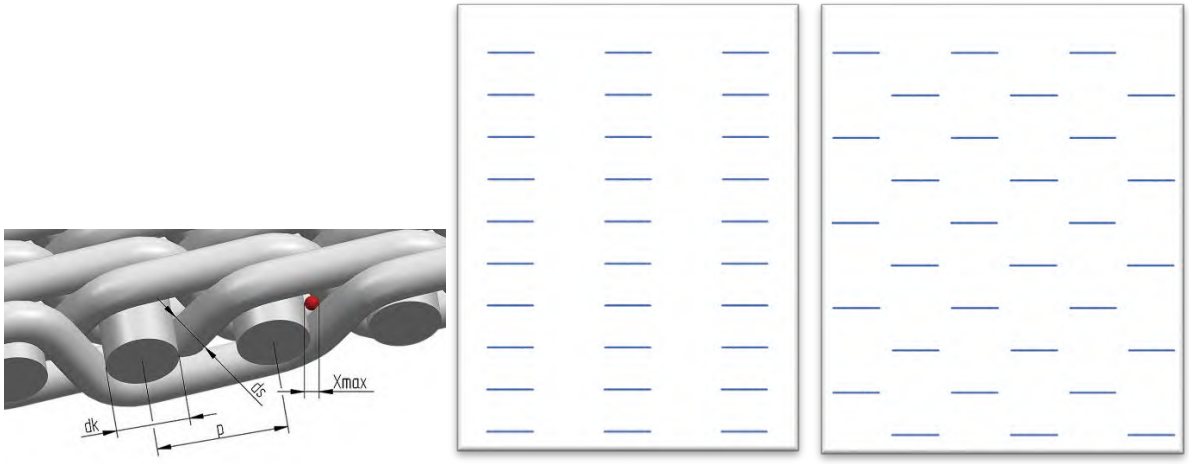

(a) (b) (c)

Figure 1: Pore geometries. (a): wire mesh, pore size 9 µm, from [3], (b): staggered slot pattern, slot size 2 x 0,045 mm², (b): shifted slot pattern, slot size 2 x 0,045 mm²

Accompanying the experiments, Direct Numerical Simulations (DNS) of Tollmien-Schlichting waves propagating over discrete suction orifices are carried out. They resolve the three-dimensional disturbances introduced by the suction orifices as depicted in Fig. 2. It can be shown in agreement between experiment and simulation, that certain slot patterns lead to additional stabilisation by longitudinal vortices. This leads to a further down-stream shift of transition additionally to the known stabilising effect of suction. The results match the findings from [4], where a stabilising effect from longitudinal vortices, introduced by discrete roughness elements, is described.

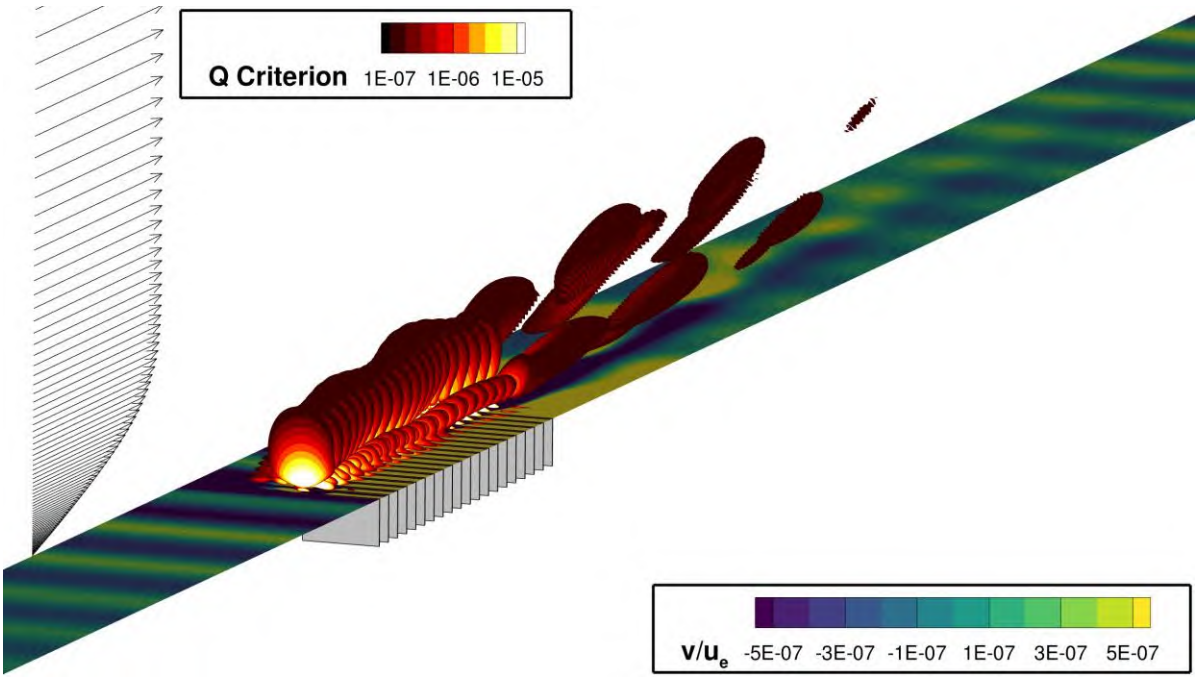

Figure 2: Wall-normal velocity of the disturbance and visualisation of longitudinal vortices by the Q-criterion (DNS results)

The results suggest that by targeted design of suction surfaces, their effectiveness can be improved significantly, which can enhance the benefit of an HLFC system.

The work was part of the DLR project LamTA. We would like to acknowledge the funding by the Deutsche Forschungsgemeinschaft (DFG, German Research Foundation) under Germany's Excellence Strategy—EXC 2163/1 – Sustainable and Energy Efficient Aviation—Project-ID 390881007. The authors gratefully acknowledge the scientific support and HPC resources provided by the German Aerospace Center (DLR). The HPC system CARA is partially funded by "Saxon State Ministry for Economic Affairs, Labour and Transport" and "Federal Ministry for Economic Affairs and Climate Action." The HPC system CARO is partially funded by "Ministry of Science and Culture of Lower Saxony" and „Federal Ministry for Economic Affairs and Climate Action".

Literature:

[1] R. von Soldenhoff, H. Lüdeke: "Interaction of Boundary Layer and Suction Chamber of a Laminarization System", AIAA Journal, Vol. 63, No. 4 (2025), doi/abs/10.2514/1.J064184

[2] R. von Soldenhoff, H. Lüdeke: "Entwicklung und Erprobung neuartiger Absaugoberflächen zur Laminarhaltung der Grenzschicht", DLRK (2022)

[3] Haver & Boecker: https://www.haverboecker.com/de/produkte/filtergewebe/minimeshr-spezifikationen/#image-5095, accessed on 09 September 2025

[4] J. Fransson, A. Talamelli, L. Brandt, C. Cossu: "Delaying Transition to Turbulence by a Passive Mechanism", PRL 96, 064501 (2006)

Mitteilung

Fachgruppe (Topic Group): Transportflugzeugkonfigurationen

Parametric investigation of the flow-physical effects of Boxwing-Configurations in combination with Distributed Electric Propulsion in cruise and STOL conditions

Alex Gothow, Thomas Grund, Julien Weiss
Technische Universität Berlin, Institute of Aeronautics and Astronautics,Marchstraße 12 10587 Berlin, a.gothow@tu-berlin.de

The present study is part of the LuFo project DOXWING, which investigates the synergy effects between boxed-wing configurations (BW) and distributed propulsion systems (DP), with the aim of quantifying the aerodynamic advantages and conceptual performance gains for medium-range transport aircraft based on the ATR72-500 taken as reference.
The BW geometry reduces induced drag and increases span efficiency compared to conventional cantilever wings, while DP further augments aerodynamic efficiency through propeller–wing interaction effects such as slipstream blowing and swirl recovery. [1, 2] Building on previous conceptual design studies, the boxed-wing architecture is shown to achieve glide-ratio improvements of up to 14% and a reduction of fuel consumption of around 9% relative to conventional reference aircraft. [1] It also shows that the BW aircraft benefits from rising oil prices, with direct operating costs per nautical mile falling by up to 10% compared to a conventional reference aircraft as oil prices rise. [3] Distributed propulsion integration has been demonstrated to provide additional aerodynamic gains and mission-level benefits, with system-level design studies reporting significant improvements in fuel efficiency. [4] Recent investigations of distributed propeller placement confirm that wingtip-mounted or partially distributed configurations can achieve greater cruise efficiency than uniform spanwise distributions. [5, 6]
The present work proposes that merging the boxed-wing layout with distributed propulsion can amplify the induced-drag reduction of the wing with the efficiency benefits of propeller–wing integration.
The wing model used is based on a NACA65(3)-218 airfoil that is scaled to a chord length of 150mm with a wingspan of 1000mm for each wing. The high-lift system consists of a simple hinged flap on both wing with a chord of 45mm. Figure 1 represents the model inside the low speed wind tunnel NWK at the Chair of Aerodynamics at TU-Berlin with a horizontal gap of both wings of 0.6 chords and a stagger of 1 chord. In the present project a prop with 256mm diameter with constant pitch from Ramoser (varioProp) is used.

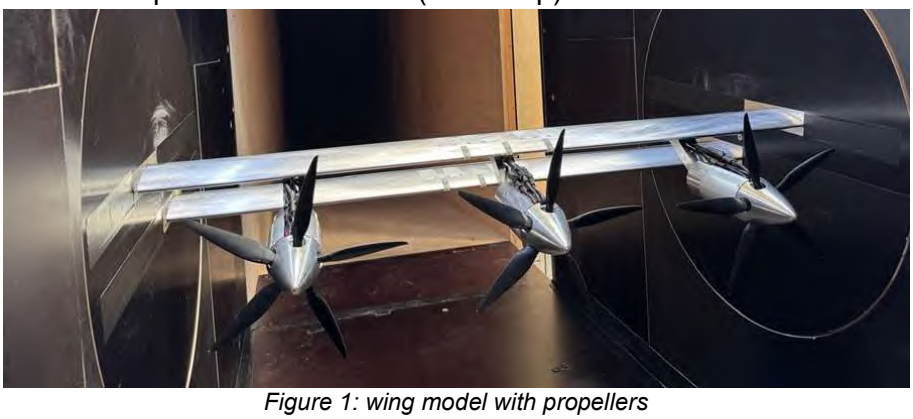

Figure 1: wing model with propellers

Parameter Study:
The main objective of this study is to perform a parameter study with the following settings while investigating the propeller slipstream effects with focus on laminar flow:

- The stagger is ranging from -3 to 3 (positive and negative stagger).
- The propeller arrangement is preset to three different positions with tractor and OTW mountings.

- For each propeller arrangement, the propeller position can be varied in streamwise direction, while the vertical direction is fixed.
- The wing inclination angle can be varied up to ±15°.
- The flap angles of each wing are variable up to ±45°.
- Duing the initial study, the gap is fixed at 0.6 chords.

Initial Results:
Figure 2 shows initial results comparing the unpowered single wing (blue) wih the unpowered bi-plane configuration in planar setting (red), where the stagger is 0, the unpowered non-planar bi-plane setting (magenta), where the stagger is 1 and the powered non-planar bi-plane setting (cyan). The figure shows that the planar configuration results in a decrease of lift coefficient while the non-planar setting results in an increase of lift coefficient. That indicates that the stagger has significant influence on lift coefficient even in the unpowered scenario. Adding distributed propulsion to this configuration results in an additional increase in lift coefficient of about 32.7%.

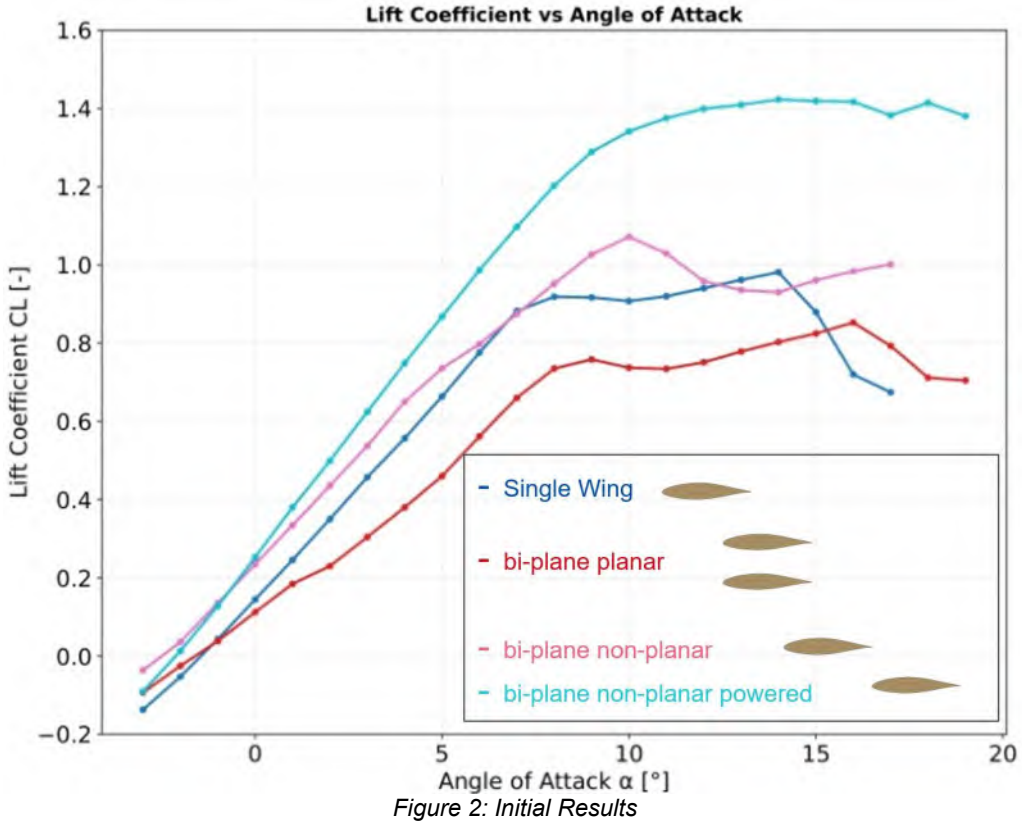

Figure 2: Initial Results

References
[1] Schiktanz, Daniel & Scholz, Dieter. (2011). Box Wing Fundamentals – An Aircraft Design Perspective. Journal of Aircraft.
[2] Keller, D. Towards higher aerodynamic efficiency of propeller-driven aircraft with distributed propulsion. CEAS Aeronaut J 12, 777–791 (2021). https://doi.org/10.1007/s13272-021-00535-5
[3] Jemitola, Paul & Fielding, J.P.. (2012). Box wing aircraft conceptual design. 28th Congress of the International Council of the Aeronautical Sciences 2012, ICAS 2012. 1. 570-579.
[4] Biser, Filipenko, Boll, Kastner, Atanasov, Hepperle, Keller, Vechtel, Noe: Design Space Exploration Study and Optimization of a Distributed Turbo-Electric Propulsion System for a Regional Passenger Aircraft - AIAA Propulsion and Energy 2020 Forum, 2020
[5] Schollenberger, Michael & Kirsch, Bastian & Lutz, Thorsten & Krämer, Ewald & Friedrichs, Jens. (2024). Aerodynamic interactions between distributed propellers and the wing of an electric commuter aircraft at cruise conditions. CEAS Aeronautical Journal. 15. 10.1007/s13272-023-00706-6.
[6] Tom C. Stokkermans, Sebastiaan Nootebos and Leo L. Veldhuis. "Analysis and Design of a Small-Scale Wingtip-Mounted Pusher Propeller," AIAA 2019-3693. AIAA Aviation 2019 Forum. June 2019.

Supported by:
Federal Ministry for Economic Affairs and Climate Action
on the basis of a decision by the German Bundestag

Mitteilung

Fachgruppe: Transportflugzeugkonfigurationen

Aerodynamic Design of an HLFC Wing for a Long-range Transport Aircraft

Damla San, Samarth Kakkar, Marco Hillebrandt, André Bauknecht, Thorsten Lutz
Institute of Fluid Mechanics, Technische Universität Braunschweig
Hermann-Blenk-Str. 37, 38108 Braunschweig, Germany
damla.san@tu-braunschweig.de

To meet the environmental targets set by Flightpath 2050 [1] while maintaining competitiveness in the international market, new technologies to reduce emissions and fuel consumption must be developed. Aerodynamic design plays a central role in this effort by enabling more fuel-efficient aircraft through reductions in aerodynamic drag. While numerous theoretical concepts for drag reduction exist, their industrial application is often limited. A promising approach with significant potential is the delay of laminar–turbulent transition, thereby maintaining laminar flow over large portions of the aircraft surface. For long-range aircraft with highly swept wings, this can be realized using Hybrid Laminar Flow Control (HLFC) systems [2], which combine natural laminar flow airfoil designs with active flow control techniques such as boundary-layer suction.

This study presents the numerical aerodynamic design and analysis of a long-range passenger aircraft equipped with an HLFC system, conducted within the German LuFo project Multi-Functional Leading Edge for an Energy-Efficient Aircraft (MUVE) funded by BMWE. The reference configuration is based on the high-aspect-ratio wing developed in the INTELWI project [3], featuring a leading-edge sweep of 37° inboard and 32° outboard, a wingspan of 64.80 m, and an aspect ratio of 12.4. The design point corresponds to a cruise condition at $M = 0.83$, $C_L = 0.47$, $Re = 47 \times 10^6$, and a flight altitude of 36000 ft. In the present study, only the clean wing and fuselage are considered, while future work will include the engine to assess its influence on transition.

The HLFC application is restricted to the outer wing section, extending from the engine pylon to the wingtip, where laminar flow is promoted by suction panels along the leading edge in combination with tailored wing-shape modifications. Aerodynamic design and suction distribution optimization are performed at selected airfoil sections along the span using the in-house 2.75D HLFC design tool conFLOW [3] in cruise conditions, while the baseline wing planform and spanwise lift distribution are kept unchanged. The overall reference geometry and representative span locations are shown in Figure 1.

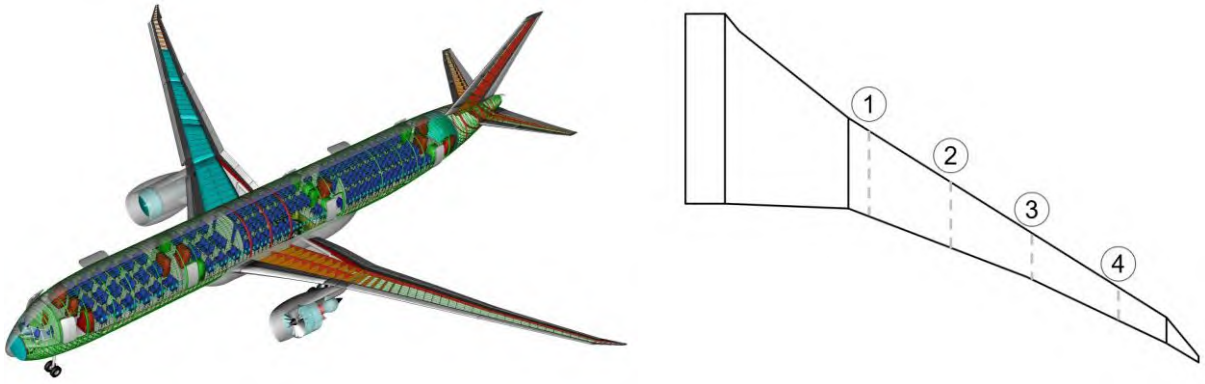

Figure 1 – Reference Geometry and Optimization Sections

conFLOW employs a Bayesian optimization-based methodology, utilizing conFLOW as the black-box analysis function, to minimize drag as a function of airfoil shape and suction distribution under prescribed flow conditions, while satisfying geometric and performance

constraints [5]. The presence of a transition prediction module in conFLOW enables the optimizer to identify the requirement of maximizing the laminar extent of the boundary layer to minimize the aerodynamic drag objective. The tool integrates a 2D flow solver (MSES), a boundary-layer solver (COCO), and a linear stability solver (LILO) to capture viscous crossflow and Tollmien-Schlichting effects consistently. Off-design conditions are incorporated by varying the design lift coefficient by ±0.1, and the total drag is calculated as the sum of drag values at three lift points. To limit rear loading, a minimum pitching moment coefficient of greater than −0.15 was imposed. Additionally, the leading-edge radius was constrained to be no less than 0.8% of the airfoil chord to ensure practical feasibility, while the maximum allowable radius was restricted based on the K-criterion to prevent premature transition caused by attachment line transition. Sections 1 and 2 shown in Figure 1, together with their suction distributions, are obtained directly from conFLOW. To ensure a spanwise-uniform geometry and avoid surface irregularities, the optimized airfoil from Section 2 is also applied to Sections 3 and 4, where twist and suction distributions are adapted to match the target lift distribution. Since Reynolds number variations along the span are small, the aerodynamic characteristics of Section 2 remain valid at the neighboring stations, allowing the same airfoil geometry to be used consistently. Figure 2 presents the pressure distribution and drag polar of the optimized airfoil, which achieves the design cruise lift coefficient of 0.6 and maintains laminar flow up to 60% chord, indicating effective boundary-layer control and low viscous drag.

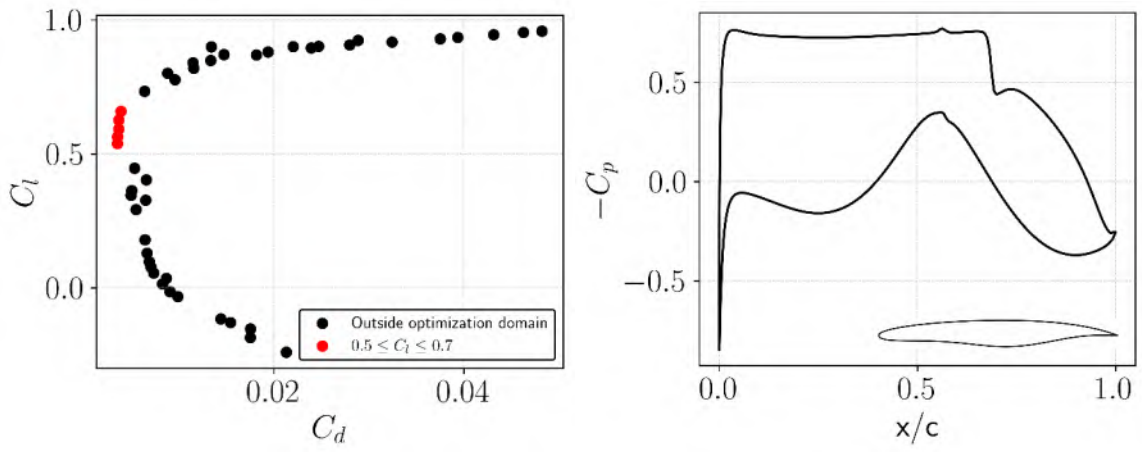

Figure 2 – Drag Polar and Pressure Distribution of the Optimized Airfoil

The wing geometry has been updated with the newly optimized airfoils, and twist optimization is currently being performed using a coupled CFD–structural simulations to better assess the spanwise lift distribution in the deformed flight shape. The next step will be to apply the suction distributions obtained from conFLOW to evaluate the actual laminar extent achievable on the real wing. This will complete the first phase of the MUVE project, laying the foundation for a leading-edge design capable of enabling laminar flow control, maneuver load alleviation, and high-lift performance.

REFERENCES

[1] Krein, Axel, and Gareth Williams. "Flightpath 2050: Europe's vision for aeronautics." Innovation for sustainable aviation in a global environment. IOS Press, 2012. 63-71.
[2] Seitz, Arne, and Karl-Heinz Horstmann. "Design studies on NLF and HLFC applications at DLR." Proceedings of the 27th International Congress of the Aeronautical Sciences, Nizza, France. 2010.
[3] Wunderlich, Tobias Franziskus, et al. "Untersuchungen zu hochgestreckten, last-geregelten, ultra-effizienten, intelligenten Flügeln INTELWI-DLR Schlussbericht." (2024).
[4] Prasannakumar, Adarsh, et al. "Design of Hybrid-Laminar-Flow-Control Wing and Suction System for Transonic Midrange Aircraft." Journal of Aircraft 61.3 (2024): 709-732.
[5] Kakkar, Samarth, et al. "High Dimensional Bayesian Optimization for Aerodynamic Design of Airfoils and Wings with Hybrid Laminar Flow Control." Available at SSRN 5316824.

Mitteilung

Fachgruppe: Turbulenz und Transition

Outer-layer self-similarity in spatially developing turbulent boundary layers

Jason Appelbaum, Tobias Gibis, Sergio Pirozzoli, Christoph Wenzel
appelbaum@iag.uni-stuttgart.de
Institut für Aerodynamik und Gasdynamik (IAG)
Universität Stuttgart

A direct numerical simulation (DNS) has been performed [1] to investigate changes in the properties of a turbulent boundary layer (TBL) in the Reynolds number (Re) range where the outer region of the TBL has established self-similarity.

Boundary layers are a fundamental feature of nearly every engineering system in which fluid transport or transport through a fluid is required. Yet, wall-bounded turbulence is still a relatively difficult phenomenon to predict economically with sufficient accuracy. Modern industrial CFD techniques rely heavily on wall models for predicting the properties of turbulent shear layers, however the success of such models is dependent on the experiments and high-fidelity simulations used to extract key scaling behavior. Both physical experiments and virtual experiments (DNS) have their own strengths and limitations. Laboratory experiments can relatively easily reach high Re and average over long periods of time with effectively zero marginal cost, however some quantities such as surface shear stress are difficult to directly measure with high accuracy. DNS offers full access to the spatiotemporal flow field but is often limited in Re due to its exponential computational resource scaling. However, the steady increase in high-performance computing (HPC) capacity has made DNS excursions into previously sparsely explored Re regimes possible.

The present study examines a zero-pressure-gradient (ZPG) TBL spatially developing into a particularly significant Re regime, namely one in which the outer ~85% of the boundary-layer thickness becomes self-similar, meaning that it is independent of Re when normalized by a specific set of local length and velocity scales. The boundary layer is allowed to spatially develop, uninterrupted, from a very early post-transitional state into this Re regime.

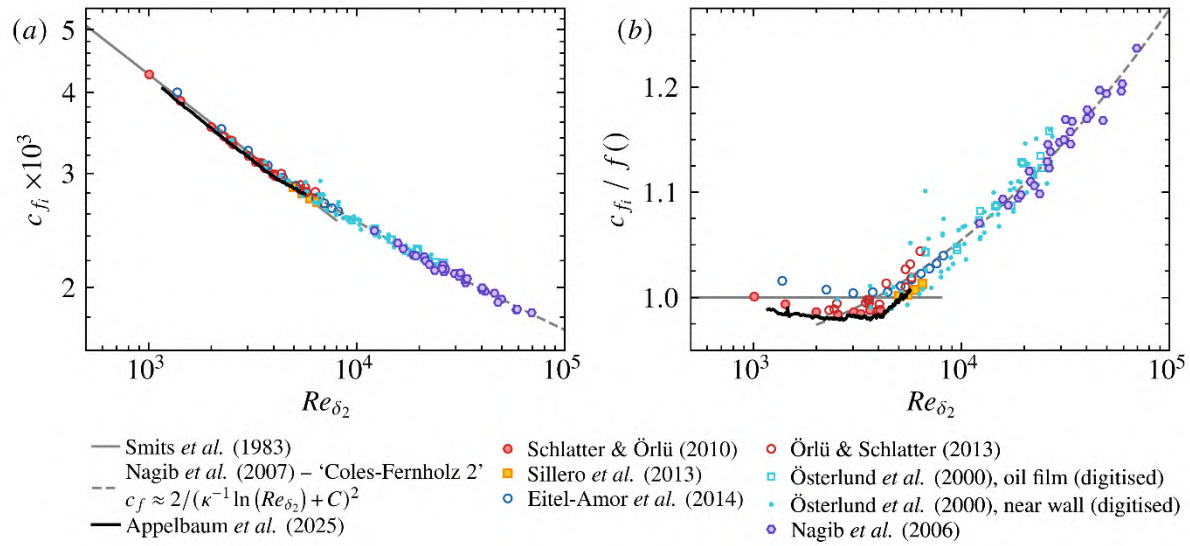

Figure 1: (a) Incompressible-transformed skin-friction coefficient cf vs Reynolds number. (b) All data normalized by power-law correlation of [2] for visualization purposes. Incompressible reference data are from [3] [4] [5] [6] [7] [8].

The present DNS dataset is therefore useful for answering several questions about the scaling properties of boundary layers, for example the characterization of changes in dynamics

around the point of self-similarity establishment, which has been well-captured. Motivation for the study design was based on evidence found in literature, namely the crossing of two widely used cf(Re) correlations, where cf is the skin-friction coefficient. For high Re, the state-of-the-art correlation form is analytically derived assuming inner and outer layer self-similarity, the free constants of which have been determined using data from experiments [3] [4] leveraging oil-film interferometry to directly measure wall shear stress. At low Re, where the outer layer is still developing, the empirically determined power-law from [2] is often used. The crossing of these two correlations gave predictive hints as to the Re at which a ZPG boundary layer is expected to become self-similar.

Figure 1(a) shows the progression of the present [1] incompressible-transformed cf(Re), along with the mentioned correlations [2] [4], two incompressible DNS [5] [6], one LES [7] and three experimental references [8] [3] [4]. Panel (b) shows all datasets normalized by the low-Re power law for ease of visualizing fine trends. As can be seen, the present dataset globally matches the trend of the established correlations as well as the available references and can therefore be considered as a plausible bridge connecting lower-Re DNS and higher-Re experiments.

Notably, the present dataset captures a relatively sharp ‘bend’ in cf(Re) associated with the onset of outer-layer self-similarity, a feature which has not received much coverage in boundary layer literature, but which may provide valuable physical insights into the evolution of canonical TBLs as they take on a fully developed state.

The STAB contribution will provide details about the DNS and characterize the TBL flow field, with particular emphasis on properties around the ‘bend’ in cf and establishment of self-similarity.

References

[1] J. Appelbaum, T. Gibis, S. Pirozzoli and C. Wenzel, "The onset of outer-layer self-similarity in turbulent boundary layers," *Journal of Fluid Mechanics,* vol. 1015, p. A37, 2025.

[2] A. J. Smits, N. Matheson and P. N. Joubert, "Low-Reynolds-Number Turbulent Boundary Layers in Zero and Favorable Pressure Gradients," *Journal of Ship Research,* vol. 27, pp. 147-157, 09 1983.

[3] J. M. Österlund, "Experimental studies of zero pressure-gradient turbulent boundary layer flow," Royal Institute of Technology, Department of Mechanics, 1999.

[4] H. M. Nagib, K. A. Chauhan and P. A. Monkewitz, "Approach to an asymptotic state for zero pressure gradient turbulent boundary layers," *Philosophical Transactions of the Royal Society A: Mathematical, Physical and Engineering Sciences,* vol. 365, pp. 755-770, 2007.

[5] P. Schlatter and R. Örlü, "Assessment of direct numerical simulation data of turbulent boundary layers," *Journal of Fluid Mechanics,* vol. 659, pp. 116--126, 2010.

[6] J. A. Sillero, J. Jiménez and R. D. Moser, "One-point statistics for turbulent wall-bounded flows at Reynolds numbers up to δ+ ≈ 2000," *Physics of Fluids,* vol. 25, p. 105102, 10 2013.

[7] G. Eitel-Amor, R. Örlü and P. Schlatter, "Simulation and validation of a spatially evolving turbulent boundary layer up to Reθ=8300," *International Journal of Heat and Fluid Flow,* vol. 47, pp. 57-69, 2014.

[8] R. Örlü and P. Schlatter, "Comparison of experiments and simulations for zero pressure gradient turbulent boundary layers at moderate Reynolds numbers," *Experiments in Fluids,* vol. 54, p. 1547, 2013.

Mitteilung

Fachgruppe: Turbulenz und Transition

Progress with verification and stabilization of Reynolds stress models using the CFD Software by ONERA, DLR, Airbus (CODA)

Keerthana Chandrasekar Jeyanthi[1], Tobias Knopp[1], Johannes Löwe[1], Michael Werner[2],
[1]DLR, Institut für Aerodynamik und Strömungstechnik, Abteilung C²A²S²E
[2]DLR, Institut für Aerodynamik und Strömungstechnik, Abteilung Hochgeschwindigkeitskonfigurationen,
Bunsenstraße 10, 37073 Göttingen, keerthana.chandrasekarjeyanthi@dlr.de

Turbulence modelling stands as the cornerstone of Computational Fluid Dynamics (CFD) enabling accurate flow simulations and design optimization across a wide range of industrial applications. A CFD simulation software, also known as flow solver, offers several turbulence models to owing to the varying complexity and capabilities of different models. An industrial CFD software must deliver stable simulations across various cases providing accurate, reliable results. These key aspects, namely robustness and accuracy, also depend on the different turbulence models provided within the software, thereby demanding the software developers to perform extensive testing and validation of each model. The testing, in general, includes the fundamental verification and validation cases but not restricted to more complex verification cases involving several flow features like three-dimensional (3D) separation, vortices, etc. The main aim of this work is to present the experience obtained from the verification of three-dimensional test cases for the

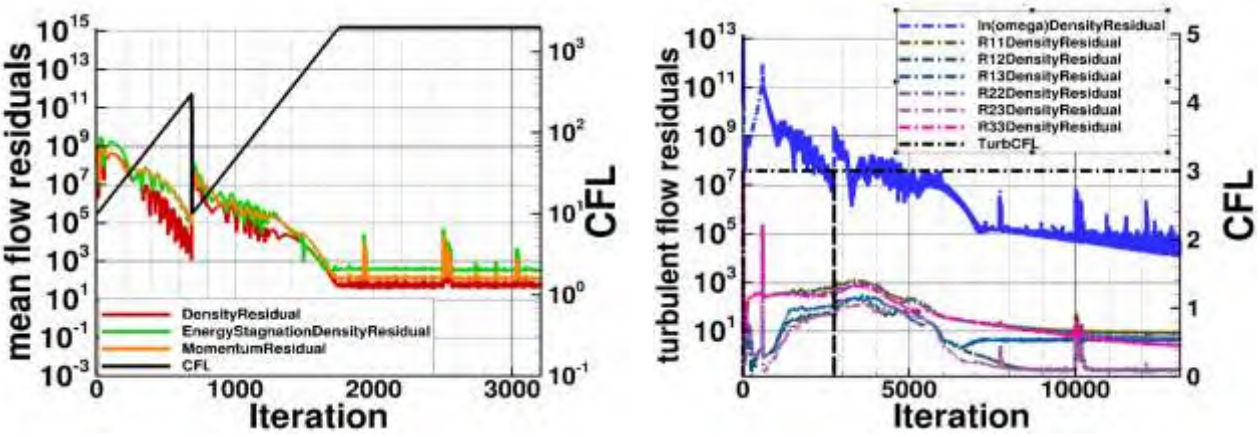

Figure 1 Left: Convergence of mean flow residuals for ONERA M6 wing on the finest mesh with 11 million elements with the weak coupling of mean flow and turbulent equations in CODA. Right: Convergence of turbulence residuals for the same case where we perform 4 iterations on the turbulent equations for 1 iteration on the mean flow

Reynolds stress turbulence model available in the next generation flow solver CODA. The focus is on robustness and accuracy issues as well as on efficiency aspects.

CODA [1] is the CFD software being developed as part of a collaboration between the French Aerospace Lab ONERA, the German Aerospace Center (DLR), Airbus, and their European research partners. CODA is jointly owned by ONERA, DLR and Airbus. CODA offers a few industrially relevant turbulence models such as the eddy viscosity models (EVMs) of Spalart-Allmaras and Shear Stress Transport model (SST) by Menter which are known for their simplicity, efficiency and performance. When higher accuracy is needed for complex turbulent flows involving separation, flow over curved surfaces, vortical flows, Reynolds stress models (RSM) come into

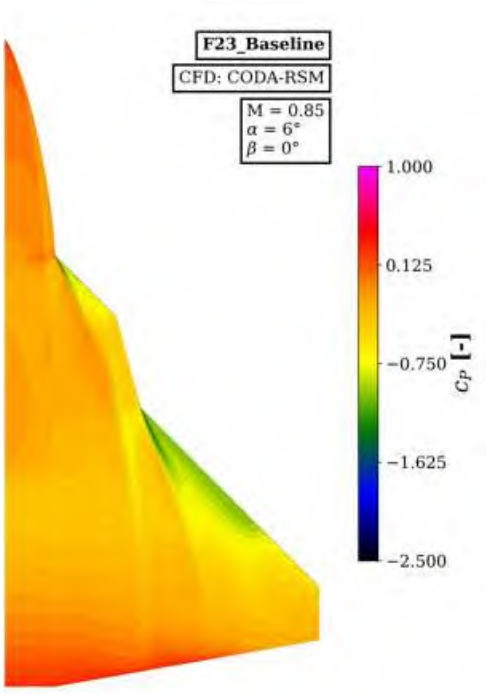

Figure 2 Coefficient of pressure (Cp) distribution for DLR F23 configuration for angle of attack 6° and Mach 0.85

play where the EVMs can fall short. CODA provides the mostly widely used industrial RSM model: Speziale-Sarkar-Gatsky/Launder-Reece-Rodi(SSG/LRR) [2] model with the ln(ω) variant of the length scale equation. The preliminary verification and validation of the SSG/LRR-ln(ω) in CODA has been provided in a previous work. The current work targets verification of the model with 3D test cases like the transonic flow around the ONERA M6 wing, the DLR-F23 and the transonic drag-prediction workshop (DPW) CRM case using reference results from the DLR TAU code and CFL3D. We also describe several challenges encountered while performing these verification tests. Some strategies were attempted to navigate the difficulties and the ongoing efforts are focused to gain a better understanding from the experience. Enforcement of realizability constraints [3] was necessary for cases with flow features like shock-induced separation, vortical flows, etc. We enforced the realizability constraints using a smoothed-clipping approach to guarantee the differentiability of the Reynolds stress equations for automatic differentiation. CODA implements a strongly coupled system for mean flow and turbulence equations, hence the other strategy adopted was to have a weak coupling of the equations following the studies from Langer et al [4]. We observed that the weak coupling could improve the robustness of the system but may degrade the performance of the simulation depending on the test case simulated. For 3D transonic cases, we encountered severe restriction of the turbulent CFL number (see Figure 1). The restriction was partially circumvented by changing the convection scheme for the turbulence equations. A Roe scheme [5] for mean flow and a more dissipative convective flux for the turbulence equations like local Lax–Friedrichs (LLF) or simplified upwind scheme helped to navigate the restriction for a few cases like the ONERA M6 and DLR-F23 (see Figure 2). We conclude with the importance of realizability constraints for the stability of the RSM model along with our findings on the coupling strategies of the mean flow and turbulence equations and the CFL number dependence of the turbulence equations. Finally, we also emphasize the importance of an appropriate convection scheme for the turbulence equations.

Bibliography

[1] T. Leicht, D. Vollmer, J. Jägersküpper, A. Schwöppe, R. Hartmann, J. Fiedler and T. Schlauch, "DLR-Project Digital-X: Next generation CFD solver 'Flucs'," *Deutscher Luft- und Raumfahrtkongress 2016, Braunschweig,* no. 420027, 2016.

[2] B. Eisfeld and O. Brodersen, "Advanced Turbulence Modelling and Stress Analysis for the DLR-F6 configuration," *AIAA Paper,* 2005.

[3] U. Schumann, "Realizability of Reynolds-stress turbulence models," *The Physics of Fluids,* vol. 20, no. 5, pp. 721-725, 1977.

[4] S. Lange and G. Suarez, "Loosely coupled and coupled solution methods for the RANS equations and a one-equation turbulence model," *Computers & Fluids,* vol. 232, p. 105186, 15 01 2022.

[5] P. L. Roe, "Approximate Riemann solvers, parameter vectors, and difference schemes," *Journal of Computational Physics,* vol. 43, no. 2, pp. 357-372, 1981.

Mitteilung

Fachgruppe: Turbulenz und Transition

The Occurrence of turbulent spots during free flight in the convective atmosphere

U. Deck
Institut für Aerodynamik und Gasdynamik, Universität Stuttgart, Wankelstraße 3,
70563 Stuttgart, ulrich.deck@iag.uni-stuttgart.de

Turbulent spots are temporal and local finite turbulent boundary layer flows occurring in laminar or transitional boundary layer flows [1]. Their propagation velocity does not agree with the local free stream velocity, and turbulent spots are stretched since their leading edge velocity is roughly 88% of the local free stream velocity. In contrast, their trailing edge velocity is only 50% of the local free stream velocity. Both velocities were measured with flat plate test cases by Klebanoff [2], these measurements are enlarged by Gostelow [3] for different values of a streamwise pressure gradient. The occurrence of turbulent spots can increase viscous drag if they occur frequently. The frequency of occurrence is evaluated in this study using the hotfilm sensor signals from intensive free-flight measurements. The hot-film sensors are glued to the surface of a natural laminar flow airfoil. Further details concerning the measurement setup and free flight campaigns can be found in previous publications [4, 5]. Turbulent spots cause clear peaks and a temporally higher fluctuation of the hotfilm voltage signal. The MATLAB function “findpeaks” is elaborated to identify these local maxima. A minimum peak prominence of U = 0.03V and a maximum peak width of N_S = 1000S (sampling frequency f_S = 50kHz) samples are used to distinguish the peaks from other random disturbance signals. The identified peaks are displayed with the hotfilm voltage signals and the angle of attack signal for reference. Two typical measurement sub-sections with one peak detected per section are shown in Fig. 1.

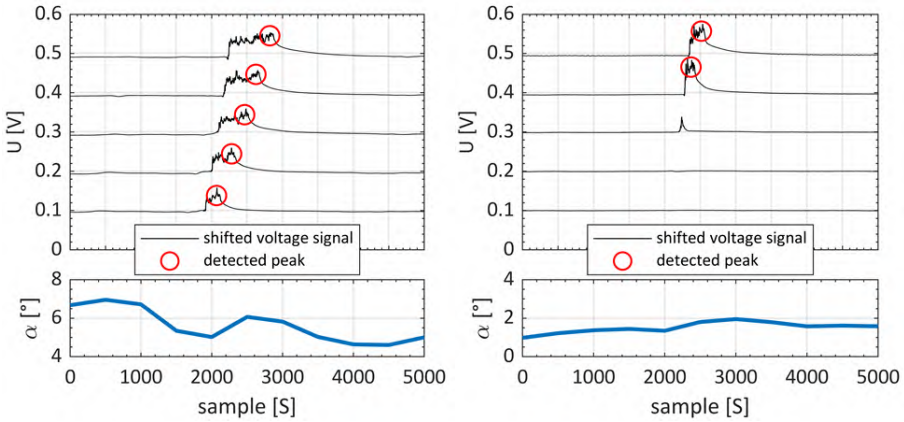

Fig. 1 *Time series of the staggered hotfilm voltage signals from the pressure side for two measurement sub-sections with t = 0.1sec duration. The voltage signal of each sensor location is shifted by ΔU = 0.1V to distinguish the individual signals. The angle of attack signal is shown as a reference.*

The time series of the staggered hotfilm voltage signals in Fig. 1 unveils the expected turbulent spot behavior. The narrow, turbulent boundary layer flow regime is distinguishable from the surrounding laminar boundary layer flow. The absolute value and fluctuation of the hotfilm voltage signal are increased for the turbulent boundary layer flow regime. The turbulent boundary layer is stretched further downstream due to a turbulent spot's slower trailing edge velocity.
The next step is to count the peaks, respectively, the turbulent spots, and display the overall spot count in a contour chart against the angle of attack and hotfilm sensor location for different inflow turbulence strengths. For both sides of the airfoil, it is visible that most of the turbulent spots are detected at the angles of attack and sensor locations with transitional boundary layer flow, which is expected from the literature [6]. However, turbulent spots also occur in the laminar boundary layer flow regions. Especially for the pressure side, displayed in the lower row of Fig. 2, it is visible that the frequency of turbulent spot occurrence is increased for high angles of attack when inflow turbulence increases. Interestingly, there might also be an increase in

the frequency of turbulent spot occurrence with increasing angle of attack for severe inflow turbulence. The scattered occurrence in this regime is caused by the availability of measurement sections at all. In the transitional boundary layer flow regime on the pressure side, the distribution of spot occurrence becomes more blurred for higher inflow turbulence.

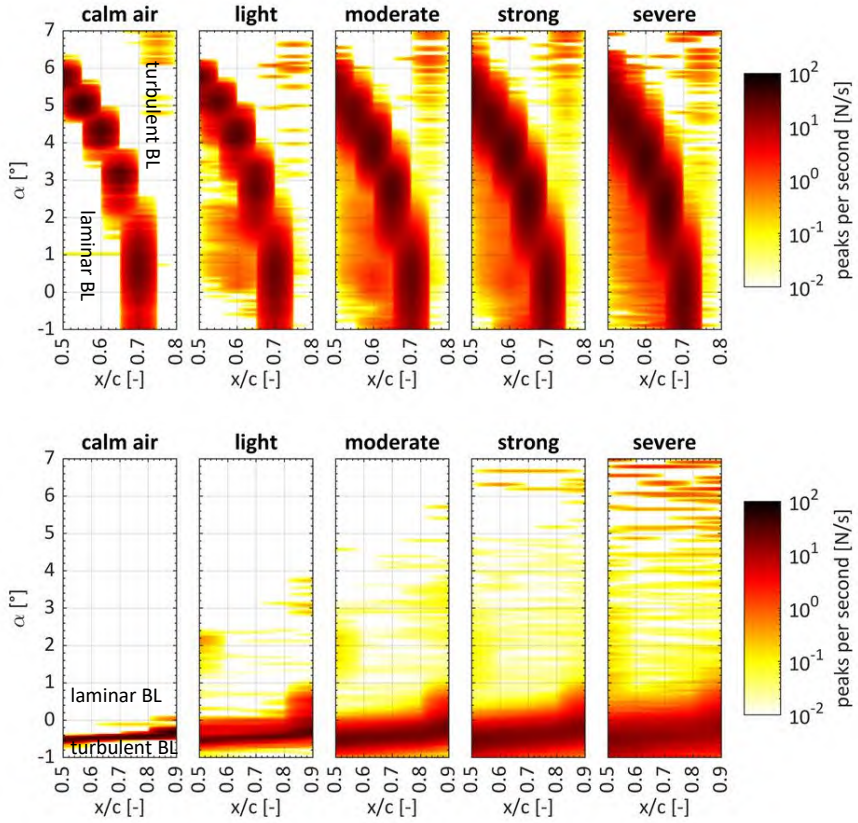

Fig. 2 *Frequency of turbulent spot occurrence for the suction side (upper row) and the pressure side (lower row). Increasing turbulence from left to right.*

For the suction side, the upper row in Fig. 2, an increase in the frequency of turbulent spot occurrence for higher inflow turbulence is visible. Unfortunately, peaks are also detected in the turbulent boundary layer flow regime at high angles of attack and rearward sensor locations for the suction side. Of course, these peaks are not caused by turbulent spots, but there may be some fluctuation in the turbulent boundary layer because of the onset of a boundary layer separation. For both sides of the airfoil, it is interesting how well the maximum of the spot occurrence hints at the transition location for all sensor locations and turbulence categories. This is expected since turbulent spots occur during the natural transition process. Spot detection might also be a good criterion for transition detection.

To summarize, results from free-flight hot-film measurements are analyzed to identify turbulent spots. Resulting frequency distributions show the spot occurrence probability for a wide range of angles of attack, for several chord-wise locations on both airfoil sides, and for distinguishing inflow turbulence strength. Most of the detected spots occur in transitional boundary layer flows. But there is also an increase in the spot count visible in the laminar boundary layer flow regime for increasing turbulence strength. Next to these results, the final presentation will show the measurement setup and further results, such as an evaluation of the average spot width.

[1] Emmons H.W., (1951), “The laminar-turbulent transition in a boundary layer – part I”, J. Aeronaut. Sci. 18:490-98

[2] Klebanoff, P.S., Schubauer, G.B., (1955) “Contributions on the Mechanics of Boundary-Layer Transition” NACA-TN-3489

[3] Gostelow J.P., Melwani N., Walker G.J., (1996), “Effects of streamwise pressure gradient on turbulent spot development” Journal of Turbomachinery, ASME Vol. 118, pp. 737-743

[4] Deck U., Würz W. (2023) “Freiflugmessungen der Profilpo-laren eines Laminarprofils unter konvektiven Anströmbe-dingungen“ Deutscher Luft- und Raumfahrtkongress, Stuttgart 2023

[5] Deck U., Würz W. (2025) „The influence of turbulence on the laminar-turbulent transition in the wind tunnel and during free flight” CEAS Aeronautical Journal

[6] Wu, X., (2023), “New Insights into turbulent Spots”, Annu. Rev. Fluid Mech. 2023, 55:45-75

Mitteilung

Fachgruppe: Turbulenz und Transition

Kinetic Energy Budget of Secondary Motions in Sinusoidally-tempered Vertical Turbulent Pipe Flow

Felix Finke, Christian Bauer, Claus Wagner
Institut für Aerodynamik und Strömungstechnik, DLR
Bunsenstraße 10, 37073 Göttingen
felix.finke@dlr.de

Solar power towers represent one of the most promising concentrated solar power technologies for future large-scale renewable energy generation. In such plants, a heliostat field focuses solar radiation onto one side of the central vertical receiver, imposing a highly non-uniform heat flux on the fluid as it ascends and descends within the receiver tubes [1]. To get a better understanding of the secondary motions occurring in such flows, the present study investigates the kinetic energy budget of secondary motions in a sinusoidally tempered vertical turbulent pipe flow using direct numerical simulations. Thus, the incompressible Navier–Stokes equations with the Boussinesq approximation and the energy equation in their dimensionless form,

$$\frac{\partial \vec{u}}{\partial t} + \vec{u} \cdot \nabla \vec{u} + \nabla p = \left(\frac{1}{Re_b}\right) \nabla^2 \vec{u} + \left(\frac{Gr}{Re_b^2}\right) \theta \, \delta_{ij}, \tag{1}$$

$$\nabla \cdot \vec{u} = 0, \tag{2}$$

$$\frac{\partial \theta}{\partial t} + \vec{u} \cdot \nabla \theta = \left(\frac{1}{Pr \, Re_b}\right) \nabla^2 \theta, \tag{3}$$

are discretized using a finite-volume method with fourth-order spatial accuracy [2], and are integrated in time employing a semi-implicit second-order Euler–Leapfrog scheme [3]. The grid resolutions are adopted from previous works [4, 5, 6]. Normalizing equations (1) to (3) with the bulk velocity u_b and the pipe diameter D results in the bulk Reynolds number $Re_b = u_b D/\nu$, the Prandtl number $Pr = \nu/\kappa$, and the Grashof number $Gr = g\beta\Delta T u_b^3/\nu^2$. Here, ν is the kinematic viscosity, κ is the thermal conductivity, g is the gravitational acceleration, β is the thermal expansion coefficient, and ΔT is the temperature difference between the maximum and minimum imposed wall temperature. In the present case the characteristic parameters are set to $Re_b = 5300$, $Pr = 0.71$, and $Gr = 9.5 \times 10^6$. The flow geometry is a smooth-walled pipe of length $L = 21D$, with no-slip and impermeability boundary conditions at the wall and the wall temperature varied according to $\theta_w = 0.5\, sin(\varphi)$, where φ is the azimuthal direction. The temperature is normalized with ΔT and the arithmetic mean of the wall temperatures T_0, leading to $\theta = (T - T_0)/\Delta T$.

The buoyancy force induces acceleration (deceleration) of the warm (cold) flow regions, which in turn gives rise to secondary motions, as shown in **Figure *1***(a), where the mean temperature profile is superimposed with the velocity field of the mean secondary flow, $\langle u_\varphi \rangle_{zt} \, \vec{e}_\varphi + \langle u_r \rangle_{zt} \, \vec{e}_r$. As expected, the fluid moves upward from the warmest to the coldest flow region, traveling through the pipe center where the the maximum temperature gradient occurs, and returns downward along the wall. **Figure *1***(b,c,d) show some examples of different terms of the kinetic energy budget of these secondary motions. **Figure *1***(b) depicts the production term, which is responsible for the energy transfer between secondary motions and the turbulent fluctuations. The production mechanism causes the strongest energy transfer into the turbulent velocity field in the region of maximum velocity gradients, i.e. near the lower part of the pipe wall, whereas in the remaining near-wall regions of the pipe, a reverse transfer occurs, feeding energy back from the fluctuating velocity field into the mean secondary flow. The dissipation from the secondary motions presented in **Figure *1***(c) is strictly negative and restricted to regions close to the pipe wall, attaining its minimum where the secondary motions are most intense.

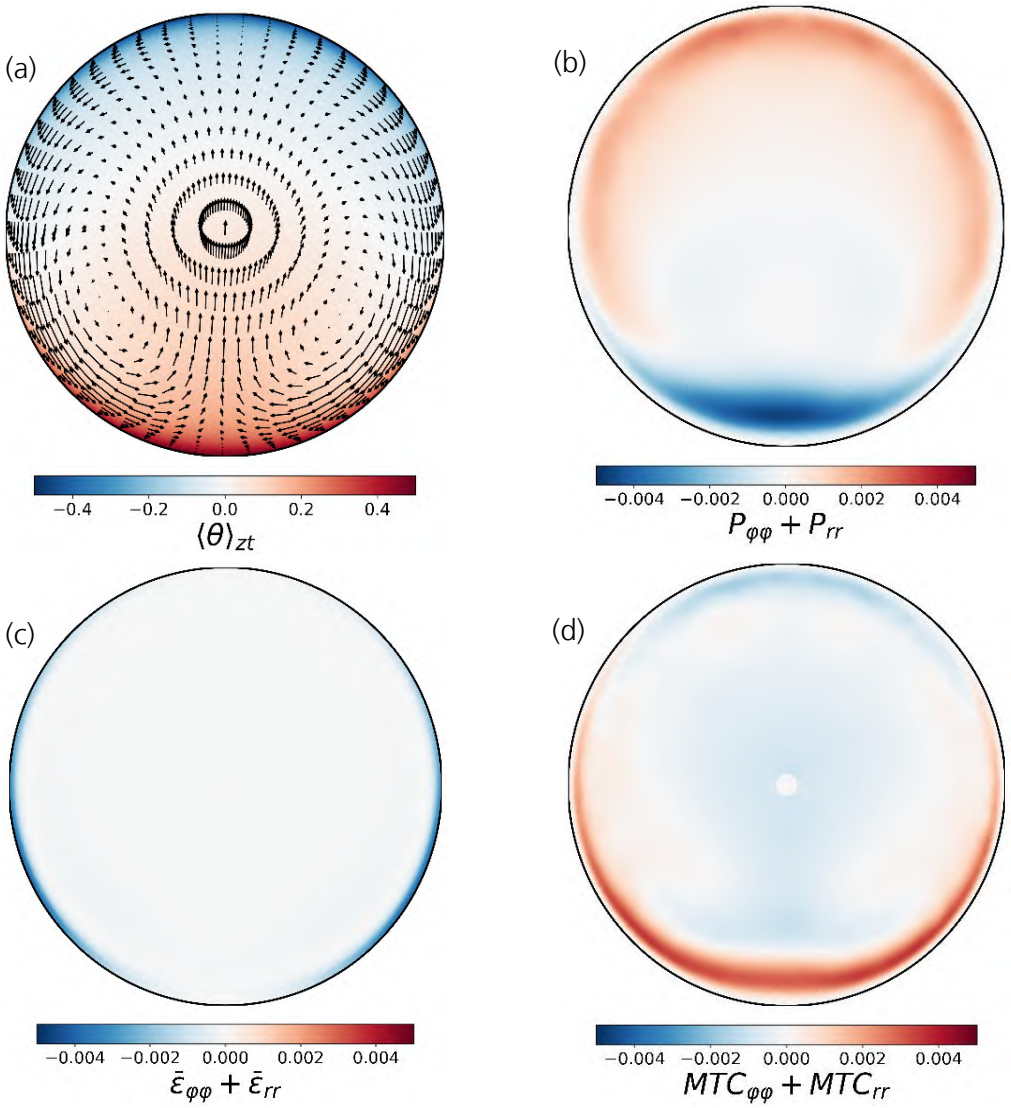

Figure 1: *(a) Mean temperature **θ** and velocity profile of the mean secondary flow . (b) Production of turbulent kinetic energy due to the mean secondary flow. (c) Dissipation due to the mean secondary flow. (d) Convection of the mean secondary flow due to turbulent fluctuations.*

At the bottom center, the wall-parallel velocity component vanishes due to flow symmetry, which minimizes shear between the fluid and the wall and thus reduces the dissipation to nearly zero in this region. **Figure 1**(d) shows the convection of secondary flow kinetic energy due to turbulent fluctuations. This term reaches its largest positive values in the warmest flow regions along the lower part of the pipe wall. On the opposite wall, a less pronounced negative minimum appears. The kinetic energy budget of the secondary motions will be discussed in more detail at the workshop.

[1] A. Antoranz, O. Flores and M. García-Villalba, "Turbulent hear transfer and secondary motions in a non-uniformly heated pipe with temperature-dependent fluid properties," *International Journal of Heat and Fluid Flow,* vol. 115, p. 109791, 2025.

[2] D. Feldmann and C. Wagner, "Direct Numerical Simulation of Fully Developed Turbulent and Oscillatory Pipe Flows at Re τ = 1440," *Journal of Turbulence,* vol. 13, no. 32, 2012.

[3] O. Shishkina and C. Wagner, "Stability Conditions for the Leapfrog-Euler Scheme with Central Spatial Discretization of any Order," *Applied Numerical Analysis & Computational Mathematics, vol. 1,* pp. 315-326, 2004.

[4] C. Bauer, D. Feldmann and C. Wagner, "On the convergence and scaling of high-order statistical moments in turbulent pipe flow using dierect numerical simulations," *Physics of Fluids,* vol. 29, no. 12, 2017.

[5] T. Wetzel and C. Wagner, "Buoyancy-induced effects on large-scale motions in differentially heated vertical channel flows studied in direct numerical simulations.," *International Journal of Heat and Fluid Flow,* vol. 75, pp. 14-26, 2019.

[6] A. Dachwitz, C. Bauer and C. Wagner, "Streaky structures in a sinusoidally-tempered vertical turbulent pipe flow," Proceeding of the 10th International Symposium on Turbulence, Heat and Mass Transfer, THMT-23, Rome, 2023.

Mitteilung

Fachgruppe: Numerische Aerodynamik

Experimental investigation and data-driven turbulence modeling for flow separation and reattachment

C. Grabe*, T. Knopp, A. De Vincenzo, R. Geisler, M. Costantini, D. Schanz, A. Schröder.
DLR, Institute of Aerodynamics and Flow Technology, Bunsenstrasse 10,
D-37073 Göttingen, Germany

Introduction

The reliable prediction of turbulent boundary-layer separation and reattachment using the Reynolds-Averaged Navier-Stokes (RANS) equations is a long-standing area of research. No generally accepted solution has yet been established, however, the need for a solution for flows at high Reynolds numbers remains necessary from an aeronautical perspective and is therefore the subject of this work.

To evaluate the prediction quality of RANS turbulence models requires representative experimental data. This includes the measurement of relevant quantities on the surface (pressure, skin friction) as well as in the flow field (velocities, Reynolds stresses). While existing experimental data are widely used for validation, there is an unresolved anomaly between the prediction of flow over the backward-facing step (BFS, sudden geometry change) and backward-facing rounded steps (continuous geometry change). While flow reattachment is usually well predicted by standard RANS models for the BFS, they lack prediction accuracy for curved steps. To shed some light on this apparent contradiction, a new, parametric backward-facing ramp experiment was designed and measured in the course of the DLR-project ADaMant. The ramp geometry was selected over a rounded step because there is comparatively less reliable reference data. The details of this experiment, which comprises three ramp angles (25°, 45° and 90°), are given in [1]. This work shows first steps towards the comparison with numerical simulations using standard RANS models building on the evaluation of the measured data [2].

To improve RANS turbulence models for flow separation and reattachment, a data-driven approach was investigated based on the Field Inversion and Machine Learning (FIML) technique [3]. In this two-step approach, the RANS turbulence model is augmented by an extra term that is optimized using a gradient-based approach to yield the target distribution of a quantity of interest (e.g. the skin friction coefficient) for a certain testcase. In a second step this extra term, which initially depends on the coordinates of the testcase used for optimization, is then trained to depend on flow features, identified as relevant to predict the flow correctly. With the second step the augmented model is applicable to other testcases. In the current work, Field Inversion was performed for a curved step testcase and a BFS testcase optimizing an augmented Spalart-Almaras (SA) turbulence model. After investigating methods to identify relevant flow features, also known as feature engineering, the Machine Learning step was replaced by a turbulence modeling step to modify the SA-neg model.

Results

The first part covers the status of evaluation of the ADaMant ramp-familiy experiment. While the experiment covered three different ramp geometries at four different Reynolds numbers (based on the length of the flat plate upstream of the ramp, Re = 1.2, 1.6, 2.2 and 2.7 x 10^6) the numerical study focussed on the three geometries for one Reynolds number only (Re = 1.6 x 10^6). For all three geometries, the pressure distributions are compared to the experimental data. Additionally, velocity profiles and qualitative flow features from the experiment and the numerical simuations are presented and discussed. The comparison of the pressure distribution for the 90° ramp and a fully-turbulent SA-neg simulation is depicted in figure 1.

In the second part the results from the data-driven turbulence modeling activity are presented, focussing on the results from the Field Inversion step, the different feature engineering approaches tested and the final modification of the SA-neg turbulence model for the cases investigated. Figure 2 shows the skin friction distribution of two training testcases used in this study, a Curved Step (CS) [4] and a Backward-Facing Step (BFS) [5], comparing the reference data

(LES data for the CS, experimental data for BFS), the simulation results obtained with the original SA-neg turbulence model and the modified SA-neg turbulence model. Besides classical quantities typically used as features in turbulence modeling, the work of Arun and Colonius [6] on the normality-based framework is also considered.
In the future, after full analysis of the ADaMant ramp experiment, it will be included into the training for the data-driven turbulence modeling approach in order to derive a modified turbulence model for reliable prediction of flow separation and reattachment.

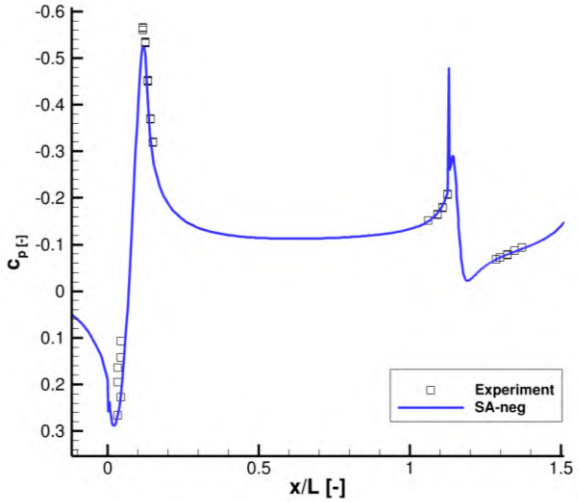

Figure 1. Comparison of pressure distribution: experimental data and RANS simulations using the SA-neg model (SA-neg) for the 90° ramp case and Re = 1.6 x 10^6. L: Length of the flat plate, ramp positioned at x/L = 1.24

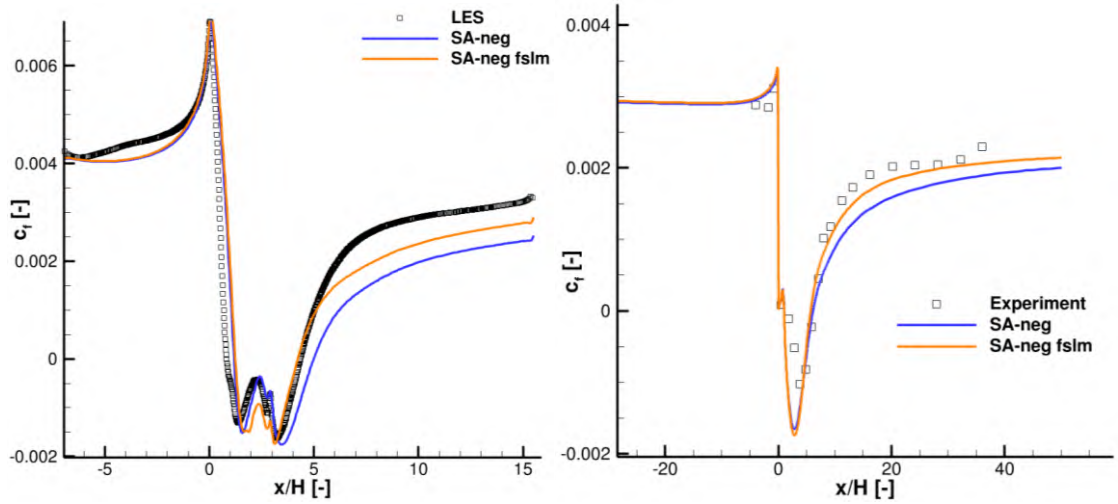

Figure 2. Skin-friction distribution for two training testcases, Curved Step (CS) on the left and Backward-Facing Step (BFS) on the right. Comparison between reference data, simulations using the original SA-neg turbulence model and the modifued SA-neg turbulence model (fslm: feature shear layer modification). H: Height of the step.

References

[1] Grabe C. (2022) DLR-Project ADaMant: Adaptive, Data-driven Physical Modeling towards Border of Envelope Applications. DLRK 2022, Dresden, Germany, 27–29 Sept. 2022.
[2] Guerin, M. et al. (2024) Analysis of Separated Shear Flow and Reattachment over a Backward Facing Step using the DLR ADaMant Experiment. In: 24. STAB-DGLR-Symposium 2024, pp. 154-155.
[3] Duraisamy, K. and Parish E.J. (2016) A paradigm for data-driven predictive modeling using field inversion and machine learning, Journal of Computational Physics, Vol. 305, pp. 758-774.
[4] Bentaleb, Y et al. (2012) Large-eddy simulation of turbulent boundary-layer separation from a rounded step, Journal of Turbulence, 13, N4.
[5] Driver, D. M. and Seegmiller, H. L., (1985) Features of Reattaching Turbulent Shear Layer in Divergent Channel Flow, AIAA Journal, Vol. 23, No. 2, pp. 163-171.
[6] Arun R. and Colonius T. (2024) Velocity gradient partitioning in turbulent flows. Journal of Fluid Mechanics, Vol. 1000, R5.

Mitteilung

Fachgruppe: Turbulenz und Transition

Recent advances of hybrid RANS/LES with Reynolds-stress background modelling

Marius Herr[1], Philipp Grotowsky[1,2], Axel Probst[1]
[1]Deutsches Zentrum für Luft- und Raumfahrt,
Institut für Aerodynamik und Strömungstechnik, C²A²S²E
Bunsenstraße 10, 37073 Göttingen
marius.herr@dlr.de
[2]RWTH Aachen University
Templergraben 55, 52062 Aachen
philipp.grotowsky@rwth-aachen.de

Introduction

The combination of statistical RANS modelling with turbulence resolving LES methods (hybrid RANS/LES) enables the efficient simulation of complex, industry-relevant flows (e.g. aircrafts in high-lift configuration). In such a hybrid form, the respective RANS model mainly serves as wall model in the near-wall regions and as background model in the LES regions away from the wall. Pure RANS models that are based on differential Reynolds-stress modelling (RSM), achieve a higher accuracy for flows with rotation, streamline curvature and secondary motion compared to simpler turbulence models (e.g. eddy-viscosity models). It is expected that this accuracy advantage is still present when combined with an LES method. Recently, in [1] the robust SSG/LRR RSM-RANS model was combined with the IDDES method, a well-established representative of hybrid RANS/LES. However, so far it was not explicitly demonstrated that this newly developed RSM-IDDES captures the aforementioned complex flow phenomena properly. This study aims to fill this gap by addressing the capability of the RSM-IDDES to resolve secondary motions arising in turbulent corner flows, such as those occurring in the intersection regions of aircraft components (e.g. between nacelle, pylon and wing). Furthermore, in order to limit the computational cost of elaborate scale resolving simulations, we focus on improving the efficiency of the RSM-IDDES. To this end, two different wall function approaches are coupled to the RSM-IDDES, principally allowing a significant coarsening of the wall-normal resolution of the corresponding computational grid.

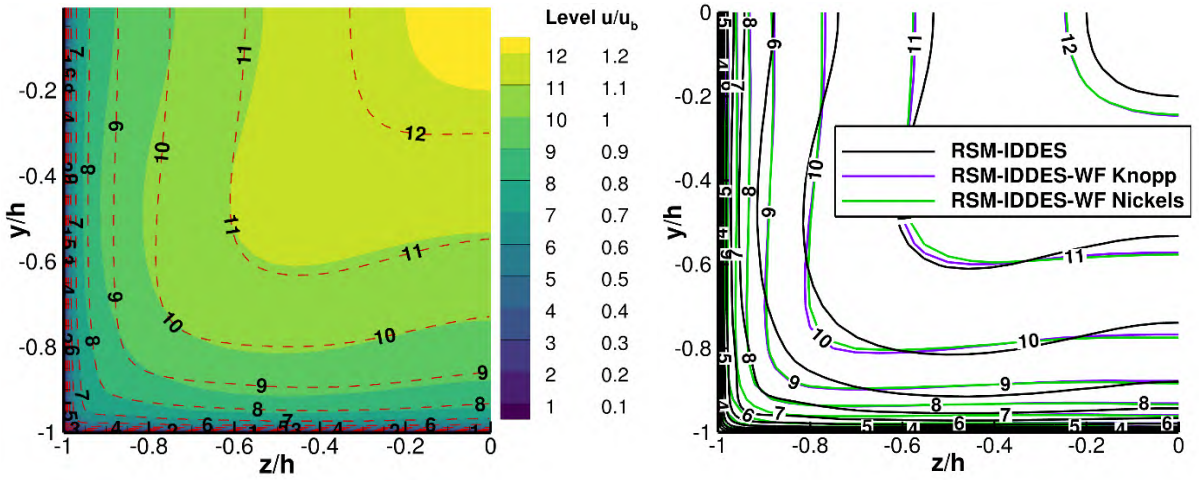

Figure 1 *Streamwise velocity distributions of a periodic, square duct flow* ***Left:*** *RSM-IDDES in comparison to DNS data [2] (dashed).* ***Right:*** *Results of RSM-IDDES in combination with analytical wall functions by Knopp [3] and Nickels [4].*

This work is part of the research unit FOR 2895, funded by the DFG, which addresses unsteady transonic effects at the industrial XRF1 aircraft configuration coupled to ultra large bypass ratio (UHBR) nacelles. A major research goal is to provide a hybrid RANS-LES method, which is able to cope with the complex flow across a full XRF1-UHBR configuration and its 3D intersections at high Reynolds numbers.

Proceeding and results

The validation of the RSM-IDDES with regard to the prediction of secondary motions is carried out using a periodic, square duct flow at $Re_\tau = 1055$ and compared to DNS data published in [2]. Figure 1 (left) depicts the corresponding RSM-IDDES results of the x-velocity component along the cross section of the test case. The time-averaged data were additionally averaged over each quadrant as well as in streamwise direction, so that the contour plot contains values from the entire flow field and simulated time. The effect of the secondary motions on the x-velocity is clearly visible in form of a slight bending of the isolines towards the corner region. Additionally, the DNS results are included in the contour plot as dashed lines, which shows overall good agreement. Furthermore, comparative simulations were carried out using an RSM-RANS (SSG/LRR) method and an IDDES variant combined with the SA-QCR-RANS eddy viscosity model (denoted as SA-QCR-IDDES). The results of the temporally and spatially averaged Re_τ values of these simulations are compared in Table 1 indicating that the best agreement with the DNS is obtained for the RSM-IDDES.

	Re_τ	relative deviation
DNS [2]	1055	-
RSM-RANS	1070	1.42%
SA-QCR-IDDES	1006	-4.64%
RSM-IDDES	1052	-0.28%

Table 1 Averaged Re_τ results for different simulation methods compared to DNS data.

To enable efficient scale resolving simulations, the analytical wall function approaches of Knopp [3] and Nickels [4] were coupled to the RSM-IDDES within the DLR TAU code. The particular aspect of Nickels' wall function is that it also takes the streamwise pressure gradient into account, which in principle facilitates an additional coarsening of the wall-normal grid resolution. Regarding the implementation, the wall boundary condition of the specific dissipation rate ω was adapted and Knoop's wall function was calibrated to a representative velocity profile of an RSM-RANS solution. Figure 1 (right) shows the x-velocity results for the RSM-IDDES with both wall function approaches in the periodic, square duct flow demonstrating good agreements with an RSM-IDDES reference solution.

In conclusion, the investigations show that the newly developed RSM-IDDES accurately captures secondary motions and is therefore validated for this type of flow. Additionally, this work demonstrates that the method can successfully be coupled to different wall function approaches leading to reliable results. Another more advanced validation case for the RSM-IDDES with wall functions will be the 2D Nasa hump flow, which is a particularly suitable test case for Nickels' wall law. Finally, this study represents a significant step towards RSM-IDDES with wall functions being applied to a full aircraft configuration at flight relevant Reynolds numbers.

References:

[1] Herr, Marius, Rolf Radespiel, and Axel Probst. "Improved delayed detached eddy simulation with reynolds-stress background modelling." Computers & Fluids 265 (2023): 106014.
[2] Pirozzoli, Sergio, et al. "Turbulence and secondary motions in square duct flow." Journal of Fluid Mechanics 840 (2018): 631-655.
[3] Knopp, Tobias, Thomas Alrutz, and Dieter Schwamborn. "A grid and flow adaptive wall-function method for RANS turbulence modelling." Journal of Computational Physics 220.1 (2006): 19-40.
[4] Nickels, T. B. "Inner scaling for wall-bounded flows subject to large pressure gradients." Journal of Fluid Mechanics 521 (2004): 217-239.

Mitteilung

Fachgruppe : Turbulenz und Transition

Stability Analysis for JAXA-Supersonic NLF Wing NEXST-1

Yuki Ide
Japan Aerospace Exploration Agency, Tokyo Japan, 182-8522, ide.yuki@jaxa.jp
(visiting researcher, High Speed Configuration Department, German Aerospace Center, Göttingen Germany, 37073, yuki.ide@dlr.de)

To study mechanisms on the boundary-layer transition in supersonic flight, we performed stability analyses of three-dimensional supersonic boundary layers formed on JAXA natural laminar flow wing, called NEXST-1 (Fig. 1) and compared the results with those of a flight test (Fig. 2). Specifically, nonlinear PSE (NPSE)-based assessments were conducted for two representative cases on the section at Y/s=0.45 (inner) and 0.77 (outer), respectively. In the former case, it was shown that disturbances with a critical wave parameter of frequency and spanwise wavenumber, predicated by linear stability theory (LST), were linearly amplified up to the region near the location of transition onset. The initial amplitude correlates with the experimental transition location was found to be approximately 10^{-6} regardless nonlinear interaction scenarios (Fig. 3). In the latter case (the section at Y/s=0.77), NPSE upheld LST results, indicating that the dominant instability on this section was crossflow instability, by showing the trends of quasi-saturation in nonlinear amplitudes and of more gradual increases in the frictional drag, in contrast to the case of Y/s=0.45.

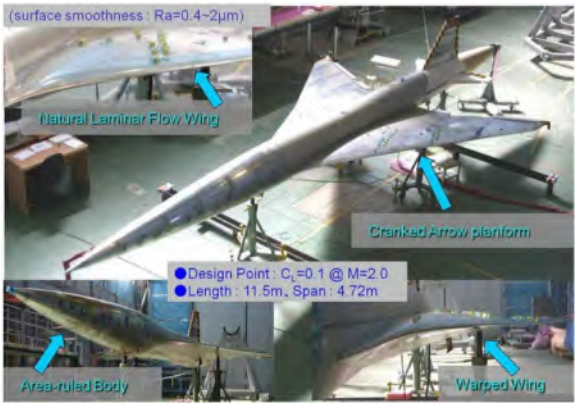

Fig. 1: JAXA unmanned-scaled experimental vehicle, NEXST-1 [1)]

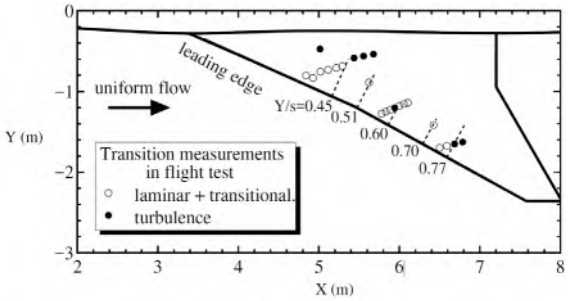

Fig. 2: Summary of the flight test on transition locations and the present sections for stability analyses [2)]

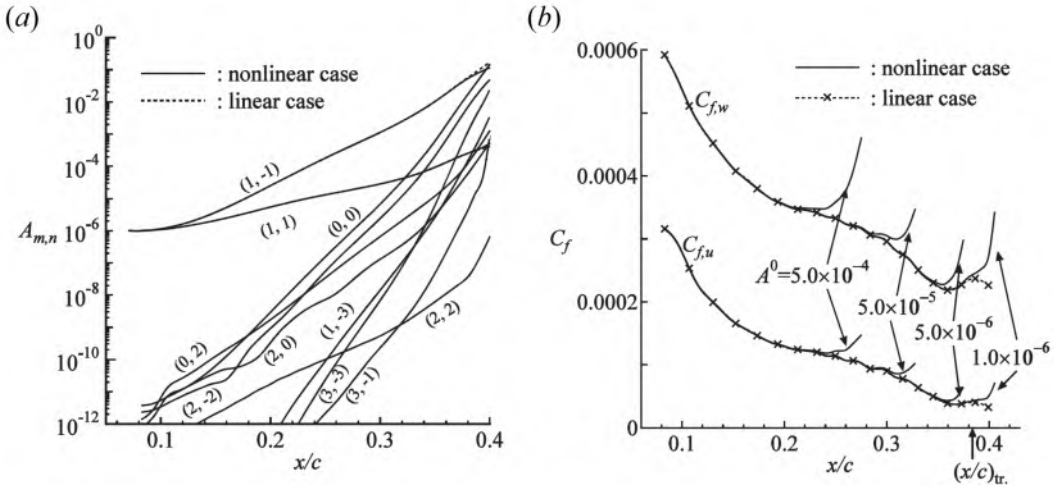

Fig. 3: (a) Nonlinear amplitude development and (b) changes in frictional drag with initial amplitude on Y/s=0.45 [3)]. Results were obtained by using NPSE.

References

1) Yoshida, K.: Supersonic Drag Reduction Technology in the Scaled Supersonic Experimental Airplane Project by JAXA, Progress in Aerospace Sciences, 45, 2009, pp. 124-146.
2) Ide, Y.: Study on Improvement of Transition Prediction Method for Three Dimensional Supersonic Boundary Layers, Ph. D dissertation, the University of Tokyo, 2016.
3) Ide, Y., Yoshida, K., and Ueda, Y.: Nonlinear Analysis of the First-Mode Dominated Transition in Supersonic Boundary Layers on Natural-Laminar-Flow Wing, Journal of the Japan Society for Aeronautical and Space Sciences, Vol.64(4), pp.296-302, (2016) (in Japanese).

Mitteilung

Fachgruppe: Turbulenz und Transition

Study of the compressible mixing-layer correction for the SST k-ω model and for the SSG/LRR-ω model and application to the simulation of plumes.

Tobias Knopp[1] and Roland Höld[2]
[1]DLR, Institut für Aerodynamik und Strömungstechnik,
Bunsenstraße 10, 37073 Göttingen, Tobias.Knopp@dlr.de
[2]MBDA Deutschland GmbH, Schrobenhausen, Roland.Hoeld@mbda-systems.de

To calculate infrared (IR) signatures generated by plumes, CFD simulations using RANS turbulence models can be used to predict species and temperature distribution as input data for the subsequent tools. RANS models were mainly developed for subsonic flows, and in some flow situations, compressibility corrections need to be applied. One such situation is compressible free-shear-layer flow relevant for the simulation of plumes. The growth of the spreading rate of high-speed mixing layers is reduced significantly compared to the incompressible regime [1], leading to a much longer extent of the region effected by the plume.

The convective Mach number M_c appears as a parameter to describe compressibility effects in mixing-layer flow from theoretical studies (see [1]). It is based on the velocity difference U_1-U_2 and the sound speeds a_1, a_2 of the two streams and is given by $M_c=(U_1-U_2)/(a_1+a_2)$. The turbulence Mach number is defined by $M_t=2k/a^2$, with k being the turbulent kinetic energy and a being the local value of the speed of sound. As M_t is computed from local flow quantities, it is attractive for use in RANS turbulence modeling to parametrize compressibility effects [2].

Although the study of the underlying physical mechanisms is still under investigation, practical modifications of RANS models were devised which attempt to describe this effect. The present work describes the validation and application of the compressibility correction by Wilcox (2006) [2], which was developed for the Wilcox k-ω [2] model, for the SST k-ω model and for the SSG/LRR-ω RSM [3] in the DLR TAU code [4]. For the Wilcox k-ω model, the modification multiplies the coefficient β^* of the magnitude of dissipation ε of turbulent kinetic energy k, given by $\rho\varepsilon=\beta^*\rho k\omega$, and the coefficient β for the destruction of ω, denoted as $\mathrm{Dest}(\omega)=\beta\rho\omega^2$, of the specific rate of dissipation ω. The modification by Wilcox (2006) proposes $\beta^*=\beta^*_{inc}[1-2F(M_t)]$ and $\beta=\beta_{inc}-\beta^*_{inc}2F(M_t)$. Here the subscript 'inc' indicates the standard coefficient for incompressible flow, and effects of changing turbulent Mach number are modeled by $F(M_t)=\max(M_t^2-M_{t,0}^2,0)$, $M_{t,0}=0.25$. Regarding the application to the RSM, the corresponding coefficients of the SSG/LRR-ω model are changed. Following the implementation in the DLR TAU code for the SST model, the blending function of the SST model is used to activate the modification only outside boundary layers.

For the test of the compressibility modification, a mixing-layer test-case was developed based on the incompressible planar mixing layer case by Delville provided at the NASA turbulence modeling resource webpage [5]. A few modifications were found to be necessary for supersonic flow speeds. The distance of the farfield boundary from the splitter plate of length c is increased and the thickness of the plate is decreased. Moreover, the taper angle in the rear part of the splitter plate is reduced. The convective Mach number is varied by changing the velocity of the high-speed stream U_h and of the low-speed stream U_l. The factor of increase of $U_h/U_{h,inc}$ and $U_l/U_{l,inc}$ was the same as the decrease of the density ρ/ρ_{inc}. The subscript 'inc' denotes values for the incompressible case. Then there is no difference in pressure, density and temparature between the upper and lower stream. Self-similar solutions for the mean velocity and for the Reynolds shear stress were found for $x/c>0.8$. The layer thickness δ_{10} was evaluated using a post-processing tool. The 10% thickness is defined as the distance between the points where the velocity is equal to $U_h-0.1\Delta U$ and $U_l+0.1\Delta U$ where $\Delta U=U_h-U_l$. The results are shown in figure 1 (left) for the SST model and the SSG/LRR-ω model without and with compressible mixing-layer modification (ML). The figure shows the spreading rate $\delta'=\mathrm{d}\delta/\mathrm{d}x$ for

the compressible flow conditions put in ratio to the incompressible case with spreading rate δ'_0, where x denotes the streamwise direction. Qualitatively, the ML modification is able to describe the reduction of δ'/δ'_0 for large M_t. However, the scatter in the reference data is obvious. Two correlations are included, i.e., the Langley curve and the curve obtained from linear stability theory by Day et al. (1998) for the amplification rate of the Kelvin-Helmholtz mode. The Langley curve was used to calibrate the function $F(M_t)$ in the ML modification by Wilcox. However, the correction appears to be a little too small if applied to the ε-equation rather than the ω-equation in the free shear layer for $0.5< M_t <1.3$, confirming the results by [6].

Regarding the calculation of IR-signatures, figure 1 (right) shows one of the driving species creating IR-signature combined with the relevant temperature. The upper part of the figure is based on the SST turbulence model using the mixing-layer correction. At the moment this CFD setting shows best comparison to experimental data in IR signature predictions. In the middle of the figure SST without mixing-layer correction is plotted which shows a far too short plume propagation in comparison to experimental data. This also is true for the RSM turbulence model given at the lower part of the figure. For RSM the mixing layer correction was not yet implemented and the CFD calculations for RSM compared to SST have been much more stable compared to SST versions. So, RSM with available mixing-layer correction has a great potential to improve CFD calculations for IR signature predictions.

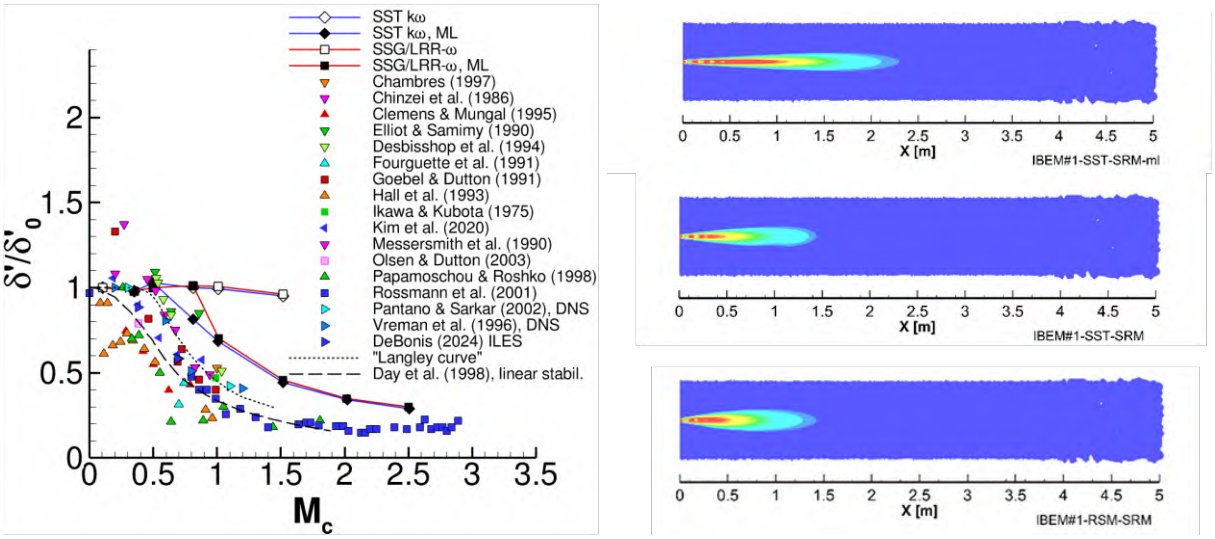

Figure 1. Left: Computed and measured spreading rate $\delta'=d\delta/dx$ for the compressible mixing layer in relation to the incompressible case with spreading rate δ'_0. Computations are for the SST model and for the SSG/LRR-ω model without and with compressible mixing layer modification denoted by ML. Right: Driving species creating IR-signature combined with the relevant temperature distribution of plumes using the SST model with compressible mixing-layer modification (ml) (top), and without modification for both the SST model (middle) and the SSG/LRR-ω (bottom).

As a conclusion, the compressible mixing-layer modification by Wilcox (2006) shows to be useful to capture compressibility effects in free-shear layer flows and in plumes. A more detailed study of the transitional regime between very small and very large values of the convective Mach number seems to be of interest for future research.

References :

[1] Smits, A. J., Dussauge, J.-P., "Turbulent Shear Layers in Supersonic Flow,", 2nd Edition, Springer, New York, 2010.

[2] Wilcox, D. C., "Turbulence Modeling for CFD", 3rd Edition, DCW Industries, 2006.

[3] Eisfeld, B., Rumsey, C., Togiti, V., Verification and validation of a second-moment-closure model. AAIA J. **54**, 1524–1541 (2016).

[4] Schwamborn, D., Gerhold, T., Heinrich, R., The DLR TAU-Code: Recent Applications in Research and Industry. In: Proc. of ECCOMAS CFD 2006, TU Delft, The Netherlands, 2006.

[5] See: https://turbmodels.larc.nasa.gov/delvilleshear_val.html (status: 27th of August, 2025).

[6] Barone, M. F., Oberkampf, W. L., Blottner, F. G., Validation Case Study: Prediction of Compressible Turbulent Mixing Layer Growth Rate. AIAA J. **44**, 1488-1497, 2006.

Mitteilung

Fachgruppe: Turbulence and Transition

The law of the wall: A phenomenological discussion for a leading order reconstruction of the mean velocity profile in fully developed turbulent channel and pipe flows

Juan A. Medina Méndez, Heiko Schmidt
Lehrstuhl Numerische Strömungs- und Gasdynamik, BTU Cottbus-Senftenberg
Siemens-Halske-Ring 15A, 03046 Cottbus
E-mail: medinjua@b-tu.de

Since early mathematical formulations or parameterizations by Prandtl, the law of the wall has been the subject of several debates in turbulence research. It is usually discussed in the context of turbulent boundary layers. Nonetheless, a specialized discussion of the law of the wall for turbulent channel and pipe flows is fully justified on the grounds of the variety of applications for which said flows can be used as surrogate models. Issues of relevance for fully developed turbulent channel and pipe flows such as the universality and extent of the logarithmic law of the wall have, to this day, not been clarified, see [1]. For practical applications concerning the use of the laws of the wall, we refer to the use case scenarios of Reynolds-Averaged Navier-Stokes (RANS) simulations utilizing linear eddy viscosity models. The applicable turbulence modeling strategy in such cases relies on the use of equilibrium assumptions on the small, unsteady scales of turbulence, i.e., the laws of the wall. This bypasses the need to resolve the full turbulence scale bandwidth.

Due to the several use cases, we discuss the topic of the derivation of the laws of the wall applicable for the mean velocity profile of fully developed (statistically stationary, and statistically streamwise homogeneous) turbulent channel and pipe flows. The starting point are the classical precepts of boundary layer theory defining the existence of an inner layer characterized by viscous scales, and an outer layer defined by outer (integral or large, macroscopic) scales. The mean velocity profile is a function F_0 of two non-dimensional quantities, see [2], i.e., $u^+ = F_0(y^*, Re_\tau)$. Note here the friction Reynolds number of the flow, Re_τ, which is defined on the basis of the usual friction velocity u_τ set by the wall-shear stress τ_w, the half-width of the channel (or the radius of the pipe) δ, and the kinematic viscosity ν. Viscous-scaled quantities are noted as ϕ^+ for any ϕ variable. Outer-scaled coordinates are denoted as $y^* = y/\delta$, with inner-scaling correspondence $y^* = y^+/Re_\tau$. The derivation procedure follows a mostly phenomenological discussion, relying heavily on Prandtl's mixing length model, as well as several precepts discussed by Clauser for the outer-layer of the mean flow. In this context, key phenomenological observations which will be used in this work, have only been achieved recently, thanks mostly to Direct Numerical Simulations (DNS). For the sake of this abstract, we focus on a derivation strategy for the logarithmic law, which we have not found elsewhere so far. Further details concerning the generalized law of the wall are reserved for the later proceedings format, in which more space is available. The derivation procedure considers Re_τ as the main input. Additionally, we rely on the use of an asymptotic value of the von Kármán constant κ, assumed to take the theoretical value derived in [3], $\kappa = (2\pi)^{-1/2} \approx 0.4$. We also resort to the following constants, which have been deemed independent of Re_τ for large Re_τ, based on the analysis of freely available DNS data [4,5,6]. The first one is the viscous coordinate of intersection of the turbulent stress and the viscous stress, $y_e{}^+$, noting the value $y_e{}^+ \approx 11$ for asymptotically large Re_τ, see [7]. The second one is the viscous coordinate corresponding to the position of the maximum of the Reynolds shear stress $\overline{u'v'}^+$, referenced as $y_{il}{}^+ = \sqrt{Re_\tau/\kappa}$, see [4].

At the wall, the wall-shear stress defines the normalization scale for the mean velocity gradient. At $y^+ = 0$, we have the viscous-scaled gradient $du^+/dy^+ = 1$. This condition leads to the

definition of the viscous sublayer law as usual, by means of a Taylor-series expansion for u^+ for small positive $y^+ \to 0$, see [2]

$$u^+ = y^+ \tag{1}$$

Next, we derive the logarithmic law for the mean velocity profile. The starting point are the fundamental precepts of the law of the wall by Prandtl and Taylor, loosely referenced by Spalding as the Prandtl-Taylor model, see [8]. These specify that the viscous sublayer extends over the range of dominance of the viscous stress, and that the turbulent layer (for the context of this abstract, the logarithmic layer), extends over the range of dominance of the turbulent stress. We specialize now on asymptotically large Re_τ. Since turbulent and viscous stresses must sum up to unity, viscous stresses dominate for $du^+/dy^+ \geq 0.5$. The before mentioned limit value, $du^+/dy^+ = 0.5$, occurs, therefore, at the intersection of turbulent and viscous stresses. This is the before mentioned ${y_e}^+$. The limit value $du^+/dy^+ = 0.5$ must be satisfied by both the viscous sublayer law, Eq. (1), and the logarithmic law, such that $u^+({y_e}^+) = {y_e}^+$. Next, we use the assumed value of κ and obtain the logarithmic law from the asymptotic indicator function $y^+ du^+/dy^+ = 1/\kappa$ [2,4], using definite integration (from ${y_e}^+$ to an arbitrary y^+),

$$u^+ = \frac{1}{\kappa} ln\left|y^+\right| + \left({y_e}^+ - \frac{1}{\kappa} ln\left|{y_e}^+\right|\right) \tag{2}$$

We can verify that the coordinate-independent term in Eq. (2) corresponds to the usually discussed value $B \approx 5$, which is cited for the log-law form $(1/\kappa)\, ln\left|y^+\right| + B$, see [2]. We will determine the lower bound of the range of validity of Eq. (2) by its intersection with an equally similar and surprisingly simple logarithmic law defined for the buffer layer (not shown here). We will also conjecture that the upper bound of the range of validity is $y^+ = Re_\tau$ at large Re_τ, or the before mentioned ${y_{il}}^+$ at lower Re_τ, where the validity of the Prandtl-Taylor model precepts is still guaranteed (dominance of turbulent stresses). Besides the buffer layer, other laws for the mean velocity profile will also follow: an inertial layer law (related to the defect law), and a wake layer law (related to the law of the wake). All layers observe relatively simple forms like Eq. (2). This stresses the importance of this work for understanding the physics of wall-bounded turbulence in comparison to the use of complex implicit equations such as the Spalding velocity profile [8]. Figures 1 and 2 show several mean velocity profiles of turbulent channel and pipe flows at different Re_τ, comparing freely available DNS data with the derived law of the wall (including all layers). Excellent agreement is noted.

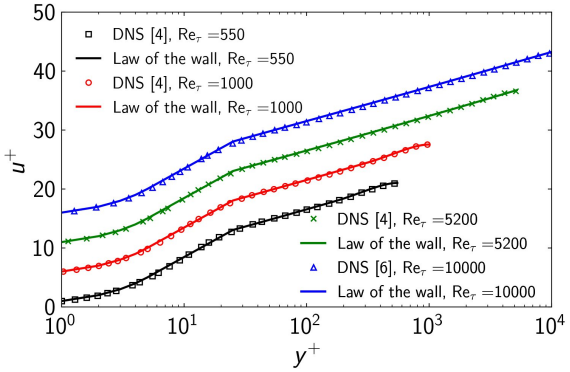

Figure 1: Channel flow velocity profiles. Larger Re_τ data is shifted upwards for improved visualization

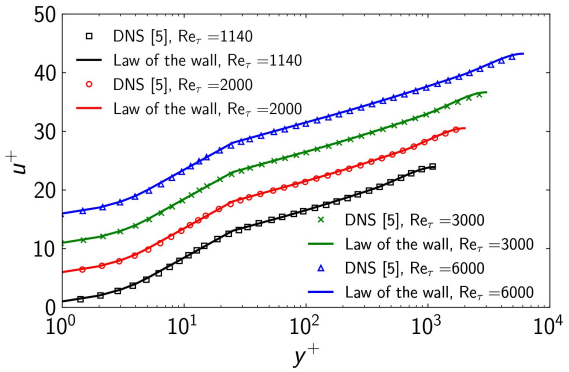

Figure 2: Pipe flow velocity profiles. Larger Re_τ data is shifted upwards for improved visualization

References

[1] I. Marusic et al. (2013), J. Fluid Mech. 716 R3. DOI: 10.1017/jfm.2012.511
[2] S. B. Pope (2000), *Turbulent Flows*. Cambridge: Cambridge University Press.
[3] H. Z. Baumert (2013), Phys. Scr. T155, 014001. DOI: 10.1088/0031-8949/2013/T155/014001
[4] M. Lee and R. D. Moser (2015), J. Fluid Mech. 774, 395-415. DOI: 10.1017/jfm.2015.268
[5] S. Pirozzoli et al. (2021), J. Fluid Mech. 925 A28. DOI: 10.1017/jfm.2021.727
[6] S. Hoyas et al. (2022), Phys. Rev. Fluids 7, 014602. DOI: 10.1103/PhysRevFluids.7.014602
[7] F. Laadhari (2002), Phys. Fluids 14, L65-L68. DOI: 10.1063/1.1511731
[8] D. B. Spalding (1961), J. Appl. Mech. 28(3), 455-458. DOI: 10.1115/1.3641728

Mitteilung

Fachgruppe: Turbulenz und Transition

A Functional Large Eddy Model Rooted in URANS

Michael E. Olsen
NASA Ames, PO Box 1, NASA Ames Research Center, michael.e.olsen@nasa.gov

The most computationally efficient LES model would be one that could produce valid flow field predictions with grids that are locally a small fraction of the turbulent energy length scale. This model would give the same (statistically) same prediction on grids finer than this 'baseline grid'. Similarly, there will be a timestep for which choosing smaller timesteps again reproduces the same statistics when averaged over a sufficiently long period --- which could be termed an "turbulent energy time scale", in analogy with the energy length scale.

A RANS model has been used successfully to provide predictions of many massively separated and unsteady flow fields of interest. The first was for rocket nozzle flow fields in severely off-design conditions where the separation point and surface pressures were correctly predicted. After that success, the model correctly predicted forces and moments for the Apollo command module $0° \leq \alpha \leq 180°$, $0.9 \leq M_\infty \leq 6$. Apollo's descendant, the CEV/MPCV command module was the next such flow field simulated, and surface pressure and integrated loads over the transonic range, along with matching the frequency content found experimentally in the transonic regime. For these cases, the model also matched the experimental result that for Mach numbers above 1.05, the flow was steady. Freestream Mach numbers below .9 became increasingly chaotic, and did not exhibit a simple periodic behavior computationally, which mimicked experimental results. Further successful massively separation predictions included the FAITH hill validation test case.

More complex physics have been added (eddy viscosity $\rightarrow$ Reynolds-stress$\rightarrow$ turbulent transport $\rightarrow$ turbulent axial length) but the general philosophy of all of these follows the "history honoring" design of the eddy viscosity model. Success on other turbulent flows with strong organized 2D structures suggested that high a Reynolds number circular cylinder in crossflow might also be reliably predicted with the simple eddy viscosity model. This classic flow field has been studied extensively (Achenbach, Roshko,) and comparison with these results will be discussed here.

The time and grid resolved simulations of this flow field will be compared to experiment. These are 2D simulations and so have more modest computational requirements than full three-dimensional case with tunnel walls require. These results give an intriguing glimpse into physical details that will certainly be found in more complete simulations. The very reasonable match to surface pressure, average wall shear, and Strouhal number gives credence that the flow field computationally simulated is likely very similar to that one would see along the center symmetry plane of the experiments. It also highlights the mixed turbulent and non-turbulent flow that is being mixed by the large vortical structures that dominate the wake of the cylinder.

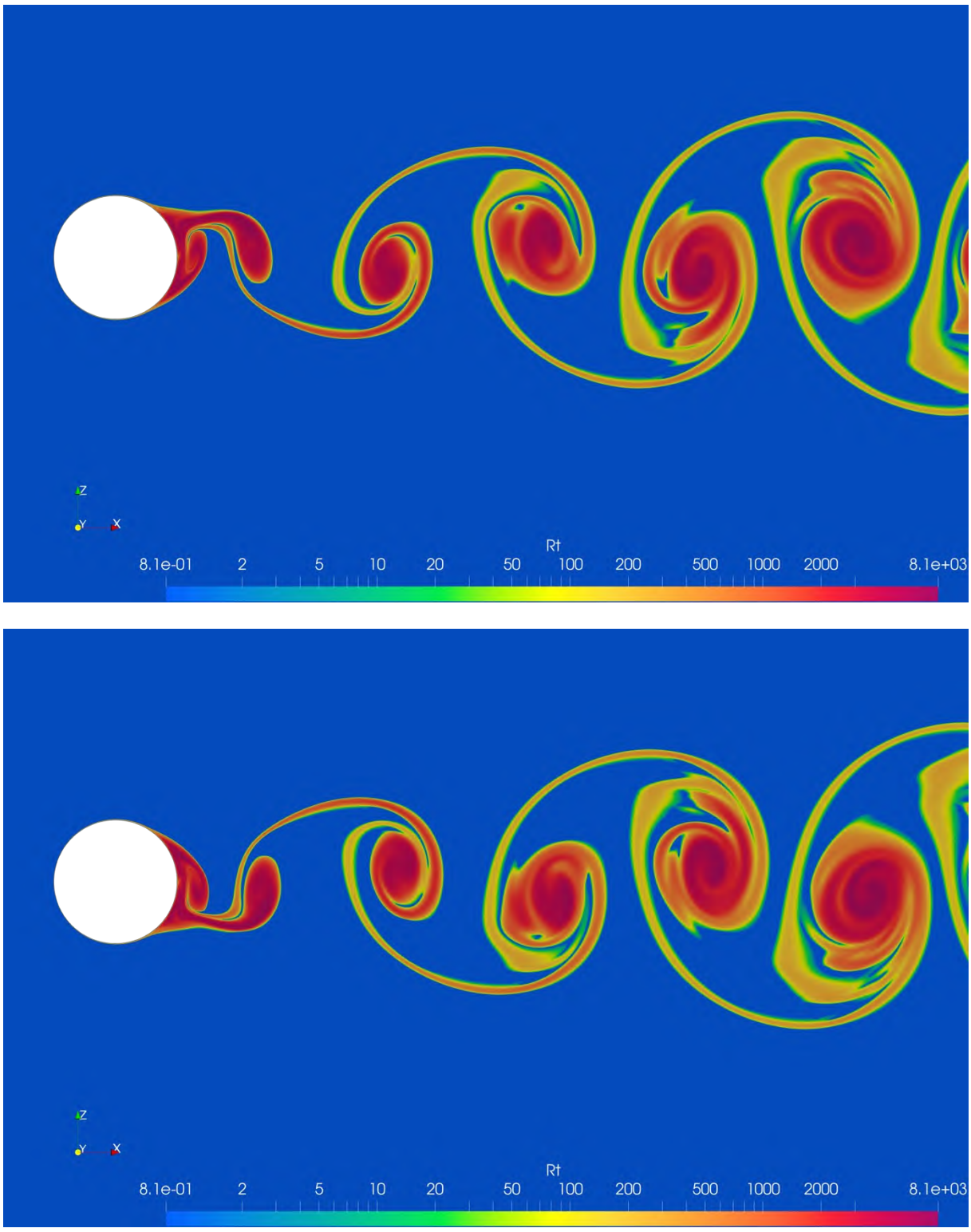

Snapshots of the wake: Medium spatial grid results.
R_T – turbulent Reynolds number ($k^{1.5}/\varepsilon$) for M=0.25, $Re_d=5\cdot10^6$, $K/D=11\cdot10^{-6}$ (surface roughness), $T_u=0.007$ (Freestream Turbulence Intensity). Entrained freestream fluid is blue, being mixed with the turbulent flow convicting from the separated zone. Compare with Van Dyke's "Album of Fluid Motion", showing the same mixing of turbulent/non-turbulent flow.

Mitteilung

Fachgruppe: Turbulenz und Transition

New Insight into Material Transport in a Turbulent Boundary Layer based on Lagrangian Areas of Minimal Stretching (LAMS)

Ulrich Rist, Matthias Weinschenk and Christoph Wenzel
Institut für Aerodynamik und Gasdynamik, Universität Stuttgart, 70550 Stuttgart
rist/weinschenk/wenzel@iag.uni-stuttgart.de

The purpose of the present contribution is identifying and studying coherent, material-based fluid motions in a spatially evolving turbulent boundary-layer (TBL) flow obtained via DNS. To this end, the Finite-Time Lyapunov Exponent (FTLE) was computed in wall-parallel slices, spaced finely enough to cover the entire three-dimensional domain. In contrast to previous investigations the present work focuses on the bright regions between the dark structures in the FTLE field (cf. Fig. 1), which have not yet been further considered in the turbulent boundary-layer literature. As these regions are detected using a Lagrangian technique and exhibit minimal local stretching in the Cauchy–Green tensor, the term *Lagrangian Areas of Minimal Stretching* (LAMS) has been proposed for them. The physical significance of LAMS lies in the fact that they track connected, material-bound fluid regions over finite time intervals. This is found to be an equally relevant phenomenon in the turbulent boundary layer compared with those areas where shear dominates (i.e. the dark regions in the FTLE field).

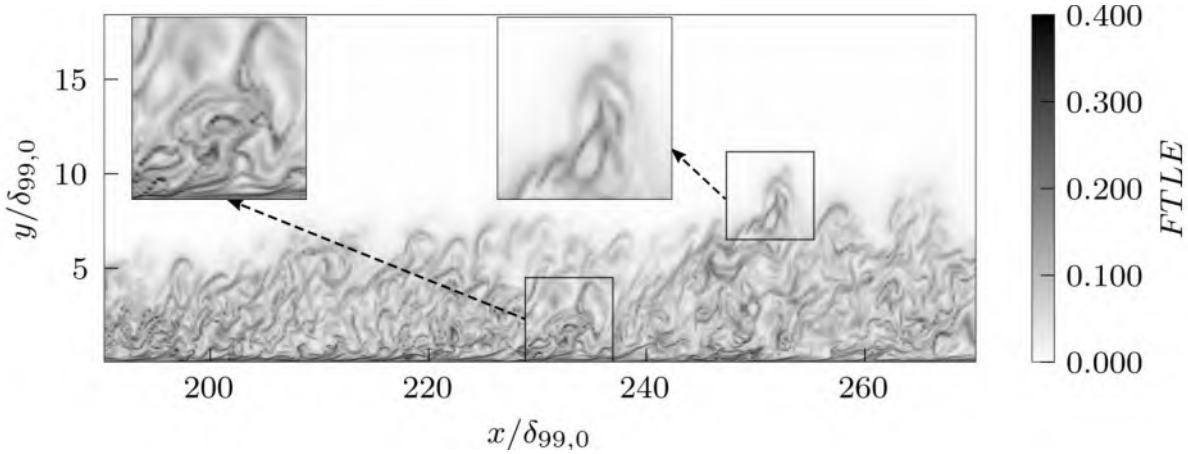

Figure 1: Streamwise-wall-normal cut through the instantaneous FTLE field of a turbulent boundary layer with enlargements on structures close to the wall and close to the edge of the boundary layer.

For a quantitative evaluation of the flow field, the histograms of all FTLE data in each wall-parallel plane have been used to define appropriate threshold values to separate areas of minimal stretching from the rest [1]. Further processing was then restricted to these LAMS. This led to the unexpected observation that LAMS are to a large extent linked to high- and low-speed streaks, with the former being particularly coherent. Further analysis of the data has shown that these regions correspond to so-called sweep (Q4) and ejection (Q2) events with a pronounced dominance of Q4 vs. Q2 events above $y^+ \approx 20$ and vice versa below.

Our analysis indicates that LAMS from both above and below are aspirated by the most intensive streamwise vortices at this wall distance. These processes and motions were confirmed through particle traces, cross-sectional views of the flow field, filtered statistical data, and evaluations of the instantaneous temperature field, which acts as a passive scalar, tracking hotter fluid rising from the wall and cooler fluid descending toward it.

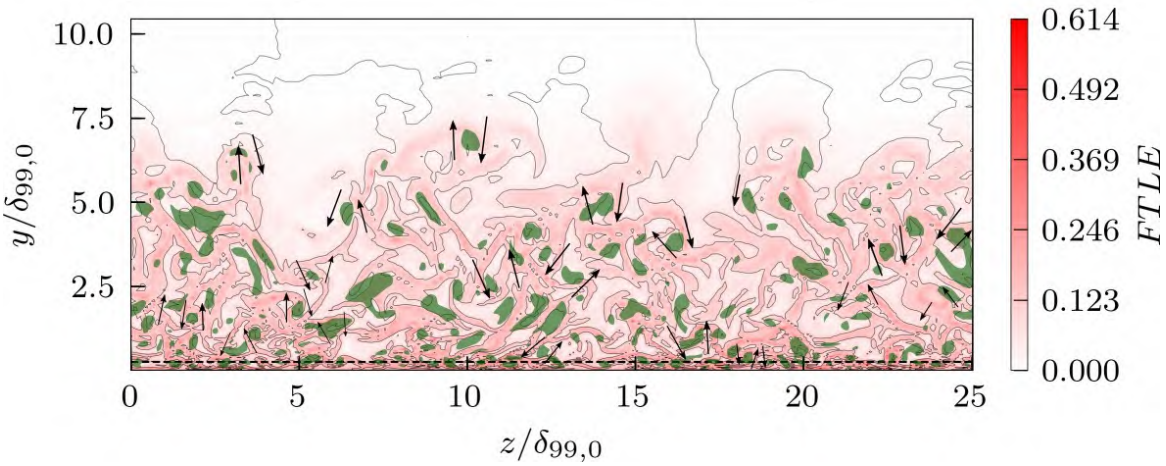

Figure 2: Comparison of the instantaneous FTLE field (red) with λ_2 vortex identification (green) [2]. The grey isoline at FTLE ≈ 0.06 surrounds LAMS. Flow vectors are exemplarily drawn based on LIC [3]. The horizontal black dashed line is at $y^+ \approx 20$.

Figure 2 shows a snapshot of the flow field in a cross section at $x = const$, i.e, normal to the mean flow, looking in downstream direction. Light-coloured areas surrounded by an FTLE-isoline visualize LAMS. Red areas correspond to areas with high stretching. Green blobs show negative λ_2 which indicates vortices, according to [2]. The exemplary flow vectors have been extracted from a corresponding LIC visualization [3] in the same plane. At the upper edge of the TBL, uprising turbulent blobs from within the boundary layer are compensated by large blobs of LAMS sinking towards the wall, e.g. at $z/\delta_{99} \approx 5$ and 17. On their way towards the wall other LAMS are driven and torn up by streamwise and obliquely oriented vortices (green blobs), a process which ends in the lower log layer at $y^+ \approx 20$. Below, at a smaller scale and hence less obvious here, LAMS are lifted from the viscous sublayer. More details will be shown in the presentation.

References:

[1] Rist, U., Weinschenk, M. &. Wenzel, C. (2023): Investigation of Lagrangian Areas of Minimal Stretching (LAMS) in a Turbulent Boundary Layer, J. Fluid Mech. **970**

[2] Jeong, J. & Hussain, F. (1995): On the identification of a vortex. J. Fluid Mech. **285**, 69–94.

[3] Cabral, B. & Leedom, LC. (1993): Imaging vector fields using line integral convolution. In Proceedings of the 20th Annual Conference on Computer Graphics and Interactive Techniques, pp. 263–270. Association for Computing Machinery (ACM).

Mitteilung

Projektgruppe/Fachkreis: Transition

Experiments on the combined influence of free-stream turbulence and roughness element on boundary layer transition

T. M. Römer, M. Kloker, U. Rist, C. Wenzel
Institut für Aerodynamik und Gasdynamik der Universität Stuttgart
Pfaffenwaldring 21, 70569 Stuttgart, roemer@iag.uni-stuttgart.de

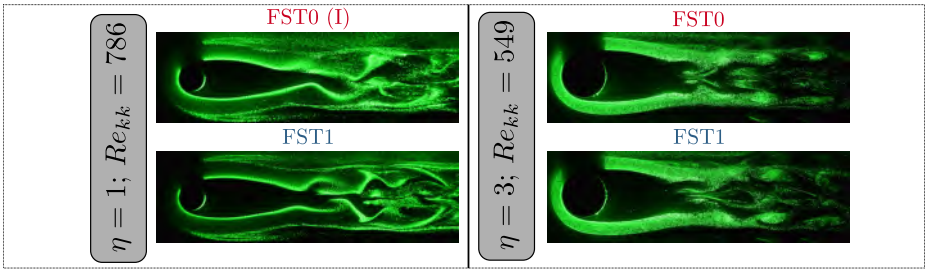

Figure 1: Top view of HBV, left thin and right thick cylinder (supercritical Re_{kk})

The effects of isolated roughness elements and free-stream turbulence (FST) on boundary-layer transition have both been studied extensively, but mostly in isolation. Their interaction is, however, of direct relevance in practical flows, for instance over turbine blades. This work addresses this gap by studying how FST affects instability mechanisms and critical/transitional Reynolds numbers in roughness-disturbed boundary layers (BL).
The experiments were conducted in the Laminar Water Channel (LWC), using cylindrical roughness elements of thin ($\eta = d/k = 1$) and thick ($\eta = 3$) aspect ratios placed within a Blasius BL at $x = 400\,\mathrm{mm}$, being d the diameter and $k = 7\,\mathrm{mm}$ the roughness height. The streamwise position was chosen to match similar $Re_{kk} = u_k k/\nu$ and k/δ_1 values from the literature [1–3], being u_k the velocity at roughness height, ν the kinematic viscosity and δ_1 the displacement thickness. FST was introduced through a passive grid (similar to [4]), giving $Tu = 1.2\,\%$ at the leading edge. The flow was analysed using hot-film anemometry, particle image velocimetry (PIV), and hydrogen-bubble visualisations (HBV).
Fig. 1 shows HBV of a thin (left) and thick (right) cylinder, without additional FST (FST0, top) and with added FST (FST1, bottom), in the supercritical Reynolds number regime. This regime is defined by the occurrence of at least one unstable eigenmode of the global linear stability analysis. For the thick cylinder ($\eta = 3$), the visualisations show a varicose (symmetric) instability in both FST0/FST1 cases. This is in accordance with e.g. [1, 2] and reveals that the instability type is not affected by FST. For the thin cylinder ($\eta = 1$) without added FST, the flow shows a sinuous (anti-symmetric) instability, also in accordance with the literature [1]. (Note that a varicose mode is also superimposed but not visible in the visualisation (details next section); hence, the sinuous mode is labelled with (I) and the varicose mode shown in the next section with (II).) However, with added FST, the instability behaves completely differently, showing a varicose instability (FST1) instead of a sinuous instability (FST0 (I)).
Fig. 2 shows, for the same supercritical Reynolds numbers as in Fig. 1, the dynamic mode decomposition (DMD) modes (left) and the power spectral density (PSD, right). The angular frequency is defined as $\omega = 2\pi f k U_\infty^{-1}$, where f denotes the measured physical frequency f [Hz] and U_∞ the free-stream velocity. The coordinate system $(x_k/y_k/z_k)$ is scaled with k and originates at the cylinder. For thick cylinders ($\eta = 3$), the results

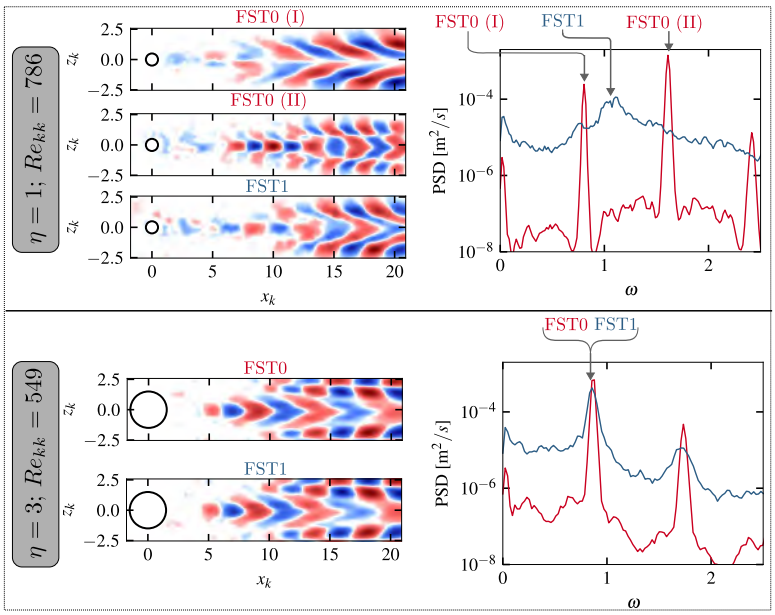

Figure 2: DMD modes (left) and PSD analysis (right) (supercritical Re_{kk})

show that the varicose instability dominates with and without FST, and neither the mode type nor its frequency is measurably influenced by FST, consistent with predictions from global linear stability theory [1]. For the thin cylinder (top figure) without FST (FST0), the DMD shows a coexistence of a sinuous FST0 (I) and varicose FST0 (II) global mode in the supercritical regime, consistent with [2]. The appearance of an additional varicose instability FST0 (II) is an (experimental) effect, resulting from their receptivity to broadband frequencies (such as low FST levels) [3]. Note that the HBV in Fig. 1 only shows a sinuous instability FST0 (I), highlighting the importance of performing additional PIV measurements. When grid-generated FST is introduced (FST1), this coexistence disappears: only a varicose mode persists at a different ω, while the sinuous mode is almost completely suppressed. This qualitative change highlights the sensitivity of thin-cylinder wakes to external forcing.

Thus, FST – in particular, the induced meandering Klebanoff modes in the BL – have a significant influence on the wake modes of cylindrical roughness elements, an effect previously not looked at. Given that the behaviour of these modes is closely linked to the critical Reynolds number [1, 3], the present study offers new insights into the underlying mechanisms of roughness-induced transition with FST. A detailed discussion of these findings, including transition Reynolds numbers for various cylinder geometries, will be presented.

References

[1] J.-Ch. Loiseau, J.-Ch. Robinet, S. Cherubini, and E. Leriche. Investigation of the roughness-induced transition: global stability analyses and direct numerical simulations. *Journal of Fluid Mechanics*, 760:175–211, 2014.

[2] D. K. Puckert and U. Rist. Experiments on critical Reynolds number and global instability in roughness-induced laminar–turbulent transition. *Journal of Fluid Mechanics*, 844:878–904, 2018.

[3] M. A. Bucci, D. K. Puckert, C. Andriano, J.-Ch. Loiseau, S. Cherubini, J.-Ch. Robinet, and U. Rist. Roughness-induced transition by quasi-resonance of a varicose global mode. *Journal of Fluid Mechanics*, 836:167–191, 2018.

[4] T. M. Römer, M. J. Kloker, U. Rist, and C. Wenzel. Experimental investigation on boundary-layer streaks induced by grid-generated free-stream turbulence in a water channel. *Experiments in Fluids*, 65(12), 2024.

Mitteilung

Fachgruppe: Turbulenz und Transition

A (very) poor man's approach to turbulence modeling

Cord Rossow, Museumstraße 4, 38100 Braunschweig
cord.rossow@dlr.de

Problem Statement:
For airfoil and wing flows, it was recently shown that zero-equation, purely algebraic turbulence models based on Prandtl's mixing length theory are able to provide adequate modeling capabilities. However, one of the shortcomings of such models is the reliance on rays normal to the wall to evaluate relevant boundary layer parameters, and the necessity for a special treatment of the wake. Thus, extending the use of algebraic models to unstructured methods was not feasible, and a strategy to overcome this limitation is required.
Objective:
Zero-equation algebraic turbulence models mainly rely on the "Mixing Length" hypothesis, which Ludwig Prandtl first proposed almost 100 years ago at the 1925 GAMM conference in Dresden [1]. In a recent contribution [2] it was shown that for airfoil and wing flows, algebraic turbulence models may provide modeling capabilities rivaling those of sophisticated one- and two-equation turbulence models. One of the main characteristics of algebraic turbulence models such as the Baldwin-Lomax [3] model is the evaluation of boundary layer parameters normal to a solid wall; essentially, algebraic turbulence models are "non-local". In structured codes, the grid lines normal to the wall are a natural choice for this evaluation, and the grid points on those lines are ordered smoothly. Another important characteristic is that the modeling ansatz has to change when transitioning from the wall boundary layer region to the turbulent wake region. In the wake region, along lines perpendicular to the main flow direction certain features of the shear layers have to be evaluated. In structured codes, these lines are also naturally provided.
The situation is completely different for unstructured codes, since here such lines are not directly available. In unstructured codes, lines normal to solid surfaces if at all are constructed for line implicit solution methods. However, it is not assured that the distribution of points along these lines fulfils certain smoothness criteria as required for adequate evaluation relevant boundary layer parameters. This is further aggravated in the wake region, since here the necessary lines have to be perpendicular to the flow direction. Since construction of lines for implicit methods is mainly based on grid features like cell aspect ratio, such lines may not be suitable for algebraic wake models. Up to now, this has impeded the implementation of zero-equation algebraic turbulence models into unstructured codes.
Strategy:
To implement algebraic turbulence models into an unstructured code, two main problems have to be attacked: the dependence on lines normal to solid surfaces needs to be abandoned, and the treatment of the wake region has to be made independent of line information. This means that essentially the non-locality of the model has to be reduced as far as possible. Therefore, to get rid of the wake treatment, it is hypothesized that for airfoil and wing flows, it is most important to assure that the Kutta condition at the trailing edge holds, and that features of the flow further down may be neglected. In the present work, this is achieved by restricting the turbulent wake region to an area scaled by a fraction of the Reynolds number reference length. For transitioning from the wall normal turbulent region to the wake region, the angle of distance vectors from the nearest wall point to a field point in the wake region is used. When this angle falls under a certain threshold, turbulence is just assumed to be a certain multiple of the molecular viscosity.
To avoid the evaluation of boundary layer parameters along lines normal to the wall, relations between flow variables at the wall, e.g., friction velocity and isentropic wall velocity, and distance of field points, were established. This allowed to estimate the location of the transition from the inner layer, where the law of the wall holds, and the outer layer where the reduction

of eddy viscosity is modeled by a Klebanoff function. Using dimensional analysis, physical insight and numerical experimentation, two formulations could be derived. It was found that for transonic flows, a blend of the two formulations gave results satisfactory for estimating the influence of turbulence on the location of shock waves.

Results:

Figures 1 and 2 show results for the flow over a flat plate comparing different turbulence models, where SA denotes the Spalart Almaras one-equation model, BL_org the Baldwin Lomax model, and PR_ml and PR_ml+ the models derived in [2]. The current model is denoted in these figures by PR_test, and it can be observed that the flow over the flat plate is predicted with comparable accuracy.

Figures 3 and 4 show computational and experimental results for the well known RAE2822 airfoil CASE 9 and 10 onflow conditions. Computations were performed with the original algebraic Baldwin-Lomax (*BL_org*) model of [3], and the algebraic model developed in this contribution (*PR_ml0*). As can be seen, the present *PR_ml*0 model delivers results comparable to the original Baldwin Lomax model, confirming that the present, simplified model provides a satisfactory capability to estimate the influence of turbulence.

Literature:

[1]Prandtl, L.: "Bericht über Untersuchungen zur ausgebildeten Turbulenz", ZAMM 5, pp.136-139, 1925.

[2]Rossow, C.-C.: "100 years of Prandtl's Mixing Length: falling short for aerodynamic analysis?", accepted for publication in Springer Nature: New Results in Numerical and Experimental Fluid Mechanics XV, Contributions to the 24th STAB/DGLR Symposium, 2024.

[3]Baldwin, B.S., Lomax, H.: "Thin Layer Approximation and Algebraic Model for Separated Turbulent Flow", AIAA Paper 78-257, 1978.

Figures:

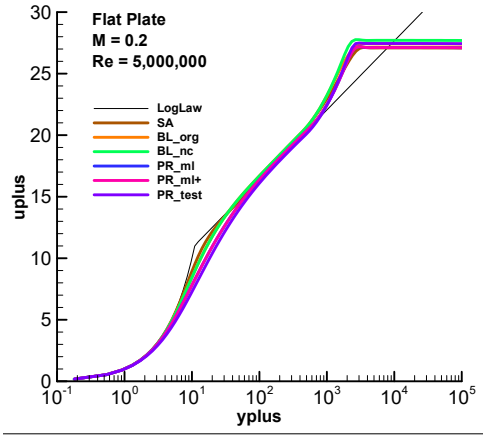

Fig. 1. Flat plate: velocity distribution

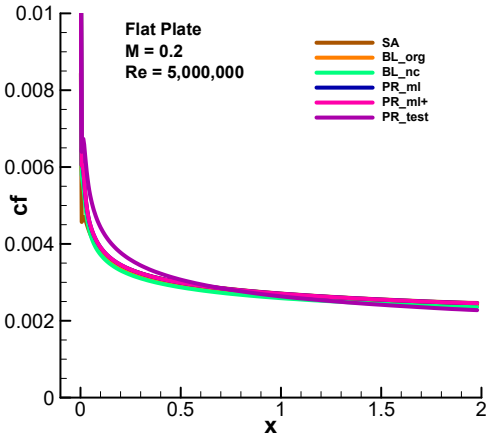

Fig. 2. Flat plate: local skin friction

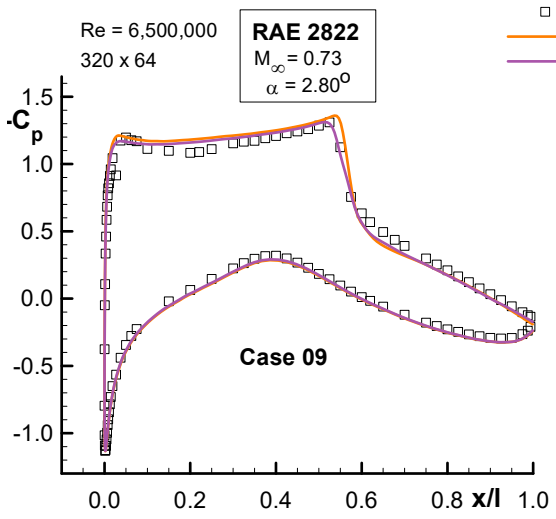

Fig. 3. Case 09: pressure distribution

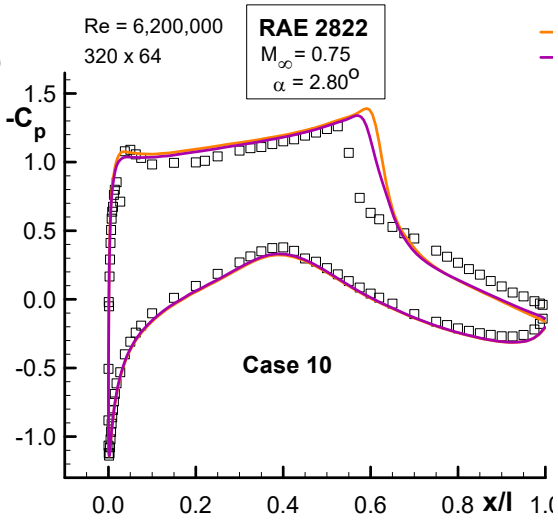

Fig. 4. Case 10: pressure distribution

Mitteilung

Fachgruppe: Turbulenz und Transition

Experiences and Lessons Learned using the FI/ML Approach for Data-driven Turbulence Modeling

Mert Can Semercioglu
DLR, Bunsenstraße 10, 37073 Göttingen, mert.semercioglu@dlr.de

Introduction:

Reynolds-averaged Navier-Stokes (RANS) turbulence models, due to their robustness and relatively low computational cost, are extensively used in aeronautical applications. Nevertheless, they show limited accuracy in complex flow conditions, such as separated flows, highly curved surfaces, and shock–boundary layer interactions. To enhance RANS predictions in such scenarios, a promising approach known as Field Inversion and Machine Learning (FI/ML) has been developed [1], which leverages data-driven techniques and machine-learning algorithms. RANS models enhanced with FI/ML have shown promising results when evaluated under flow conditions consistent with the training data, but their performance has been more limited in scenarios outside the training regime. This highlights the challenge of generalization, which has motivated the development of advanced training strategies [2], alternative machine-learning algorithms [3], conditional field-inversion techniques [4], and sensor-based modular modeling approaches [5].

Numerical methodology:

A data-driven FI approach infers a spatially-varying correction term β from experimental or high-fidelity numerical data, designed to reduce model form errors in RANS. The corresponding correction for the negative Spalart–Allmaras (SA-neg) turbulence model is presented in the equation below:

$$\frac{D\tilde{\nu}}{Dt} = \boldsymbol{\beta} P(\mathrm{U}, \tilde{\nu}) - D(\mathrm{U}, \tilde{\nu}) + \mathrm{T}(\mathrm{U}, \tilde{\nu})$$

Here, β denotes the correction field, $\tilde{\nu}$ the SA-neg variable, P the production term, D the destruction term and T the diffusion term. Each β field obtained via FI reflects the specific local and global characteristics of a given flow case, and machine-learning models aim to generalize the mapping between angle of attack, Mach number, Reynolds number, local features (η), and β. However, the FI process does not yield a unique correction field — multiple β fields can reproduce the same observational data equally well, reflecting the **multi-solution nature** of the inversion problem, which poses a significant challenge to the generalization capacity of ML-based approaches.

Results:

It is well documented in the literature that the SA-neg model tends to overpredict the eddy viscosity under adverse pressure gradient (APG) conditions. Therefore, in the modified SA-neg model, the correction field β is applied in a way that suppresses turbulence production under these conditions. To illustrate this, FI was performed on S809 airfoil at 12.2 ° under different magnitude of regularization settings (reg1, reg2). The regularization penalizes large modifications and prevents unphysical adjustment. As shown in the figure 1, the resulting correction fields β demonstrate the multi-solution nature of the inversion problem. Despite yielding similarly accurate pressure-coefficient predictions compared to the reference data, these solutions were obtained from different β distributions. The correction introduced through FI enables the reproduction of the pressure plateau in the rear region of airfoil in agreement with the experimental data, which is not captured in the baseline solution.

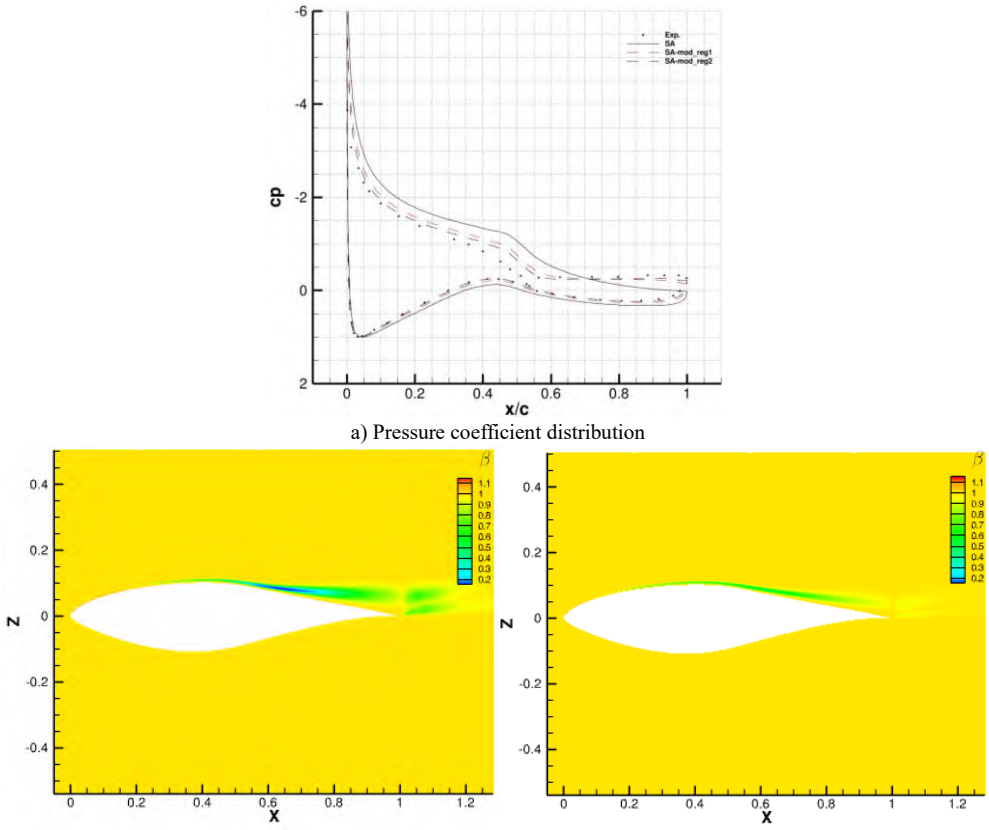

a) Pressure coefficient distribution

b) β field distributions with reg1 und reg2 parameter

Figure 1: Results on the S809 airfoil with various regularization parameter

Conclusion and Outlook:

The FI/ML approach was applied to case with APG. Under these conditions, the correction field β can capture the characteristic pressure plateau that arises due to boundary layer separation. Moreover, it becomes evident that different flow conditions yield different β fields, highlighting the multi-solution nature of the β fields. This issue has been widely studied in the literature, as it poses challenges for the generalization capacity of FI/ML-based models. Future work aims to address this problem by investigating the influence of selected flow features and the flow regime on the correction behavior.

References:

[1] Singh, A. P., and Duraisamy, K., “Using field inversion to quantify functional errors in turbulence closures,” Physics of Fluids, Vol. 28, No. 4, 2016, p. 045110. https://doi.org/10.1063/1.4947045.

[2] Köhler, Felix Rüdiger. "Advancing Reynolds-Averaged Navier–Stokes Turbulence Models with Machine Learning and Data-Driven Methods."

[3] He, Zizhou, Chenyu Wu, and Yufei Zhang. "A field inversion and symbolic regression enhanced Spalart–Allmaras model for airfoil stall prediction." *Physics of Fluids* 36.6 (2024).

[4] Wu, Chenyu, Shaoguang Zhang, and Yufei Zhang. "Development of a generalizable data-driven turbulence model: Conditioned field inversion and symbolic regression." AIAA Journal 63.2 (2025)

[5] Nishi, Yasunari, et al. "On the Generalization Capability of a Data-Driven Turbulence Model by Field Inversion and Machine Learning." Aerospace (MDPI Publishing) 11.7 (2024).

Mitteilung

Fachgruppe: Turbulenz und Transition

Numerical Study of Compressible Turbulent Asymptotic Suction Boundary Layers

A. Sunthararajan, S. A. Cifuentes Waidelich, T. Gibis, C. Wenzel
Institut für Aerodynamik und Gasdynamik der Universität Stuttgart
Wankelstraße 3, 70563 Stuttgart, sunthararajan@iag.uni-stuttgart.de

In order to advance mobility while minimizing the environmental impact of human activity, it is essential to reduce aerodynamic drag and enhance the energetic efficiency of moving bodies. A comprehensive understanding of boundary-layer control is paramount, as this layer significantly impacts skin-friction and substantial drag. In the 1930s, the effects of suction and blowing on boundary layers were examined by investigators. In a theoretical analysis, Griffith and Meredith [5] derived the first analytical solution for the velocity profile for the incompressible, two-dimensional asymptotic suction boundary layer (ASBL) and theoretically calculated performance gains for aircraft in the 10,000-lb class. Since then, ASBL has been the subject of extensive investigation, both analytically and experimentally [4, 6].

However, there is no complete analytical description of the turbulent asymptotic suction boundary layer (TASBL), which poses challenges for numerical and experimental analyses [1, 3]. Despite these difficulties, the TASBL serves as a valuable bridge between channel flows and spatially evolving boundary layers, making it a noteworthy candidate for fundamental research and for gaining insights into fundamental assumptions about energy transfer. In the context of high-speed aerodynamics and propulsion, in which compressibility and thermal loads play major roles, the compressible turbulent asymptotic suction boundary layer (TASBL) has remained largely unexplored [2].

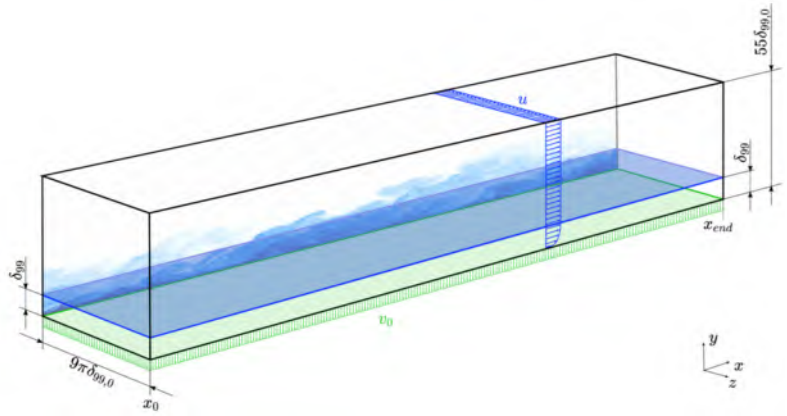

Figure 1: Simulation domain for a compressible TASBL

As an initial step toward establishing a reference database, direct numerical simulations (DNS) of compressible TASBLs have been performed at Mach number $M = 2.0$ for three suction ratios $\Gamma = (\bar{\rho}/\rho_e)\,(\tilde{v}_w/u_e) = -0.0021, -0.0023, -0.0025$, where the subscript w denotes wall values and e boundary-layer-edge values. As a point of reference, these results are complemented by a quasi-incompressible case at $M = 0.8$ with $\Gamma = -0.0025$.

The comparison reveals that key features known from incompressible TASBLs also persist in the compressible regime: the logarithmic region of the u^+ profile is extended, and the wake is absent. Compared with a non-transpired turbulent boundary layer, the compressible TASBL exhibits a higher friction Reynolds number Re_τ and reduced turbulent fluctuations. Moreover, the recovery factor r is unity, meaning that the total enthalpy at the wall ($h_{t,w}$) equals that of the outer freestream ($h_{t,e}$), independent of Mach number. As a result, the total shear stress in the near-wall region is not constant. Both findings stand in contrast to the canonical non-transpired turbulent boundary layer [2].

Owing to its spatially non-growing nature, the compressible TASBL is already self-similar in its temporal mean and can therefore be described by a single-layer behavior only depending on inner scales. In the outer region, however, a dependence on the edge Mach number M and suction ratio Γ persists, suggesting that inner viscous units do not consistently scale the turbulent motions of the outer layer across all cases. The best collapse of outer-region profiles for TASBLs at different Mach numbers and suction ratios is achieved using the Zagarola-Smits scale, whereas a van Driest-transformed velocity profile fails to collapse fully in the logarithmic region for a compressible TASBL, in contrast to the incompressible TASBL [2].

In addition, the following observations are made: increasing Γ reduces the log-law slope, lowers fluctuation magnitudes, shifts their peaks outward, increases near-wall anisotropy, and decreases turbulent kinetic energy throughout the layer. The turbulent Prandtl number deviates from its quasi-constant behavior only very close to the wall, exhibiting a small peak that moves outward as Γ and M rise; farther out, it approaches values similar to those in non-transpired compressible TBLs. Crucially, equal Γ does not guarantee dynamical equivalence between compressible and incompressible TASBLs: while the skin-friction coefficient c_f may match, the shear-stress distributions do not [2].

In the accompanying presentation, the findings will be presented in refined form and set into context through a structured overview of the study.

References

[1] A. Bobke, R. Örlü, and P. Schlatter. "Simulations of turbulent asymptotic suction boundary layers". In: *Journal of Turbulence* 17 (Feb. 2016), pp. 157–180. DOI: 10.1080/14685248.2015.1083574.

[2] S. A. Cifuentes Waidelich. "Direct Numerical Simulation of Compressible Turbulent Asymptotic Suction Boundary Layers". Master's Thesis. Stuttgart: Universität Stuttgart, Oct. 2021.

[3] M. Ferro, B. E. G. Fallenius, and J. H. M. Fransson. "Experimental study on turbulent asymptotic suction boundary layers". In: *Journal of Fluid Mechanics* 915 (May 25, 2021), A80. DOI: 10.1017/jfm.2021.76.

[4] J. H. M. Fransson and P. H. Alfredsson. "On the disturbance growth in an asymptotic suction boundary layer". In: *Journal of Fluid Mechanics* 482 (May 10, 2003), pp. 51–90. DOI: 10.1017/S0022112003003926.

[5] A. A. Griffith and F. W. Meredith. "The possible improvement in aircraft performance due to the use of boundary layer suction." In: *Royal Aircraft Establishment* 3501 (1936).

[6] J. M. Kay. "Boundary-Layer Flow along a Flat Plate with Uniform Suction". In: *Aeronautical Research Council* (1948).

Mitteilung

Fachgruppe: Turbulenz und Transition

Application of the DLR γ Transition Transport Model in the CFD Software by ONERA, DLR and Airbus (CODA) for Aeronautical Industrially Relevant Flows

V. Togiti
DLR, Institute of Aerodymiacs and Flow Technology, Dept.: $C^2A^2S^2E$
Lilienthalplatz 7, 38108 Braunschweig
vamshi.togiti@dlr.de

Introduction

Reducing aerodynamic drag while improving performance of modern civil aircraft has become crucial to lower energy consumption, thereby reducing environmental pollution. Towards this goal, one of the promising approaches is to employ laminar-flow technologies, in which laminar-turbulent transition is shifted downstream. In aircraft design optimization, modern computational fluid dynamics (CFD) flow solvers capable of predicting accurately the turbulent onset plays a key role. For this, transition transport models are often favored due to their simplicity and integrability in a CFD flow solver.
Recently, a new CFD flow solver is being developed jointly by Airbus, ONERA and DLR with the aim to provide a flow solver with high flexibility and high degree of innovation for a wide range of multidisciplinary applications using modern software techniques and utilizing latest HPC architectures. The new flow solver CODA (CFD by ONERA, DLR and Airbus) [1] operates on unstructured grids employing cell-centered schemes. It combines second-order finite volume and higher-order Discontinuous-Galerkin (DG) methods. The new generation flow solver addresses efficient utilization of current and upcoming high-performance computing cluster.
In CODA, for predicting transitional flows accurately, the DLR γ transition transport model [2] is implemented and assessed for various canonical test cases. The model can predict the transition caused by Tollmien-Schlichting instabilities, laminar separation and crossflow instatbilities. In CODA, the γ transition transport model is coupled with the SA-neg and SST k-ln(ω) turbulence models. The present work focuses on the application of γ transition transport model for the aeronautical industrially relevant flows.

Results

Numerical investigations are conducted for the flow over a NLF(1)-0416 [3] airfoil and a NLF(2)-0415 infinite swept wing (ISW) [4] using the CODA solver. For the NLF(1)-0416 case, investigations are conducted at a Reynolds number based on chord length of 4 million and Mach number of 0.1 and turbulence intensity of 0.03% for the incidence angles ranging from -6^o to 12^o. For this configuration, at the aforementioned flow conditions, transition occurs due to Tollmien-Schlichting instabilities on the upper side of the airfoil and on the lower side transition is caused by laminar separation. While for the NLF(2)-0415 ISW case, investigations are conducted at Reynolds numbers of 1.9 million and 3.7 million, incidence angle of -4° and the sweep angle of 45°. At these flow conditions, transition occurs due to crossflow instability on the upper side of the wing.
Transition locations delivered by CODA for the NLF(1)-0416 airfoil at different incidence angles are shown in Fig 1(a) and compared with experimental data and TAU predictions. In the experimental data, *'Exp. laminar'* indicates the location up to which a laminar region is observed, while *'Exp. turbulent'* displays the turbulent region. The comparison with the experiments unveils that the transition locations delivered by CODA are within the experimental transitional range, showing agreement with experiments and TAU predictions. The comparison of skin-friction distribution at the incidence angle of 0^o shown in Fig. 1(b) displays CODA delivering c_f distribution almost identical to TAU except in the transition region due to difference in predicted transition location.
For the NLF(2)-0415 case, where the transition is caused by the crossflow instability, the c_f distribution shown in Fig. 2 indicates the skin-friction distribution delivered by CODA agree well with the TAU predictions, including the transition locations.

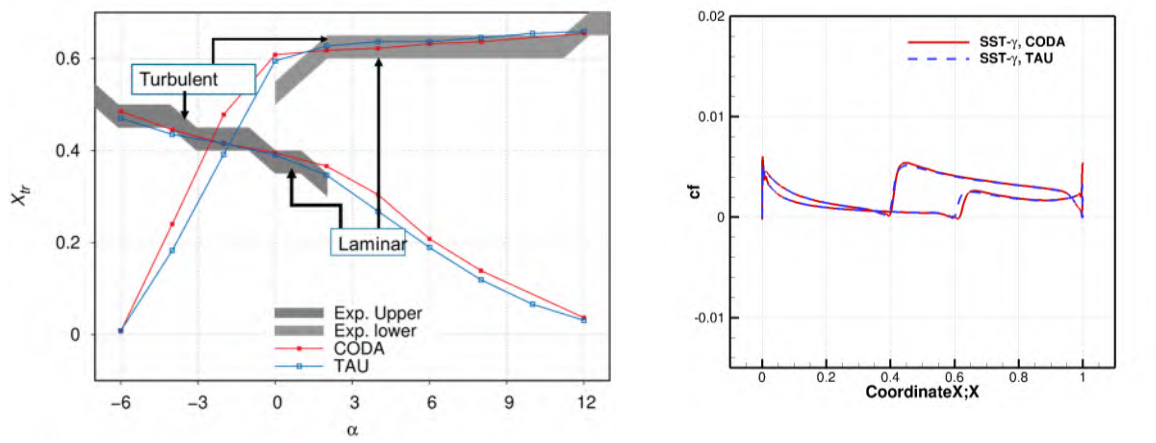

(a) Transition locations (b) Skin-friction coefficient at α = 0°

Figure 1 NLF(1)-0416 airfoil

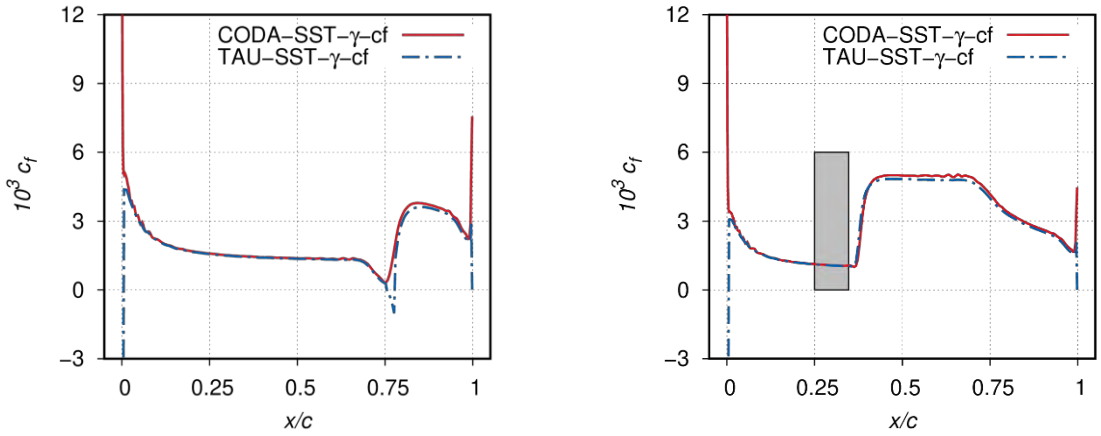

(a) Re 1.9x10 6 (b) Re 3.7x10 6

Figure 2 NLF(2)-0415 infinite swept wing; skin-friction distributions on the upper side.

At the workshop, the application of γ transition transport model for flows over 3D configurations, such as the TU-Braunschweig Sickle Wing and TELFONA pathfinder wing, will be presented and the predictions for the γ model coupled to the SST-k-ln(ω) and SA-neg models delivered by CODA will be compared to experiments and TAU results and discussed.

Acknowlegements: CODA is the computational fluid dynamics (CFD) software being developed as part of a collaboration between the French Aerospace Lab ONERA, the German Aerospace Center (DLR), Airbus, and their European research partners. CODA is jointly owned by ONERA, DLR and Airbus.

References:

[1] Leicht, T., Vollmer, D., Jägersküpper J., Schwöppe, A., Hartmann, R, Fiedler, J., Schlauch T. "DLR-PROJECT DIGITAL-X NEXT GENERATION CFD SOLVER 'FLUCS' ", DLRK-2016, DocumentID: 420027.
[2] François D., Krumbein, A., Krimmelbein, N., Grabe, C., "Simplified Stability-Based Transition Transport Modeling for Unstructured Computational Fluid Dynamics", AIAA SciTech Forum,2022, DOI: 10.2514/6.2022-1543.
[3] Somers, D. M., "Design and Experimental Results for a Natural-Laminar-Flow Airfoil for General Aviation Applications," Tech. Rep. NASA-TP-1861, NASA Langley Research Center Hampton, VA, United States, 1981.
[4] Dagenhart, J. R., and Saric, W. S., "Crossflow Stability and Transition Experiments in Swept-Wing Flow," Tech. Rep.NASA/TP-1999-209344, National Aeronautics and Space Administration, 1999.

Mitteilung

Fachgruppe: „Turbulenz und Transition“

Effects of scalene triangular transverse bars on the structure of turbulent channel flow

Oleksandr Zhdanov, Angela Busse
Fachgebiet Numerische Fluiddynamik, Technische Universität Berlin
Müller-Breslau-Straße 15, 10623 Berlin
angela.busse@tu-berlin.de

Introduction

The fluid dynamic effects of surface roughness strongly depend not only on the height of the features of a rough surface but also on their distribution and shape, i.e., on the topography of a rough surface. Key topographical parameters that are known to have a strong roughness effect include the skewness of the height distribution, the effective slope of the roughness, and the degree of anisotropy of the surface [1]. The term directional roughness is used to describe strongly anisotropic roughness such as rough surfaces composed of ridges or bars which are oriented in the streamwise or the spanwise direction of the mean flow. The present study concerns a special category of directional roughness which breaks the backwards-forwards (or left-right) statistical symmetry of the near-wall turbulent flow. This is achieved by constructing rough surfaces using bars / ridges with scalene triangular cross-sections instead of the widely used symmetric cross-sections such as rectangular, semi-circular or equilateral triangular shapes. The focus of the present study is on the spanwise aligned configuration, which allows to determine the effect of windward slope versus effective slope on the fluid dynamic roughness effect and the structure of near-wall turbulence.

Methodology

Direct numerical simulations of turbulent channel flow are performed for a series of spanwise bar surfaces using the code iIMB [2] which employs an iterative version of the embedded boundary method of Yang & Balaras [3] for resolving the surface roughness. The friction Reynolds number is fixed at $Re_\tau = 550$; periodic boundary conditions are applied in the streamwise and spanwise directions of the channel. In all cases, the upper and lower walls of the channel are entirely covered by the triangular bars (see figure 1 (a)). The bar height is fixed to 8% of the channel half height. A wide range of triangular shapes has been investigated to cover several effective slopes ($ES = 0.167$ ... 0.5) as well as most of the possible range of windward face angles α up to $\alpha = 90°$.

Results and Discussion

Conventionally, the influence of surface slope on the fluid dynamic roughness effect has been parametrised using the effective slope (or frontal solidity). However, the present data demonstrate that for surfaces with a leeward – windward slope imbalance these parameters are not sufficient to capture the roughness effect, since at fixed effective slope the Hama roughness function ΔU^+ shows a strong dependency on the windward face angle [4] (see also figure 1 (b)). A clear signature of the windward face angle can also be observed in the Reynolds and dispersive stress statistics, as well as spanwise spectra of the streamwise turbulent velocity fluctuations where a secondary peak emerges for higher windward face angles (see figure 1 (d)).

Conclusions and Outlook

The present results for rough surfaces with imbalanced windward and leeward slopes demonstrate that the windward slope / face angle is an important parameter to consider in addition the effective slope / frontal solidity of a rough surface. The windward slope significantly affects not only the resulting downward shift in the mean velocity profile but also influences the structure of the near-wall turbulence. This investigation is ongoing and will be extended by conducting further spectral analysis of the near-wall turbulent fluctuations and by considering the effect of windward versus effective slope on ejection and sweep events using local and global quadrant analysis.

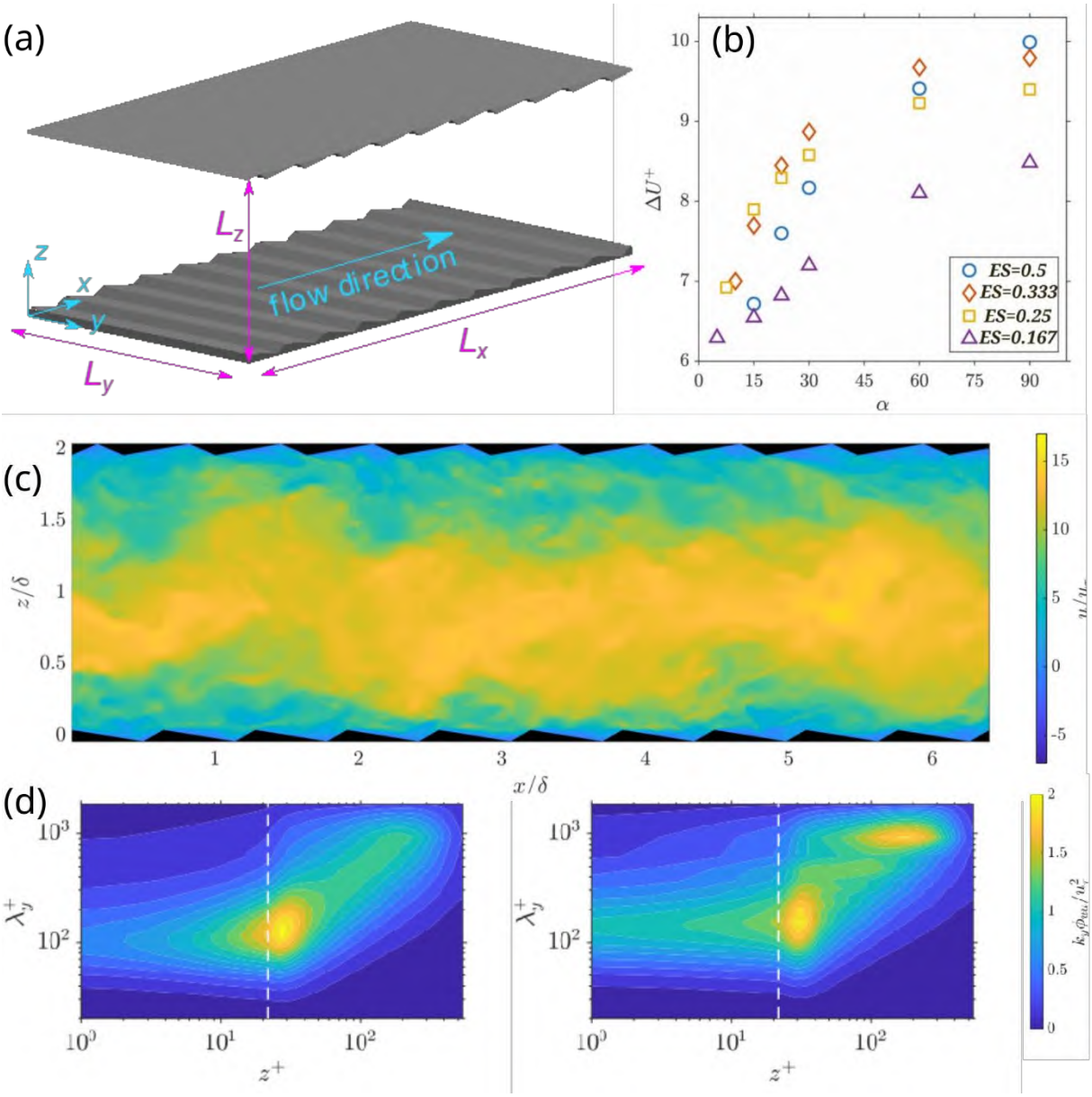

Figure 1 (a) Schematic representation of the flow domain; (b) roughness function as a function of windward face angle; (c) visualization of instantaneous streamwise velocity in a longitudinal cross-section ($ES = 0.25$, $\alpha = 30°$); (d) spanwise spectra of streamwise velocity fluctuations for $ES = 0.167$ and $\alpha = 5°$ (left) and $\alpha = 90°$ (right).

References

[1] Chung, Hutchins, Flack & Schultz, Annual Review of Fluid Mechanics 53:439-71 (2021)
[2] Busse, Lützner & Sandham, Computers & Fluids 116, 129–147 (2015)
[3] Yang & Balaras, Journal of Computational Physics 215(1):12–40 (2006)
[4] Zhdanov, Jelly & Busse, International Journal of Heat and Fluid Flow 116:109897 (2025)

Mitteilung

Fachgruppe: Windenergie

Sound Directivity Measurement at The WiValdi Research Wind Park

Alexandre Suryadi*, Philipp Seelemeyer, Heino Bucholz, Michael Pott-Pollenske, Shy-Yea Lin, and Michaela Herr
Institute of Aerodynamics and Flow Technology
Lilienthalplatz 7 38108 Braunschweig
*alexandre.suryadi@dlr.de

Wind turbine acceptance continues to be a subject of considerable debate, primarily due to concerns regarding noise emissions. While advancements in modern wind turbines have significantly reduced mechanical noise, aerodynamic noise has become the predominant issue. Key topics within wind turbine aeroacoustics include infrasound, low-frequency noise, and amplitude modulation (AM). Amplitude modulation arises from blades encountering varying wind speeds at different elevations, as well as changes in sound directivity perceived by stationary observers as the blades rotate. This effect modulates trailing-edge noise, resulting in a characteristic "swish" at the blade-passing frequency. Effective mitigation of this phenomenon necessitates the development of designs for low-noise blade and noise mitigating add-ons. To complete the design cycle, a robust noise prediction tool needs to be developed and validated. One such tool was presented in Ref. [1].

To address the validation process, directivity measurements were undertaken at the WiValdi Research Wind Park (DLR Krummendeich) utilizing twelve GPS-synchronized microphones positioned at 30-degree intervals and 100 meters from the OPUS 2 wind turbine (4.2 MW Enercon E115, 115-meter rotor diameter), see Figure 1. With the exception of the reduced distance, which was chosen to enhance signal-to-noise ratio, the arrangement of an ½ inch microphone covered by a wind ball on top of a 1-meter, 1-centimeter-thick wooden base plate conformed to IEC 64100-11 standards [2]. The measurement campaign occurred on 19 February 2025, between 09:45 and 12:00 UTC; the OPUS 2 turbine operated until 11:00, after which it was rendered inoperative for 48 minutes, followed by a single start-stop cycle. Meteorological data were collected via a GPS-synchronized wind cup and vane installed on a met mast situated 715 meters from the turbine. Throughout the measurement, the OPUS 1 turbine was not operational.

A two-minute segment was selected under steady atmospheric and turbine operating conditions. Signal processing comprised short-time Fourier transform analysis (Hann window, 50% overlap; temporal and frequency resolutions of 43 ms and 11.71 Hz, respectively), a 6 dB reduction to correct for sound reflection from the plate base, temporal averaging to remove noise spikes in the spectrum, and averaging over each rotor revolution (4.6 s). Background noise was measured over six minutes to ensure a signal-to-noise ratio exceeding 10 dB in the 200 Hz to 7000 Hz range, with extraneous noise from human activities excluded.

Figure 2 presents two directivity plots of an A-weighted sound pressure level at 1kHz and rotor phases of 74° and 134°, referenced to the blade's vertical and upward orientation (0°). At 74°, Figure *2*(a), sound pressure level peaked towards the east as the blade descended; at 134°, Figure *2*(b), sound levels increased towards the south, though not surpassing the previous peak in Figure 2(a).

The present field measurement effectively captures the dynamics of sound directivity associated with amplitude modulation. Further investigations aimed at correcting for outdoor sound propagation are ongoing, and comparative analyses with numerical noise prediction methods will be addressed in future work.

References

[1] C. Appel, "Noise prediction for wind energy turbines based on CAA methods," in *10th International Conference on Wind Turbine Noise*, 2023.

[2] International Electrotechnical Commision, "Wind Energy Generation Systems - Part 11-2: Acoustic Noise Measurement Techniques - Measurement of Wind Turbine Sound Characteristics in Receptor Position," 2024.

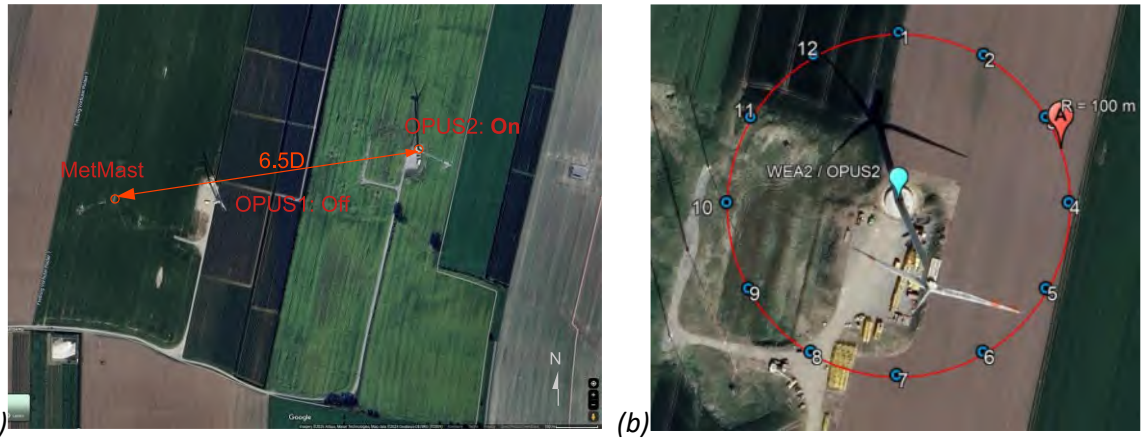

(a) (b)

Figure 1 (a) Site map of WiValdi research wind park (DLR Krummendeich) showing the met mast and OPUS 1 and 2: two 4.2 MW Enercon E115 wind turbines, and (b) the 12 microphone positioned around OPUS2.

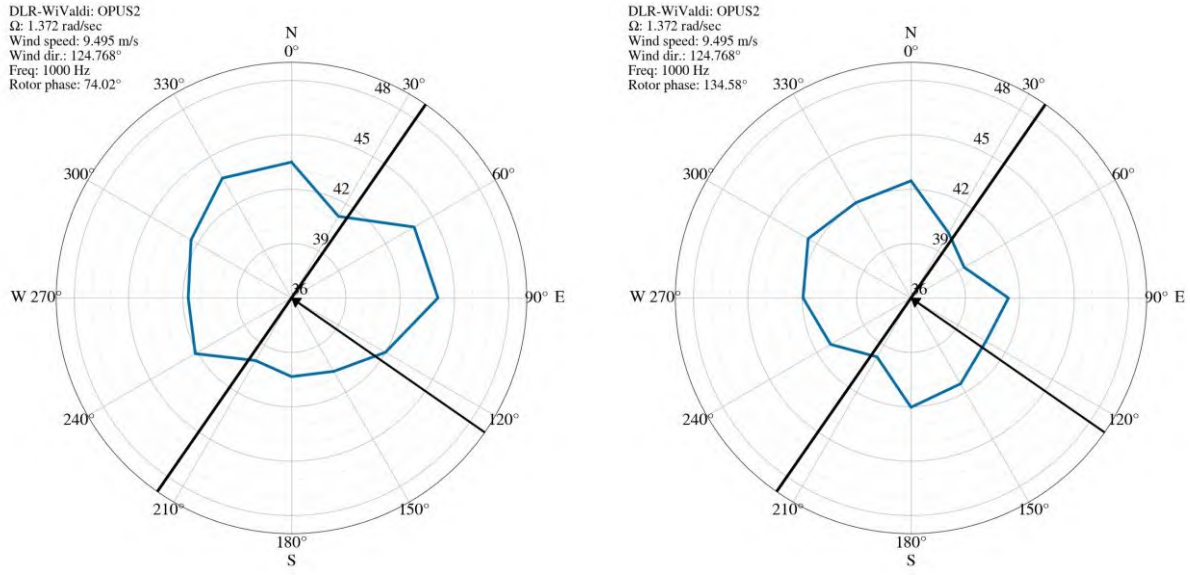

(a) (b)

Figure 2 Directivity plots of an A-weighted sound pressure level of two rotor phases (in blue). The rotor plane is indicated by the black line and the wind direction by the arrow. In (a) sound directivity where one of the blades descending and in (b) the sound directivity where the blade has revolved 60° from (a).

Namensverzeichnis der Autorinnen und Autoren